Transport Process Chemical Engineering Phase II Edition

Kataoka, Kunio

(Citation)
Transport Process Chemical Engineering Phase II Edition:vi, [1]-199

(Issue Date)
2023-11

(Resource Type)
learning object

(Version)
Version of Record

(JaLCDOI)
https://doi.org/10.24546/0100485268

(URL)
https://hdl.handle.net/20.500.14094/0100485268

TRANSPORT PROCESS CHEMICAL ENGINEERING PHASE II EDITION

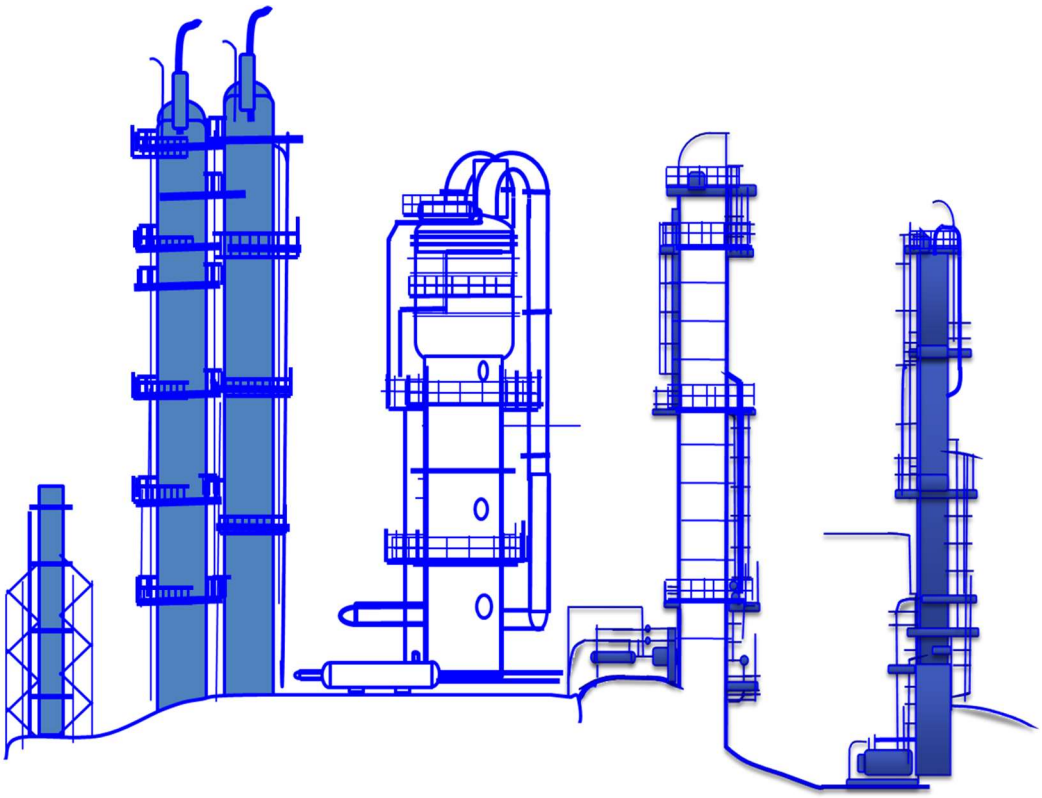

Kunio KATAOKA

PREFACE

This volume is supposed to serve as a progressive book advanced for the second-phase study of "Transport Process Chemical Engineering" in the graduate course of Chemical Engineering.
The previous course in the undergraduate course began with derivation of the fundamental laws in PART I to be followed by understanding the rate-based concept of transport processes. In the successive stage, we learned the models of interphase transport of momentum, heat, and mass applicable to a variety of chemical equipment. In the latter half stage, we considered how to combine these models with the practical design of popular unit operations. As the fundamental consideration of mass transfer problems, we studied gas absorption in Chapter 10 of PART I and distillation in Chapters 11 and 12 of PART II. We treated such complicated processes macroscopically in the form of interphase mass transport, but those simple models did not take into consideration fully the effect of gas or vapor bubbles dispersed in the continuous liquid or vapor phase. In addition, some transport processes accompanied with phase transformation or chemical reaction were treated in the successive chapters. In the remaining portion, some topics of fluid mechanics (e.g. turbulent flow) in transport phenomena were treated to grasp more precisely the role of fluid motion in transport processes.

Several advanced, comprehensive themes are incorporated for enlarging the boundaries of chemical engineering knowledge in this volume.

We will therefore begin the Chapter 21 of PART III with reconsidering the interphase mass transport in the dispersed system. In the following chapter, we will take an interest especially in liquid-liquid extraction as an appropriate example of dispersed system process.

In Chapter 23, we will be concerned a little with the effect of dramatically-changing thermophysical properties of supercritical fluid on the transport process as a new technology.

The primary objective of this volume is to inspire students with courage studying positively some transport processes in relation to the practical issues of energy and resource conservation. The chemical process industries consume a lot of energy for executing various practical chemical processes. Chapter 24 of PART IV will offer some effective energy-saving technologies for global issues of energy conservation from a thermodynamic viewpoint. In particular, the heat pump technology is worthy to be studied. As its example, we will try to understand the heat pump technology for a distillation plant. There an example of innovative development due to HIDiC technology for practical energy saving problems will be reviewed. This volume will pay a little bit bigger attention to the study of concrete concepts of practical chemical equipment design. In Chapter 25, as an example, it will be instructive to reconsider the concept of the practical design of a real packed distillation column from a viewpoint of simultaneous interphase transfer of enthalpy and mass. This design concept is based upon the control volume consideration which bridges the gap between the ideal and real chemical equipment design models.

In the next chapter (Chapter 26), we had better consider some topics in thermal engineering from a thermodynamic viewpoint. When the transport process engineering deals with very complicated processes, we are very often saved by the concept of thermodynamics based on a quasi-static change from an ideal state to another ideal state. The practical design of steam ejectors will be treated based on the thermodynamical concept because the transport phenomena occurring in an ejector are too complicate to analyze precisely.

In Chapter 27, we will study several examples of visualization techniques as to how to observe various dynamic transport phenomena.

It can be considered to be very interesting to observe time-dependent and/or local flow structures accompanied with heat and mass transfer. The observation experience of this kind will be a help to our analytical understanding of the chemical engineering fundamentals.

In the final chapter, we would like to end this course considering some nonlinear dynamics in relation with the instability and complex dynamic processes accompanied with liquid-phase chemical reactions.

This course makes it an educational rule to encourage readers and/or students to make efforts for how to make creative problems rather than for how to solve questions.
We would like to emphasize that it is much more important to make creative problems than to solve given problems.

We would not deny that AI (Artificial Intelligence) programs can answer a variety of questions intelligently, present an appropriate advice, and make deductions about real-world facts. When the AI machine receives a new observation, that observation is classified based on his previous experiences for integrating a wide range of problem-solving techniques. The AI does not work unless any problems are given. There is an undesirable possibility that the AI may give us an inappropriate answer from the insufficiently accumulated databases.

We emphasize that it is of great importance how to accumulate various useful actual data and facts observed into the data bases of the AI not only for machine learning but also for data mining. Machine learning has intimate relations with optimization, e.g. minimization of some loss function or maximization of efficiency in transport processes. Data mining may give knowledge discovery in data bases, e.g. discovery of unknown properties in the transport process data.

Human intelligence stands on mind, consciousness and aspiration. It is human beings that create many challenging problems throughout industry and academia. From that consciousness, we are also studying how to make creative problems in this kind of chemical engineering courses.

It is hoped that this volume will provide a valuable aid to those who are interested in more challenging creative problems.

If a reader wants to understand the fundamental ideas and/or concept of the preceding volume for the respective topics of this volume, he can access the following URL web site for the previous volume:

Kansai Chemical Engineering: https://www.kce.co.jp/en/library
Kobe University: https://.doi.org/10.24546/90008260

KUNIO KATAOKA
*Emeritus Professor
Dept. of Chemical Science and Engineering,
Kobe University
*Honorary Advisor
Kansai Chemical Engineering Co., Ltd.

Kobe
November 2023

CONTENTS

PART Ⅲ

PART Ⅳ

PART Ⅲ

CHAPTER 21

TRANSPORT PROCESSES IN DISPERSED SYSTEMS

21.1 Transport Phenomena in Particles/Droplets Suspended or Dispersed in a Flowing Fluid

This course is basically concerned with the macroscopic or bulk behavior of fluids rather than with the microscopic or molecular behavior. This is the concept of a continuum. Even in this viewpoint, there are quite a few dispersed systems used for various industrial purposes: small liquid or solid particles suspended in gas (e.g. aerosol), fine liquid droplets in liquid (e.g. emulsion), solid-in-liquid slurry, and liquid-liquid and/or solid-liquid colloids.

For example, we can consider a liquid mixture agitated in a tank, which consists of many liquid droplets/gas bubbles/solid particles suspended in an agitated bulk liquid. This kind of flow systems are very often utilized for various chemical reaction, extraction, absorption, and crystallization processes. Especially in case that the number of suspended solid particles and the solid percentage are very large, the dispersed system should be regarded as a slurry. We should consider the effective physical properties such as apparent viscosity resulting from the interaction of suspended particles.

Furthermore, if the size of particles or droplets is very small, the dispersed system is called “colloid,” which can be defined as a mixture in which one substance consisting of microscopically dispersed insoluble particles/droplets is suspended in another substance. The difference between the solution and colloid is that a colloid has a dispersed phase and a continuous phase, while in a solution, the solute and solvent constitute only one phase. Therefore, the interface between the dispersed particle/droplet and the continuous phase is a very important factor.

Firstly, we will begin by studying the basic properties of dispersed system.

21.1-1 Solid or liquid particles suspended in a flowing fluid

Heat or mass transfer between a fluid and suspended particles is very often encountered in various industrial situations. Firstly only for simplicity, heat and mass transfer from solid particles suspended in a fluid flow will be studied here. Beside the physical properties of solid and fluid, another important factor, i.e. the shape of particles can be treated as sphere of equivalent diameter.

As we already learned in Chapter 9.7-3, the heat transfer around a submerged sphere in a uniform flow field of velocity v_∞ is given by the following Ranz and Marshall correlation[1)]:

$$\frac{h_m D_p}{\kappa_f} = 2.0 + 0.60 \left(\frac{D_p \rho_f v_\infty}{\mu_f}\right)^{1/2} \left(\frac{Cp\, \mu_f}{\kappa_f}\right)^{1/3} \quad 1 < Re < 7 \times 10^4,\ 0.6 < \mathrm{Pr} < 400 \quad (9.7\text{-}8)$$

The similar form of the mass transfer correlation is also given by

$$\frac{k_m D_p}{D_{AB}} = 2.0 + 0.60 \left(\frac{D_p \rho_f v_\infty}{\mu_f}\right)^{1/2} \left(\frac{\mu_f}{\rho_f D_{AB}}\right)^{1/3} \qquad (21.1\text{-}1)$$

These equations indicating an analogy between heat and mass transfer have been obtained for a single droplet or particle placed in a uniform flow field. The Eq.(21.1-1) can be used for analyzing the interphase mass transfer such as evaporation from a liquid droplet, dissolution from a liquid droplet or a solid particle, and deposition to a droplet or particle.

If you want to use the above correlations in an agitated vessel, the fluid velocity v_∞ should be interpreted as a representative relative velocity between the moving particle and the flowing fluid velocity.

Since the structure of the agitated flow is very complicated, it may be a problem what definition should be adopted as the representative relative velocity taking into account the turbulence.

1. Ranz, W. E. and W.R. Marshall, Jr.: *Chem. Eng. Prog.,* vol.48, 141, 173 (1962)

Terminal Velocity

If the size of particles is very small (*e.g.* of the order 0.1 mm), the velocity of the fluid relative to the particle, sometimes called slip velocity, can be taken as the terminal velocity in the gravitational field by using Stokes' law:

$$u_t = \frac{g(\rho_s - \rho_f){D_p}^2}{18\,\mu_f} \qquad Re_p = \frac{\rho_f u_t D_p}{\mu_f} < 2 \qquad (21.1\text{-}2)$$

This indicates the balance between the gravity force accompanied by the buoyancy force and the drag force exerted by the flowing fluid.

For example, a 0.1 mm dia. solid particle of density 2.5×10^3 kg/m^3 falling in water at 20 ˚C should have the following terminal velocity:

$$u_t = \frac{(9.8)(2.5-1)\times 10^3 (0.0001)^2}{18(0.001)} = 0.00817 \ \text{m/s}$$

where

$$Re_p = \frac{(1{,}000)(0.00817)(0.0001)}{0.001} = 0.817 < 2$$

Behavior of a single liquid droplet flying in a hot gas stream

Let us consider a liquid droplet flying in a hot gas stream. In the case of a spray dryer, liquid droplets ejected from a nozzle placed at the ceiling center of the dryer are falling downwards by gravity in contact with an upward-flowing hot gas, in which the droplet size is reducing accompanied with evaporation due to the heat transfer from the hot gas. For the calculation of the droplet trajectory within the dryer vessel and the evaporation time required, we should consider the force balance including the drag resistance force $R\,(R_x,\ R_y)$ and the heat transfer between the falling droplet (temperature T) and the hot gas stream (temperature T_{hg}) taking into account the reduction of droplet size.

We are supposed here to consider the evaporation of the liquid droplet in the first half time period.

It should be kept in mind for spray dryers that the droplet of aqueous solution will undergo the drying process changing into a porous solid particle of solute in the latter half time period.

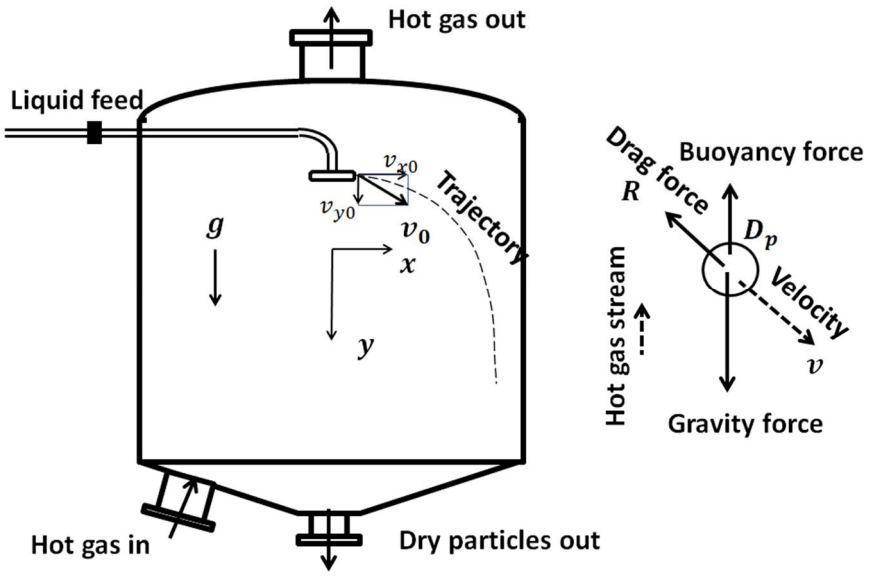

Fig.21.1-1 Trajectory of a liquid droplet falling downward in a spray dryer

Let us consider a single droplet issuing at the initial velocity $v_0\,(v_{x0}, v_{y0})$.

The force balance equation for a single droplet (diameter D_p, density ρ) is given by

$$\left(\rho\,\frac{\pi}{6}\,{D_p}^3\right)\frac{d^2x}{dt^2} = -\rho_{hg}R_x \tag{21.1-3}$$

$$\left(\rho\,\frac{\pi}{6}\,{D_p}^3\right)\frac{d^2y}{dt^2} = -\rho_{hg}R_y + \left(\rho - \rho_{hg}\right)\frac{\pi}{6}\,{D_p}^3 g \tag{21.1-4}$$

The y coordinate is parallel to the gravity acceleration and the x coordinate is horizontal.

The drag resistance force can be expressed as the following function of relative velocity v:

$$R = \frac{\pi}{4}{D_p}^2\,C_D\left(\frac{1}{2}\,v^2\right) \tag{21.1-5}$$

$$v = \sqrt{{v_x}^2 + {v_y}^2} \tag{21.1-6}$$

where C_D is the drag coefficient for spheres moving relative to a fluid with velocity $(v_x,\ v_y)$, which has a meaning similar to friction factor f for pipe flows.

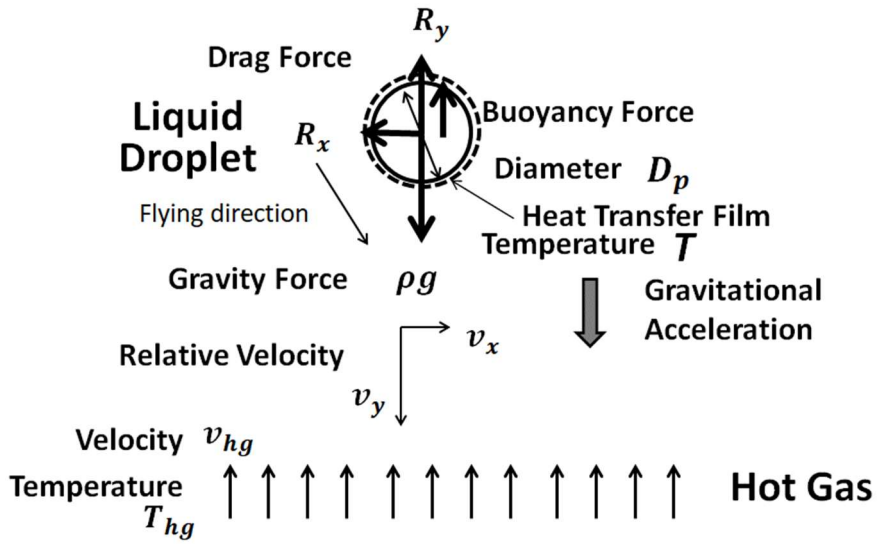

Fig.21.1-2 Force and heat balances of a liquid droplet falling in a hot gas stream

The drag coefficient is known to be a function of Reynolds number[2] (see Chapter 7.5):

$$C_D = f(Re_p)$$

The Stokes law followed by the two empirical correlations is available:

$C_D = \frac{24}{Re_p}$ $Re_p < 0.1$ (Stokes' law) (21.1-7)

$C_D = \frac{18.5}{Re_p{}^{3/5}}$ $2 < Re_p < 500$ (approximate correlation for intermediate region) (21.1-8)

$C_D \cong 0.44$ (constant) $500 < Re_p < 2 \times 10^5$ (Newton's law of drag force) (21.1-9)

2. Bird, R. B., Stewart, W. E., and Lightfoot, E. N., "Transport Phenomena," Wiley, New York, p.193 (1960)

The heat balance equation for a single solid particle can be expressed as

$$\rho Cp \left(\frac{\pi}{6} D_p{}^3\right)\frac{dT}{dt} = h_m(\pi D_p{}^2)(T_{hg} - T) \quad (21.1\text{-}10)$$

One example of the heat balance equations for a single droplet can also be written by

$$-\frac{d}{dt}\left(\rho \frac{\pi}{6} D_p{}^3\right) = h_m(\pi D_p{}^2)(T_{hg} - T)/\lambda \quad (21.1\text{-}11)$$

Here λ is the latent heat of evaporation. The left side indicates the mass reduction of the droplet due to evaporation.

This equation can be obtained assuming constant density ρ of the liquid from the condition that the droplet temperature T is kept constant at the saturation temperature such as the boiling point or the wet bulb temperature.(see Chapter 13.2)

The heat transfer coefficient h_m averaged over the droplet surface can be evaluated by the above Ranz and Marshall correlation.

When the droplet size is reduced to a certain critical size, the droplet terminal velocity becomes equal to the hot gas velocity, and then the droplet becomes stationary. After that, the droplet will turn to flying upward with the hot gas because the terminal velocity of the droplet becomes smaller than the velocity of the hot gas.

For the case of spray dryers in the latter half time period, we should deal with a drying process of a liquid droplet containing solute substances. The droplet is dried to reach a certain particle size of dried porous solid.

[PROBLEM 21.1-1]

A benzene droplet of $D_p = 3$ mm is falling vertically downward at the initial velocity $v_0 = 0$ m/s and temperature $T_p = 80$℃ (boiling point at normal pressure) in the stationary superheated vapor of benzene (normal pressure, $T_p = 105$ ℃) in a big vessel. The size of the falling droplet D_p decreases due to the evaporation by the heat transfer with the superheated vapor. In this case, the liquid droplet is kept at the normal boiling point. Obtain the temporal variation of the droplet velocity and size.

21.1-2 Interphase mass transfer from a single liquid droplet

Fig.21.1-3 shows a single droplet suspended in an extracting solvent S. The droplet contains an extractable component (solute) B and the original solvent (diluent) A. The solute concentration is given by C_{BA}. The bulk concentration of the solute in the solvent S is given by C_{BS}.

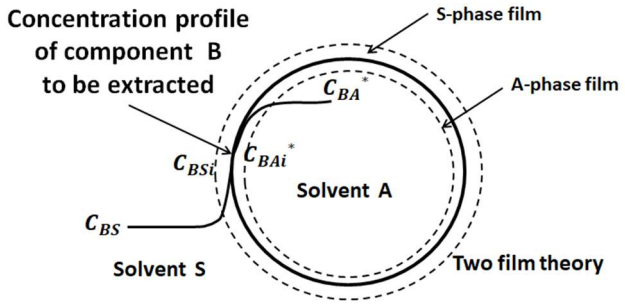

$$N_B = k_B A (C_{BSi} - C_{BS}) = K_B A (C_{BA}^* - C_{BS})$$

Fig.21.1-3 Interphase mass transfer from a single liquid droplet of solvent A suspended in a solvent S with uniform velocity

Regarding the correlation of mass transfer around a sphere, the analogy between heat and mass transfer holds as shown by the Ranz-Marshall equation[3]:

$$\frac{k_{xm} d_p}{D_{AB}} = 2.0 + 0.60 \left(\frac{d_p \rho_f v_\infty}{\mu_f}\right)^{1/2} \left(\frac{\mu_f}{\rho_f D_{AB}}\right)^{1/3} \quad (21.1\text{-}12)$$

[EXAMPLE 21.1-1]

Let us consider how to experimentally evaluate the mass transfer coefficient in the solvent S-phase film around liquid droplets containing a solute B in the original solvent (diluent) A.

(1) Firstly, the extracting solvent S (volume V_S) is put in a turbine-agitator tank.

(2) The original mixture B in A to be extracted has the initial concentration C_{BA0} in mass %. By using a pipette-type droplet feeder, its liquid droplets of approximately constant size d_p are carefully poured into the solvent S.

(3) The total volume of the original mixture supplied amounts to V_A.

Therefore, the total number N of droplets fed is given by

$$N = V_A/(\pi/6)\, {d_p}^3 \quad (21.1\text{-E1})$$

It can be assumed for simplification that the number of uniform-size droplets are suspended in the continuous phase solvent S with uniform velocity.

At time $t = 0$, the liquid extraction is started by rotating the turbine agitator at a rotation number for the droplets so as not to be collided and broken up.

The suspended droplet size can be assumed constant during the whole extraction period. We also assume an isothermal condition.

Explain how to estimate the film coefficient of mass transfer by assuming uniform concentration of B inside those droplets.

Solution:

Let us pay attention to a single droplet being suspended in the solvent S.

Only for simplicity, we assume uniform velocity stream with the relative velocity (slip velocity) U_s between the droplet and the ambient fluid. For example, the representative velocity of the agitated liquid should be defined as the time-averaged turbulence intensity.

We can also regard U_s as the terminal velocity.

In this condition, time-dependent mass balance can be expressed as

$$-(\pi/6)\, {d_p}^3 \frac{dC_{BA}}{dt} = k_{BS} \left(\pi {d_p}^2\right) (C_{BSi} - C_{BS}) \quad (21.1\text{-E2})$$

$$V_S\, C_{BS} + V_A\, C_{BA} = V_A\, C_{BA0} \tag{21.1-E3}$$

where k_{BS} is a S-phase film coefficient of mass transfer around the droplet. For simplification, these volumes V_S, V_A of the two phases can be assumed to be constant during the whole extraction period. The concentration B in the S-phase will increase with time while the concentration B in the A-phase droplet will decrease as the extraction proceeds.

As distinct from Fig.21.1-3, we assume the concentration of solute B kept uniform inside the droplet.

Since the uniform concentration of component B in the droplet is in equilibrium with the interfacial concentration C_{BSi}, we assume a linear equilibrium relationship given by a distribution coefficient K in the limited range of solute concentration:

$$C_{BSi} = K\, C_{BA} \tag{21.1-E4}$$

Here the distribution coefficient K is defined as the solute concentration ratio of the extract phase to the raffinate phase in an equilibrium condition.

In a limited concentration range of solute B, *K* can be assumed to be constant.

Substituting Eq.(21.1-E3) with Eq.(21.1-E4) into Eq. (22.1-E2),

$$-\frac{d\, C_{BA}}{dt} = \frac{6\, k_{BS}}{d_p}\left(K + \frac{V_A}{V_S}\right)\left[C_{BA} - \frac{(V_A/V_S)}{K + (V_A/V_S)}\, C_{BA0}\right]$$

That is

$$-\frac{d\, C_{BA}}{dt} = a(C_{BA} - b) \tag{21.1-E5}$$

where

$$a = \frac{6\, k_{BS}}{d_p}\left(K + \frac{V_A}{V_S}\right) \quad \text{and} \quad b = \frac{(V_A/V_S)}{K+(V_A/V_S)}\, C_{BA0} \tag{21.1-E6}$$

I.C. at $t = 0$ $\quad C_{BA} = C_{BA0}$

The following solution is obtained

$$C_{BA} - b = (C_{BA0} - b)\exp(-at)$$

Or

$$\frac{C_{BA} - b}{C_{BA0} - b} = \exp(-at)$$

$$\frac{C_{BA} - \frac{(V_A/V_S)}{K+(V_A/V_S)} C_{BA0}}{C_{BA0} - \frac{(V_A/V_S)}{K+(V_A/V_S)} C_{BA0}} = \exp\left[-\frac{6\, k_{BS}}{d_p}\left(K + \frac{V_A}{V_S}\right)t\right] \tag{21.1-E7}$$

If we plot the experimental data of the time-dependent solute concentration C_{BA} as in semi-logarithmic coordinates of Fig.21.1-E1, the film coefficient of mass transfer k_B can be evaluated from the slope of experimental line

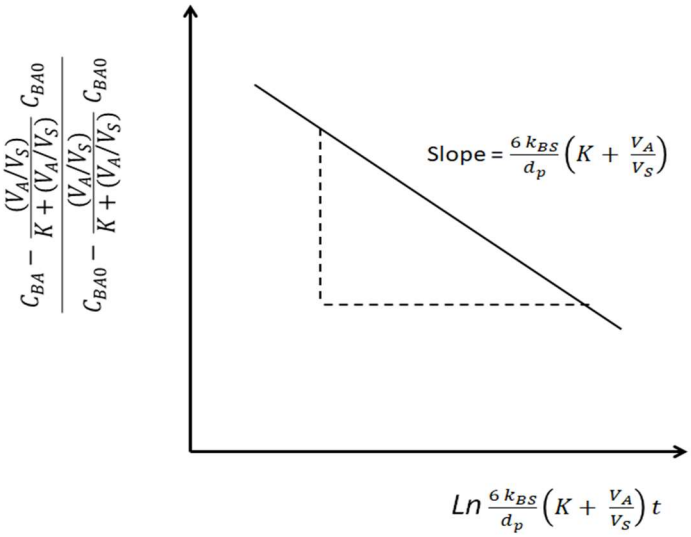

Fig.21.1-E1 Calculation of mass transfer coefficient from the slope of the straight line plotted in the semi-logarithmic coordinates

It should be kept in mind that the above example should be regarded as a simplified case of batch operation with an assumption of smooth mass transfer from a single droplet suspended in a mild stream of the extracting solvent.

The mass transfer coefficient k_{BS} can be expressed as the Sherwood number:

$$Sh_{dp} = k_{BS}d_p/D_{BS}. \tag{21.1-13}$$

For a simple case, the Sherwood number can be considered to depend on the droplet Reynolds number as follows:

$$Sh_{dp} = a\,{Re_{dp}}^{b}{Sc_c}^{d} \tag{21.1-14}$$

When Re_{dp} is sufficiently low, the following Ranz and Marshall equation[3] can be applied with an assumption of the Stokes' terminal velocity u_t.

$$\frac{k_{BS}d_p}{D_{BS}} = 2.0 + 0.60\left(\frac{d_p\,\rho_{ex}\,u_t}{\mu_{ex}}\right)^{1/2}\left(\frac{\mu_{ex}}{\rho_{ex}D_{BS}}\right)^{1/3} \tag{21.1-15}$$

where ρ_{ex}, μ_{ex}, D_{BS} are liquid density, viscosity, and diffusivity of the extract phase.

3. Bird, R. B., Stewart, W. E., and Lightfoot, E. N., "Transport Phenomena," Wiley, New York, p.647 (1960)

However in the flow condition of agitated vessel, the Reynolds number of turbine agitator may be adopted as follows:

$$Re_{dp} = \frac{\rho_{ex}d^2N}{\mu_{ex}} \tag{21.1-16}$$

where d, N are impeller diameter and rotation number of the turbine agitator.

When the Reynolds number is very low, there is a possibility of obtaining the following simple correlation:

$$\frac{k_{BS}d_p}{D_{BS}} = a\left(\frac{\rho_{ex}d^2N}{\mu_{ex}}\right)^{1/2}\left(\frac{\mu_{ex}}{\rho_{ex}D_{BS}}\right)^{1/3} \quad (21.1\text{-}17$$

According to the literature, many empirical correlations are available for the film coefficient of mass transfer k_{BS} around a droplet.

For the film coefficient of mass transfer k_{BS} around droplets suspended in an agitated stream, the following empirical equation is also available[1]:

$$\frac{k_{BS}D}{D_{BS}} = 0.052\left(\frac{d^2N\,\rho_c}{\mu_c}\right)^{0.833}\left(\frac{\mu_c}{\rho_c D_{BS}}\right)^{0.5} \quad (21.1\text{-}18)$$

where D is the agitated tank diameter, d the diameter of impeller, N the rotation number of agitator, ρ_c, μ_c, and D_{BS} the density, and viscosity, and diffusivity of the continuous phase.

1) Barker, J.J. and Treybal, R.E., *AIChE Journal*, **6**, 289 (1960)

For a single rigid droplet suspended in the uniform stream with slip velocity u_p, the Ranz-Marshall correlation can be applied for a single rigid droplet:

$$Sh_{BS} = 2 + C\,Re_p{}^{1/2}Pr_S{}^{1/3} \quad (21.1\text{-}19)$$

Here the coefficient C varies slightly from 0.6, depending on investigators.

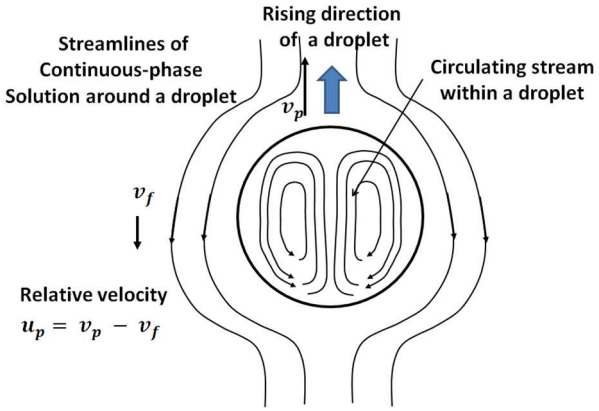

Fig.21.1-4 Circulating stream inside a liquid droplet rising in a continuous-phase liquid

In the case when such a circulating flow exists inside a droplet, another film coefficient of mass transfer k_{BA} in the droplet diluent A phase is added in the consideration based on the two-film theory:

$$\frac{1}{K_E} = \frac{1}{k_{BS}} + \frac{m}{k_{BA}} \quad (21.1\text{-}20)$$

This implies that the overall resistance $1/K_E$ to mass transfer consists of the S-phase film resistance and the A-phase film resistance lying in series.

In this condition, the mass transfer coefficient k_{BS} is given by taking into account the effect of inside-circulating flow as:

$$Sh_{BS} = 2 + \left(4/\sqrt{6\pi}\right)f_e{}^{1/2}\,Pe_{pS}{}^{1/2} \quad (21.1\text{-}21)$$

Here the Peclet number for mass transfer is defined as $Pe_{pS} = Re_pSc_S = d_pu_p/D_{BS}$, where the relative velocity u_p between the droplet and the continuous phase S is used.

You can understand that Eq.(22.1-15) is similar in form to Ranz-Marshall equation for a rigid particle.

The coefficient f_e is a coefficient modifying the Peclet number talking into account the effect of inside circulating flow.

Regarding the film coefficient k_{BA} of mass transfer inside a droplet, various equations are reported.

One simple equation is a function of the droplet Peclet number defined as

$Sh_{BA} = \left(4d_p/l\right)\varphi_e \, Pe_{pA}$ and $Pe_{pS} = Re_p Sc_A = d_p u_p / D_{BA}$ (21.1-22)

The coefficient φ_e is also a coefficient modifying the droplet Peclet number and l is the characteristic moving distance of droplets. The functional form of those coefficients f_e and $\left(4d_p/l\right)\varphi_e$ are too complicated to discuss in detail here.

21.1-3 Surface tension acting on liquid droplets

Surface tension is acting on the surface of droplets in contact with gas or immiscible liquid.

As shown in Fig.21.1-5, within the bulk liquid, interior molecules have many neighboring molecules, so that intermolecular forces work every direction and keep balance. However the molecules at the surface are pulled inward and sideways by other molecules, but not outward away from the surface. The tangential force is referred to as the surface tension. The surface tension works to reduce the surface area to a minimum. Droplets are pulled into a spherical shape by the imbalanced cohesive forces. This force balance creates some internal pressure. That is, if the pressure on the inside surface differs from the outside pressure, the pressure difference times surface area results in additional pressure rise. Therefore the boiling point of the droplet liquid becomes somewhat higher than the environment.

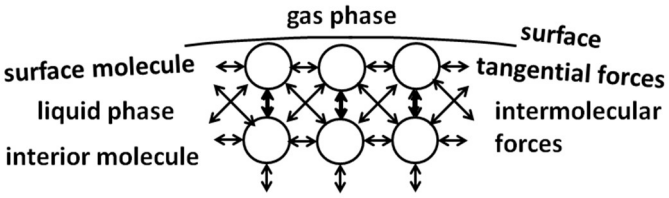

Fig.21.1-5 Generation of surface tension from intermolecular force balance near the gas-liquid interface of a droplet

Water has a surface tension (72.8 mN/m at 20°C) higher than most other liquids.

The pressure difference between inside and outside of the spherical droplet has the following relation with the curvature radius R:

$\Delta p = 2\left(\sigma/R\right)$ (21.1-23)

This equation can be derived by the following force balance:

$(\pi/4)\ D^2 \Delta p = \pi D \sigma \ \rightarrow \ \Delta p = 4\sigma/D = 2\left(\sigma/R\right)$

For the case of water at 20°C and 1 atm, a water droplet of 1 mm diameter has 145.6 Pa in the internal pressure rise.

Surfactants adsorbed on the outside surfaces of droplets can keep them stable without agglomeration in a liquid bulk. Surfactants reduce the surface tension of water. Emulsions are a kind of colloid in which surface tension plays a role.

21.2 Structure of Dispersed System

21.2-1 Effect of surfactant adsorbed on liquid surface

Due to the adsorption of surfactant molecules on the liquid surface, the droplet surface is very much higher in surfactant concentration than the continuous liquid volume phase.

A simplest emulsion structure is accompanied with ions such as OH^- adsorbed on the emulsion droplet producing a charge. A dilute O/W emulsion is stabilized due to the electrostatic repulsion.

As shown in Fig.21.2-1, a surfactant molecule has a long hydrophobic tail and a hydrophilic head of surfactant. For the case of cationic surfactants and anionic surfactants, the surfactant head has surface active ions.

Surfactants adsorbed to the surface improve the dispersion in the oil and water phases.

Molecular alignment at gas-liquid or oil-water interface forms monolayer structure.

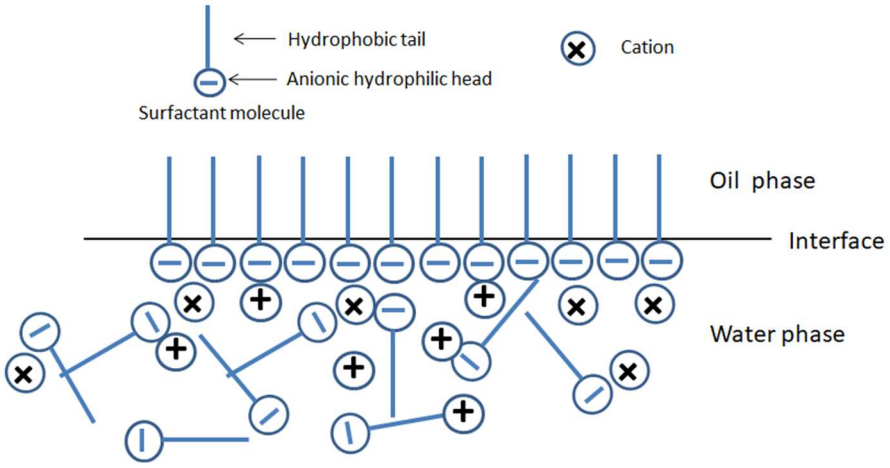

Fig.21.2-1 Monolayer structure due to molecular alignment at oil-water interface

Regarding the emulsion formation by using turbulent flows, viscous forces of the turbulent flow cause shear stresses to act on the interface between the droplets and the continuous phase. If the turbulent eddies are much larger than the droplets, they exert shear stresses on the interface of droplets, and then cause the droplet breakup into smaller droplets.

21.2-2 Alignment structure of adsorbed surfactant molecules

When the droplet surface is fully covered with adsorbed surfactant molecules, micelles are formed.

A micelle is an aggregate of surfactant molecules dispersed in a liquid colloid. That is, micelles form only when the concentration of surfactant is greater than the critical micelle concentration (CMC), and the temperature of the system goes beyond the critical micelle temperature. Regarding a normal phase micelle (oil-in-water micelle), the micelle in aqueous solution forms an aggregate with the hydrophilic head region in contact with surrounding solvent (water), confining the hydrophobic tail regions inside.

Fig.21.2-2 shows a structure of normal phase micelle of an oil droplet in water, where a fatty acid soap serving as the surfactant forms such a micelle structure.

For example, when the concentration of stearate ions goes beyond the critical value (CMC), stearate ions come inside the bulk phase with their heads ($-COO^-$) pointing outward and the tail pointing toward the center of droplet sphere. This aggregation forms the ionic micelles in the continuous phase solution.

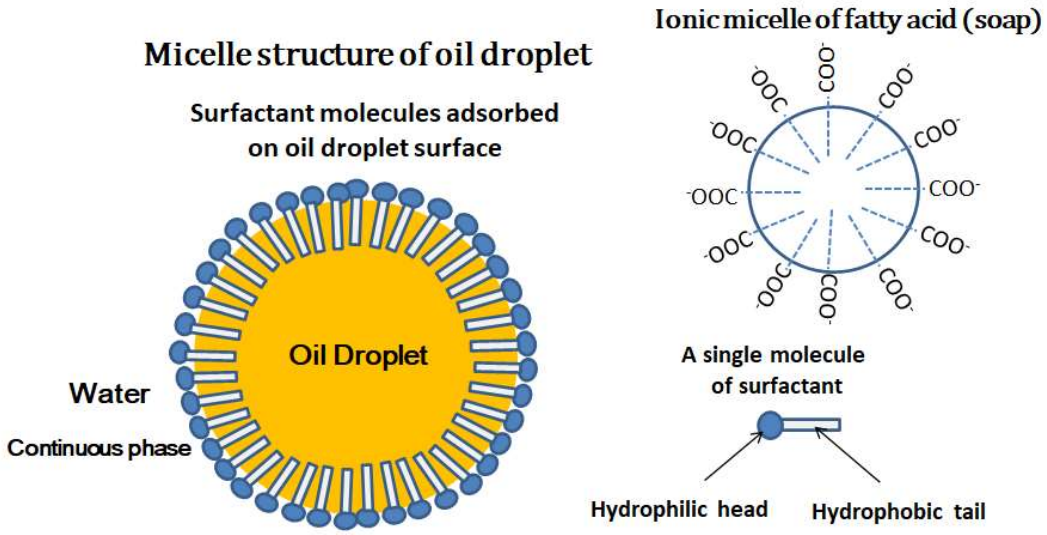

Fig.21.2-2 Structure of normal phase micelle of an oil droplet and ionic micelle of fatty acid.

Inverse micelles have the hydrophilic headgroups directed to the center with the hydrophobic tails extending out (water-in-oil).

The CMC (Critical Micelle Concentration) is minimum concentration at which surfactant molecules begin to form micelles in the continuous phase solution.

21.3 Viscosity of Dispersed Systems

21.3-1 Definition of viscosity

In Chapter 2.5, we dealt with non-Newtonian Fluids. Fig.21.3-1 (or Fig.2.5-1) shows their rheological models indicating the relation between the shear stress and the velocity gradient (i.e. rate of strain). We know that several kinds of fluids which do not obey Newton's law of viscosity have an important relation with the dispersed system to be studied in this chapter.

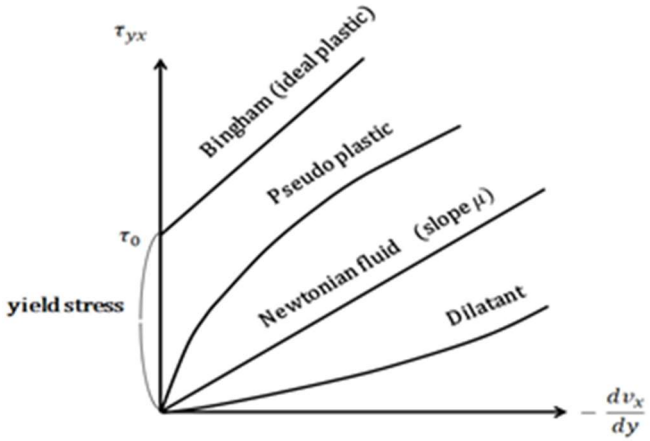

Fig.21.3-1. Schematic picture of shear stress against velocity gradient for non-Newtonian fluids

For simplicity, in this chapter, the steady-state rheological behavior of most fluids is expressed by the following generalized form:

$$\tau_{yx} = -\eta \frac{dv_x}{dy} \qquad (2.5\text{-}1)$$

Here the proportional constant η is called "apparent viscosity." If η is independent of the rate of shear, the behavior reduces to Newtonian, with $\eta = \mu$.

21.3-2 Slurry and solid-in-liquid mixtures[1)]

A slurry consists of solid particles suspended in a liquid. For example, a slurry transporting pipeline is used for a coal mine (mixture of coal and water) from its pond to its destination such as a coal power plant. When the particle concentration of solid goes beyond 10 wt%, the slurry generally begins to behave as non-Newtonian.

The density of slurry can be calculated by the following equation:

$$\rho_m = \frac{100}{(C_W/\rho_S)+[(100-C_W)/\rho_L]} \qquad (21.3\text{-}1)$$

where

ρ_m: density of slurry mixture (kg/m^3)
C_W: solid concentration (wt%)
ρ_S: density of solid in mixture (kg/m^3)
ρ_L: density of liquid in mixture (kg/m^3)

If the concentration is expressed in volume per cent,
C_V : concentration of solids by vol%
Φ: volume fraction, $\Phi = C_V/100$

The viscosity of a dilute suspension can be approximated by the Einstein equation:

$$\mu_m = \mu_L\,(1 + 2.5\,\Phi) \quad \text{for} \quad \Phi < 0.01 \qquad (21.3\text{-}2)$$

For higher-concentration suspension, the viscosity of the slurry is given by the modified equation[1)]:

$$\mu_m = \mu_L\,[1 + 2.5\,\Phi + 10.05\,\Phi^2 + 0.00273\exp(16.6\,\Phi)] \qquad (21.3\text{-}3)$$

---

1. Thomas, D.G., Transport characteristics of suspension: VIII A note of the viscosity of Newtonian suspensions of uniform spherical particles, *J. Colloid Science,* 267-277 (1965)

[EXAMPLE 21.3-1]

Calculate the viscosity of a slurry mixture of solid particles (50 wt%, density= 2,100 kg/m^3) in water.

The density and viscosity of water are given by 1,000 kg/m^3 and 0.001 Pa s

Since $C_W = 50\ wt\%$,

$$\rho_m = \frac{100}{(50/2100)+[(100-50)/1000]} = 1{,}355 \quad (\text{kg/m}^3) \qquad (21.3\text{-E}1)$$

The volume per cent is

$$C_V = 50\,(1355/2100) = 32.3\ \text{vol\%} \quad \text{Then} \quad \Phi = C_V/100 = 0.323 \qquad (21.3\text{-E}2)$$

Using the water viscosity $\mu_L = 0.001$ Pa · s,
the viscosity of the slurry calculated by Eq.(21.3-3) becomes

$$\mu_m = 0.001\,[1 + 2.5 * 0.323 + 10.05 * 0.323^2 + 0.00273\exp(16.6 * 0.323)]$$
$$= 3.44 \times 10^{-3}\ \text{Pa} \cdot \text{s}. \qquad (21.3\text{-E}3)$$

This implies that the slurry mixture has 3.4 times the water viscosity.

[PROBLEM 21.3-1]

Consider the production of the iron ore slurry to be supplied to the pelletizing process of a steel maker.

The particles of the iron ore crushed have average size of 40 μm and density of 3,600 kg/m^3. If 40 ton of the iron ore is used for the slurry, how much water (1,000 kg/m^3, 0.001 $Pa \cdot s$) is required for producing the solid concentration of 30 wt%.? Calculate the viscosity of the iron ore-in-water slurry. Only for simplification, the particle shape can be assumed to be spherical. Usually a small quantity of additive is necessary but its effect can also be neglected here.

[PROBLEM 21.3-2]

We would like to prepare a slurry consisting of Magnetite powder in water at 25℃. The solid weight per cent is given by $C_w = 50$ wt%. The Magnetite solid density $\rho_s = 5{,}200\ kg/m^3$.
The average particle size is about 0.3 μm.
Calculate the volume ratio of the slurry Φ, the density of the slurry ρ_m, and the slurry viscosity μ_m.

21.3-3 Bingham plastic fluids

Slurries and emulsions often exhibit the non-Newtonian behavior.
The Bingham model is expressed as

$$\tau_{rz} = -\mu_0 \frac{d v_z}{dr} + \tau_0 \quad \text{if } \tau_{rz} > \tau_0$$
$$\frac{d v_z}{dr} = 0 \quad \text{if } \tau_{rz} < \tau_0 \qquad (21.3\text{-}4)$$

where τ_0 is the yield stress and μ_0 is a Bingham model dynamic viscosity similar to the Newtonian viscosity. (This model is firstly introduced in Chapter 2.5 of PART I)

Similarly to the Newtonian flow model, the pressure drop over the length *L* of a horizontal pipe (Inside diameter *D*) can be expressed in the form of friction factor definition as

$$\Delta p = 4 f \frac{L}{D} \frac{1}{2} \rho {v_{av}}^2 \qquad (21.3\text{-}5)$$

Swamee & Aggarwal[1] propose the following friction factor for laminar Bingham plastic flow:

$$f_L = \frac{16}{Re}\left[1 + \left(\frac{He}{6.22\,Re}\right)^{0.958}\right] \qquad (21.3\text{-}6)$$

The original equation has 64 instead of 16 owing to the different definition of friction factor.
The constant 16 of this equation was modified for the above definition of friction factor.
Here the Hedstrom number is defined for Bingham plastic model by:

$$He = \frac{\rho D^2 \tau_0}{{\mu_0}^2} \qquad (21.3\text{-}7)$$

[EXAMPLE 21.3-2]

A Bingham plastic fluid ($\rho = 1{,}100\ kg/m^3$ at 25℃) is flowing in laminar flow regime with volumetric flow rate 0.0025 m^3/s in a horizontal circular pipe of *D* = 0.10 m. The pressure drop over *L* = 20 m is measured as $\Delta p = 0.07$ MPa. The parameters of Bingham plastic fluid are given as
$\tau_0 = 10$ Pa and $\mu_0 = 0.035\ Pa \cdot s$
Calculate the friction factor in this flow condition.

Solution:

The Hedstrom number becomes

$$He = \frac{\rho D^2 \tau_0}{{\mu_0}^2} = \frac{(1{,}100)(0.10^2)(10)}{0.035^2} = 9.0 \times 10^4 \qquad (21.3\text{-E4})$$

The average velocity is calculated as

$$v_{av} = \frac{V}{(\pi/4) D^2} = \frac{0.0025}{(\pi/4)(0.10)^2} = 0.318 \text{ m/s}$$

The Reynolds number is given by

$$Re = \frac{D v_{av} \rho}{\mu_0} = \frac{(0.10)(0.318)(1{,}100)}{0.035} = 1{,}000 \qquad (21.3\text{-E5})$$

The friction factor by Swamee & Aggarwal[1] is calculated as

$$f_L = \frac{16}{Re}\left[1 + \left(\frac{He}{6.22\,Re}\right)^{0.958}\right] = \left(\frac{16}{1{,}000}\right)\left[1 + \left(\frac{9.0\times10^4}{6.22\times1{,}000}\right)^{0.958}\right] = 0.223 \qquad \text{(21.3-E6)}$$

[PROBLEM 21.3-3]

A Bingham plastic fluid with $\tau_0 = 8.0$ Pa, $\mu_0 = 30$ cP, and $\rho = 1{,}200$ kg/m^3 is flowing isothermally in laminar flow regime in a horizontal circular pipeline of inside diameter $D = 0.20$ m. Calculate the power requirement of the slurry pump for transporting the volumetric flow rate of 0.0040 m^3/s in the pipeline of length 25 m.

---

1. Swamee, P.K. and Aggarwal, N.: doi:10.1016/*j. petrol*.2011.01.015.

21.3-4 Emulsion and liquid-in-liquid mixtures

Usually emulsion viscosity is greater than the viscosity of either the oil or the water. When the concentration of dispersed phase becomes large, the emulsion exhibits non-Newtonian behavior. The effective viscosity of oil-in-water emulsions depends mainly on the volume fraction of dispersed phase and temperature, along with several minor effects, such as shear rate, average droplet size, droplet size distribution, viscosity and density of oil.

Similarly to the slurry viscosity, a simple viscosity correlation of water-in-oil emulsion has the following form:

$$\mu_{mix} = \mu_{oil}\,(1 + 2.5\,\Phi + 10\,\Phi^2) \qquad \text{(21.3-8)}$$

where μ_{mix} is emulsion viscosity, μ_{oil} the viscosity of pure oil (continuous phase), and Φ the volume fraction of dispersed water phase (vol. of water/mixture)

This equation can also be regarded as the modified Einstein equation.

Generally the emulsion viscosity tends to increase with the droplet size decreasing. An empirical correlation of emulsion viscosity with droplet size is reported in the low concentration region for the O/W emulsions.

Fig.21.3-2 shows an experimental result[1)] of the relative viscosity of corn oil-in-water emulsion in relatively low volume fraction of oil phase. Here the relative viscosity η/η_c can be defined as the ratio of emulsion viscosity to the viscosity of continuous phase fluid (water in this case).

The diagram indicates that the emulsion viscosity tends to certainly decrease with emulsion droplet size and increases with total surface area of dispersed phase (Corn oil in water emulsion, Surfactant: fatty acid ester of poly-glycerol, 25℃)[1)]

The total surface area is calculated as the total surface area of all the oil droplets contained in unit volume of emulsion:

$$S = \frac{(\text{surface area of a single droplet})\times(\text{number of droplets contained})}{\text{unit volume of emulsion}} \qquad \text{(21.3-9)}$$

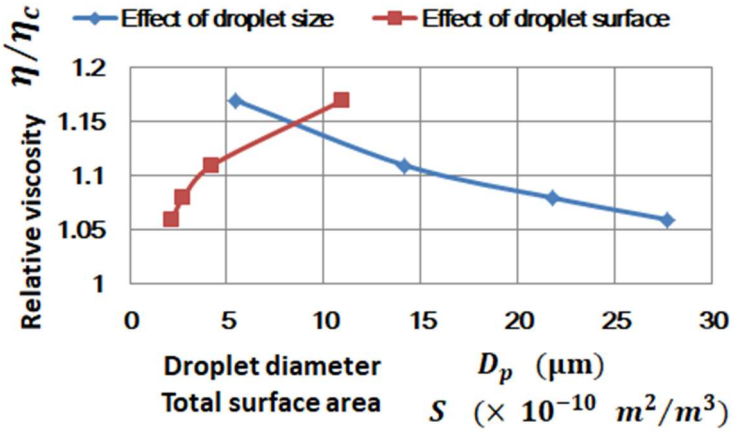

Fig.21.3-2 Effects of droplet size and droplet surface area on viscosity of corn oil-in-water emulsion

1) Asano, Y. and Sotoyama, K., The Viscosity Characteristics of The O/W Emulsions, *Nippon Shokuhin Kagaku Kogaku Kaishi*, Vol. 45, 435-439 (1998)

Inverse emulsion (water-in-oil) is mostly encountered as one of the important problems in oil transporting pipelines. Undesirable effects caused by the emulsions are related to higher viscosity, larger pressure drop, and more difficulty in oil-water separation.

At low concentration of emulsion droplets, the emulsion system can be assumed to behave as Newtonian fluid. When the oil droplet concentration goes beyond a critical volume fraction, the emulsion system will start to exhibit non-Newtonian pseudoplastic behaviors.

The oilfield emulsions behave as shear-thinning or pseudoplastic fluids (i.e., as shear rate increases, viscosity decreases). It is known that there is significant delay in the transition from laminar to turbulent regime in water-in-oil emulsion flows but such transitional delay is not observed for the case of oil-in-water emulsions. It is known that the emulsion exhibits non-Newtonian behavior when the dispersed phase (water) volume fraction becomes greater than approximately 40%. However when the volume fraction of water (dispersed phase) increases above a certain critical value, e.g. 90%, the emulsion "inverts" to an oil-in-water emulsion, and the water, which was the dispersed phase, now becomes the continuous phase.

[PROBLEM 21.3-3]

It is necessary to emulsify 0.02 m^3 of soy bean oil with 0.1 m^3 of water by adding a small quantity of surfactant. The pure soy bean oil has viscosity of 0.054 $Pa \cdot s$ at 25℃.

Calculate the viscosity of soy bean oil-in-water emulsion at 25℃.

The effect of oil droplet size on the emulsion viscosity, which is not so large, may not be taken into account.

[PROBLEM 21.3-4]

For the preparation of emulsion polymerization of styrene monomer, we are planning to make the styrene monomer emulsion by using an agitated tank equipped with turbine-blade agitator. Styrene monomer 0.5 ton (density 902 kg/m^3, viscosity 0.006 $Pa \cdot s$ at 25℃) and 1 kg of sodium dodecyl sulfate as emulsifier agent are used to produce 1 ton of styrene monomer emulsion. The emulsion droplet size is controlled to be 0.1 μm on the average. For simplicity, it can be assumed that double emulsion (water-in-oil-in-water) droplets are not formed.

Calculate the number of emulsion droplets produced, the quantity of water required, the volume

fraction of dispersed phase, and the emulsion viscosity at 25℃.

21.4 Pipe Flow of Dispersed Systems

21.4-1 Pipe flow of solid particles dispersed system

Slurries can be classed as either ”homogeneous” or “heterogeneous”: a homogeneous slurry such as high pulp density slurry does not tend to separate immediately into solid and liquid when it becomes still and a heterogeneous one such as ion-powder slurry tends to separate immediately when its flow is halted. The subject of slurry rheology is quite complex, so we will deal with an example of simple heterogeneous slurry being transported in a horizontal pipeline.

When the velocity of slurry flow reduces to a certain critical value, the solid particles form a bed at the bottom of the pipe. Therefore it is important to avoid settling of solids by keeping the flow velocities above a certain level. This is called “critical slurry velocity” or “limiting settling velocity”. In addition, when the solid concentration becomes above several percent, the friction losses or pressure drops increase above 1.5 ~ 4 times the friction losses of water flow.

The calculation of slurry pipe flows will be studied with the next example.

[EXAMPLE 21.4-1]

We want to transport $M_s = 6$ kg/s of solid powder (density $\rho_s = 2{,}100\ kg/m^3$, particle size $D_p = 100$ μm) with water at 25℃ by using a horizontal pipeline of length $L = 100$ m. A steel pipe with relative roughness $\epsilon/D = 0.001$ will be used. Its inside diameter D should be determined by a trial-and-error method. Fig.21.4-E1 shows a horizontal pipeline for transporting the slurry of solid powder-in-water mixture.

Calculate the inside diameter of the pipeline and the power requirement for pumping the $C_w = 35$ wt% slurry.

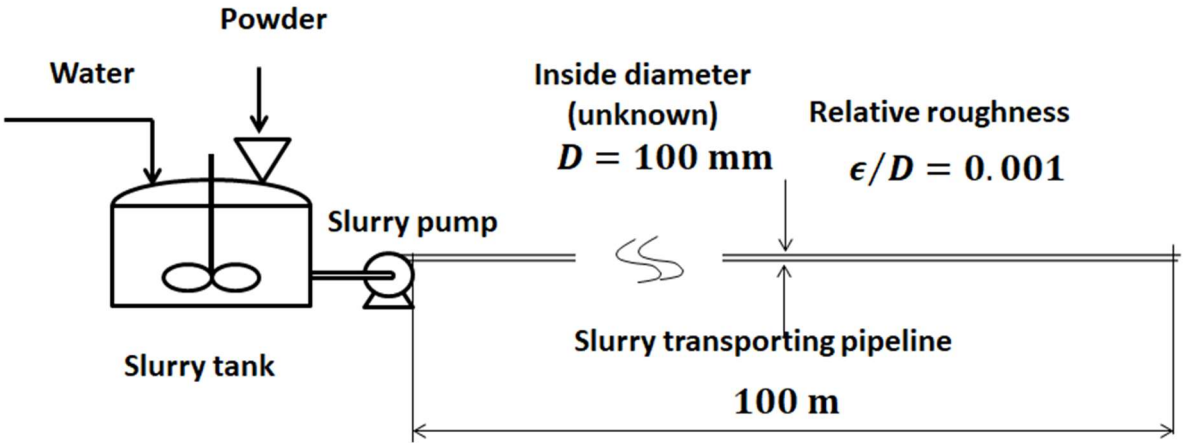

Fig.21.4-E1 Horizontal pipeline transporting slurry mixture

Solution:

We should begin by calculating the water required to add to the solids to achieve the required solid concentration.

The mass flowrate of water required for making the slurry is calculated as

$$M_w = \left(\frac{M_s}{C_w/100}\right) - M_s = \left(\frac{6}{0.35}\right) - 6 = 11.14\ \text{kg}/s \qquad (21.4\text{-E1})$$

The volumetric flow rate of the slurry is

$$Q_{mix} = \frac{M_s}{\rho_s} + \frac{M_w}{\rho_w} = \frac{6}{2100} + \frac{11.14}{1000} = 14.0 \times 10^{-3}\ \text{m}^3/\text{s} \qquad (21.4\text{-E2})$$

The mean density of the slurry is

$$\rho_{mix} = \frac{M_w + M_s}{Q_{mix}} = \frac{11.14+}{14.0\times 10^{-3}} = 1{,}220\ \mathrm{kg/m^3} \quad \text{(21.4-E3)}$$

The volumetric concentration of solid in the slurry is

$$C_V = \frac{(M_S/\rho_S)}{Q_{mix}} = \frac{(6/2100)}{(14.0/1000)} = 0.204 \quad \text{(21.4-E4)}$$

In this condition of the solid concentration, the slurry can be assumed to exhibit Newtonian viscosity.

It is necessary to consider the flow velocity in slurry transport systems to avoid settling of solid particles.

The limiting settling velocity V_{lim} is expressed by the following equation with the Durand factor[1] F_L (dimensionless):

$$V_{lim} = F_L \sqrt{2\ g\ D\ (\rho_s - \rho_L)/\rho_L} \quad \text{(21.4-E5)}$$

This equation can be empirically derived for turbulent flows by considering the following force balance of the downward gravitational force with the upward force acting on particles:

$$F_{down} = (\rho_S - \rho_L) g\ (\pi/6) {D_p}^3 \times (1 - C_V)^n \quad \text{(21.4-E6)}$$

$$F_{up} = \rho_L (\pi/4) {D_p}^2\ {V_{edd}}^2$$

where V_{edd} is the turbulent fluctuation velocity.

From these two equations, we obtain

$$V_{edd} = \sqrt{\frac{(\rho_S - \rho_L)}{\rho_L} g\ \frac{2}{3}\ D_p \times (1 - C_V)^n} \quad \text{(21.4-E7)}$$

The turbulent fluctuation velocity can be related with the limiting settling velocity V_{lim} taking into consideration the power P_{dis} dissipated per unit mass of fluid:

$$P_{dis} = \lambda_L \frac{{V_{lim}}^3}{2\ D} \quad \text{(21.4-E8)}$$

where λ_L is a kind of friction factor (called "Darcy Weisbach friction factor")

Many various models are found in most texts on slurry pumping, if required.

1. Durand, R., The Hydraulic Transportation of Coal and Other Materials in Pipes, Colloq. of National Coal Board, London, pp.39-55 (1952)

Only for convenience and simplicity, the following empirical equation for the Durand factor is utilized:

$$F_L = 4\ {C_V}^{1/5} \left(\frac{D_p}{D}\right)^{1/6} \quad \text{(21.4-E9)}$$

where C_V is the volumetric concentration of the slurry, D_p the particle diameter, and D the pipe inside diameter.

From here, let us start the trial-and-error calculation by assuming the pipe diameter $D = 0.1$ m.

The Durand factor is calculated as

$$F_L = 4\ (0.204)^{1/5} \left(\frac{0.00010}{0.10}\right)^{1/6} = 0.921 \quad \text{(21.4-E10)}$$

Therefore substituting the Durand factor, the limiting settling velocity becomes

$$V_{lim} = (0.921)\sqrt{2\ (9.8)\ (0.10)\ (2100 - 1000)/1000} = 1.61\ \mathrm{m/s} \quad \text{(21.4-E11)}$$

The average velocity of the slurry is given by

$$V_{mix} = \frac{Q_{mix}}{(\pi/4)\ D^2} = \frac{14.0 \times 10^{-3}}{(\pi/4)\ 0.10^2} = 1.78\ \mathrm{m/s} \quad \text{(21.4-E12)}$$

Therefore the result $V_{mix} > V_{lim}$ implies that the assumed pipe diameter $D = 0.1$ m is appropriate for the stable slurry pumping.

The slurry viscosity with relatively high solid concentration is calculated by Eq.(21.3-3) ,

$$\mu_m = \mu_L\,[1 + 2.5\ \Phi + 10.05\,\Phi^2 + 0.00273\exp(16.6\,\Phi)] \qquad (21.3\text{-}3)$$

Here $\Phi = C_V = 0.204$ and $\mu_L = 0.001$ Pa · s in this case.
Then

$$\mu_{mix} = (0.001)[1 + 2.5 \times 0.204 + 10.05 \times 0.204^2 + 0.00273\exp(16.6 \times 0.204)] = 0.00201 \text{ Pa} \cdot \text{s} \qquad (21.4\text{-E13})$$

The Reynolds number is calculated as

$$Re_{mix} = \frac{D\,V_{mix}\,\rho_{mix}}{\mu_{mix}} = \frac{(0.10)(1.78)(1220)}{0.00201} = 108{,}000 \qquad (21.4\text{-E14})$$

As shown in Fig.21.4-E2, the friction factor is obtained from the dotted line of Fig.21.4-E2 (see Fig.7.3-1 of PART I),

f = 0.0055 for $\epsilon/D = 0.001$ at $Re_{mix} = 108{,}000$

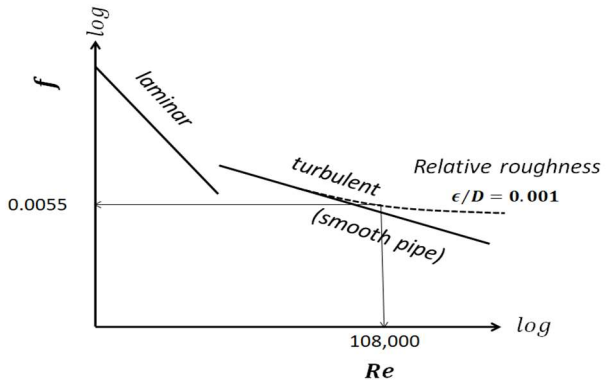

Fig.21.4-E2 Friction factor vs. Reynolds number for slurry flows

The pressure drop over the horizontal pipeline of 100 m is calculated by the following equation:

$$\Delta P = 4\,f\,\frac{L}{D}\,\frac{1}{2}\,\rho_{mix}{V_{mix}}^2 = 4(0.0055)\,\frac{100}{0.10}\,\frac{1}{2}\,(1220)(1.78^2) = 42{,}500 \text{ Pa} \qquad (21.4\text{-E15})$$

$$= 42{,}500 \text{ kg/(m s}^2\text{)}$$

Finally the theoretical power requirement for the slurry pump is given by

$$W_{th} = -W = Q_{mix}(m^3/s) \times \Delta P\ (kg/m\,s^2) = (14.0 \times 10^{-3})\,(42{,}500) = 595 \text{ W} \cong 0.6 \text{ kW}. \qquad (21.4\text{-E16})$$

It should be kept in mind that if possible, we should consider the pump efficiency as well as the friction losses of pipe fittings such as valves, bends and so on.

[PROBLEM 21.4-2] (see [PROBLEM 21.3-1])

We are planning to transport the iron ore slurry through a long steel pipeline to the pelletizing plant. As in Problem 21.3-1, the particles of the iron ore crushed have average size of 40 μm and density of 3,600 kg/m^3. If $M_s = 18$ ton/h of the iron ore is transported with the solid concentration of 30 wt%., how much M_w ton/h of water (1,000 kg/m^3, 0.001 Pa · s) is required ? Determine the appropriate inside diameter of the pipeline.

21.4-2 Pipe flow of liquid droplets dispersed systems

Regarding the emulsion flow at low concentration of emulsion droplets, the emulsion system exhibits Newtonian behaviors. However there is a possibility of undesirable adverse effects related to higher viscosity and larger friction loss. For the case of water-in-oil emulsion flow, there may be a significant

delay in the transition from laminar to turbulent regime. However such a delay does not seem to be observed for the case of oil-in-water emulsion. It can be said that the emulsion viscosity strongly depends on the viscosity of the continuous phase. When the water concentration increases beyond a certain critical value, the water-in-oil emulsion will undergo the phase inversion into the oil-in-water one.

According to the surface tension theory, emulsification takes place by reduction of interfacial tension between the dispersed phase and the continuous phase. An appropriate surfactant can increase the kinetic stability of an emulsion so that the size of the emulsion droplets is kept unchanged over time. Emulsion stability can be regarded as the system ability to resist changes in physicochemical properties over time. This indicates the effect of surfactant adsorbed layer on the emulsion stabilization.

The effect of emulsions on the flow friction factor of pipe flows[1)] exhibits different behaviors for turbulent flow regimes depending upon unstable emulsions or surfactant-stabilized emulsions. For the case of unstable emulsions in turbulent flow, the experimental friction factor may become much lower than the usual values of single-phase flow calculated by the Blasius equation (see Eq.(7.3-12)). This is called “drag-reduction behavior”. However for the case of surfactant-stabilized emulsions in turbulent flow, it is known that no drag-reduction behavior appears. This may be due to the fact that the dispersed droplets smaller than turbulent eddies flow along with them.

For simplicity, we do not deal here with multiple emulsions such as “water-in-oil-in-water” and “oil-in-water-in oil” emulsions.

1) Dol, S-S and Sen, L-J, The effect of flow-induced oil-water emulsions on pressure drop, *J. Theoretical and Applied Mechanics,* Vol.2, 73-78 (2019)

[EXAMPLE 21.4-2]

Consider a crude oil containing some volume of water being transported by a turbine pump in a pipeline shown in Fig.21.4-E3. The inside diameter and the length of the pipeline are 100 mm and 100 m, respectively. The density of the pure oil with no water content is $\rho_{oil} = 880$ kg/m^3. The flowrate of the oil mixture is $V = 30$ m^3/h. Its water content is 20% in volume. The density of the oil mixture becomes $\rho_{mix} = 900$ kg/m^3. Small amount of surfactant is added into the crude oil mixture for stabilization. It has been confirmed at the flow condition that the oil-water mixture can become a water-in-oil emulsion in the downstream region. The viscosity of pure crude oil (0% water content) is measured in advance as $\eta_{oil} = 0.008$ Pa· s at 25℃. It can be considered that the pure crude oil exhibits Newtonian property.

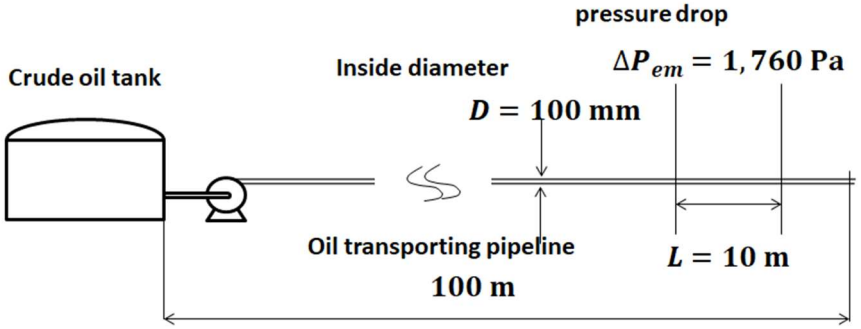

Fig.21.4-E3 Crude oil transporting pipeline

The pressure drop measured over the straight pipe of length 10 m in the downstream region is measured as 1,760 Pa. Calculate the effective viscosity of the oil mixture.

Solution:

We begin by calculation of the pressure drop for the pure crude oil in the same condition as for the real oil mixture of interest.

The pressure drop is expressed with the definition of friction factor as

$$\Delta P = 4f\ \frac{L}{D}\ \frac{1}{2}\ \rho\langle v\rangle^2 \qquad (7.2\text{-}10)$$

The average velocity in the straight pipe region is calculated as

$$\langle v\rangle = \left[\frac{V}{(\pi/4)D^2}\right]^{1/2} = 1.06\ \text{m/s} \qquad (21.4\text{-E17})$$

The Reynolds number is given by

$$Re = \frac{D\,v\,\rho}{\mu} = \frac{(0.10)(1.06)(880)}{0.008} = 11{,}660 \qquad (21.4\text{-E18})$$

According to Fig.21.4-E4 (see Fig.7.3-1), the friction factor for Newtonian fluids is given at the Reynolds number to be $f = 0.0075$.

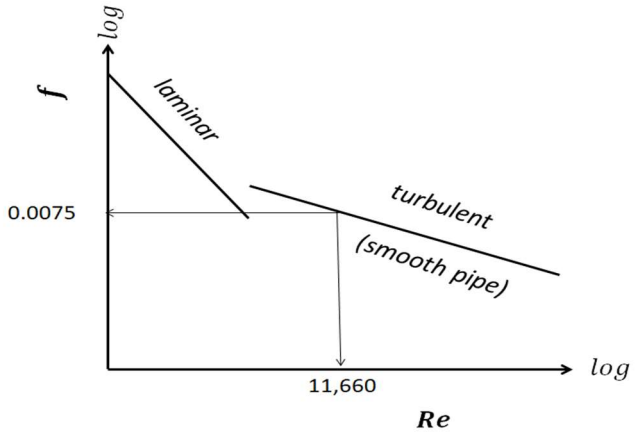

Fig.21.4-E4 Friction factor vs. Reynolds number for pipe flows

Therefore the pressure drop for the pure oil in the fully-developed region can be calculated as follows:

$$\Delta P_{oil} = 4(0.0075)\ \frac{10}{0.10}\ \frac{1}{2}\ (880)(1.06)^2 = 1{,}480\ \text{Pa} \qquad (21.4\text{-E19})$$

The real pressure drop for the oil mixture measured in the downstream region is given by $\Delta P_{mix} =$ 1,760 Pa

It can be assumed in the fully-developed region with the same flowrate that

$$\frac{\Delta P_{mix}}{\Delta P_{oil}} = \frac{f_{mix}\times\rho_{mix}}{f_{oil}\times\rho_{oil}} = \frac{1760}{1480} = 1.19 \qquad (21.4\text{-E20})$$

The pressure drop of the crude oil mixture becomes 1.19 times as large as the pressure drop for pure crude oil (0% water content).

Therefore the friction factor of the oil mixture becomes

$$f_{mix} = \left(\frac{f_{oil}\times\rho_{oil}}{\rho_{mix}}\right)\left(\frac{\Delta P_{mix}}{\Delta P_{oil}}\right) = \frac{0.0075\times880}{900} \times 1.19 = 0.0087 \qquad (21.4\text{-E21})$$

This value is obtained at $Re_{mix} = 7{,}000$ in Fig.7.3-1.

The viscosity of the oil mixture is calculated as

$$\eta_{mix} = \frac{D\,\langle v\rangle\,\eta_{mix}}{Re_{mix}} = \frac{(0.10)(1.06)(900)}{7000} = 0.0136 \qquad (21.4\text{-E21})$$

$$\eta_{mix}/\eta_{oil} = 0.0136/0.008 = 1.7 \qquad (21.4\text{-E22})$$

The viscosity of the oil mixture with water content of 20% becomes 1.7 times the viscosity of the pure oil with no water content.

This kind of emulsion (water-in-oil) is mostly encountered as one of the important problems in oil transporting pipelines. Undesirable effects caused by the emulsions are related to higher viscosity, larger pressure drop, and more oil-water separation difficulty.

An emulsion polymerization will be studied in Chapter 28.3 of this volume.

[EXAMPLE 21.4-3]

Consider an agitated tank baffled for producing an emulsion of fatty acid methyl ester in water. 0.1 m^3 of oleic acid methyl ester and 1.0 m^3 of water are put in the tank (1.5 m^3).
A 6 bladed disk turbine as the agitator is rotated at 80 rpm to make an emulsion. The temperature is kept at 40℃ with the jacket outside the tank.
The dimensions of the agitator and vessel are
Diameter of impeller $d = 0.8$ m, tank diameter $D = 1.0$ m, impeller width $b = 0.1$ m, depth of liquid in vessel $H = 1.4$ m, height of impeller above tank floor $H_p = 0.7$ m, width of baffles $j = 0.05$ m,

By the preliminary examination, the effective viscosity and density of the stable emulsion of the same content are confirmed to be $\eta_{em} = 0.00105$ Pa · s and $\rho_{em} = 970$ kg/m^3 at 40℃.

Calculate the power requirement at steady emulsion state.

It may be assumed that the sample emulsion for the preliminary test should have the same properties as the real emulsion of interest.

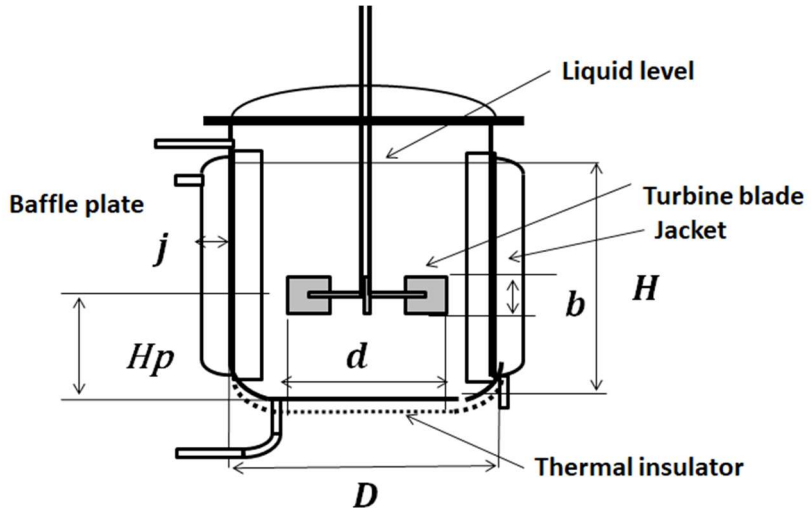

Fig.21.4-E5 Agitated vessel with a 6-blade disk turbine impeller for emulsification

Solution:

The Reynolds number defined by Eq.(20.2-1) of PART II is calculated as

$$Re = \frac{d^2\, N\, \rho_{em}}{\eta_{em}} = \frac{(0.8^2)\,(80/60)\,(970)}{0.00105} = 788{,}300 \qquad (21.4\text{-E23})$$

According to Fig.20.2-3 of PART II, the power number is obtained as shown in Fig.21.4-E6:
$Np = 6.0$ at $Re = 788{,}300$ for 6-bladed disk turbine with baffled tank

From Eq.(20.2-2) of PART II, the power requirement is given by

$$P_w = \rho_{em}\, N^3\, d^5\, Np = (970\ kg/m^3)\,(80/60\ s)^3\,(0.8\ m)^5(6.0) = 4{,}520\ \text{W} \qquad (21.4\text{-E24})$$

Theoretical power requirement is given by 4.52 kW.

This emulsion can be considered to exhibit Newtonian behavior because of the low concentration (ca. 9%) of emulsion droplets.
It can be understood that this emulsion should have 1.5 times the viscosity of pure water (0.0007 Pa · s at 40℃).

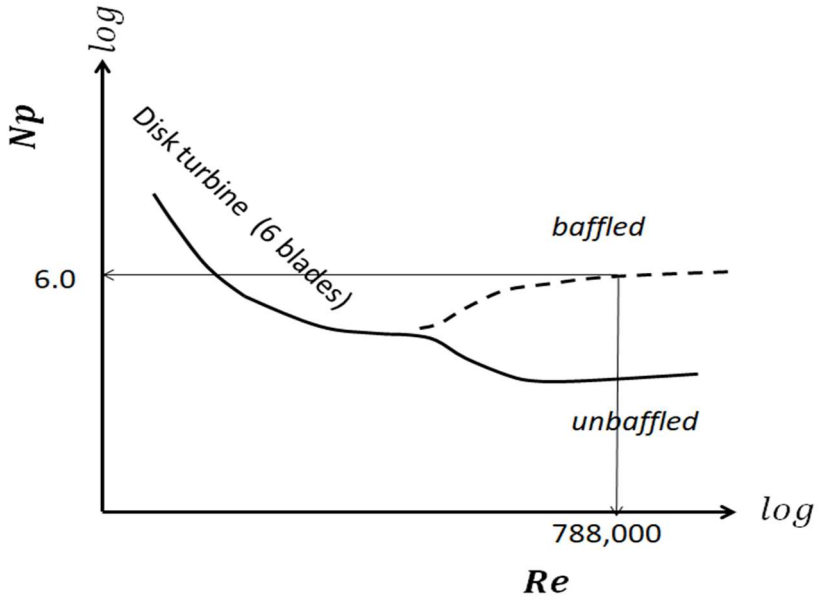

Fig.21.4-E6 Power number vs. Reynolds number

This is an example of oil-in-water emulsion. Roughly speaking, the emulsion exhibits non-Newtonian behavior when the volume fraction of the dispersed phase goes beyond 40%. When the fraction is greater than 90%, the phase inversion to the water-in-oil will occur.

[PROBLEM 21.4-3]

One of the pasteurization processes of cows' milk is conducted by using a batch jacketed agitator tank. Cows' milk is an emulsion whose constituents are about 87% water, 4% fat, 3.4% protein 4.8% lactose, and 0.8%minerals. It can be considered that the raw milk exhibits Newtonian behavior.

The agitator is a 6-bladed disk turbine impeller. The first treatment is heated keeping at 62℃ for 30 min by the 70℃ hot water flowing in the jacket. The next treatment is cooled by the cooling water replaced in the same jacket.

Let us consider that an emulsion of cow's raw milk 2 ton is heated for pasteurization at 62℃ in the jacketed agitator tank. The dimensions of the agitator tank are given by

Turbine impeller diameter $d = 0.5$ m, width $b = 100$ mm,

Tank diameter $D = 1$ m, and baffle plate width $j = 50$ mm

The rotation number of the impeller is set at $N = 50$ RPM.

The physical properties are given at 62℃ are: density $\rho = 1{,}020$ kg/m^3, viscosity $\mu = 1.2$ mPa · s, heat capacity $Cp = 3.93$ kJ/kg K, thermal conductivity $\kappa = 0.6$ W/m K,

The correlation of the heat transfer coefficient on the inside wall of the agitator tank is given by Eq.(20.3-1) of PART II:

$$Nu = 0.44\, Re^{2/3} Pr^{1/3} (\mu/\mu_w)^{0.14} \qquad (20.3\text{-}1)$$

Since the temperature difference between the bulk and the jacket wall is small, the viscosity correction term can be assumed to be unity.

For simplification, the heat transfer coefficient of the jacket-side wall can be assumed as $h_o = 1{,}160$ W/m^{2}K. The hot water temperature in the jacket is also assumed as 70℃ averaged between the inlet and the outlet of the jacket.

(1) Calculate the power requirement of the agitator.

(2) Calculate the heat transfer area required for the pasteurization process by heating.

21.5 Emulsion

Let us consider a stable suspension of very small droplets of one liquid in another with which it is immiscible. This is called “emulsion.” That dispersed mixture of two or more immiscible liquids are usually characterized by the terms water-in-oil (dispersed water droplets in oil) and oil-in-water (dispersed oil droplets in water). The bulk liquid surrounding these dispersed droplets is called “continuous phase.” For example, an oil phased emulsion features water small droplets, where the dispersed phase uniformly distributes throughout the continuous phase of oil.

Almost all emulsions are inherently unstable due to the thermodynamic incompatibility of the oil and water phases at the interface. Therefore a surfactant is usually used for emulsion stability preventing the dispersed droplets from collision and coalescence.

Many food mixtures such as mayonnaise, yogurt, homogenized milk, and vinaigrette can be regarded as stable oil-in-water food emulsions, and butter is one of the water-in-oil emulsion.

The size of dispersed liquid droplets usually lies in 100 ~ 400 nm.
Usually an emulsion mixture is made using some kinds of surfactants as an emulsifier to stabilize dispersed droplets. The mechanical method of emulsion formation usually requires high shear mixing or homogenization. Emulsions appear white when all light is scattered equally, but high-frequency (short wavelength) light will be scattered more for very dilute emulsions, so the emulsion will appear bluer (Tyndall effect).

21.5-1 Emulsification and emulsion viscosity

Generally speaking, higher mixing speed and longer mixing duration can produce more stable emulsions with smaller dispersed droplets. Usually an emulsifier is a substance called surfactant or “surface-active agent” that stabilizes an emulsion by reducing the surface tension at the oil-water interface.

In the emulsification process, one immiscible liquid is dispersed in another immiscible liquid.
Emulsifiers having more or less solubility either in oil or water as emulsifiers are those compounds that have a polar or hydrophilic means water-soluble part and a non-polar or hydrophobic means water-insoluble part.

The following three mechanisms of emulsification are available: (1) Reduction of interfacial tension between the dispersed phase and the dispersion medium, (2) Repulsion force acting between the dispersed droplets where a repelling film is formed over the one phase by the emulsifying agent, and (3) Viscosity increased by some emulsifying agents forms globules of the dispersed phase stable in the dispersion medium.

Emulsification is accomplished by lowering the interfacial tension between the two phases. Successively a repelling film created over a single phase separates into globules by the emulsifying agent. If some viscous substances such as glycerol or CMC (carboxymethyl cellulose) are added, the emulsion is preserved due to the viscosity increase.

Fundamentally the viscosity of an emulsion depends on the initial viscosity of the bulk phase μ_0 and the volume fraction of the droplets φ. The equation of the emulsion is expressed as

$$\mu = \mu_0(1 + a\,\varphi) \tag{21.5-1}$$

Here the Einstein equation[1] gives $a = 2.5$ for solid rigid particles dispersed.
However we should be careful about the unfavorable results obtained because the viscosity tends to extremely rise in the volume fraction above a certain upper limit value.

If the concentration of dispersed-phase liquid is low, the effective viscosity of the emulsion can be expressed as the Taylor equation[1] for the emulsion of solid particles suspended in the continuous phase of water.

If the dispersed liquid droplets having a circulating flow inside has very large viscosity η', the internal circulating flow is suppressed. The constant a of Eq. (21.5-1) approaches 2.5.
This indicates that such liquid droplets behave like solid rigid particles.

For the case of liquid droplets having circulating flows inside, the emulsion viscosity μ is lowered and the constant a is given by the equation:

$$a = \frac{\mu_0 + 2.5\,\eta'}{\mu_0 + \eta'} \qquad (21.5\text{-}2)$$

Here η' is the viscosity acting within the dispersed oil droplets.

According to Taylor (1934)[1)], for dilute simple emulsion with no interaction between the droplets, the relative viscosity of emulsion is given by

$$\eta_r = \frac{\eta_e}{\eta_C} = 1 + \left[2.5\left(\frac{k+0.4}{k+1}\right)\right]\varphi \qquad (21.5\text{-}3)$$

where η_e is the effective viscosity of emulsion and $k = \eta_D/\eta_C$ is the ratio of the viscosity of the dispersed phase (η_D) to that pf the continuous phase (η_C).

1. Taylor, G. I., *Proc. Roy. Soc.,* (London), **A146**, 501 (1934).

[PROBLEM 21.5-1]

An O/W emulsion at 25℃ consists of 10 vol% corn oil (viscosity 52.3 mPa·s) and 90 vol% water (viscosity 1 mPa·s) with small quantity of surfactant (PGE). Calculate the relative viscosity η_r of the emulsion at 25℃.

Except for very viscous mixtures, the power requirement of emulsification can be calculated by the same as the usual power number correlation $Np = f(Re)$ for single-liquid agitation (see Chapter 20.2). Usually the emulsification by agitation utilizes a rotating impeller immersed in the liquid mixture. The basic requirements regarding the shape and arrangement of the vessel, the arrangement of the impeller, and the baffle plates are essentially the same as those for dispersing finely divided solids in liquids, which are discussed in Chapter 20 of Vol.1.

For the case of emulsion, the size of droplets dispersed should have a wide range varying locally with location in the vessel. There are different shear stress zones distributed within the agitated vessel.

There are many small droplets near the impeller and many larger droplets in the low shear stress region far from the impeller. If possible, it is much better to practically measure the emulsion viscosity by a viscometer. We can check whether the emulsion tested should have non-Newtonian properties or not.
The mixing condition and agitator power requirement should be calculated by using the measured viscosity of the emulsion in the equation of the power requirement correlation database.

[EXAMPLE 21.5-1]

By using an agitated vessel with an immersed six-bladed disk turbine impeller, a fatty acid ester and water are agitated to obtain an emulsion with $\eta'/\mu_0 = 4.8$. The conditions of agitation by the disk turbine are: $N = 180$ rpm, blade diameter $d = 400$ mm, tank diameter $D = 800$ mm, depth of liquid $H = 800$ mm, impeller height from tank floor $H_p = 250$ mm. The viscosity of the ester droplets of fatty acid ester is assumed to be 0.0038 Pa s. The water viscosity $\mu_0 = 0.001$ Pa s (assumed 25℃). The volume fraction of the ester in the mixture is approximately 15%, i.e. $\varphi_D = 0.15$.
Calculate the power requirement.

Solution:

The densities of the dispersed-phase and continuous-phase are $\rho_D = 870$ kg/m^3, $\rho_C = 998$ kg/m^3.

The constant of Eq.(21.5-2) relating with the circulating flow inside a droplet) becomes

$$a = \frac{\mu_0 + 2.5\,\eta'}{\mu_0 + \eta'} = \frac{0.001 + 2.5(0.0048)}{0.001 + 0.0048} = 2.24 \qquad \text{(21.5-E1)}$$

The average density and viscosity of the emulsion are calculated by Eqs.(21.5-3) and (21.5-4):

$$\rho_{av} = \rho_C \varphi_C + \rho_D \varphi_D = (998)(0.85) + (870)(0.15) = 978.8 \text{ kg/m}^3 \qquad \text{(21.5-E2)}$$

$$\mu_{em} = \mu_0(1 + a\,\varphi_C) = 0.001(1 + 2.24 \times 0.85) = 0.0029 \text{ Pa s} \qquad \text{(21.5-E3)}$$

The Reynolds number is calculated as

$$Re = \frac{\rho_{av} d^2 N}{\mu_{em}} = \frac{(978.8)(0.40)^2(180/60)}{0.0029} = 162{,}000 \qquad \text{(21.5-E4)}$$

According to Fig.20.2-3 in Chapter 20 of PART II, the unbaffled 6 blades disk turbine impeller gives the power number $Np = 1.1$ at $Re = 162{,}000$.

Therefore the power requirement becomes

$$P_w = Np \times (\rho_{av} N^3 d^5) = 1.1 \times [(978.8)(3.0)^3(0.40)^5] = 2980 \text{ kg m}^2/\text{s}^3 = 2.98 \text{ kW} \qquad \text{(21.5-E5)}$$

[PROBLEM 21.5-2]

We are requested to produce a corn oil emulsion by using an agitated vessel equipped with a six-bladed disk turbine impeller. A corn oil and water are mixed at 25℃ to obtain an emulsion with the relative viscosity of $\eta_e = 1.3$. The conditions of agitation by the disk turbine are: $N = 200$ rpm, blade diameter $d = 300$ mm, tank diameter $D = 700$ mm, depth of liquid $H = 700$ mm, impeller height from tank floor $H_p = 250$ mm. The viscosity of the corn oil droplets is assumed to be 0.054 Pa s. The water viscosity $\mu_0 = 0.001$ Pa s (assumed 25℃). The effect of the added surfactant on the viscosity behavior can be assumed to be negligible. The volume fraction of the corn oil in the mixture is approximately 15%, i.e. $\varphi_D = 0.15$.

We can consider the rheological behavior of the emulsion to be Newtonian because of the small volume fraction of the dispersed phase.

Calculate the power requirement.

At any rate, it is outside of this text territory to describe further the rheological and/or colloidal behavior of various viscous emulsions, which becomes very difficult especially in the developing term of non-steady state variation.

21.5-2 Rheological behavior of emulsion

The rheological effect of microstructural mechanism of emulsions is so complicated that the theoretical approaches are beyond the territory of this course. Therefore some of the simple models will be studied here. The flow field of a highly concentrated O/W emulsion exhibits laminar regime but does not form a parabolic velocity profile in a pipe flows. For example, a dense emulsion like mayonnaise or yogurt exhibits non-Newtonian behaviors. Emulsion viscosities η are also a function of shear rate $\dot{\gamma}$.

Oil-in-water emulsion

Let us consider an oil-in-water emulsion such as mayonnaise.

If the emulsion viscosity η decreases with increasing the shear rate $\dot{\gamma}$, the emulsion is called “shear-thinning”. The emulsions made up from small droplets are usually more viscous than the emulsions made up from bigger droplets. When the oil fraction in volume increases, the viscosity is increased. This is due to the fact that the continuous-phase fluid film surrounding the dispersed droplets becomes thin. Figure 21.5-1 indicates a schematic picture of the apparent viscosity of the shear-thinning emulsion varying with the shear rate.

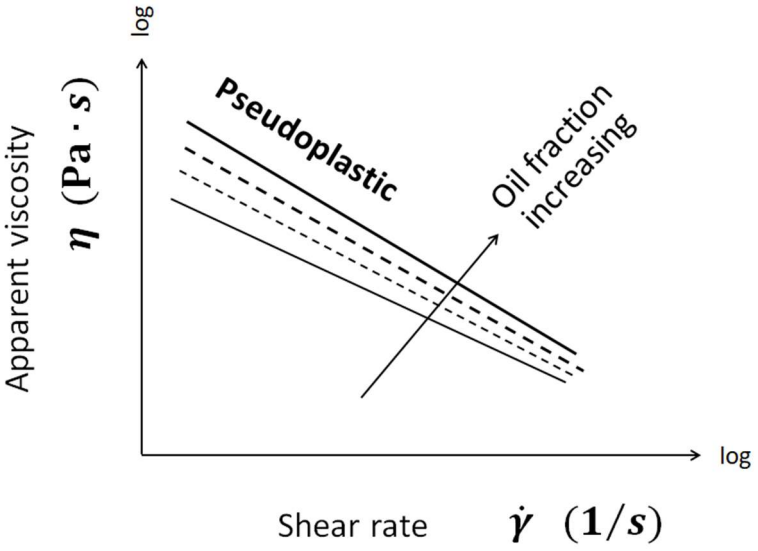

Fig.21.5-1 Typical variation of apparent viscosity with shear rate for shear-thinning emulsions

The region of shear rate where the emulsion viscosity decreases with increasing shear rate is called "Power-model region":

$$\eta = K\,\dot{\gamma}^{n} \qquad (21.5\text{-}4)$$

The HB consistency index *K* changes with oil concentration but the flow behavior index *n* hardly changes. As shown in Fig.21.5-2, however there are two shear rate regions turning away from the Power law.

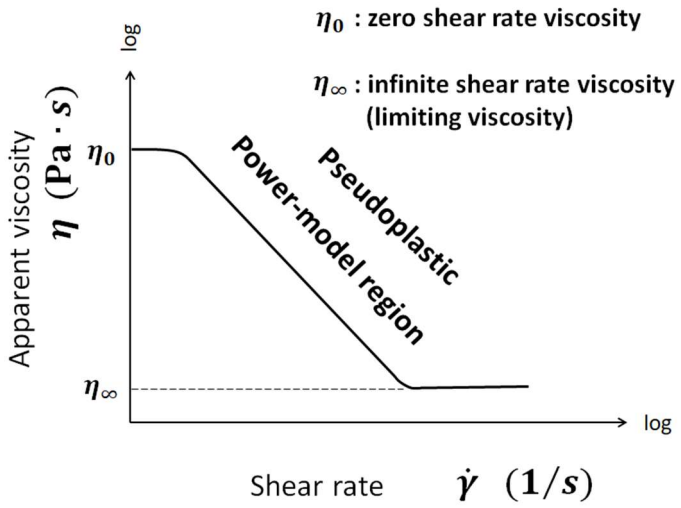

Fig.21.5-2 Zero-shear-rate viscosity and infinite-shear-rate viscosity

As shown in Fig.21.5-2, when the shear rate approaches zero, shear stress does not approaches zero, that is, some yield stress η_0 exists. On the other hand, at very high shear rates, the apparent viscosity becomes constant. This is called "limiting viscosity", i.e. infinite shear rate viscosity.

It is known that as the shear rate increases with time, the apparent viscosity of emulsions decreases.

This is also called “shear thinning behavior”, which is termed “pseudoplastic”. The shear thinning behavior occurs due to a gradual orientation of fluid elements such as liquid droplets or molecules in the flow direction to reduce friction and the deformation of the microstructures.

The shear thinning behavior is described by the following Herschel-Bulkley model[1]:

$$\tau = \tau_0 + K\,\dot{\gamma}^n \qquad (21.5\text{-}5)$$

This can be regarded as the power-law model accompanied with a yield stress.
The apparent viscosity is given by the Power-law model based on the same concept:

$$\eta = k\,\dot{\gamma}^{n-1} \qquad (21.5\text{-}6)$$

where τ, τ_0, $\dot{\gamma}$, and η are shear stress (Pa), yield stress (Pa), shear rate (1/s), and apparent viscosity (Pa · s), respectively..
The K is a constant called the HB consistency index.
The shear rate $\dot{\gamma}$ can also be expressed as the velocity gradient: $-(dv_x/dy)$.
The yield stress is an important parameter for stability of foods such as mayonnaise.
Usually the exponent *n* of pseudoplastic fluids lies in the range $0.4 < n < 0.7$.
Mayonnaise consists of very many oil droplets forming the dispersed phase and small quantity of continuous-phase water which forms a very thin film around those oil droplets.

1) Herschel, W.H. and Bulkley, R., *Kolloid Zeitschrift,* vol.39(4), 291-300 (1926)

Regarding time-dependent shear thinning behavior, when the shear rate increases with time, the shear stress becomes higher than when the shear rate decreases. The shear stress results in the reordering of fluid elements or molecules to reduce the overall stress. This hysteresis shown in Fig.21.5-3 can be considered as one of the thixotropic behaviors.[2]

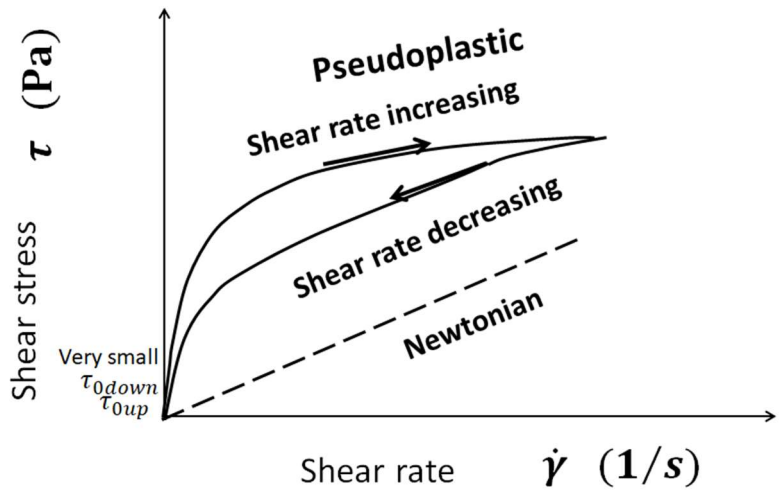

Fig.21.5-3 Hysteretic property of shear-thinning behavior of high-concentrated emulsion

It should also be kept in mind that there exist shear-thickening fluids. A dilatant (termed shear thickening) has the viscosity increasing with shear rate. Shear thickening is observed only in some suspension mixtures. Shear thickening viscosity can also be expressed by the Power-law model:

$$\eta = k\,\dot{\gamma}^{n-1} \qquad (21.5\text{-}7)$$

A mixture of cornstarch and water is an example of shear-thickening.
The dilatant behavior occurs when *n* is greater than unity.

2. Yuceer, M., Ilyasoglu, H., Oezcelik, B., *J. Appl. Poult. Res.*, **25**, 518-527 (2016)

21.5-3 Velocity distribution of non-Newtonian fluid pipe flow

It is comprehensible to reconsider the rheological characteristics of the dispersed systems before closing this chapter.

Consider laminar flow in a circular pipe with the pressure drop $p_0 - p_L$ from pipe length $z = 0$ to L. Here v_z is axial velocity component and $R = D/2$ is the inner radius of the pipe.

[Power law model]

As in Chapter 6.4, the power low model for a circular pipe flow is given by

$$\tau_{rz} = m \left(-\frac{dv_z}{dr}\right)^n \tag{21.5-8}$$

According to Eq. (6.4-E8) in Chapter 6.4, the laminar flow of the power law model in a circular pipe has the following velocity distribution:

$$v_z = \left(\frac{p_0 - p_L}{2\,mL}\right)^{1/n} \frac{n}{1+n} R^{\frac{1+n}{n}} \left[1 - \left(\frac{r}{R}\right)^{\frac{1+n}{n}}\right] \tag{21.5-9}$$

By using Eq. (21.8-9), the average velocity can be calculated as

$$v_{zav} = \frac{\int_0^R v_z\, 2\pi r\, dr}{\int_0^R 2\pi r\, dr} = \left(\frac{p_0 - p_L}{2\,mL}\right)^{1/n} \frac{n}{1+3n} R^{\frac{1+n}{n}} \tag{21.5-10}$$

Therefore

$$\frac{v_z}{v_{zav}} = \frac{1+3n}{1+n} \left[1 - \left(\frac{r}{R}\right)^{\frac{1+n}{n}}\right] \tag{21.5-11}$$

[Bingham model]

As in Chapter 2.5, the Bingham model is given by

$$\tau_{rz} = -\mu_0 \frac{d\,v_z}{dr} + \tau_0 \qquad \text{if } \tau_{rz} > \tau_0$$

$$\frac{d\,v_z}{dr} = 0 \qquad \text{if } \tau_{rz} < \tau_0$$

where τ_0 is the yield stress and μ_0 is a Bingham model parameter similar to the Newtonian viscosity.

The velocity distribution is given by

$$v_z = \frac{p_0 - p_L}{4\,\mu_0 L}\left(R - r_y\right)^2 \left(1 - \frac{r - r_y}{R - r_y}\right) \qquad r_y < r < R$$

$$v_z = v_{zmax} = \frac{p_0 - p_L}{4\,\mu_0 L}\left(R - r_y\right)^2 \qquad 0 < r < r_y$$

where r_y is the radial position called the yield radius where the shear stress becomes $\tau_{rz} = \tau_0$.

The average velocity is given by

$$v_{zav} = \frac{(p_0 - p_L)}{24\,\mu_0 L}\frac{1}{R^2}\left(3R^4 - 4\,r_y R^3 + r_y{}^4\right)$$

Then

$$\frac{v_z}{v_{zav}} = 6\left(\frac{R - r_y}{R}\right)^2 \frac{1 - \dfrac{r - r_y}{R - r_y}}{3R^4 - 4\,r_y R^3 + r_y{}^4}$$

By using the above equations, we can compare various non-Newtonian flids in velocity distribution with Newtonian fluid. These results are given in Fig.21.5-4, where two cases of the pseudoplastic fluids depending on the power model with n = 0.6 and 0.25 and the Bingham plastic fluid case with the yield radius $r_y/R = 0.25$ are shown. Mayonnaise (n = 0.6) and ketchup (n = 0.25) are given as two examples of the pseudoplastic.

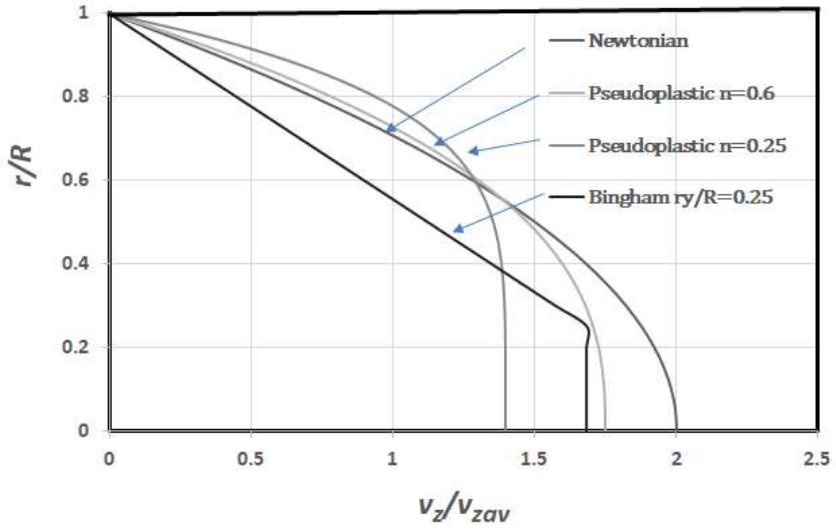

Fig.21.5-4 Comparison of non-Newtonian flows with Newtonian flow with respect to velocity profile of laminar flow in a circular pipe.

[PROBLEM 21.5-3]

We know as the Bingham plastic behavior that a toothpaste is pushed out in the form of cylindrical solid from its tube. Calculate the velocity profile of v_z/v_{zav} vs. r/R when the yield radius by $r_y/R = 0.45$ and plot its result as in Fig.21.8-4.

21.5-4 Shear-thinning emulsion

Since shear rate $\dot{\gamma}$ in the agitated vessel varies with distance from the impeller, it depends on three-dimensional velocity gradients. As shown in Fig.21.5-5, local shear rate becomes lowest near the vessel walls and at the free surface of the agitated fluid while the apparent viscosity becomes lowest near the impeller and highest at the walls. Local shear rates become so high near the edges of the impeller that larger dispersed droplets undergo large stresses enough to be broken into smaller droplets.

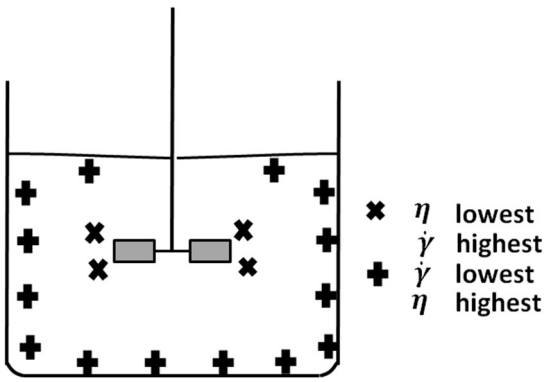

Fig.21.5-5 Local distributions of shear rate and apparent viscosity of shear-thinning emulsion in an agitated unbaffled vessel

Figure 21.5-6 gives several rheological models of dispersed systems summarized. Many shear-thinning emulsions may have small yield stresses at the point of zero shear rate.

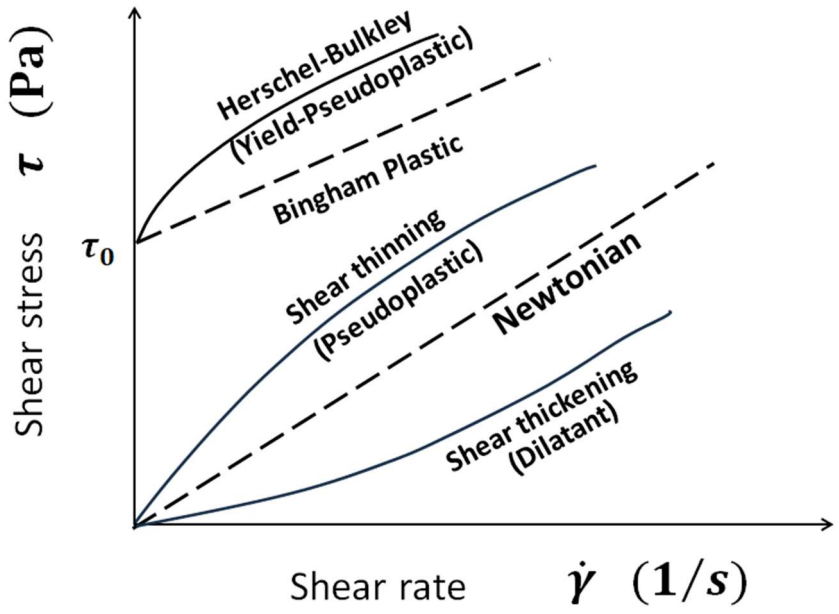

Fig.21.5-6 Non-Newtonian properties of various dispersed systems

Nomenclature

A	mass transfer area, [m^{2}]
a	constant of Eq.(21.5-1) for viscosity of dispersed sytems,, [-]
C	concentration, [kg/m^{3}]
C_D	drag coefficient, [-]
Cp	heat capacity, [J/kmol K]
C_V, C_W	solid concentration, [vol%], [wt%]
d	impeller diameter, [m]
D	tube diameter or tank diameter, [m]
D_{BS}	diffusivity of B in S, [m^{2}/s]
Dp	diameter of a particle or droplet, [m]
F_L	Durand factor, [-]
f	friction factor, [-]
f_e, φ_e	coefficient modifying Peclet number, [-]
g	gravitational acceleration, [m/s^{2}]
He	Hedstrom number defined by Eq.(21.3-7)
h_m	heat transfer coefficient averaged, [W/m^{2}K]
k_m	mass transfer coefficient averaged, [kmol/m^{2}s]
K	overall mass transfer coefficient, [m/s] or HB model consistency index, [-] (Herschel-Bulkleymodel)
L	tube length, [m]
l	characteristic moving distance, [m]
N	number of droplets, [-] or rotation number, [1/s]
Nu	Nusselt number, [-]
N_p	Power number
Pe	Peclet number, [-]
Pr	Prandtl number, [-]
r_y	yield radius, [m]
R_x, R_y	resistance force, [N]
Re	Reynolds number, [-]
Sc	Schmidt number, [-]
Sh	Sherwood number, [-]
T	temperature, [K]
t	time, [s]
u_t	terminal velocity, [m/s]
v	fluid velocity, [m/s]

V_{lim}	limiting settling velocity, [-]
x, y	horizontal or vertical coordinate, [m]
$\dot{\gamma}$	shear rate, [1/s]
η	apparent viscosity, [Pa s]
κ	thermal conductivity, [W/m K]
λ	latent heat of evaporation, [J/kg]
$\boldsymbol{\lambda_L}$	Darcy-Weisbach friction factor, [-]
μ	viscosity, [Pa s]
ρ	density, [kg/m^3]
σ	surface tension, [N/m]
τ_{rz}, τ_{yx}	shear stress, [Pa]
τ_0	yield stress, [Pa]
Φ	volume fraction, [-]
φ	volume fraction of droplets, [-]

Subscripts

B	solute
em	emulsion
ex	extract
f	film or fluid
hg	hot gas
i	interface
L	liquid phase
mix	mixture
p	particle or droplet
s	solid
S	solvent
∞	uniform flow

CHAPTER 22

EXTRACTION ENGINEERING

22.1 Liquid Extraction

Separation of close-boiling mixtures often becomes a technical problem as to which method may be used, distillation or extraction. When either distillation or extraction may be used, the choice is usually distillation in spite of the large heating and cooling duties. Extraction utilizes differences in the solubility of the components rather than the differences in their volatility. The liquid extraction is used to separate two mutually soluble liquids by adding a third liquid (*solvent*) having a preferential solubility for one of the components of the mixture. The liquid-liquid extraction can be used if at least one of the liquid components (e.g. solvent) must be sufficiently insoluble so that two liquid phases are formed. In usual cases the liquid-liquid extraction is conducted in isothermal operation with negligibly small thermal energy consumption.

22.1-1 Liquid-liquid Equilibrium

The phase equilibria in liquid extraction give the distribution of a solute B between two immiscible liquids A and S. Firstly only for simplicity, let us consider the situation where the mutual solubility of liquids A and S is negligible even in the presence of component B.

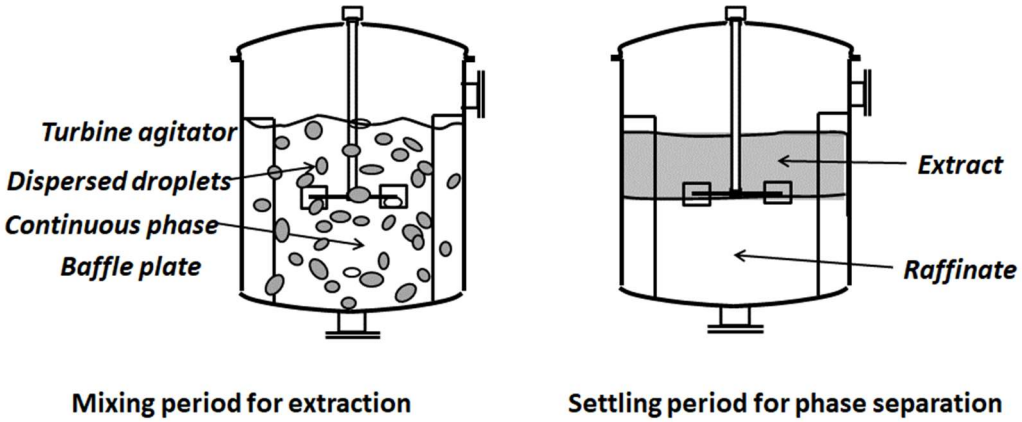

Fig.22.1-1 Batch extractor of baffled agitation tank

For a batch tank-type extractor shown in Fig.22.1-1, the original solution (*feed*) after adding the solvent is mixed by a turbine or propeller stirrer installed in the tank. During that period, the solute transfers in some degree depending on their solubility from the continuous phase (the original solution) to the dispersed liquid droplets (the added solvent). When the stirrer is shut off, two immiscible layers are formed by gravity. The solvent layer is called *extract* and the other layer composed of the remainder of the original solution plus a small amount of the solvent is termed the *raffinate*.

In this Chapter, we will study the ternary case where the solvent S is immiscible with the initial solution diluent A. This system consists of three components where one phase has some solute B dissolved in diluent A and the other phase has some other solute B extracted in solvent S.

One example is the recovery of acetic acid from its dilute aqueous solution by isopropyl ether used as the extracting solvent. Isopropyl ether and water are practically immiscible in mixture. When isopropyl ether is added to the aqueous solution, some of the acetic acid dissolves in this extracting solvent and two liquid layers are formed. The extract (isopropyl ether) layer contains only acetic acid and ether, while the raffinate (water) layer contains acetic acid and water. At equilibrium conditions, there must be a definite relationship in the acetic acid concentration between the extract and the raffinate.

Let X_0 represent the kg of acetic acid (i.e., the extractable component) per kg of water in the initial solution, S_0 the kg of isopropyl ether (i.e., the extracting solvent) added, H_0 the kg of water in the initial solution. After mixing, Y_1 and X_1 the equilibrium concentrations of acetic acid in the extract and the raffinate as kg/kg of isopropyl ether and kg/kg of water.

The overall mass balance is given by

$$X_0H_0 = X_1H_0 + Y_1S_0 \qquad (22.1\text{-}1)$$

The phase equilibrium relationship is usually expressed on an equilateral triangular graph drawn with an isothermal condition and at an appropriate pressure keeping the whole system liquid.

A typical simplest example is given by Fig.22.1-2, where A, B, S are the feed solvent (diluent), solute, and solvent, respectively. The liquid pairs B-A and B-S are completely miscible but A and S can give the mutually saturated solutions at G and H owing to their limited dissolubility.

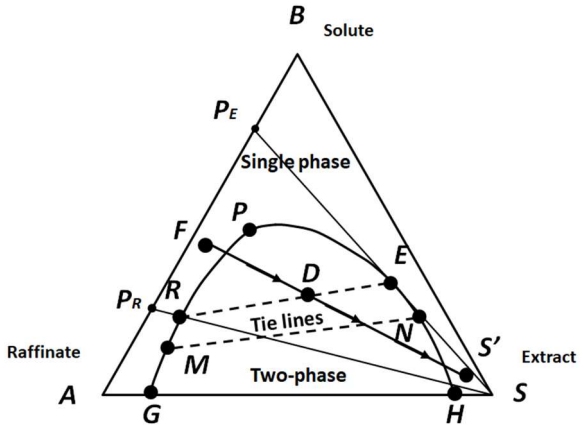

Fig.22.1-2 Triangular diagram for ternary system with partial miscibility of solvent and diluent.

As seen in Fig.22.1-2, if some of B is added to such mixtures G and H, the two mixtures A and S become more soluble. In this case, the saturated composition gives a solubility curve GMPNH.

The concentrations represented by the triangular diagrams are based on the entire mixture. Therefore the concentration of the three components must add to unity:

$$x_A + x_B + x_S = 1$$

The two phases become one at the point P called "plait point." There the solute B provides equilibrium liquids distributing between the saturated phases at points M and N joined by a tie line.

When the solvent S is added into the feed with composition given by F, the mixture composition moves along the line from F to S'. If the mixture composition lying at D within the curve GMPNH is settled, the mixture solution will is separated into the two equilibrium phases. Their equilibrium compositions are given by points R and E, respectively. At this condition, the mass balance is given by

$$R + E = D \quad \text{and} \quad \overline{RD}/\overline{DE} = E/R \qquad (22.1\text{-}2)$$

The S-phase composition moves along the curve HEP whereas the A- phase composition moves along the curve GRP.

Using the concentration of B at points M and N, the distribution coefficient m is defined in units of

mole fraction as:

$$m = \frac{x_{BN}}{x_{BM}} \quad (22.1\text{-}3)$$

The distribution coefficient K is also expressed as the mass fraction ratio:

$$K = \frac{X_{BN}}{X_{BM}} \quad (22.1\text{-}4)$$

Finally the point M coincides with the point N at the plait point P, where the A phase (*raffinate*) and S phase (*extract*) are combined into a single-phase mixture.

If the solvent S is removed from one phase of extracted mixture of composition E, an A-phase of mixture with concentration P_E is obtained at the point PE. Similarly if the solvent S is removed from the other phase of extracted mixture of composition R, another A-phase of mixture with concentration P_R is obtained at the point PR.

[EXAMPLE 22.1-1]

An aqueous solution of acetic acid contains 40 kg of acetic acid in 1000 kg of water. The initial solution is to be extracted by 800 kg of isopropyl ether. The batch extraction is to be performed at 20℃, where the equilibrium relationship between the acetic acid concentration in the extract and raffinate may be expressed in a low concentration range as

$$Y_1 = 0.225\,X_1 + 0.95\,{X_1}^2 \quad (22.1\text{-E1})$$

If an equilibrium condition is attained between the two phases in a single batch extraction process, how many kg of acetic acid can be recovered by the isopropyl ether?

Solution

Firstly we use Eq.(21.1-1),

$$X_0H_0 = X_1H_0 + Y_1S_0 \quad (22.1\text{-}1)$$

$$0.04 \times 1000 = 1000\,X_1 + 800\,Y_1$$

Substituting the equilibrium relationship $Y_1 = 0.225\,X_1 + 0.95\,{X_1}^2$,
the following equation is obtained:

$${X_1}^2 + 1.5525\,X_1 - 0.05263 = 0 \quad (22.1\text{-E2})$$

From the equation, we can obtain the following solution:

$$X_1 = 0.0332 \text{ and } Y_1 = 0.00851 \quad (22.1\text{-E3})$$

$Y_1S_0 = (0.00851)(800) = 6.81$ kg.

The result implies that 6.81 kg of acetic acid is removed from the initial aqueous solution by a single (one-stage) extraction operation.

The recovery factor for one stage is given by

$$r_{ex} = Y_1S_0/X_0H_0 = (0.00851)(800)/(0.04)(1000) = 0.17 \quad (22.1\text{-E4})$$

It should be kept in mind that this equilibrium composition can be obtained in acid concentration between the extract and raffinate if the two liquid layers formed by a batch extraction are settled down into two phases of extract and raffinate after a sufficiently long time. It is possible to combine a series of these stages so that the recovery factor for the extracting component can be improved.

One example of countercurrent cascade systems of mixer and settler combinations is shown in Fig.22.1-3.

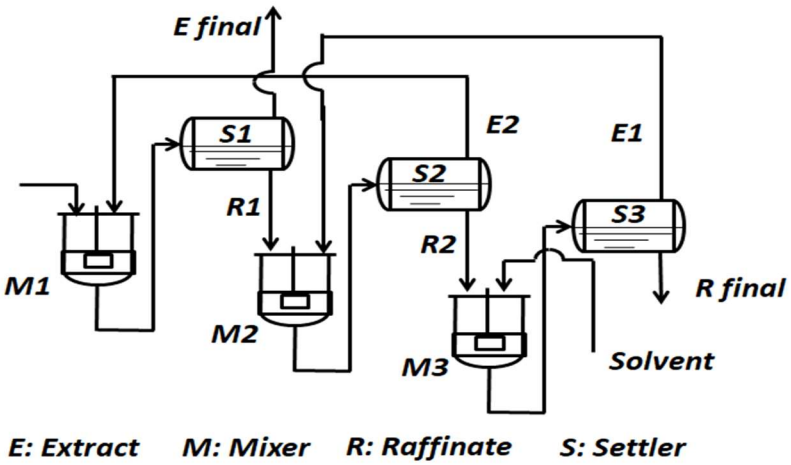

Fig.22.1-3 A mixer-settler extractor

In extraction processes, it is essentially important to promote mass transfer between two liquids. Extractors can be made compact if one liquid is dispersed and suspended in the second as small droplets. The advantage lies in the establishment of a very large contacting-surface between the two liquid phases.

While mixing the solution, the interphase mass transfer of *solute* takes place between the original solution and the solvent.

Continuous flow extractors comprise a train of the mixer and settler. Fig.22.1-3 shows an example of a three-stage continuous flow extractor called "Mixer-settler."

The mixer is usually a small agitated tank provided with supply lines and a draw-off line. The settler is a simple continuous decanter.

Consider the mass transfer of component B from droplets of the original solution solvent (diluent) A to the continuous phase of solvent S. For a baffled vessel extractor, the shape of droplets often becomes non-spherical and the droplet size varies locally.

The average droplet size can be expressed as

$$d_{p,av} = \frac{\sum n_i {d_{pi}}^3}{\sum n_i {d_{pi}}^2} \qquad (22.1\text{-}5)$$

For simplicity, let us consider a single spherical droplet suspended in the stream of continuous-phase extracting solvent. The relative velocity of the droplet is given as the slip velocity v_p.

If the droplet size d_p is of the order 1 mm or less, the slip velocity in the gravitational field becomes Stokes' terminal velocity, as in solid particles:

$$v_p = \frac{g(\rho_s - \rho_f){d_p}^2}{18\,\mu_f} \qquad (22.1\text{-}6)$$

The droplet is so small that it does not break up into two or more smaller droplets.

The mass-transfer rate is increased with the slip velocity and further enhanced with the intra-mixing within the droplet.

Therefore the so-called two-film theory should be applied. We should consider the mass transfer in the liquid film of continuous-phase as well as inside the droplet

Assume the clean condition without surface-active agents and impurities on the interface of droplet surface,

Except for the time of droplet formation, unless the droplet size is relatively larger than a few mm, the mass transfer correlation will become similar to that for solid spheres, e.g., Ranz-Marshall equation.

22.2 Extraction Technology

Liquid-liquid extraction takes place with two liquids immiscible in each other. One liquid is of organic nature (oil) while the other is aqueous (water).

The liquid extraction is often used when distillation and rectification are difficult or ineffective in relation to the energy saving. Regarding a simple batch operation, a quantity of feed mixture containing solute B in diluent A may be mixed with a quantity of the extracting solvent S in an agitated vessel, after which the two layers are settled and separated into the extract (B in S) and raffinate (B in A).

For the case of extracting solute B in a diluent A into organic phase S, the distribution coefficient is defined as

$$K = \frac{y_B \text{ (kg solute B/kg extract S)}}{x_B \text{ (kg solute B/kg raffinate A)}} \qquad (22.2\text{-}1)$$

The distribution coefficient can be obtained from the slope by plotting y_B against x_B. The large values are desirable since less solvent is required for a given degree of extraction.

If several contacts are necessary, continuous flow operation becomes economical. A mixer-settler extractor (see Fig.22.1-3) is adequate in simple extractions.

The batch extraction is usually operated in a stirred tank.

22.2-1 Liquid-liquid equilibria of ternary system

(a) Triangular coordinates

When the mutual solubility of the original solvent A and the extracting solvent S cannot be neglected, the solubility and equilibrium are expressed on triangular coordinates shown in Fig.22.2-1.

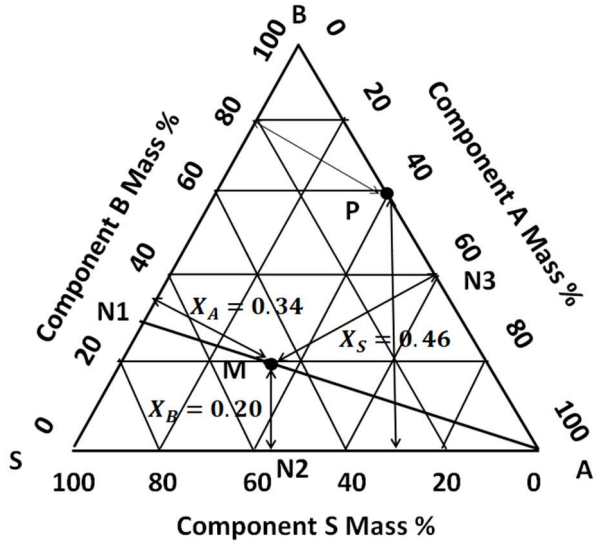

Fig.22.2-1 Triangular diagram for a ternary system

For a ternary mixture, a solute B is placed at the apex. Usually mass fractions or per cent may be used as the concentration units for extraction.

According to the geometric principle, Fig.22.2-1 indicates that the sum of the perpendicular distances from any point to the three sides of an equilateral triangle equals the altitude of the triangle.

$$\overline{MN1} + \overline{MN2} + \overline{MN3} = 1 \qquad (22.2\text{-}2)$$

For an example, the point M indicates a mixture of $X_B = 0.2, X_A = 0.34,$ and $X_S = 0.46$ in mass fraction.

The sum of those concentrations must be unity,

$$X_A + X_S + X_B = 1 \qquad (22.2\text{-}3)$$

Concentrations given by triangular diagrams are based on the entire mixture. For example, the point P of Fig.22.2-2 indicates a mixture of X_A =0.41, $X_S = 0.03$ and X_B =0.56 in mass fraction.

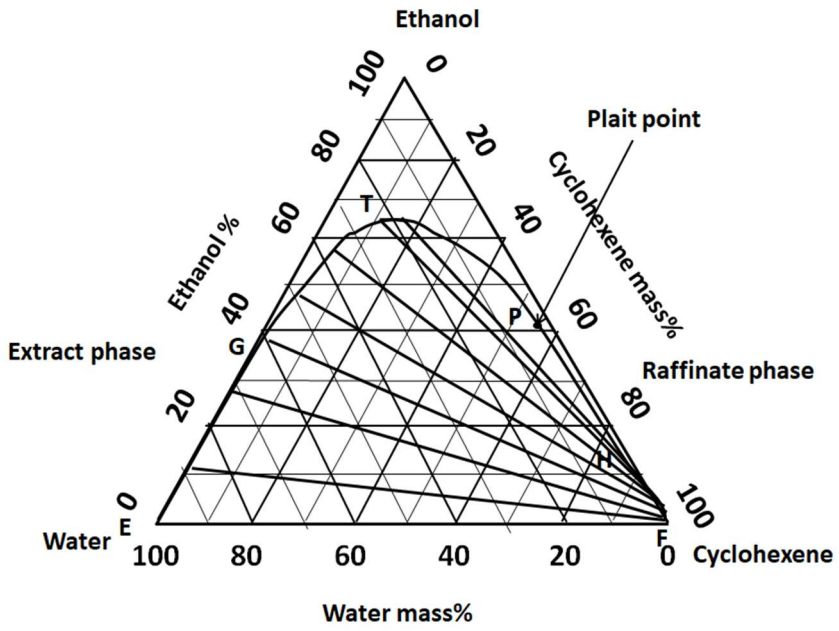

Fig.22.2-2 Triangular phase diagram for a ternary system of ethanol-cyclohexene-water in mass %

Fig.22.2-2 is a triangular diagram for the ternary system of ethanol B, cyclohexene A, and water S in the isothermal condition at 25˚C. The water S is the solvent for extracting the solute ethanol B from the diluent cyclohexene A. The solubility curve can be obtained by the following procedure.

In this ternary system, the points E and F existing almost at the bottom ends of the triangle imply the immiscibility between A and S.

Firstly if ethanol is added to a two-layer mixture of water and cyclohexene, the ethanol distributes between the two layers, and the composition of the layers give two solubility curves, one for the cyclohexene layer (raffinate phase) and the other for the water layer (extract phase). The curve EGTPHF is called “solubility curve.” The line E→G→T→P gives the compositions of the saturated water phase, and line F→H→P compositions of the saturated cyclohexene phase. The point P where the two phases become identical is called a plait point.

Straight lines connecting points on the two solubility curves is called a tie line, the ends of which indicate the points for two phases in equilibrium. The tie lines shown in the figure are given by some experimental data. As can be seen from the figure, the line length decreases as the plait point is approached. Each point within the space below the equilibrium curve EGTPHF called a dome lies on a tie line, and therefore an infinite number of such tie lines exist.

If the ethanol concentration in one phase (water) y_B is plotted against the ethanol concentration in the other phase (cyclohexene) x_B, the distribution curve with slope m can be obtained as shown below in the figure.

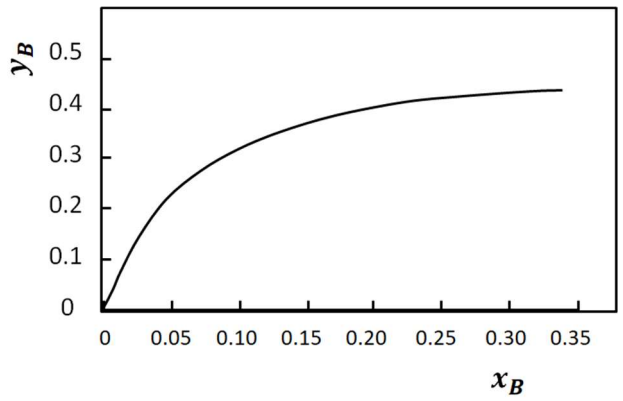

Fig.22.2-3 Distribution curve for a ternary system of water-ethanol-benzene (Solute: ethanol, Diluent: water, Solvent: benzene)

Local slope of the curve indicates the distribution coefficient: $m = y_B/x_B$.

This equilibrium relationship expressed in mole fraction can be understood as follows.

Since the fugacity of solute B, f_{BA} in the A-phase is equal to f_{BS} in the S-phase in an equilibrium condition,

$$f_{BA} = f_{BS} \tag{22.2-4}$$

If the pressure is low enough, the fugacity becomes equal to the pressure of an ideal gas.

The ratio of mole fraction gives the reciprocal of activity coefficient ratio, i.e. the reciprocal of distribution coefficient:

$$\frac{x_{BA}}{x_{BS}} = \frac{\gamma_{BS}}{\gamma_{BA}} = 1/m \tag{22.2-5}$$

(b) Rectangular coordinates

A disadvantage of the triangular diagrams is that their scales can be neither changed nor enlarged when it is necessary to follow changes in a narrow concentration range. Therefore the rectangular diagram shown in Fig.22.2-4 is very convenient and recommendable. The composition of point P is given by solute = x_{CP}, solvent= x_{BP}, and diluent $x_{AP} = 1 - x_{BP} - x_{CP}$.

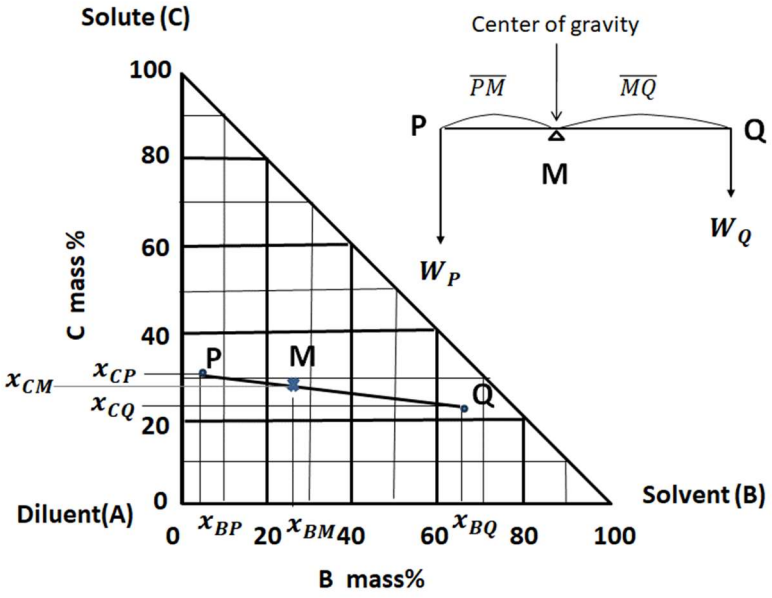

Fig.22.2-4 Rectangular coordinate diagram for a ternary system

Center-of- Gravity Principle (Principle of Leverage)

If W_P kg of liquid mixture (x_{AP}, x_{BP}, x_{CP}) is mixed with W_q kg of liquid mixture (x_{AQ}, x_{BQ}, x_{CQ}), the obtained mixture $W_M = W_p + W_q$ kg should have the following material balance:

$$W_M = W_p + W_q \quad (22.2\text{-}6)$$

$$W_M x_{BM} = W_p x_{BP} + W_q x_{BQ} \quad (22.2\text{-}7)$$

$$W_M x_{CM} = W_p x_{CP} + W_q x_{CQ} \quad (22.2\text{-}8)$$

From these equations,

$$\frac{W_p}{W_q} = \frac{x_{BQ} - x_{BM}}{x_{BM} - x_{BP}} = \frac{x_{CQ} - x_{CM}}{x_{CM} - x_{CP}} \quad (22.2\text{-}9)$$

As can e seen from Fig.22.2-4, the above equation indicates that the position of the obtained mixture is located at point M on the line PQ where the line length ratio $\overline{MQ}/\overline{MP}$ is given by the mass ratio W_p/W_q. This rule is called "Center-of-Gravity Principle."

The composition of the obtained mixture is given by

$$x_{BM} = \frac{x_{BQ} + (W_p/W_q)\, x_{BP}}{1 + W_p/W_q} \quad (22.2\text{-}10)$$

$$x_{CM} = \frac{x_{CQ} + (W_p/W_q)\, x_{CP}}{1 + W_p/W_q} \quad (22.2\text{-}11)$$

[Example 22.2-1]

A batch agitated tank extractor is used to separate ethanol from its mixture with cyclohexene by using clean water. The liquid-liquid equilibrium diagram for the ternary system at 25℃ is shown below.

The feed of cyclohexene mixture $W_F = 50$ kg contains 30 wt% of ethanol only. The W_F kg feed mixture and the W_S kg of the solvent (water) are put into the agitated tank extractor and then after the sufficient agitation, the upper cyclohexene layer settled down is taken out as the raffinate product. Its composition is required to have 99 wt% cyclohexene. How much water W_S is necessary for one batch operation?

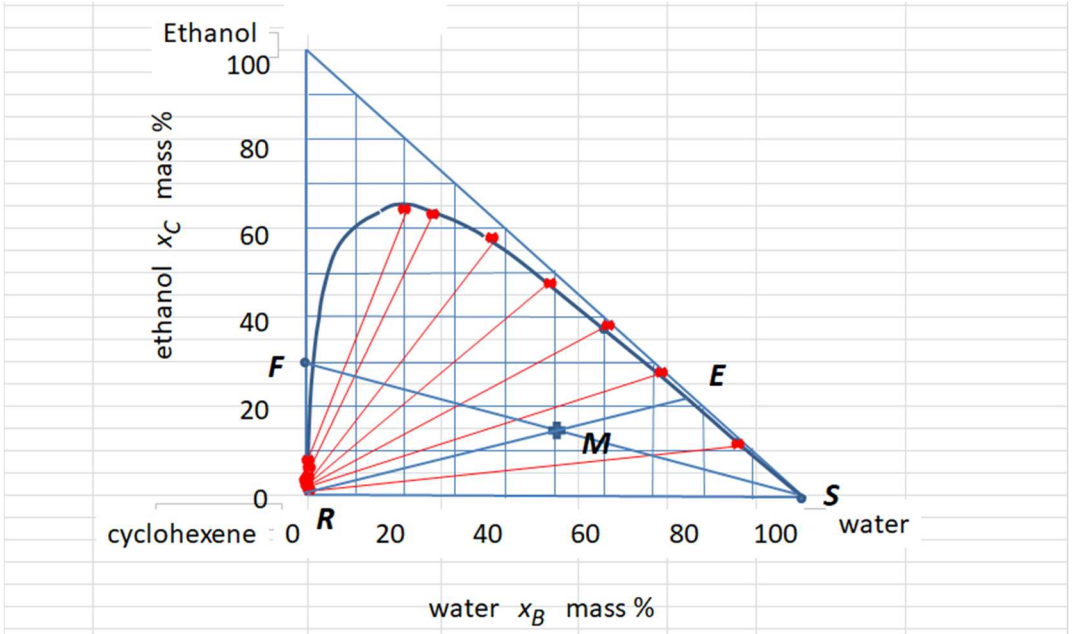

Fig.22.2-E1 Rectangular coordinates of liquid-liquid equilibrium diagram for a ternary system of ethanol, cyclohexene, and water.

Solution:

On the rectangular diagram, the feed is located at Point F and the solvent (clean water).is located at the right corner of the triangle S. The composition of the raffinate product should be $x_{CR} = 0.01$, $x_{AR} = 0.99$, and $x_{BR} = 0$. Therefore the point R is located at $x_{CR} = 0.01$ just on the vertical axis.

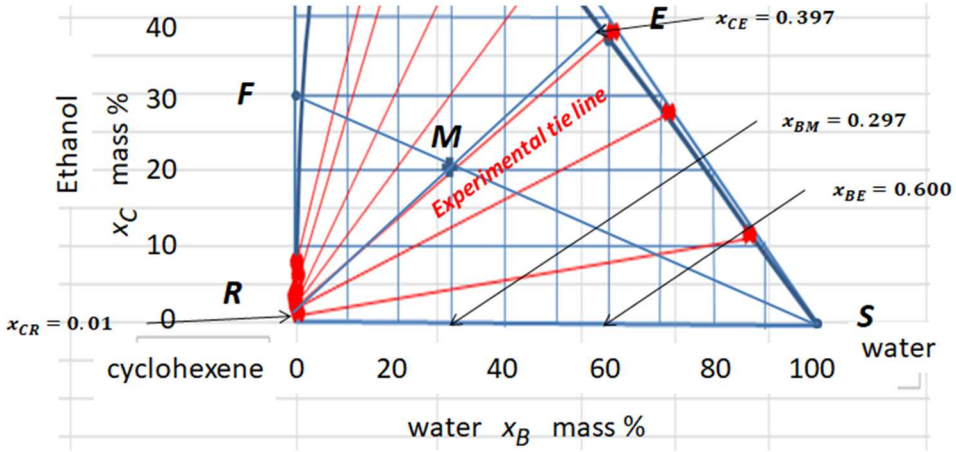

Fig.22.2-E2 Calculation of solvent quantity required using experimental tie lines on a rectangular diagram

Fig.22.2-E2 is the equilibrium diagram region below 40 wt% ethanol enlarged. The tie line RE drawn along the experimental tie line from the point R can get the point E on the equilibrium curve, which indicates $x_{CE} = 0.397$.

If we assume that the solvent (water) is immiscible with the diluent (cyclohexene), all the cyclohexene of the feed is left into the raffinate phase.

$W_F\, x_{AF} = R\, x_{AR}$

That is,

$R = W_F\, x_{AF} + R\, x_{CR}$ (22.2-E1)

Therefore

$R = \frac{W_F\, x_{AF}}{(1 - x_{CR})} = \frac{(50)(0.70)}{(1-0.01)} = 35.4$ kg

The following two equations are obtained by the principle of leverage:

$W_F(x_{BM} - x_{BF}) = W_S(x_{BS} - x_{BM})$ (22.2-E2)

$R\,(x_{BM} - x_{BR}) = E\,(x_{BE} - x_{BM})$ (22.2-E3)

$R + E = W_F + W_S$ (22.2-E4)

Since

$x_{BF} = 0, x_{BS} = 1.0, x_{BR} = 0,\ x_{BE} = 1 - x_{CE} = 0.60,\ W_F = 50,\ R = 35.4$

From these equations

$W_S = 21.1$ kg, $E = 35.7$ kg, and $x_{BM} = 0.297$.

The 35.4 kg of raffinate contains 99 wt% of cyclohexene and 1 wt% of ethanol is obtained by using 21.1 kg of clean water.

22.2-2 Unsteady mass transfer problems in liquid-liquid extraction

Actually speaking, as distinct from the above example, there is a possibility of collision and breaking-up of droplets depending upon the Reynolds number.

In particular, mass transfer is greatly strengthened owing to unsteady strong shearing stresses in the vicinity of the agitator blade tips or at the instant when droplets are formed. The mechanism for the mass transfer in this unsteady condition is very difficult to investigate but very attractive to utilize for designing practical commercial-scale extractors.

Mass transfer in the period of droplet formation due to shear stresses

The radical variation in the fluid velocity and droplet surface makes the analysis and modeling difficult. The following mass transfer coefficients can be assumed according to penetration theory.

$k_c = C_c\sqrt{D_{Bc}/\theta_c}$ (continuous phase) and $k_d = C_d\sqrt{D_{Bd}/\theta_d}$ (dispersed phase)

where C_c and C_d are empirical constants to be determined by experiment.

Here θ_c and θ_d are time-constants characteristic for periodical surface renewal.

This suggests that when these time constants become small, the mass transfer is enhanced.

You can call to mind that the mass transfer coefficient is proportional to the square root of diffusivity divided by contact time. (see Eqs.(6.7-14)and (16.1-13))

22.2-3 Continuous extractors

Various extraction columns similar to distillation columns are available depending on the requirements of individual extraction processes.

The tie lines for design computations of extractors are obtained by interpolation with the aid of the distribution curve from experimentally observed tie lines

Countercurrent multistage liquid-liquid extraction systems

Let us consider the design method for a stripping packed column shown in Fig.22.2-5. In a manner similar to distillation column design (PART II, p.128~133), firstly the number of theoretical stages required for the specification of a desired composition change is stage-by-stage calculated. Secondly the actual height of the packed column is determined by use of the height equivalent to a theoretical plate, i.e. HETP (see PART II, p.147~148).

However a difficult problem may arise that the assumption of constant molar flow rates of the streams is often impermissible in extraction calculations with mass fraction units. In addition, since the diluent and solvent usually have small mutual miscibility, the extract phase contains solute B in solvent S with concentrations $y_B, y_S,$ and small y_A, while the raffinate phase contains solute B in diluent A with concentrations x_B, $x_A,$ and small x_S. Consider the case when the raffinate is heavier in fluid density than the extract. The original mixture (feed rate $R_0 = F$) of solute B dissolved in diluent A is fed from the top of the column. A pure solvent S (feed rate Q) is supplied from the bottom of the column.

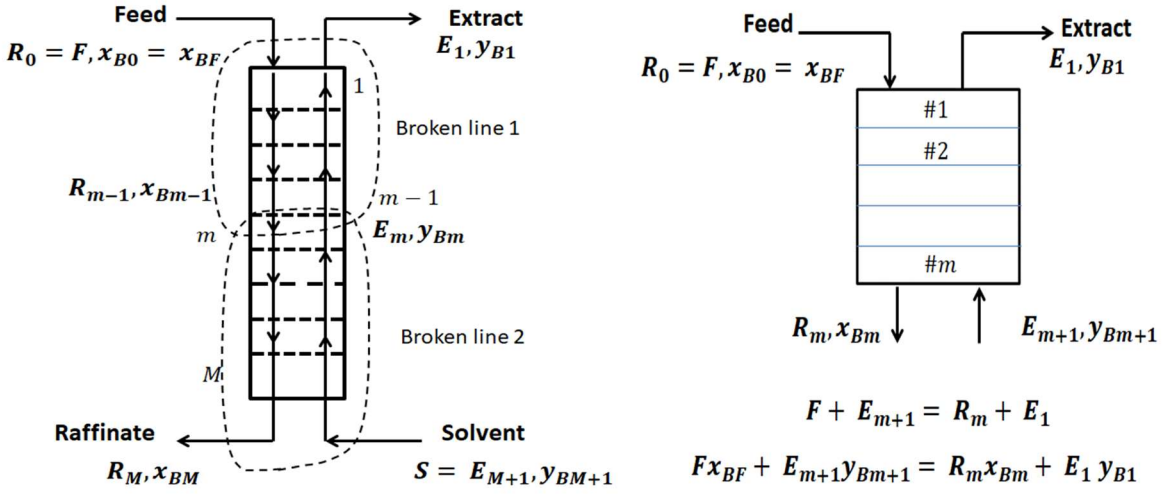

Fig.22.2-5 Countercurrent multi-staged extractor with no reflux

22.2-4 Stage-by-stage design calculation of a continuous extractor

The overall mass balance gives $F + S = E_1 + R_M$

This equation indicates that the straight line $\overline{FS}$ intersects the straight line $\overline{E_1 R_M}$ at the point M on the triangular diagram.

The mass balance set up over each shell from the top is given by

1st stage (shell 1): $F + E_2 = R_1 + E_1$ (22.2-12)

1st ~2nd stage (shell 2): $F + E_3 = R_2 + E_1$ (22.2-13)

1st ~Mth stage (shell M), $F + E_{M+1} = R_M + E_1$, and $E_{M+1} = S$ (22.2-14)

Therefore

$$F - E_1 = R_1 - E_2 = R_2 - E_3 = \cdots = R_M - E_{M+1} \equiv L \text{ (constant)} \quad (22.2\text{-}15)$$

Similarly for the component B

$$F\,x_{BF} - E_1 y_{B1} = R_1 x_{B1} - E_2 y_{B2} = R_2 x_{B2} - E_3 y_{B3} = \cdots = R_M x_{BM} - E_{M+1} y_{BM+1} \equiv L\,x_L \text{ (constant)} \quad (22.2\text{-}16)$$

These two equations imply that as shown in Fig.22.2-6 , the extensions of operating lines $\overline{FE_1}$, $\overline{R_1 E_2}$, $\overline{R_2 E_3}$,--- $\overline{R_M E_{M+1}}$ cross at a common point O.

The mass balance at steady state is set up over the shell (enclosed by the broken line 2) between the bottom and stage *m* as $R_M + E_m = R_{m-1} + S$

$$R_{m-1} - E_m = R_M - S = L \quad (22.2\text{-}17)$$

Here $E_{M+1} = S$ is the solvent being supplied from the bottom, and L implies the net downward flow.

The mass balance for the solute B: $R_M x_{BM} + E_m y_{Bm} = R_{m-1} x_{Bm-1}$

or

$$R_{m-1} x_{Bm-1} - E_m y_{Bm} = R_M x_{BM} \quad \text{or} \quad y_{Bm} = (R_{m-1}/E_m) x_{Bm-1} - (R_M/E_m) x_{BM} \quad (22.2\text{-}18)$$

This is an equation of operating line with slope R_{m-1}/E_m.

In the case when the raffinate does not contain any solvent S, i.e. $x_{Sm} = x_{SM} = 0$ and $y_{SM+1} = 1$, the mass balance at each stage m for the extracting solvent S reduces to:

$$E_m y_{Sm} = S \quad (22.2\text{-}19)$$

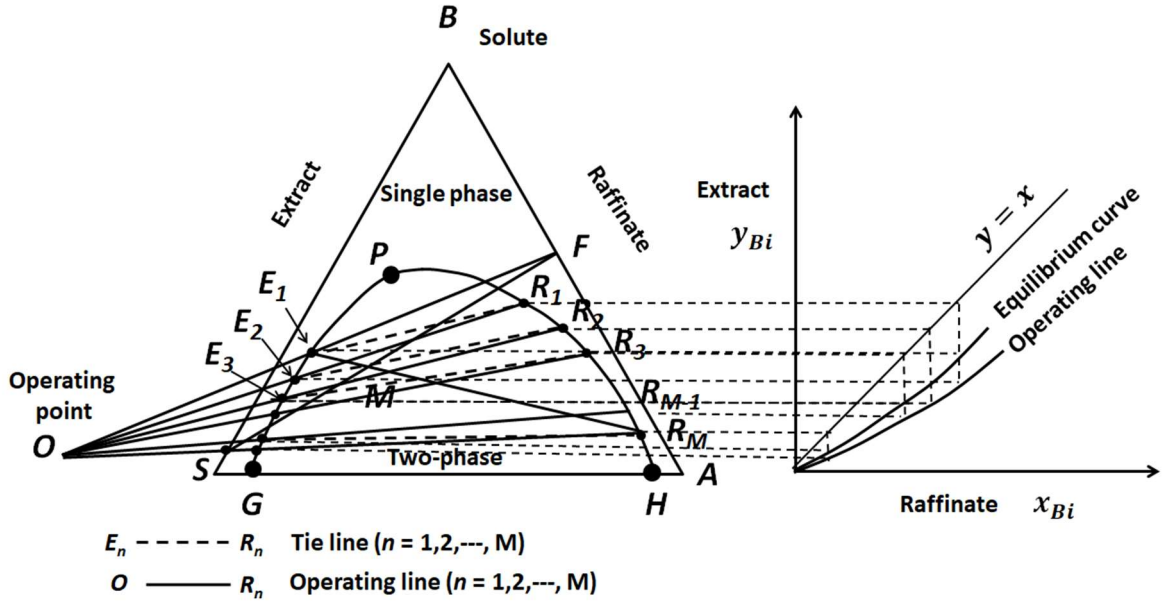

Fig. 22.2-6 Stage-by-stage calculation of a countercurrent multi-staged extractor

If we assume an equilibrium curve shown in Fig.22.2-6, we can calculate stage-by-stage the number of equilibrium stages required for attainment of the raffinate concentration x_{BM} as the bottom product. Eqs.(22.2-15) and (22.2-16) give the stage-by-stage changes in composition of the countercurrent streams.
The following operating line equation can also be obtained:,

$$y_{Bm} = (R_{m-1}/E_m)x_{Bm-1} - (R_M/E_m)x_{BM} \quad (22.2\text{-}20)$$

[EXAMPLE 22.2-2]

We need to extract propanoic acid from its mixture with heptane by means of clean water as the extracting solvent. The extraction method is adopted for energy saving instead of distillation. The heptane solution as the feed includes 30 wt% of propanoic acid but does not contain any water.
A continuous countercurrent column shown in Fig.22.2-E3 is used. The propanoic acid concentration of the final effluent raffinate is required to be 3 wt% or less. Here we assume the distribution of a solute C between two immiscible liquid B (water) and A (heptane).

As distinct from the last example, the raffinate phase is lighter in density than the extract phase. Therefore the heptane mixture to be extracted is supplied from the bottom at a feed rate of 100 kg/h. Water as the extracting solvent is fed from the top at a rate of 30 kg/h. The entire system can be assumed to be kept isothermal at 50˚C.

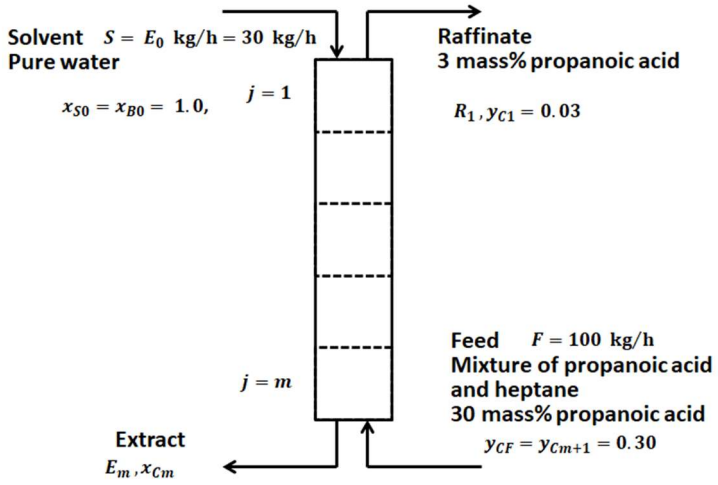

Fig. 22.2-E3 Countercurrent extractor

The data of equilibrium curve and tie line are listed in Table 22.2-E1.

Table 22.2-E1 Liquid-liquid equilibrium data for ternary system of propanoic acid, heptane, and water (50℃)

(Tie line data) Composition in mass fraction

LEFT PHASE			RIGHT PHASE		
propanoic acid	Water	heptane	propanoic acid	Water	Heptane
0.06018	0.00174	0.93808	0.26968	0.71208	0.01824
0.11920	0.00229	0.87851	0.41475	0.55794	0.02731
0.20659	0.00543	0.78799	0.56583	0.40638	0.02778
0.27829	0.00874	0.71297	0.64951	0.32088	0.02962
0.35494	0.01432	0.63074	0.70801	0.24795	0.04404
0.41980	0.01887	0.56133	0.73535	0.20205	0.06259

(Equilibrium curve data) Composition in mass fraction

LEFT PHASE			RIGHT PHASE		
propanoic acid	Water	heptane	propanoic acid	Water	Heptane
0.037764	0.001837	0.96040	0.69349	0.07396	0.23255
0.076646	0.002144	0.92121	0.70746	0.08167	0.21087
0.116696	0.002460	0.88084	0.72680	0.08990	0.18330
0.160141	0.005843	0.83402	0.73515	0.11117	0.15367
0.203963	0.006946	0.78909	0.75160	0.13543	0.11297
0.250630	0.009145	0.74022	0.75075	0.16801	0.08124
0.298177	0.010362	0.69146	0.76350	0.19346	0.04303
0.349324	0.012746	0.63793	0.74260	0.21275	0.04465
0.403104	0.015253	0.58164	0.71807	0.25764	0.02428
0.471757	0.024100	0.50414	0.68882	0.31118	0
0.554265	0.036771	0.40896	0.63792	0.36208	0
0.693489	0.073963	0.23255	0.50684	0.49316	0
			0.31355	0.68645	0

The liquid-liquid equilibrium data for the ternary system is given in the triangular coordinate diagram shown in Fig.22.2-E4.

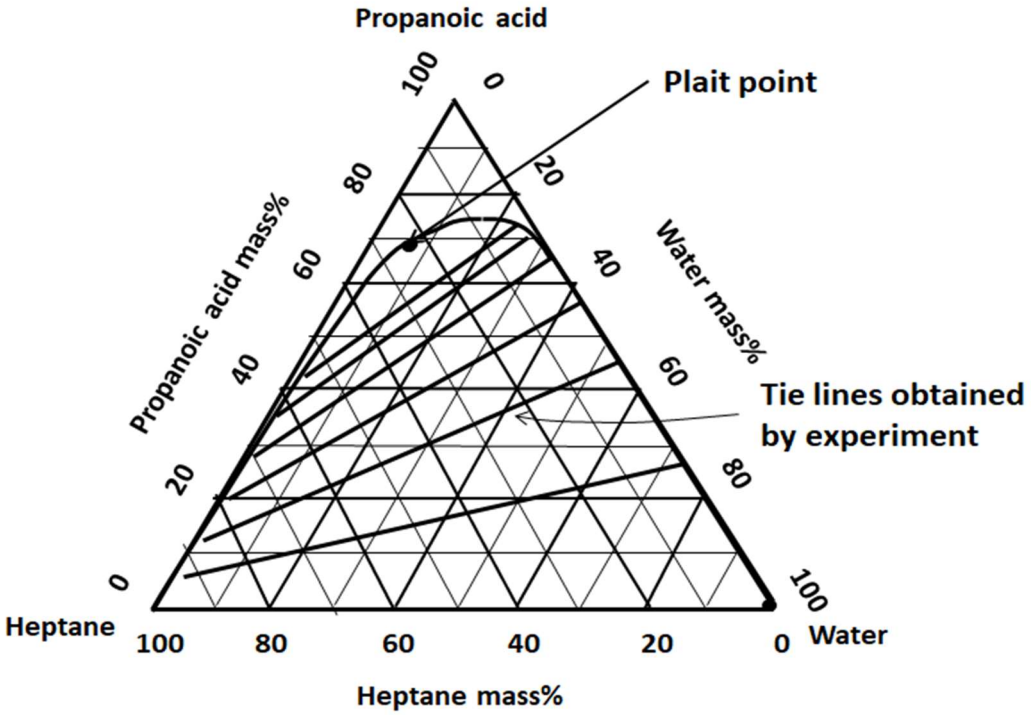

Fig.22.2-E4 Triangular diagram of a ternary system of propanoic acid, heptane, and water at 50˚C

Calculate the number of ideal stages with no reflux required for this specification of extraction by using the ideal stage concept.

Solution:

Let us designate propanoic acid, water, and heptane to be component C, component B, and component A, respectively.

The compositions of the extract phase and the raffinate phase are expressed by x and y in mass fraction, respectively.

According to the condition of specification,
Heptane mixture (feed): $F = R_{m+1} =$ 100 kg/h, (solute) $y_{CF} = y_{Cm+} = 0.30$
Final effluent raffinate: R_1 and (solute) $y_{C1} = 0.03$
Extracting solvent (water): $S = E_0 =$ 30 kg/h, (solute) $x_{AS} = x_{A0} = 0$, (solvent) $x_{S0} = 1.0$,
Effluent extract: E_m, x_{Cm}

First of all, let us draw the line FS from point F ($y_{Cm+1} = 0.3$, $y_{Am+} = 0.7$) to point S ($x_{S0} = x_{B0} = 1.0$) on the triangular or rectangular coordinates.

The feed is located at Point F $(y_{FA} = y_{Am+1} = 0.70, y_{FC} = y_{Cm+1} = 0.30, y_{FB} = y_{Bm+1} = 0)$. The clean water as the solvent is located at Point S $(x_{A0} = 0, x_{C0} = 0, x_{B0} = 1.)$.
From the material balance of solute between the top and bottom of the entire system

$$F + S = E_m + R_1 = M \quad \text{(22.2-E5)}$$

$$F\,y_{CF} + S\,x_{CS} = E_m x_{Cm} + R_1 y_{C1} = M\,x_{CM} \quad \text{(22.2-E6)}$$

From the first equation, $F + S = M = 100 + 30 = 130$ kg/h
The solute concentration of mixture M is given by Point M:

$$x_{CM} = \frac{F\,y_{CF} + S\,x_{CS}}{F+S} = \frac{(100)(0.30)+(30)(0)}{100+30} = 0.231 \quad \text{(22.2-E7)}$$

The final raffinate condition is specified at R_1 as

$$y_{C1} = 0.03$$

Since the point R_1 indicates $y_{C1} = 0.03$ and $y_{A1} = 0.97$, the mass balance of diluent A gives the final raffinate flow rate R_1:

$$F\,y_{AF} = R_1 y_{A1} \quad \text{or} \quad R_1 = F\,y_{AF}/y_{A1} = (100)(0.70)/0.97 = 72.2 \text{ kg/h} \quad \text{(22.2-E8)}$$

From Eq.(22.2-E5) and Eq.(22.2-E6)

$$x_{CM} = \frac{E_m\,x_{Cm} + R_1\,y_{C1}}{M}, \quad \text{(22.2-E9)}$$

$$x_{Cm} = \frac{M\,x_{CM} - R_1\,y_{C1}}{E_m} \quad \text{(22.2-E10)}$$

Since $M = F + S = 100 + 30 = 130$ kg/h,
$E_m = M - R_1 = 130 - 72.2 = 57.8$ kg/h

Therefore, as shown in Fig.21.6-E6, the solute concentration of the extract is given by the Point E_m

$$x_{Cm} = \frac{M\,x_{CM} - R_1\,y_{C1}}{E_m} = \frac{F\,y_{CF} + S\,x_{CS} - R_1 y_{C1}}{E_m} = \frac{(100)(0.30)+(30)(0)-(72.2)(0.03)}{57.8} = 0.482 \quad \text{(22.2-E11)}$$

The mass balance set up over each shell from the top is given by

$$1^{st} \text{ stage (shell 1): } S + R_2 = R_1 + E_1 \quad \text{(22.2-E12)}$$

$$1^{st} \sim 2^{nd} \text{ stage (shell 2): } S + R_3 = R_1 + E_2 \quad \text{(22.2-E13)}$$

$$1^{st} \sim m^{th} \text{ stage (shell m), } S + F = R_1 + E_m, \quad \text{and } R_{m+1} = F \quad \text{(22.2-E14)}$$

Therefore

$$S - R_1 = E_1 - R_2 = E_2 - R_3 = \cdots = E_m - R_{m+1} \equiv L \text{ (constant)} \quad \text{(22.2-E15)}$$

Similarly for the component C

$$S\,x_{CS} - R_1 y_{C1} = E_1 x_{C1} - R_2 y_{C2} = E_2 x_{C2} - R_3 y_{C3} = \cdots = E_m x_{Cm} - R_{m+1} y_{Cm+1} \equiv \equiv L\,x_L \text{ (constant)} \quad \text{(22.2-E16)}$$

The straight line given by the final extract and raffinate $\overline{R_1 E_m}$ must pass through point M. The extension of the line passing through the points R_1 and M crosses the equilibrium curve at point E_m. This point M indicates the solute concentration:

$$x_{CM} = \frac{R_1 y_{C1} + E_m x_{Cm}}{M} = \frac{(72.2)(0.03)+(57.8)(0.482)}{130} = 0.231 \quad \text{(22.2-E17)}$$

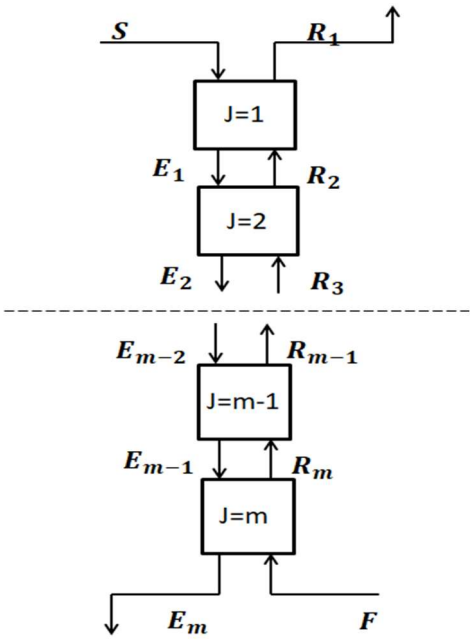

Fig.22.2-E5 Countercurrent multi-stage extractor for stage-by-state calculation

The material balance set over each stage of the countercurrent multi-stage extractor is calculated stage-by-stage as follows. These results are also shown in Fig.22.2-E6.

he final extract flow solute concentration

$$x_{Cm} = (100 \times 0.30 - 72.2 \times 0.03)/57.8 = 0.482 \quad (22.2\text{-E18})$$

The necessary number of stages m will be determined by the following step-by-step calculation.

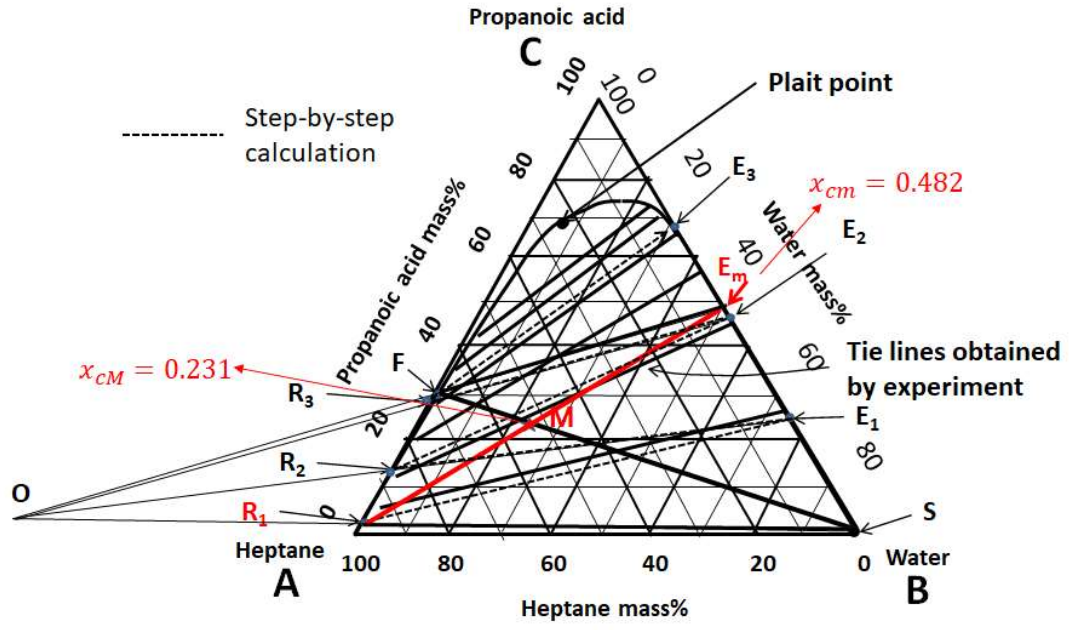

Fig.22.2-E6 Step-by-step method for calculating the number of stages

In the equilibrium stage model, the extract stream E_m and the raffinate stream R_m leaving the m^{th} stage are in equilibrium.

Since $E_m = 57.8$ kg/h and $R_1 = 72.2$ kg/h, the concentration of C (propanoic acid) in the final extract E_m is calculated as

$$x_{Cm} = (100 \times 0.30 - 72.2 \times 0.03)/57.8 = 0.482 \quad \text{(22.2-E19)}$$

Therefore by reference to the experimental tie lines, as shown in Fig.21.6-E6, the tie line expressed by the broken line E_1R_1 gives $E_1: x_{C1} = 0.25$ and $R_1: y_{C1} = 0.03$. The next operating line obtained from E_1R_2 using the operating point O indicates $y_{C2} = 0.14$ at point R_2.

According to the assumption of immiscible liquids A and S, the mass balance equations regarding the diluent A (heptane) give the following quantities:

$$R_1\, y_{A1} = R_2 y_{A2} \quad \text{or} \quad R_2 = R_1\, y_{A1}/y_{A2} = (72.2)(1 - 0.03)/(1 - 0.14) = 81.4 \text{ kg/h}$$

$$E_1 = S + R_2 - R_1 \quad \text{or} \quad E_1 = 30 + 81.4 - 72.2 = 39.2 \text{ kg/h} \quad \text{(22.2-E20)}$$

The tie line R_2E_2 has $E_2: x_{C2} = 0.47$ at E_2. The operating line E_2R_3 gives $y_{C3} = 0.29$ at point R_3. That is, $y_{A3} = 0.71$.

$$R_3 = R_1\, y_{A1}/y_{A3} = (72.2)(1 - 0.03)/0.71 = 98.6 \text{ kg/h} \quad \text{(22.2-E21)}$$

$$E_2 = S + R_3 - R_1 = 30 + 98.6 - 72.2 = 56.4 \text{ kg/h} \quad \text{(22.2-E22)}$$

As can be seen from Fig.22.2-E6, the next tie line R_3E_3 gives $E_3: x_{C3} = 0.68$ but this value has gone very much beyond the point E_m ($x_{Cm} = 0.482$).

It can be considered from the result that the number of ideal stages should be more than 2 but lie near 2.

[PROBLEM 22.2-1]

Let us reconsider the same problem as EXAMPLE 22.2-2. An organic solution 100 kg/h of heptane containing propanoic acid is fed from bottom into the counter-current extractor shown in Fig.22.2-P1. The solute propanoic acid needs to be recovered by clean water which is supplied at a rate of 50 kg/h into the top of the counter-current extractor. The heptane solution as the feed includes 40 wt% of propanoic acid but does not contain any water.

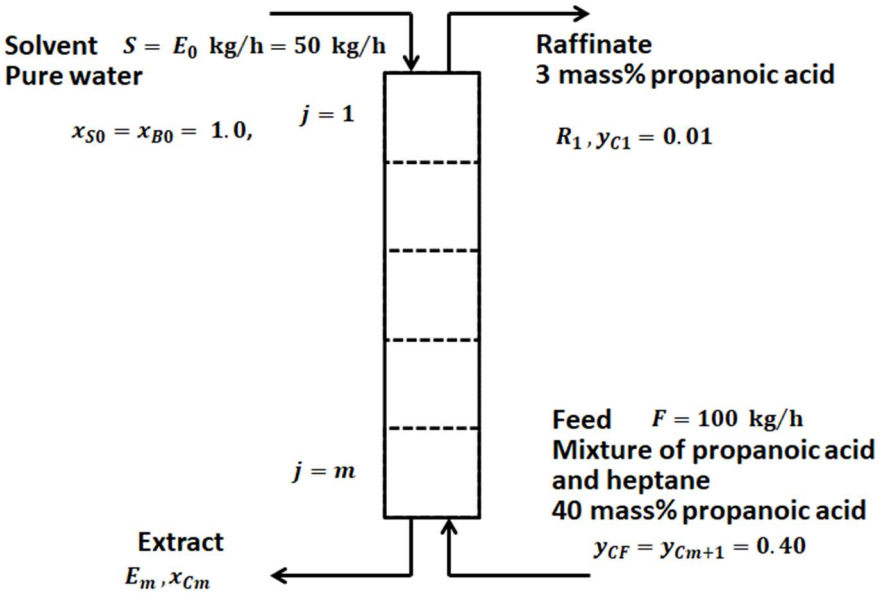

Fig.22.2-P1 Continuous counter-current extractor

The propanoic acid concentration of the final effluent raffinate is required to be 1 wt% or less. Here we assume the distribution of a solute C between two immiscible liquid B (water) and A (heptane).

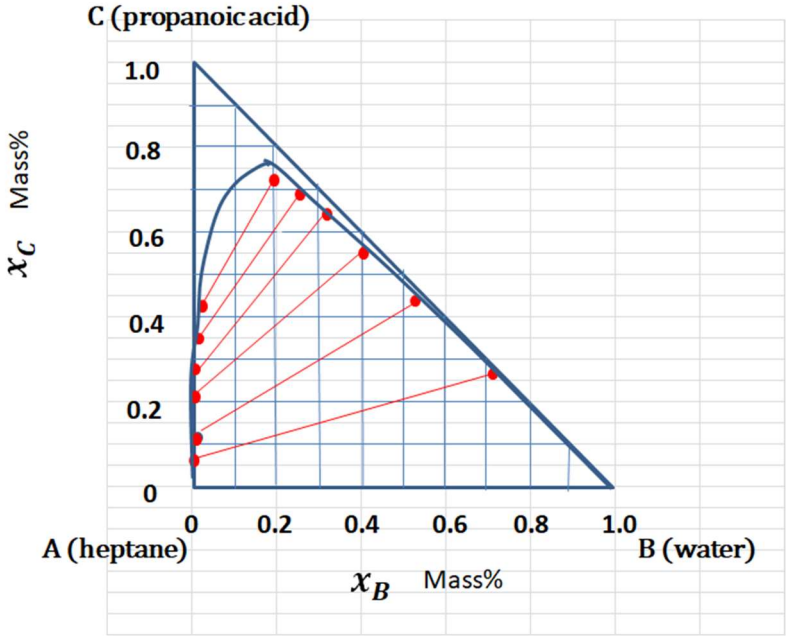

Fig.22.2-P2 Rectangular diagram of a ternary system of propanoic acid, heptane, and water at 50˚C

As shown in Fig.22.2-P2, the rectangular diagram of equilibrium and some tie lines are also obtained from Table 22.2-E1 of EXAMPLE 22.2-2..

The entire system is also kept isothermal at 50˚C.

Calculate the number of ideal stages with no reflux required for this specification of extraction by using the ideal stage concept.

As in the above example and problem, we can assume that the raffinate stream leaving each stage does not include any solvent owing to the immiscible liquid pair of A and S. Since the solvent rate 30 kg/h or 50 kg/h may be considerably small as compared to the feed rate 100 kg/h, we should be careful of preventing the solvent stream from flooding in the practical operation.

As distinct from distillation, the difference in density between the extract liquid and raffinate liquid is not so large. It should be kept in mind as a practical problem that it is also considerably difficult to separate the extracting mixture into the extract and raffinate in each stage.

22.3 Solid Extraction – Leaching

Leaching or solid extraction is a unit operation obtaining valuable soluble matters from the inside of an insoluble solid body. The properties of the solids may change considerably in the leaching operation. Granular or porous-matrix solids may be effective when soluble material is removed.

As an example of leaching processes, we can give a tea bag containing dried tea leaves to be soaked in hot water. The tea flavor substance is extracted from the tea leaf solid by the hot water used as the solvent. Leaching process is controlled by the following three subprocesses: (1) dissolution of solute from solid in solvent, (2) diffusion of solute through pores of the solid particles and (3) transfer of solute into bulk solvent.

22.3-1 Equilibrium stage

In leaching, if sufficient solvent is present to dissolve all the solute in the entering solid and there is

no adsorption of solute by the solid, equilibrium is attained when the solute completely dissolves and the concentration of the solution becomes uniform. Ideal single stage can also be expressed as in Fig.22.3-1.

If the concentration of the liquid retained by the solid (underflow) leaving the stage of interest is equal to that of the concentrated liquid (overflow) leaving the same stage, that is, $x_{Ai} = y_{Ai}$, this stage is called "equilibrium (ideal) stage."

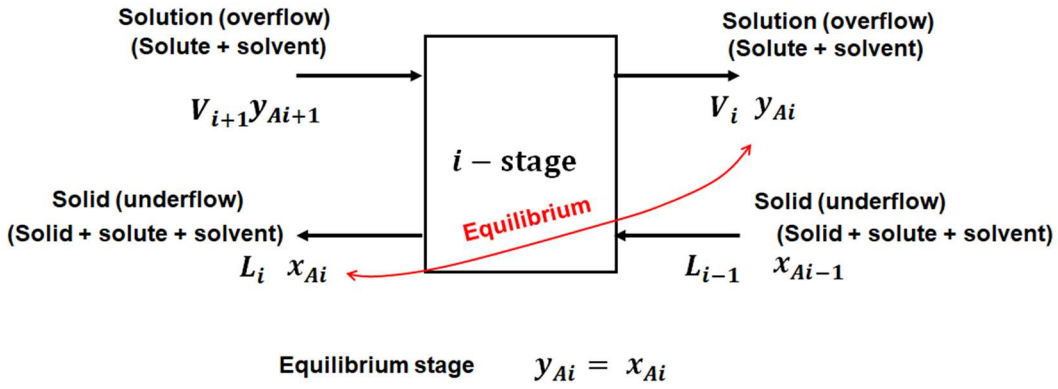

Fig.22.3-1 Definition of equilibrium stage in a continuous leaching system

This definition is similar to the definition of ideal stage in multi-staged distillation column. (see Fig.11.2-10 in Chapter 11)

Fig.22.3-2 shows a continuous countercurrent cascade. The V phase is the liquid solution (solute + solvent) overflowing from stage to stage in the right direction (from stage N toward stage 1) counter to that of the underflowing slurry (solute + solvent + solid) of the solute-retained solid. The L phase is the liquid solution included in the solid flowing from stage 1 toward N. Exhausted solids are discharged from stage N while concentrated solution issues from stage 1 as the overflow product. The solute-free solid is insoluble and inert in the solvent. Therefore the flow rate of the solid is constant throughout the cascade on the dry solute-free basis.
Two definitions of solute concentration in the overflow and underflow, respectively.
x: solute concentration in the underflowing solution
y: solute concentration in the solution included in the underflowing slurry
V: flow rate of overflow solution
L: flow rate of underflow of the liquid retained by the solid based on a definite flow of dry solute-free solid
x_a: solute concentration of the solution included in the entering solid slurry
x_b: solute concentration of the solution included in the leaving solid slurry
y_a: solute concentration in the concentrated solution leaving stage 1
y_b: solute concentration in the fresh solvent entering the stage N

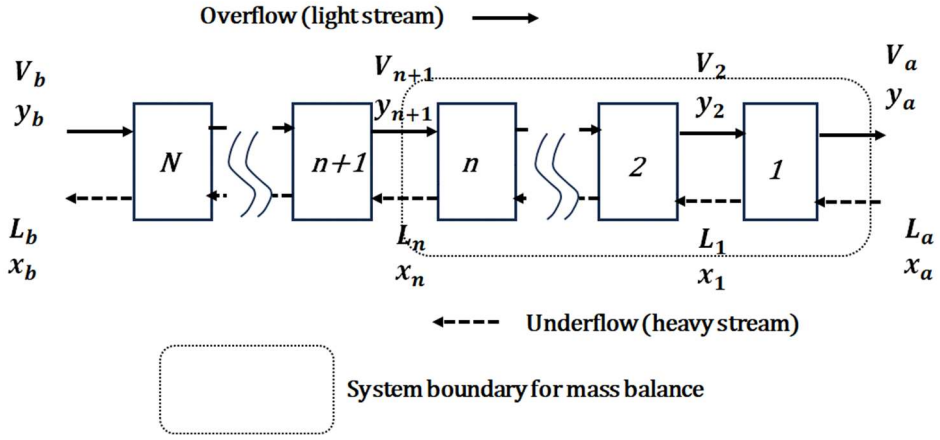

Fig.22.3-2 Continuous countercurrent leaching cascade

22.3-2 Design calculation of a counter-current leaching system

In a similar manner to the step-by-step calculation for trayed distillation column, a design calculation method can be derived for staged counter-current leaching systems.

Operating Line

Mass balance set up over the system boundary indicated by the dotted line in Fig.22.3-2 gives

$$V_{n+1} + L_a = V_a + L_n \quad (22.3\text{-}1)$$

$$V_{n+1}y_{n+1} + L_a x_a = V_a y_a + L_n x_n \quad (22.3\text{-}2)$$

From these two equations, we obtain the following operating line equation:

$$y_{n+1} = \frac{L_n}{L_n+(V_a- L_a)}\, x_n + \frac{V_a\, y_a- L_a\, x_a}{L_n+ (V_a- L_a)} \quad (22.3\text{-}3)$$

The line of this equation passes through points (x_a, y_a) and (x_b, y_b).

Usually the density and viscosity of the solution vary remarkably with solute concentration. The liquid retained by the solid from the lower-numbered stages is more than that from the higher-numbered stages: $L_n > L_{n+1}$. Therefore the slope of the operating line may vary from unit to unit. However if we can assume that the mass of the retained solution is independent of solute concentration, L_n = constant, the operating line is straight.

This is called "constant underflow condition."

$$L_{n+1} = L_n = ---= L_a = L \quad (22.3\text{-}4)$$

$$V_{n+1} = V_n = ---= V_a = V \quad (22.3\text{-}5)$$

We will consider the constant underflow case only for understanding the fundamentals.

Firstly the operating line equation is simplified as

$$y_{n+1} = \frac{L}{V}\, x_n + y_a - \frac{L}{V}\, x_a \quad (22.3\text{-}6)$$

The following material balance is given for the first stage:

$$L_0 + V_2 = L_1 + V_1 = M \quad (22.3\text{-}7)$$

$$L_0 x_0 + V_2 y_2 = L_1 x_1 + V_1 y_1 = M\, x_M \quad (22.3\text{-}8)$$

For the dry inert solid movement,

$$B = N_0\, L_0 + 0 = N_1\, L_1 + 0 = N_M\, M \quad (22.3\text{-}9)$$

Similarly the material balance equation for an arbitrarily chosen stage *n* becomes

$$L_{n-1} + V_{n+1} = L_n + V_n = M \quad (22.3\text{-}10)$$

$$L_{n-1}x_{n-1} + V_{n+1}y_{n+1} = L_n x_n + V_n y_n = M\, x_M \quad (22.3\text{-}11)$$

The dry inert solid movement is given by

$$B = N_{n-1}L_{n-1} = N_n\, L_n = N_M\, M \quad (22.3\text{-}12)$$

A very important parameter is the underflow function $U(x)$ kg solution/kg solid.
The definition means how much the solution is carried by the solid in the underflow.
The function depending on the properties of the solid, of the solution, and of the equipment used to separate the overflow (filtration, decantation, thickening, etc.) should be experimentally determined.

[EXAMPLE 22.3-1]

A soybean crude oil is produced by the leaching process of a solid feed F =1,000 kg/h (e.g. flaked soybeans) containing 75wt% insoluble solid (including proteins) and approximately 25wt% oil to be extracted. A continuous countercurrent leaching battery is used. Pure solvent (e.g. n-hexane) 900 kg/h is supplied to extract 95% of the solute (e.g., soybean oil). The solid discharging as the slurry from the final stage N entrains a limited rate of liquid solution. By a preliminary test, we get such an empirical underflow function that each kg of solid carries (0.9 + 0.3 x) kg of the solution of solute mass fraction x. We assume that the leaching process can be treated as an ideal stage-to-stage cascade neglecting the effect of the substances other than the oil contained in the soybeans.

Calculate how many ideal stages are necessary for the desired extraction.

Solution:

Fig.22.3-E1 indicates the entire cascade system with the operating condition.

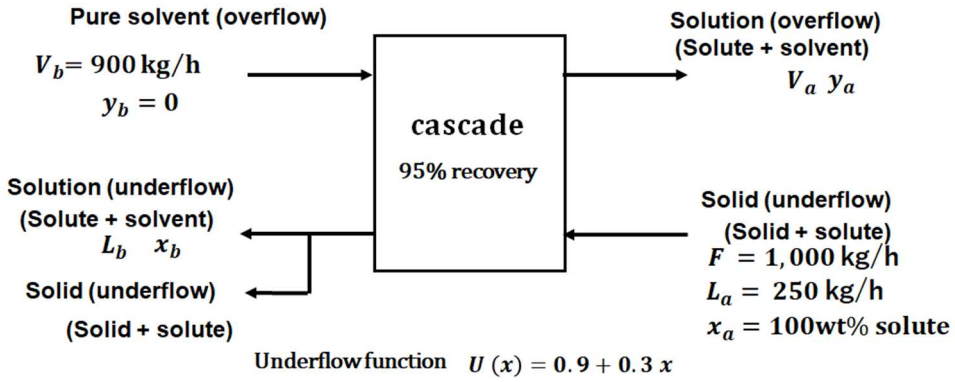

Fig.22.3-E1 Entire system of countercurrent leaching cascade with operating conditions (Subscript a: solid feeding entrance and exit of overflow solution, subscript b: solvent entrance and exit of underflow slurry)

The countercurrent cascade consists of a series of (thickener type) liquid-solid separator units, in each of which the solid from the previous unit is mixed with the liquid from the succeeding unit and the mixture is allowed to settle. The solid is then transferred with the entrained solution in the form of slurry to the next succeeding unit by slurry pumps. The separated liquid is transferred in the form of overflow to the previous unit. An appropriate mixer and settler should be chosen for the individual units.

Usually the cascade system has a decanter to separate the entrained solution from the ex-service solid after stage N.

Let us begin by material balance calculation:
The feed F= 1,000 kg/h for the underflow contains 250 kg/h of solute in solid with no solvent.
Solid: 750 kg/h, Solute: 250 kg/h, Solvent: 0 kg/h, therefore $L_a = 250$ kg/h and $x_a = 1.0$
That is, the composition of the solution in the feed is $x_a = 250/250 = 1.0$ on the solid-free basis.
Pure solvent to be supplied has the following quantities:
Solid: 0 kg/h, Solute: 0 kg/h, Solvent: 900 kg/h, therefore $V_b = 900$ kg/h and $y_b = 0$

The underflow function given by the problem can be applied as the underflow solution leaving each stage:

$L_n = (F - L_a)\,U(x) = (750)(0.9 + 0.3\,x_n)$ kg/h (22.3-E1)

The recovery condition indicates the flow of unrecovered solute leaving stage N with the solid as

$L_b\,x_b = (1 - 0.95)L_a\,x_a = (0.05)(250)(1.0) = 12.5$ kg/h (22.3-E2)

Because the underflow leaving Stage N should also follow the underflow function,

$L_b\,x_b = (750)(0.9 + 0.3\,x_b)\,x_b = 12.5$ kg/h

From this equation with respect to x_b, we obtain

$x_b = 0.0184$ (22.3-E3)

Then $L_b = (750)(0.9 + 0.3 \times 0.0184) = 679$ kg/h (22.3-E4)

This rate of the solution is discharged with the underflow from stage N.

The rate of the overflow issuing from stage 1 is given by the total mass balance:

$V_a = L_a + V_b - L_b = 250 + 900 - 679 = 471$ kg/h (22.3-E5)

Therefore the overflow concentration is calculated from the solute balance

$y_a = \frac{L_a x_a + V_b y_b - L_b x_b}{V_a} = \frac{(250)(1.0)+(900)(0)-(679)(0.0184)}{471} = 0.5043$ (22.3-E6)

[First stage]

Since the feed to the battery (at Stage 1) does not obey the underflow relationship, the feed point F is not on the operating line. Therefore the mass balance around the first stage should be considered separately from the other stages (2 to N):

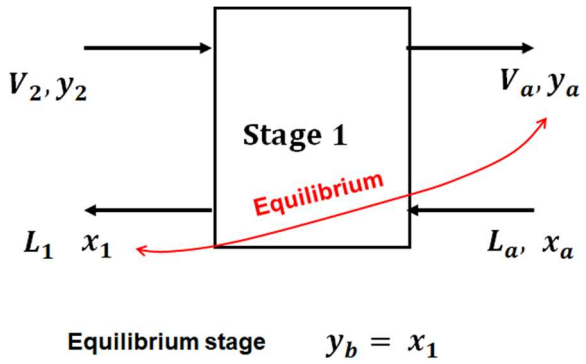

Fig.22.3-E2 Material balances around stage 1

The first stage is also an equilibrium stage expressed by

$x_1 = y_a$ (22.3-E7)

Therefore $x_1 = 0.5043$

$L_1 = (750)(0.9 + 0.3 \times 0.5043) = 788.5$ kg/h (22.3-E8)

The total balance around Stage 1 gives

$V_2 = V_a + L_1 - L_a = 471 + 788.5 - 250 = 1{,}010$ kg/h (22.3-E9)

The solute balance around Stage 1 gives the solute concentration of the overflow entering Stage 1 as

$y_2 = \frac{V_a\,y_a + L_1\,x_1 - L_a\,x_a}{V_2} = \frac{(471)(0.5043)+(788.5)(0.5043)-(250)(1.0)}{1{,}010} = 0.3814$ (22.3-E10)

[Stages 2 to N]

From here, we can begin the calculation for the stages 2 to N after checking if the operating line can be assumed to be straight.

Let us consider the control volume indicated by the dotted line in Fig.22.3-E3. Here the right-side end of the control volume is indicated by A.

At the end A: $L_1/V_2 = 788.5/1{,}010 = 0.781$
At the end b: $L_b/V_b = 679/900 = 0.754$
Although the slope changes by 3.46% from the ends A to b, we assume that the operating line is approximately straight.

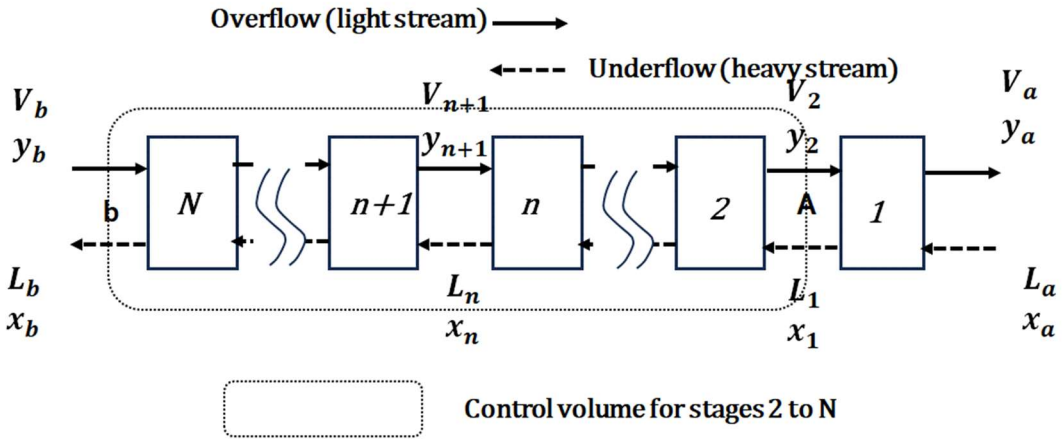

Fig.22.3-E3 Control volume for calculation of stages 2 to N

In this condition, we can estimate the required number of ideal stages by the Kremser equation[1] for stages 2 to N:

$$N' = \frac{\ln\left(\frac{x_1 - x_1^*}{x_b - x_b^*}\right)}{\ln\left(\frac{x_1 - x_b}{x_1^* - x_b^*}\right)} = \frac{\ln\left(\frac{x_1 - y_2}{x_b - y_b}\right)}{\ln\left(\frac{x_1 - x_b}{y_2 - y_b}\right)} = \frac{\ln\left(\frac{0.5043 - 0.3814}{0.0184 -}\right)}{\ln\left(\frac{0.5043 - 0.0184}{0.3814 - 0}\right)} = 7.84 \quad \text{(22.3-E11)}$$

Here since we are considering the region of Stages 2 to N,

$$x_1^* = y_2 = 0.3814 \qquad x_b^* = y_b = 0$$
$$x_1 = 0.5043 \qquad x_b = 0.0184 \quad \text{(22.3-E12)}$$

The calculated result $N = 7.84$ means the required number of stages except for stage 1. Therefore we should add 1 for the plus 1 meaning the first stage.

As a result, the required number of equilibrium stages is given by

$$N = N' + 1 = 7.84 + 1 = 8.84 \quad \text{(22.3-E13)}$$

The required number of equilibrium stages is determined to be approximately 9.

We can also determine the required number of ideal stages by the McCabe-Thiele graphical method[2].

You can remember the McCabe-Thiele method as a very convenient design concept of distillation columns. (see Chapter 11.2-2-4 of PART II)

22.3-3 McCabe-Thiele graphical method for design of a continuous leaching system

We can also gain a better understanding of the above leaching process by the McCabe-Thiele step-by-step calculation procedures shown below. [2]

[Stage 1]

The stage is an equilibrium stage with $y_a = x_1 = 0.5043$s

$$y_2 = \frac{V_a\, y_a + L_1\, x_1 - L_a\, x_a}{V_2} = \frac{(471)(0.5043) + (788.5)(0.5043) - (250)(1.0)}{1{,}010} = 0.3814$$

Therefore $L_1 = 788.5$ kg/h and $V_2 = V_a + L_1 - L_a = 471 + 788.5 - 250 = 1{,}010$ kg/h

[Stage 2]
Stage 2 is also an equilibrium stage: $y_2 = x_2 = 0.3814$
From the underflow function, we obtain the underflow rate from Stage 2:
$L_2 = (F - L_a)(0.9 + 0.3\,x_2) = (750)(0.9 + 0.3 \times 0.3814) = 760.8$ kg/h
Then the overflow is $V_3 = V_2 + L_2 - L_1 = 1{,}010 + 760.8 - 788.5 = 982.3$ kg/h
The operating line gives
$y_3 = \frac{L_2}{V_3}\,x_2 + \frac{V_a\,y_a - L_a\,x_a}{V_3} = \frac{760.8}{982.3} \times 0.3814 + \frac{(471)(0.5043)-(250)(1.0)}{982.3} = 0.2827$

[Stage 3]
Stage 3 is also an equilibrium stage: $y_3 = x_3 = 0.2827$
From the underflow function, we obtain the underflow rate from Stage 3:
$L_3 = (F - L_a)(0.9 + 0.3\,x_3) = (750)(0.9 + 0.3 \times 0.2827) = 738.6$ kg/h
Then $V_4 = V_3 + L_3 - L_2 = 982.3 + 738.6 - 760.8 = 960.1$ kg/h
The operating line gives
$y_4 = \frac{L_3}{V_4}\,x_3 + \frac{V_a\,y_a - L_a\,x_a}{V_4} = \frac{738.6}{960.1} \times 0.2827 + \frac{(471)(0.5043)-(250)(1.0)}{960.1} = 0.2045$

[Stage 4]
Stage 4 is also an equilibrium stage: $y_4 = x_4 = 0.2045$
From the underflow function, we obtain the underflow rate from Stage 4:
$L_4 = (F - L_a)(0.9 + 0.3\,x_4) = (750)(0.9 + 0.3 \times 0.2045) = 721.0$ kg/h
Then $V_5 = V_4 + L_4 - L_3 = 960.1 + 721.0 - 738.6 = 942.5$ kg/h
The operating line gives

$$y_5 = \frac{L_4}{V_5}\,x_4 + \frac{V_a\,y_a - L_a\,x_a}{V_5} = \frac{721.0}{942.5} \times 0.2045 + \frac{(471)(0.5043) - (250)(1.0)}{942.5} = 0.1432$$

[Stage 5]
Stage 5 is also an equilibrium stage: $y_5 = x_5 = 0.1432$
From the underflow function, we obtain the underflow rate from Stage 5:
$L_5 = (F - L_a)(0.9 + 0.3\,x_5) = (750)(0.9 + 0.3 \times 0.1432) = 707.2$ kg/h
Then $V_6 = V_5 + L_5 - L_4 = 942.5 + 707.2 - 721.0 = 928.7$ kg/h
The operating line gives

$$y_6 = \frac{L_5}{V_6}\,x_5 + \frac{V_a\,y_a - L_a\,x_a}{V_6} = \frac{707.2}{928.7} \times 0.1432 + \frac{(471)(0.5043) - (250)(1.0)}{928.7} = 0.0956$$

[Stage 6]
Stage 6 is also an equilibrium stage: $y_6 = x_6 = 0.0956$
From the underflow function, we obtain the underflow rate from Stage 6:
$L_6 = (F - L_a)(0.9 + 0.3\,x_6) = (750)(0.9 + 0.3 \times 0.0956) = 696.5$ kg/h
Then $V_7 = V_6 + L_6 - L_5 = 928.7 + 696.5 - 707.2 = 918.0$ kg/h
The operating line gives

$$y_7 = \frac{L_6}{V_7}\,x_6 + \frac{V_a\,y_a - L_a\,x_a}{V_7} = \frac{696.5}{918.0} \times 0.0956 + \frac{(471)(0.5043) - (250)(1.0)}{918.0} = 0.0589$$

[Stage 7]
Stage 7 is also an equilibrium stage: $y_7 = x_7 = 0.0589$
From the underflow function, we obtain the underflow rate from Stage 7:
$L_7 = (F - L_a)(0.9 + 0.3\,x_7) = (750)(0.9 + 0.3 \times 0.0589) = 688.3$ kg/h
Then $V_8 = V_7 + L_7 - L_6 = 918.0 + 688.3 - 696.5 = 909.8$ kg/h
The operating line gives

$$y_8 = \frac{L_7}{V_8}\,x_7 + \frac{V_a\,y_a - L_a\,x_a}{V_8} = \frac{688.3}{909.8} \times 0.0589 + \frac{(471)(0.5043) - (250)(1.0)}{909.8} = 0.0308$$

[Stage 8]
Stage 8 is also an equilibrium stage: $y_8 = x_8 = 0.0308$

From the underflow function, we obtain the underflow rate from Stage 8:
$L_8 = (F - L_a)(0.9 + 0.3\,x_8) = (750)(0.9 + 0.3 \times 0.0308) = 681.9$ kg/h
Then $V_9 = V_8 + L_8 - L_7 = 909.8 + 681.9 - 688.3 = 903.4$ kg/h
The operating line gives

$$y_9 = \frac{L_8}{V_9}\,x_8 + \frac{V_a\,y_a - L_a\,x_a}{V_9} = \frac{681.9}{903.4} \times 0.0308 + \frac{(471)(0.5043) - (250)(1.0)}{903.4} = 0.0094$$

The goal concentration of the underflow from the final stage N is given by $x_b = 0.0184$ as the condition required for the recovery rate 0.95.

The above result $y_9 = 0.0094$ indicates that the goal value is stepped over when the underflow passes through Stage 9. This suggests the final stage.
The McCabe-Thiele stage-by-stage calculation is expressed by Fig.22.3-E4.

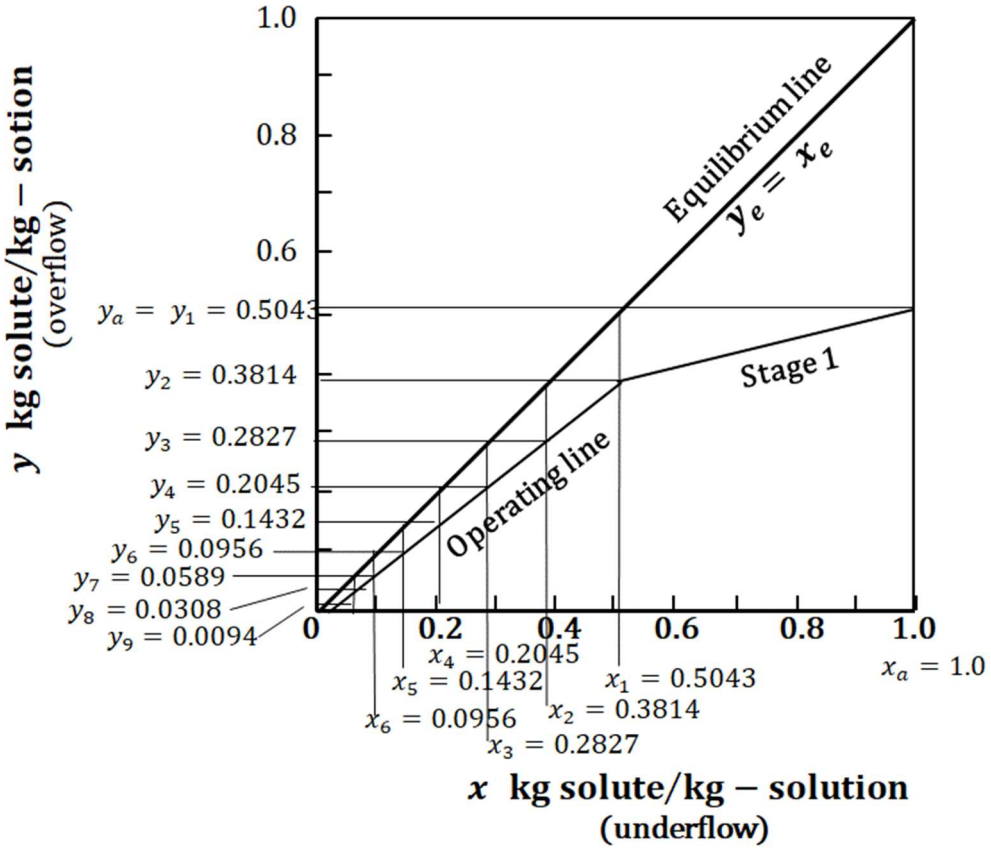

Fig.22.3-E4 McCabe-Thiele graphical calculation for leaching

It has been found that the same result is also attained by the McCabe-Thiele method.[2] This suggests that the required number of equilibrium stages is approximately 9.

Although the calculation method for variable underflow is a little bit difficult and different from that for constant underflow, we will close the section of leaching with this simplest example.

1) Kremser, A., Natl. Petr. News, vol.22(21), 42 (1930)
2) McCabe, W. L. and Thiele, E. W., *Ind. Eng. Chem*., vol.17, 605 (1925)

22.3-4 Continuous leaching process equipment

Finally an example of real continuous leaching process equipment is shown in Fig.22.3-3. This equipment is a kind of counter-current multi-staged column which is equipped with rotating conical disks perforated. A pair of upright cone and upside-down cone constitutes one stage. The feed consisting of insoluble solid and its contained solute is supplied from the top of the column while the solvent is fed into the bottom. The underflow containing the solid, solute, and solvent flows downward stage-to-stage along the slopes of conical disks inward and outward. The overflow containing the dissolved solute with the solvent flows upward passing not only in the space between conical disks but also through the perforation holes. The final effluent of the overflow is obtained as the product from the nozzle set at the top of the column. The final underflow discharging in the form of slurry from the bottom of the column is moved to a decantation or filtration system for recovering the dissolved-solute solution entrained with the solid.

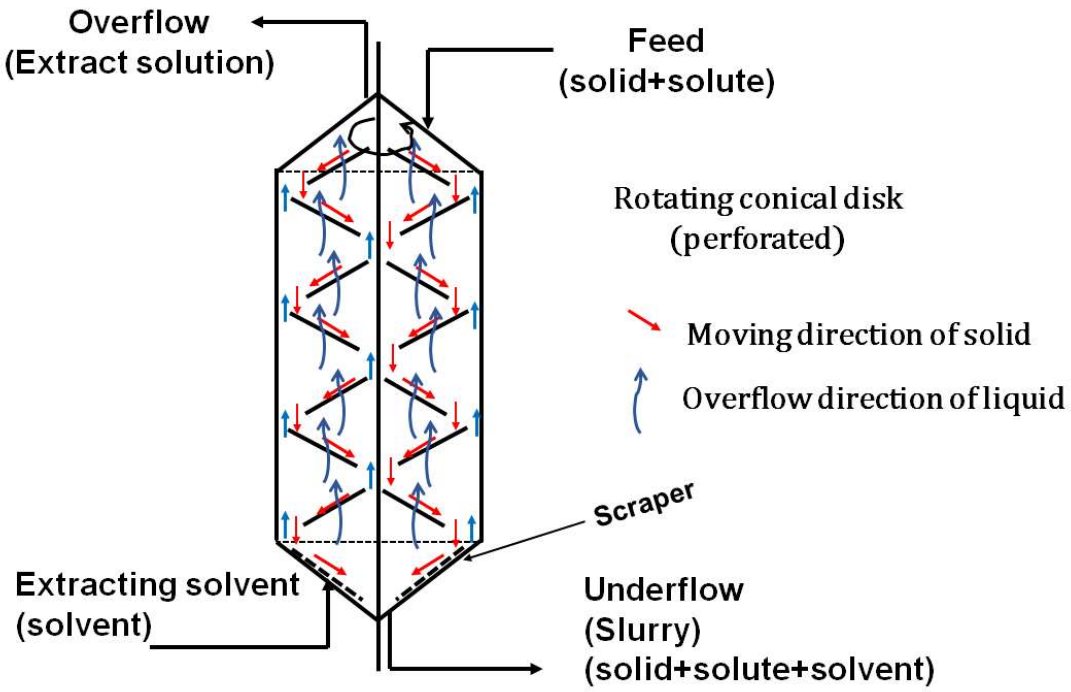

Fig.22.3-3 An example of continuous leaching process equipment

[PROBLEM 22.3-1]

A sunflower crude oil is produced by the leaching process of a solid feed F =1,000 kg/h (e.g. flaked seeds after pressing) containing 80wt% insoluble solid and approximately 20wt% oil to be extracted. A continuous countercurrent leaching battery is used. Pure solvent (e.g. n-hexane) 800 kg/h is supplied to extract 95% of the solute (i.e., sunflower seed oil). The flaked solid seeds discharging as the slurry from the final stage N entrains a limited rate of liquid hexane solution. By a preliminary test, we get such an empirical underflow function that each kg of solid carries $(1.6 + 0.4\,x)$ kg of the solution of solute mass fraction x. We assume that the leaching process can be treated as an ideal stage-to-stage cascade neglecting the effect of the substances other than the oil contained in the sunflower seeds.

Calculate how many ideal stages are necessary for the desired extraction.
(The treatment of producing the sunflower seed oil comprises (1) grinding and flaking of the seeds into meal, (2) pressing and squeezing, (3) leaching, (4) solvent recovering, and (5) oil refining. Roughly speaking, the sunflower seed oil contains about 40% oleic acid, mono-unsaturated fat and 60% linoleic acid, polyunsaturated fat. The value 20 wt% given above means the average composition of the total fatty components.)

Nomenclature

d_p	droplet diameter, [m]
E	extract rate, [kg/s]
F	feed rate, [kg/s]
f_{BA}	fugacity of B in A-phase, [Pa]
H	mass of feed mixture, [kg]
K	distribution function defined by Eq.(22.2-1), [-]
k_c, k_d	mass transfer coefficients of continuous phase and dispersed phase [kmol/m^{2}s]
L	underflow rate in continuous leaching, [kg/s]
m	distribution function defined by units of mole fraction, [-]
N	total number of equilibrium stages, [-]
N'	number of ideal stages calculated by Kremser equation, [-]
R	raffinate rate, [kg/s]
S	mass of solvent, [kg]
V	overflow rate in continuous leaching, [kg/s]
X	mass of solute in raffinate or feed, [kg]
Y	mass of solute in extract or solvent, [kg]
x, y	concentrations of solute in raffinate and extract of continuous liquid extraction, [kg/kg]
x, y	concentrations of solute in underflow and overflow of continuous leaching, [kg/kg]
v_p	slip velocity or terminal velocity, [m/s]
θ_c, θ_d	time constant of continuous-phase and dispersed-phase characteristic for periodical surface renewal, [s]

Subscripts

A	diluent
B	solute
i	interface
S	solvent

CHAPTER 23

SUPERCRITICAL FLUID TECHNOLOGY

23.1 Characteristics of Supercritical Fluid

If a gas or a liquid is heated and compressed above its critical temperature and pressure, it will reach a dynamic equilibrium and become a supercritical fluid. For example, when the temperature of water goes beyond 374 ℃ and the pressure exceeds 22 MPa, it goes into a supercritical state. There is no difference between the liquid and gas of water in the supercritical state, where they are completely blended at constant temperature and pressure. Therefore there is no phase boundary. In the region of supercritical fluid, no matter how much pressure or temperature is raised, the material cannot transform from gas to liquid or from liquid to gas phase. It also has no surface tension.

Thermophysical properties vary sharply with temperature in a narrow temperature range called the "pseudo-critical range".

Carbon dioxide also behaves as a supercritical fluid above its critical temperature (304.1 K) and critical pressure (7.38 MPa). It is very useful fluid as a solvent because its good volatility is very convenient for separation of solute from the extract (mixture of solute and CO_2 obtained by extraction).

The properties of supercritical fluids are in between pure liquid and gas as follows.

(1) Liquid like densities (100 ~ 1,000 times larger than gases)
(2) Diffusivities higher than liquids (of the order of $10^{-7} \sim 10^{-8}$ m^2/s)
(3) Good solvating power
(4) Low viscosity (10~100 times less than liquid)
(5) Reduction in surface tension
(6) Gas like compressibility

For example, a supercritical fluid is a good solvent for solid extraction (leaching) because of great possibilities of solubilization of compounds owing to its high density and good abilities of penetration into solids owing to its low viscosity.

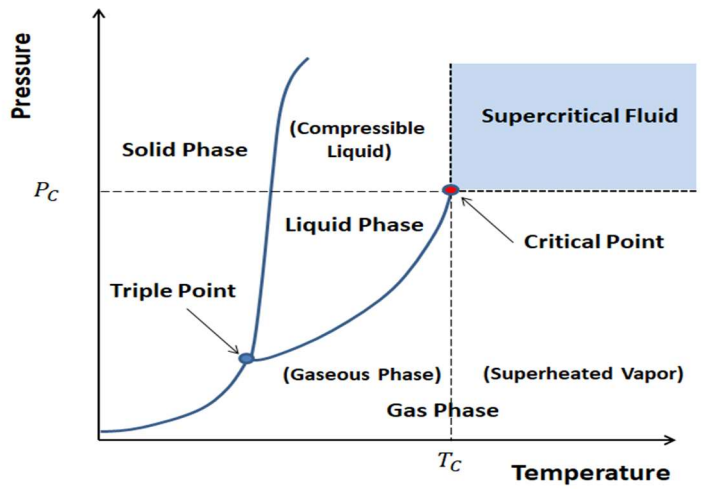

Fig.23.1-1 Schematic explanation of an idealized phase diagram

As will be mentioned later, the supercritical fluids exhibit continuous dramatic variations of physical properties when going beyond the critical point. There are many possibilities of trying various fruitful utilizations for various chemical processes.

23.1-1 Properties of supercritical fluids

Supercritical fluids have low viscosity like gas and high density like liquid. The thermos-physical properties such as density, specific heat, thermal conductivity, and diffusivity vary drastically when exceeding the critical point.

As distinct from the subcritical fluids, at supercritical pressure, the fluid phase changes from liquid to gas continuously. As shown in Fig .23.1-2, when the temperature rises across the pseudo-critical point T_{pc}, the density ρ, the thermal conductivity κ, and viscosity μ decrease drastically, and the specific heat capacity Cp shows a sharp peak in a very narrow temperature range about the pseudo-critical point.

Table 23.1 indicates the critical temperature and pressure with density of several fluids.

Table 23.1 Critical Parameter of Common Fluids

Substance	T_c $(°K)$	P_c (MPa)	ρ_c $(\mathrm{kg/m^3})$
CO_2	304.1	7.38	470
N_2O	309.6	7.34	450
NH_3	405.5	11.40	240
H_2O	647.3	22.12	340
CH_4	190.4	4.6	162

Supercritical CO_2

Supercritical carbon dioxide is very useful in various industries as a green, non-flammable, non-toxic, recyclable, and powerful solvating medium.

Fig.23.1-3 indicates continuous variation of fluid density around pseudo-critical point.

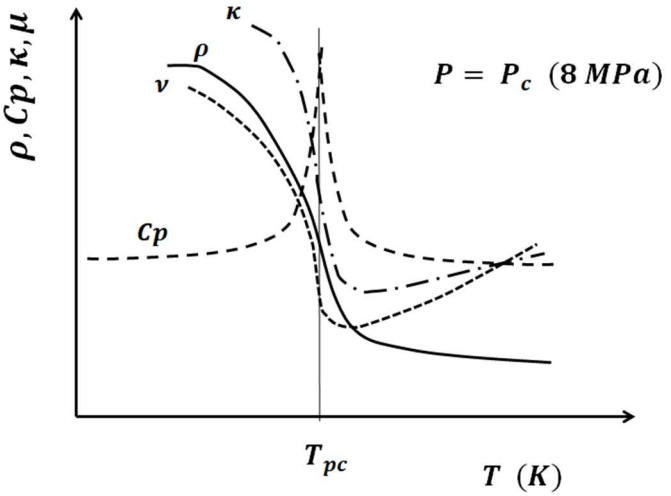

Fig.23.1-2 Schematic picture of drastic variations of fluid density, specific heat, thermal conductivity, and kinetic viscosity in the region near the critical point (e.g. CO_2)

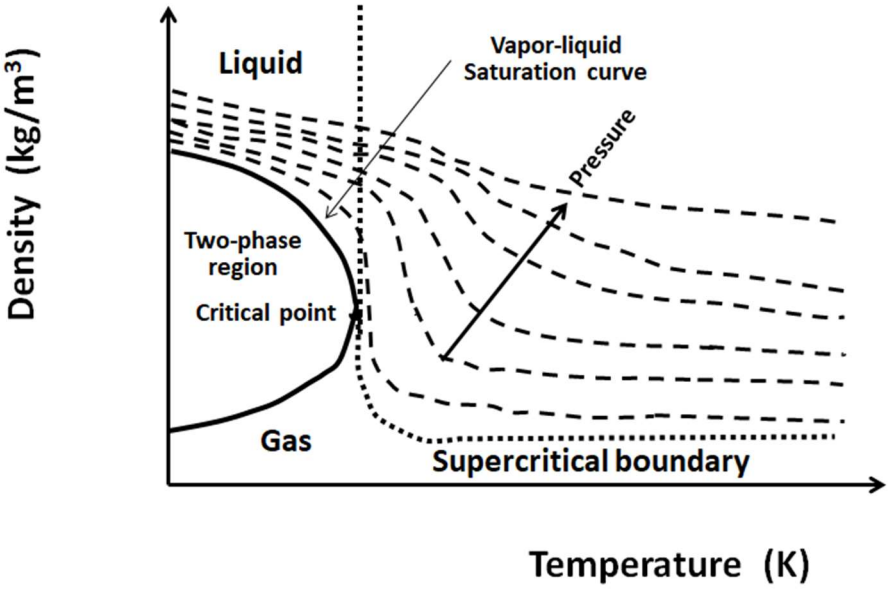

Fig.23.1-3 Variation of fluid density with temperature in regions of subcritical and supercritical states

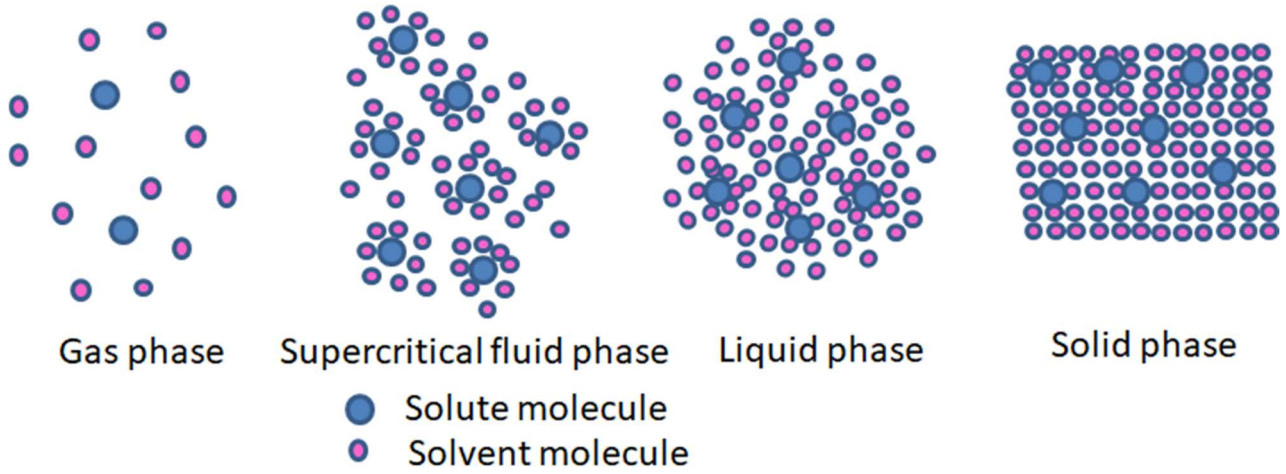

Fig.23.1-4 Schematic illustration of mixtures of solute molecules with solvent molecules

Fig.23.1-4 expresses the microstructure of the mixture of solute molecules and solvent molecules imagined in various phases.

We can expect that it is very interesting to utilize the transitional region where the critical point exists for chemical processes.

Supercritical H_2O

As can be seen from Fig.23.1-5, the thermos-physical properties of sH_2O undergo significant change in the temperature range of the pseudo-critical region (for 25 MPa between 372 and 392℃).

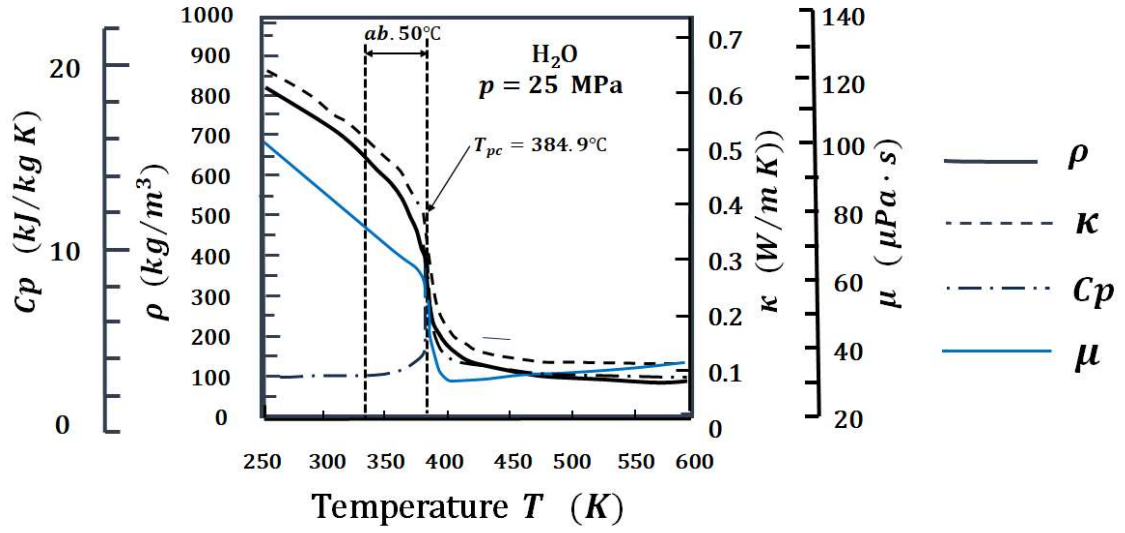

Fig.23.1-5 Thermo-physical properties of water in the vicinity of critical point

The supercritical water sH_2O is used for nuclear power plants. The thermal efficiency of supercritical water-cooled reactor with sH_2O as a coolant is better than that of light-water reactors.

There is also a possibility of the transformational technology using high-pressure sCO_2 instead of steam in a closed power cycle because of the unique properties of sCO_2 superior to steam in closed cycle to absorb thermal energy.

23.1-2 Supercritical fluid flow and heat transfer in a horizontal pipe

A supercritical fluid such as CO_2, water, and kerosene serving as the heat transfer medium plays an important role for heat transfer enhancement or deterioration in a horizontal circular pipe.

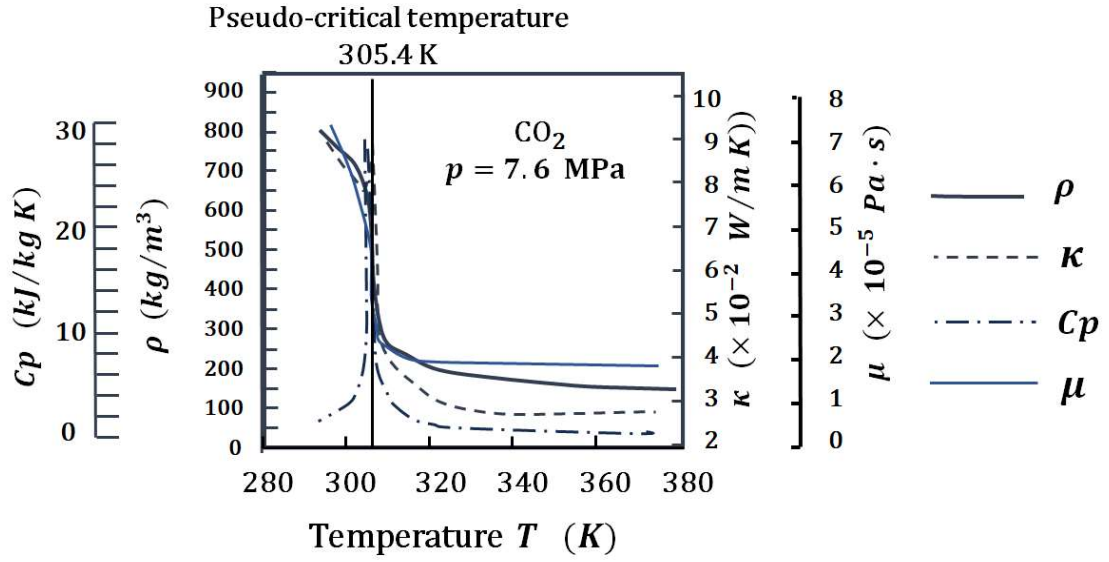

Fig.23.1-6 Thermophysical properties in the neighborhood of critical point for carbon oxide

<u>Development of a horizontal tube flow with heat transfer section</u>

According to Tian et al. (2021), as distinct from the constant property flow, a three-stage streamwise development of flow and heat transfer occurs in a horizontal pipe:

Stage I: Rapid reduction of heat transfer coefficient influenced by the development of thermal boundary layer.

Stage II: Flow stratification and secondary flow owing to the strong buoyancy effect caused by a peculiar entrance effect. The stratified flow is formed by the two different effects of the high temperature and low density fluid in the upper part of the pipe and the low temperature and high density fluid in the lower part. Owing to the strong variation of thermos-physical properties, the wall temperature of the supercritical fluid also varies circumferentially in a horizontal heated-wall tube.

Stage III: Pseudo-developed state free from the influence of the entrance condition.

At any rate, the thermos-physical properties vary remarkably not only in the stream direction but also in the radial direction. Strictly speaking, the flow characteristics of supercritical fluid will never reach a fully-developed condition. For supercritical fluid, it is technically too difficult to realize a fully-developed region under an isothermal condition. Many attempts have been made to correlate convective heat transfer data in terms of conventional dimensionless groups with some modifications to allow for the effects of thermos-physical property variations. It is still very difficult to analyze the effects of interaction of highly non-linear thermos-physical property variations (viscosity, thermal conductivity, heat capacity and density) on the convective heat transfer. That is due to the fact that the flow and heat transfer processes are linked. Very different results are also obtained depending upon whether the pipe is horizontal or vertical, and whether the flow is upward or downward in the vertical pipe.

Tian, R., He, S-S, Wei, M-S., and Shi, L., The staged development of a horizontal pipe flow at supercritical pressure, *Int. J. Heat Mass Transfer*, vol.168, Article 120841 (2021)

[EXAMPLE 23.1-1]

Let us consider a supercritical fluid flow in a horizontal heated pipe shown in Fig.23.1-7.

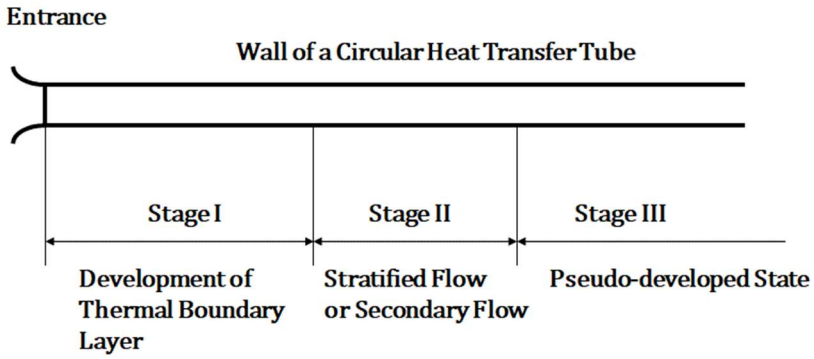

Fig.23.1-7 Three-stage development of flow and heat transfer in a horizontal heat transfer tube

According to a rough estimation due to Fig.23.1-6, density $\rho = 330\ \mathrm{kg/m^3}$, viscosity $\mu = 2.3 \times 10^{-5}\ \mathrm{Pa \cdot s}$, heat capacity $Cp = 8\ \mathrm{kJ/kg \cdot K}$, thermal conductivity $\kappa = 4.6 \times 10^{-2}\ \mathrm{W/m \cdot K}$ at 307 K.

The Prandtl number is calculated as

$$Pr = Cp\ \mu/\kappa = (8 \times 10^3)(2.3 \times 10^{-5})/(4.6 \times 10^{-2}) = 4 \qquad \text{(23.1-E1)}$$

We can understand that the supercritical CO_2 at 307 K a little bit above the pseudo-critical temperature has the Prandtl number $\mathrm{Pr} = 4$, which lies between liquid and gas.

For a capillary tube of 3 mm ID, when the flow velocity of supercritical CO_2 goes beyond 0.05 m/s, the flow will become unstable leading to the transition to turbulent flow. The critical Reynolds number is

$$Re_{cr} = \frac{(0.003)(0.05)(330)}{2.3 \times 10^{-5}} \cong 2{,}100 \qquad (23.1\text{-E2})$$

This is due to the fact that a supercritical fluid such as sCO_2 has very low viscosity for large density.

It is known in supercritical chromatography that a neat supercritical CO_2 owing to its significantly low viscosity can experience a transition from laminar to turbulent flow at a flow rate 1.3 ml/min in a microchannel of 127 μm ID. The high density with the low viscosity allows for highly compact, microchannel-based heat exchanger technology.

Vertical pipe flow systems for supercritical fluids are often encountered in nuclear or various power plants. For example, SCWR (Supercritical Water-cooled Reactor) is expected for the next generation of nuclear reactor. Supercritical water is used there as a coolant. Their flow condition in a vertical pipe is different from that of horizontal flow system in that the buoyancy force is in parallel to the main flow. As a result, peculiar phenomena of flow laminarization and heat enhancement or deterioration may appear.

We will study here the supercritical fluid flow focusing on a horizontal pipe flow system.

As distinct from the subcritical fluid flow, the flow and heat transfer does never reach an axially-asymptotic condition because of the significant variation of thermos-physical properties.
This phenomenon still remains to be examined in various conditions.
It is said that the flow and heat transfer exhibit a three-stage development, which has two entrance effect stages and in the downstream region an asymptotic development stage.
Stage 1: Rapid reduction of heat transfer coefficient is caused by the developing thermal boundary layer. When the inlet temperature is close to the pseudo-critical value, flow laminarization will take place.
Stage 2: Strong buoyance effect will play a role leading to stratification with secondary flow. This phenomenon has not been observed for the case of subcritical fluid flows.
Stage 3: The flow and heat transfer seem to be free from the influence of the entrance condition.

Due to the large density change with temperature, the fluid flow is strongly influenced by the buoyancy force perpendicular to the main flow. As a result, the mixed convection controls the dominant heat transfer mode. This could be explained in the downstream region of a horizontal circular pipe with constant wall heat-flux as follows. The buoyancy force inside the pipe drives the high-temperature and low-density fluid upward along the circumferential wall while the high-density cooler fluid downward. As can be seen from Fig.23.1-7, a secondary flow is formed. This fluid motion causes stratification, which makes the wall temperature different between the top and the bottom.
The low-velocity flow near the circumferential pipe wall is heated firstly and transported toward the top region by the secondary flow while the high-velocity bulk fluid is concentrated at the bottom owing to the high-density of the fluid. This implies non-axisymmetric flow and heat transfer field.

In this non-uniformity in the circumferential distribution of the wall temperature, the heat transfer is enhanced at the bottom but deteriorated at the top by buoyancy.

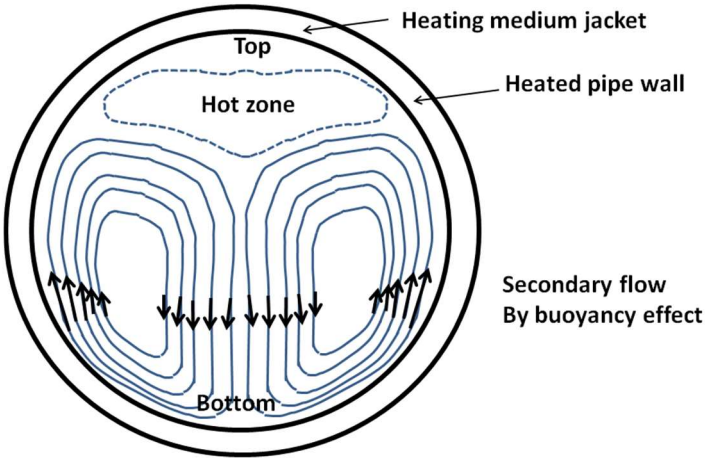

Fig.23-1-7 Stratification due to buoyancy effect in downstream region in a horizontal heated pipe (Schematic picture of pipe cross-sectional view)

For constant property flow, the entrance region (i.e. developing region) is controlled by the axial development of hydraulic and thermal boundary layers. However the flow and heat transfer at supercritical pressure does never reach a fully-developed condition.
Even in the far downstream region, the behaviors of flow and heat transfer still depend on the history of flow conditions from the entrance. Therefore it is very difficult to obtain a generalized correlation of heat transfer.

23.1-3 Nusselt correlations of supercritical fluid tube flow

The heat transfer performance of supercritical fluid is different from conventional fluids, especially in the determination of the convective heat transfer correlations. Many attempts have been made to correlate convective heat transfer data in terms of conventional dimensionless groups. However various correlations are available for different geometries and dimensions but there is a lack of a unique universal correlation. Only a few correlations are introduced below for reference.
Very early, Bringer and Smith presented the following correlation for a vertical tube flow[1]:

$$Nu_b = 0.0375\, {Re_b}^{0.77}\, {Pr_w}^{0.55} \qquad (23.1\text{-}1)$$

Yoon et al.[2] proposed the Nusselt correlation for horizontal small-channel flow in the case when the bulk temperature is higher than the pseudocritical temperature:

$$Nu_b = 0.14\, {Re_b}^{0.69}\, {Pr_b}^{0.66} \qquad (23.1\text{-}2)$$

Here the subscript b means bulk temperature.

According to Jackson (2011)[3] and Jackson et al.(1975)[4], some modifications for the effect of physical property variation are made to get the Dittus-Boelter correlation form for constant properties forced convection:

$$Nu_b = 0.0183\, {Re_b}^{0.82} {Pr_b}^{0.5} (\rho_w/\rho_b)^{0.3} (\overline{Cp}/Cp_b)^{\eta} \qquad (23.1\text{-}3)$$

$$\eta = 0.4 \quad \text{for } T_b < T_w < T_{pc}$$

$$\eta = 1.2 \quad \text{for } T_{pc} < T_b < T_w$$

Here b, w, and pc mean bulk, wall, and pseudocritical, respectively and $\overline{Cp}$ is mean specific heat averaged between T_w and T_b.

1. Bringer, R.P. and Smith, J.H., *AIChE J.*, vol.3, pp.49-55 (1957)
2. Yoon, S.H., et al., *Int. J. Refrig.*, vol.26, pp.857-864 (2003)
3. Jackson, J.D., DOI:10.1615/Ato Z.s. super_critical_heat_transfer (2011)
4. Jackson, J.D. et al., Heat transfer to supercritical pressure fluids. H.T.F.S. Design Report No.34 (1975)

23.1-4 Heat transfer equipment for supercritical fluids[5)]

Except in the region of heat transfer deterioration, the heat transfer coefficient of supercritical fluid tube flow can usually be made very high owing to its turbulent flow at a high Reynolds number since its viscosity is small for large density in the vicinity of critical point. Therefore in relation with the relief requirement, the heat exchanger operated under high pressure for supercritical fluids is usually compact as the heat transfer rate is relatively high. . We can refer to the Kwon et al. review paper of sCO2 PCHE (Printed Circuit Heat Exchanger). The PCHE is manufactured by the following procedures: (1) Etching metal plates to obtain flow channels, (2) stacking the etched plates to form exchanger blocks, (3) diffusion welding the blocks under high pressure and temperature, and (4) bonding making the stacked blocks as strong as the metal itself.

5. Kwon, J.G., Son, S., Heo, J.Y., and Lee, J-LK., Compact heat exchanger for supercritical CO2 power cycle application, *Energy Convers. Manage.*, vol.209, Article 112666 (2020)

As shown in Fig.23.1-8, a multi-stacked sheets of tube-bundle structure with staggered tube array can be considered as an example of compact sCO_2 heat exchangers. The sCO_2 is placed on the tube side because of its high pressure.

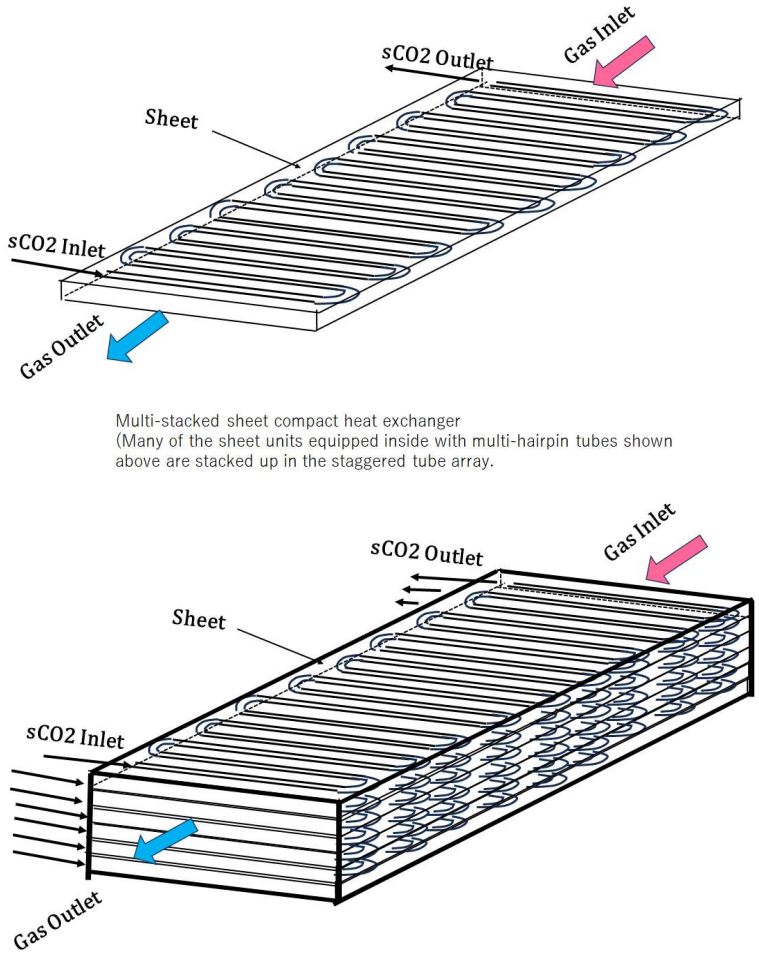

Fig.23.1-8 Configuration of a heat exchanger block unit to be stacked to form a compact sCO_2 heat exchanger.

Fitg.23.1-9 shows an example of semi-circular channel layout of PCHE.
The cross-section of the channels involves semicircular, rectangular, triangular and airfoil-shaped.

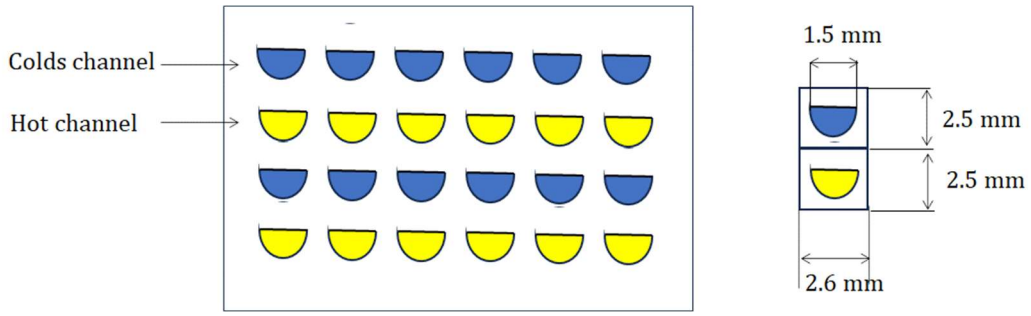

Fig.23.1-9 Configuration of etched channel layout of PCHE (Printed Circuit Heat Exchanger). Dimensions are given as an example.

Liao and Zhao (2002)[6] measured the convective heat transfer in horizontal mini- /micro-channels and reported a Nusselt correlation as a function of the Reynolds number and the Prandtl number:

$$Nu_{av} = 0.12\, {Re_w}^{0.8}\, {Pr_w}^{0.3} B \qquad (23.1\text{-}4)$$

$$B = {(Gr/Re)_b}^{0.205} (\rho_b/\rho_w)^{0.437}\, (Cp_b/Cp_w)^{0.41} \qquad (23.1\text{-}5)$$

The subscripts b and w indicate the bulk fluid and tube wall temperatures, respectively.
The above correlation equation is applicable in the pseudo-developed state region reported by Tian et al. because the entrance condition does not appear in it.
The part of Eq.(23.1-4) in front of B resembles the following constant-property flow correlation by Sieder and Tate (1936) . (see Eq.9.2-4 in Chapter 9.2).

$$\frac{h_i D}{\kappa} = 0.023 \left(\frac{D\, G}{\mu}\right)^{0.8} \left(\frac{Cp\, \mu}{\kappa}\right)^{1/3} \qquad (23.1\text{-}5)$$

The term B can be considered as the effect of buoyancy plus the correction term of thermophysical property variations characterized by the inner wall temperature with respect to bulk fluid temperature.

6. Liao, S-M and Zhao, T-S, Measurement of Heat Transfer Coefficients from Supercritical Caron Dioxide Flowing in Horizontal Mini/Micro Channels, *J. Heat Transfer*, 124 (2002)

23.2 Applicability of Supercritical Fluids

Various applications of supercritical fluid are exhibited in many industries as well as thermal and power engineering plants. Supercritical carbon dioxide is a green, economic, non-flammable, non-toxic, and recyclable medium, especially as an environmentally benign solvent.

23.2-1 Supercritical fluid extraction

It was found in 1879[7] that supercritical fluids could dissolve selected compounds and that their dissolving power was pressure-dependent, the higher the pressure, the higher the dissolving power.

7. Hannay, J. B. and Hogarth, J., On the Solubility of Solids in Gases, *Proc. Roy. Soc., London,* Vol.29, 324-326 (1879)

It is an advantageous property that a supercritical fluid shares some common features with both gases and liquids. The special combination of gas-like viscosity and diffusivity, and liquid-like density and solvating properties of a supercritical fluid indicates an excellent solvent for various applications, especially in food and pharmaceutical industries. These properties can also be used as an environmentally friendly solvent for dry cleaning.

The unique physical properties enable supercritical fluid extraction to be utilized for the extraction processes that cannot be executed by liquids due to their high density and low diffusivity and by gases due to their inadequate density.

The higher diffusivity and lower viscosity of supercritical fluids, as compared to traditional extraction liquids, help the components to be extracted faster than other techniques. In addition, when the critical pressure is removed, a supercritical fluid easily transforms to gas phase.

Therefore the most commonly used solvent is supercritical CO_2.

In particular, supercritical carbon dioxide is a very useful solvent for industrial extraction processes because of chemically stable, low-cost, non-flammable, non-poisonous working fluid. In addition, it is easy to separate the solute from the extract solution by evaporation of the supercritical CO_2 solvent.

The solid extraction "leaching" is used to dissolve soluble matter from its mixture with an insoluble solid. The leaching technology under the usual fluid condition has already been studied in Chapter 22.3. Supercritical fluid extraction is very advantageous for such leaching processes. In particular, supercritical CO_2 is becoming an important commercial and industrial solvent due to its role in chemical extraction. Fig.23.2-1 is an example of the supercritical fluid extraction systems.

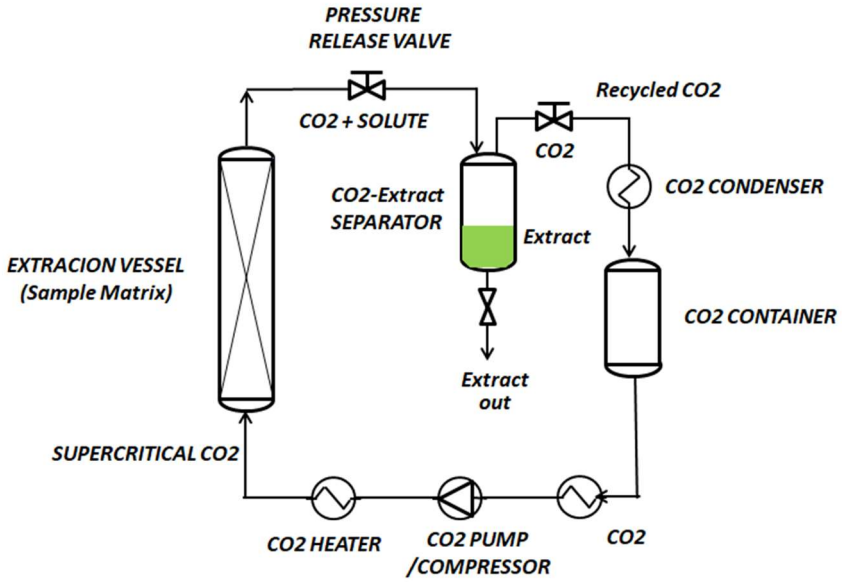

Fig.23.2-1 Supercritical fluid extraction system having a stationary solid-bed extraction vessel

Usually the extraction condition by supercritical CO_2 is above the critical temperature 31℃ and critical pressure 7.4 MPa. The supercritical CO_2 is pumped to a heater, where it is heated to supercritical conditions.

Solids such as coffee beans, soybeans, and corn-meal, etc. loaded into the pressurized extraction vessel are stationary on the perforated false bottom as a packed column. This packed bed is usually called "solid matrix." The supercritical fluid solvent passes through the solid matrix in the upward direction, where the supercritical CO_2 spreads into the solid matrix and dissolves the material to be extracted. The dissolved material swept out of the extractor undergoes the vaporization of the solvent sCO2 through the pressure release valve, and flows into a separator at low pressure. The extracted material settles out there. Then the CO_2 can be cooled, recompressed , and recycled.

The solvent is cooled before pumping to maintain liquid conditions, and then heated after pressurization. For larger industrial extractions, the energy required during each stage of the process can be calculated using the thermodynamic properties of the supercritical fluid.

Supercritical fluid extraction by sCO_2 is popularly used in various separation processes, especially for relatively non-volatile solids and liquids because the sCO_2 is non-flammable and non-hazardous: Various application to agricultural and food products such as coffee decaffeination and hops extraction.

23.2-2 Principle of supercritical fluid extraction[1)]

One example of supercritical fluid extraction systems consists of (1) Fluid reservoir (gas cylinder in case of CO_2), (2) Pump (usually reciprocating pump), (3) Extraction vessel (stationary phase for solids, high pressure 300~600 atm) or packed columns (for liquids), (4) Restrictor for maintaining pressure change inside the extraction vessel (variable nozzle, back pressure regulator), and (5) Collector (trapping system).

The supercritical fluids can dissolve some solid-like involatile substances from non-volatile solid. In order to understand the principle of supercritical fluid extraction, we very often consider the solubility of naphthalene ($C_{10}H_8$, Melting point 80.2℃) in supercritical CO_2 fluid shown in Fig.23.2-2.

Dependency of pressure on solubility of supercritical fluids[7)]

As can be seen in Fig.23.2-2, the solubility of naphthalene in sCO2 changes considerably with pressure. This suggests why the rapid expansion is convenient for precipitation of the solute dissolved in sCO_2.

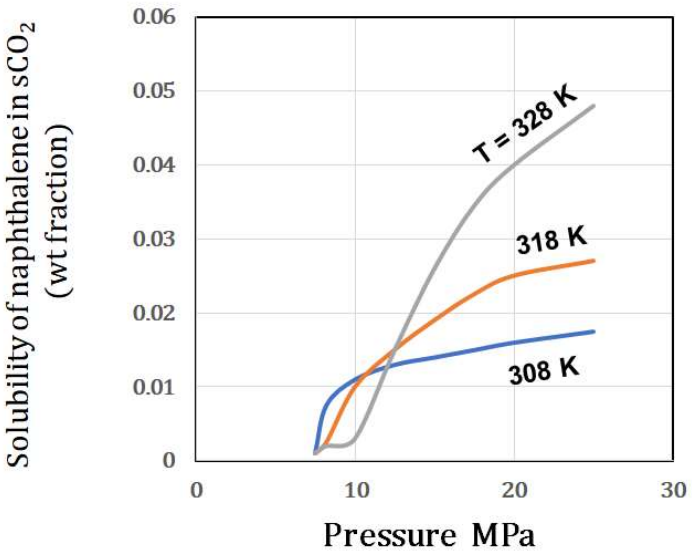

Fig.23.2-2 Solubility of naphthalene in supercritical CO_2

Let us consider a solid extraction system recovering naphthalene from a solid mixture shown in Fig.23.2.-3. The solid extraction, i.e. leaching technology and the rapid expansion method will be studied in Chapters 23.2 and 23.3. The supercritical CO_2 at selected pressure –temperature conditions of 300 bar and 55 ℃ is passed through the extraction column in which naphthalene admixed in a solid state with some other non-volatile solid. As the sCO_2 percolates through the column contents, naphthalene is dissolved, up to its solubility limit 15 wt%, and it is extracted from the solid mixture. The fluid solution of CO_2 and naphthalene issuing from the extractor is passed through the depressurizing valve and dropped in pressure to 90 bar and in temperature to 35 ℃. At 90 bar and 35 ℃, the solubility of naphthalene is only about 2 wt%. More than 90% drops out like a snow in the separator (Precipitation chamber), that is, naphthalene is separated as solid from the CO_2 gas stream. Then the gas stream is recompressed for further extraction. The solid naphthalene product is precipitated due to the rapid expansion in the precipitation chamber.

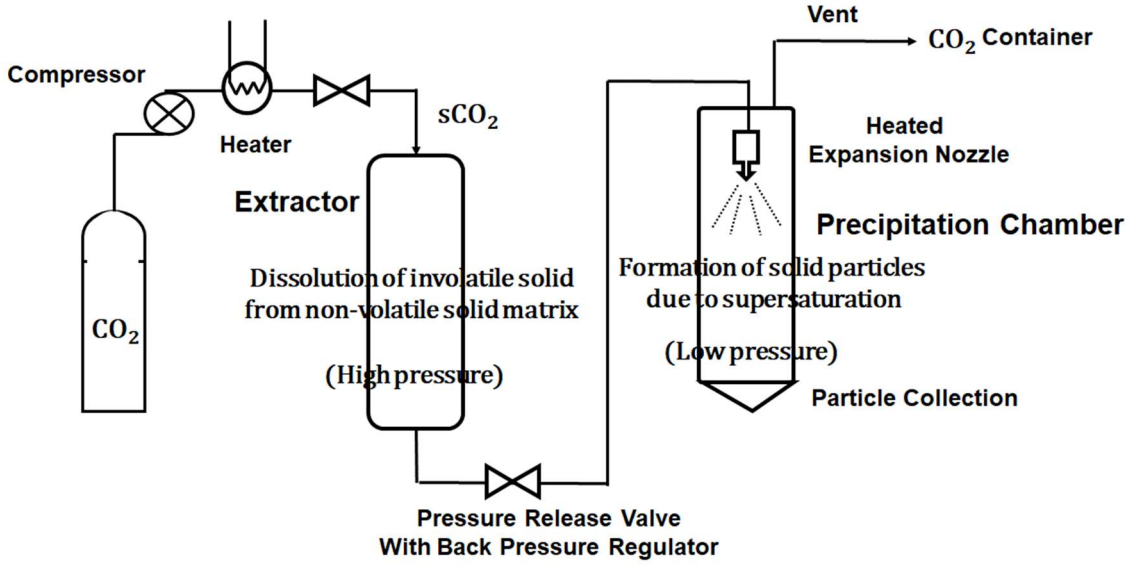

Fig.23.2-3 Extraction system of naphthalene by rapid expansion method

At high pressures, supercritical CO_2 exhibits liquid-like behavior since the solubility increases with temperature while at low pressures, the solubility rapidly decreases with temperature owing to a steep decrease in density of the gas. It seems that the intermediate pressure exists around 120 bar.
The principle of supercritical fluid extraction can be considered that the solubility of a compound (solute) above the critical temperature is sufficient to consider the supercritical fluid as a extracting medium (solvent).

One great advantage of supercritical fluid extractions is complete separation of solvent from extract and raffinate. It should be kept in mind that adequate contact time is necessary for penetration of solvent into solid particles of packed matrix.

There are two essential steps to supercritical fluid extraction: (1) transport of solid particles to be extracted toward the outside surface of particles, and dissolution of the material in the supercritical solvent and (2) diffusion of the supercritical solvent to the inside of the particle and counter-diffusion of the dissolved material from inside the particles.
This reversible release is very difficult, so not dealt with in detail here in this course.

The solid extraction by supercritical fluids is a diffusion-based process, in which the solvent fluid is required to diffuse deeply into the solid matrix and the extracted material to diffuse out of the matrix into the bulk solvent. Fortunately diffusivities are much faster in supercritical fluids than in liquids and due to the lack of surface tension and the negligibly small of viscosities, the solvent can penetrate more into the matrix inaccessible to liquids

23.2-3 Modeling diffusion of dissolved solute inside a solid particle[1)]

Fig.23. 2-4 shows the stages of the concentration profile during extraction inside a solid particle.

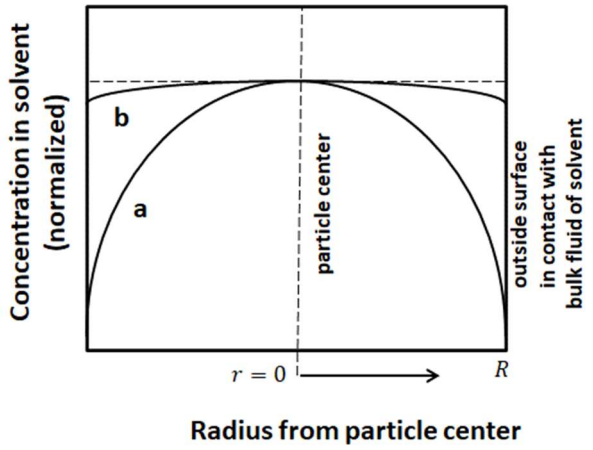

Fig.23.2-4 Schematic profile of concentration of extracted material in solvent during extraction process inside a single solid particle for two extreme cases

Profile (a) is the case of diffusion limited extraction that the material is carried away from the outside surface by the bulk fluid of solvent faster than it can diffuse from the center to the outside surface. Therefore the concentration at the outside surface drops to zero.
Profile (b) is the case of solubility limited extraction where solubility is low relative to diffusion. The dissolved material is able to diffuse to the outside surface faster than it can be carried away by the solvent, and the concentration profile becomes flat.

One great advantage of supercritical fluid extractions is complete separation of solvent from extract and raffinate. It should be kept in mind that adequate contact time is necessary for penetration of solvent into solid particles of packed matrix.

1) Sapkale, G.N., Patil, S.M., Surwase, U.S. and Bhatbhage, P.K., A review of Supercritical Fluid Extraction, *India Int. J. Chem. Sci.,* Vol.8(2), 729-743 (2010)

23.3 Leaching by Supercritical Fluids

A supercritical solvent can be used effectively for the leaching processes. The supercritical carbon dioxide is the most useful for supercritical extraction because it is very easy to separate solvent from the extract mixture obtained by leaching operation. Supercritical fluids dramatically improve not only the solubility of matters but also the permeability of cellular channels by swelling.

23.3-1 Leaching equipment

Pure supercritical fluid as the solvent is fed into the solid bed equipped in a vessel or a tank. The supercritical fluid may be percolated through stationary solid beds due to the pressure drop. There the dissolution and diffusion/mass transfer of soluble matters are also influenced very much by the surficial and internal structure of solid bodies.
The materials dissolved in the bulk of supercritical fluid are carried away downstream.
Fig.23.3-1 shows an example of decaffeination systems by using a supercritical carbon dioxide.
Decaffeination process by supercritical CO_2 takes place prior to roasting. After steaming, the green coffee beans are stacked up as a packed bed in a high-pressure vessel. The sCO_2 containing a little water is circulated through the leaching system at about 30 MPa and 65℃. Caffeine can be dissolved into the sCO_2 but the insoluble flavor compounds remain in the beans. The caffeine extracted is scrubbed from the sCO_2 with additional water, and then recovered in a distillation system.

The supercritical fluid percolates and dissolves the solid substance in the extractor, and then resulted solution with sCO_2 is rapidly depressurized through a heated nozzle at supersonic velocity into a low pressure chamber. This is called “Rapid expansion process.”

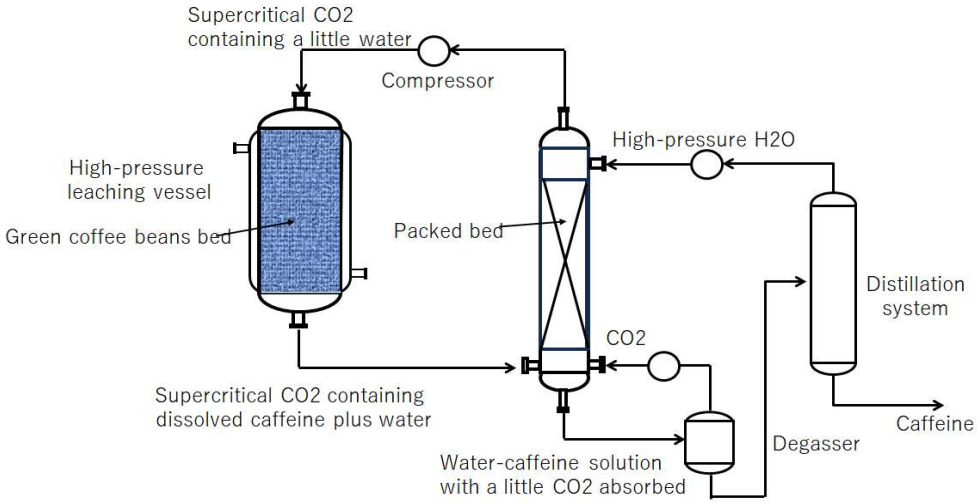

Fig.23.3-1 Leaching equipment for decaffeination by supercritical CO_2 used as a solvent

23.3-2 Rapid expansion of supercritical fluid solutions[2)]

The formation of nano- and micro-structured energetic particles results from the rapid expansion of a supercritical solution. In order to produce very fine particles, a supercritical solution of organic substances dissolved in sCO_2 is rapidly expanded through an expansion nozzle. Fig.23.3-2 shows a schematic configuration of leaching equipment accompanied with the rapid expansion precipitation system. Fig.23.3-3 shows typical variation of fluid temperature occurring in the rapid expansion of supercritical CO_2 solution.

During the rapid expansion, the density and solvent power significantly decrease, and then result in supersaturation of the solution and consequently precipitation of the solute free of a residual solvent. The precipitation of the solute from the sCO_2 solution occurs due to the rapid reduction of solute’s solubility. The precipitated solute particles have narrow particle size distribution. The higher the pressure of supercritical solution, the smaller the size of precipitated particles.

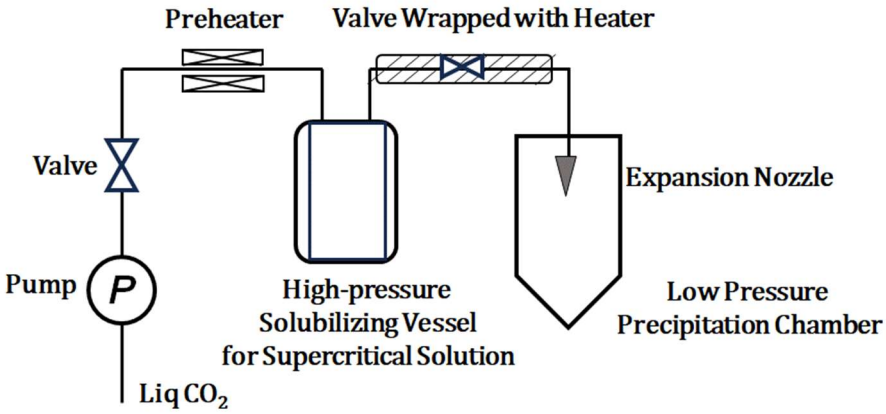

Fig.23.3-2 Schematic configuration of leaching plant accompanied with rapid expansion of supercritical carbon dioxide solution

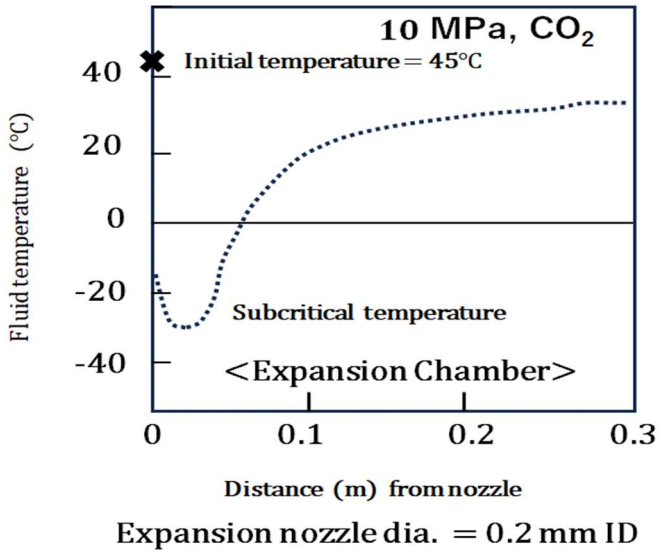

Fig.23.3-3 Variation of fluid temperature caused by rapid expansion

After leaching process, the rapid expansion of supercritical solution is also used to separate the solute as solid particles from the carbon dioxide.
Supercritical antisolvent technique using supercritical CO_2 is also very useful for microencapsulation in pharmaceutical industry.

2. Debenedetti, P.G., Tom, J.W., Kwank, X. and Yeo, S-D, Rapid expansion of supercritical solutions: fundamentals and applications, *Fluid Phase Equilibria*, vol. 82, 311-321 (1993)

Nomenclature

Cp	heat capacity, [J/kmol K]
D	tube diameter, [m]
G	mass velocity, [kg/m^{2}s]
Gr	Grashof number, [-]
h_i	heat transfer coefficient on the tube inside wall, [W/m^{2}K]
Nu	Nusselt number, [-]
P	pressure, [Pa]
Pr	Prandtl number, [-]
R	tube radius, [m]
Re	Reynolds number, [-]
T	temperature, [K]
η	exponent of Eq.(23.1-3), [-]
κ	thermal conductivity. [w/m K]
μ	viscosity, [kg/m s]
ν	kinematic viscosity, [m^2/s]
ρ	density, [kg/m^3]

Subscripts

b	bulk
C, cr	critical
pc	pseudo-critical
w	wall

PART Ⅳ

CHAPTER 24

ENERGY SAVING TECHNOLOGY

Any chemical processes cannot be executed without consumption of energy.

It is an economically important issue to reduce the energy requirement as much as possible. We know that distillation is a dominant separation technology in the chemical process industries, and at the same time, one of the largest energy-consuming unit operations. The distillation process proceeds by direct contact of the flowing-downward liquid with the flowing-upward vapor. In the case of column-type distillation systems, at the bottom reboiler, therefore, we need the heating duty for producing the vapor to be fed back into the bottom of the distillation column while the cooling duty is required at the overhead condenser to produce the reflux liquid by condensing the vapor coming out from the column top.

It is a very important issue to consider how to effectively reduce the consumption of energy.

In this chapter, we will study the energy conservation problem of a distillation column as an example.

24.1 Energy Requirement in Continuous Distillation

We already studied the energy balance in a single continuous distillation column (shown below) in Chapter 11.6（PART Ⅰ）.

Let us begin this chapter by going over that lesson with Fig.11.6-1.

A binary mixture consisting of x_F (mole fraction) of the more volatile component X and $(1 - x_F)$ of the less volatile component Y is fed at the feed rate F (kmol/h) into the central portion (i-stage) of the distillation column. The steady-state operation with reflux ratio $r = R/D$ obtains the overhead product D (kmol/h) containing x_D of component X and the bottom product B (kmol/h) containing $(1 - x_B)$ of component Y. There are several heat exchangers around the distillation column. Each exchanger should choose an appropriate pair of heating medium and cooling medium for the sake of effective energy exchange.

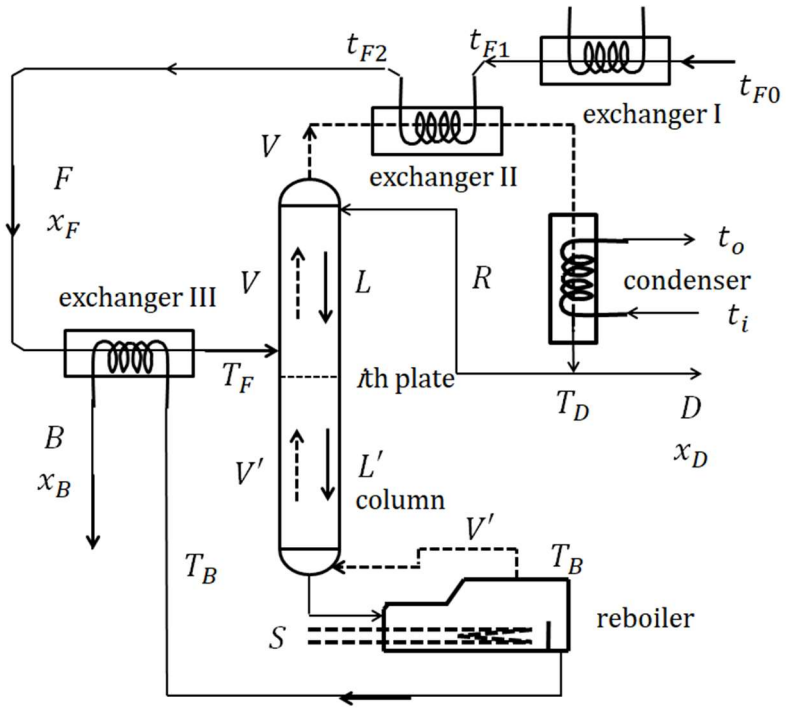

Fig.11.6-1. Flow sheet of distillation column system

First of all, the overall mass balances can be expressed as

$$F = D + B \tag{11.6-1}$$

$$F\,x_F = D\,x_D + B\,x_B \tag{11.6-2}$$

The feed is to be heated from t_{F0} to t_{F1} (K) by exchanger I, from t_{F1} to t_{F2} (K) by exchanger II, and from t_{F2} to T_F (K) by exchanger III, so that it can be introduced into the column as the saturated liquid at its bubbling point.

The molar latent heat and heat capacity of the mixture can be approximated as

$$\Delta H_M = x\,\Delta H_X + (1-x)\Delta H_Y \qquad \text{(J/kmol)}$$

$$Cp_M = x\,Cp_X + (1-x)Cp_Y \qquad \text{(J/kmol K)}$$

The vapor leaving the top of the column is to be completely condensed at its dew point T_D (K) by the exchanger II followed by the overhead condenser.

Since the vapor flow rate in the rectifying section is given by

$$V = (r+1)D,$$

the total rate of heat released in condensation of the vapor becomes

$$(r+1)D\,[x_D\Delta H_X + (1-x_D)\Delta H_Y]$$

Assuming that the average heat capacity Cp_M does not depend on temperature, the rate of heat transfer at exchanger II is given by

$$F\,[x_F Cp_X + (1-x_F)Cp_Y](t_{F2} - t_{F1})$$

If a cooling water enters the overhead condenser at t_i (K) and leaves at t_o (K), the heat balance set up at the condenser gives the water flow rate W (kg/h) as

$$(r+1)D\,[x_D\Delta H_X + (1-x_D)\Delta H_Y] - F\,[x_F Cp_X + (1-x_F)Cp_Y](t_{F2} - t_{F1}) = W\,Cp_w(t_o - t_i) \tag{11.6-7}$$

where Cp_w is the heat capacity of water in (J/kg K).

The bottom product leaves the reboiler at its bubbling point T_B (K). If the heating duty is provided by condensation of steam at pressure P_S (Pa) in the jacket of the reboiler, the heat required for vaporizing V' (kmol/h) of the bottom liquid is given by

$$V'[x_B \Delta H_X + (1 - x_B)\Delta H_Y] = S\,\Delta H'_S \quad (11.6\text{-}8)$$

From this equation, the required steam, S (kg/h) can be calculated.

By heat balance set up at exchanger III, the outlet temperature t_B (K) can be calculated.

$$F\,[x_F Cp_X + (1 - x_F)Cp_Y](T_F - T_{F2}) = B[x_B Cp_X + (1 - x_B)Cp_Y](T_B - t_B) \quad (11.6\text{-}9)$$

We already learned the heat balance up to this position in Chapter 11.6.

Take a look at Figure 11.6-1. We employed three exchangers to preheat the feed mixture to be distilled.

[PROBLEM 24.1-1]

Regarding the flow sheet of heat exchangers around the distillation system in Fig.11.6-1, we can consider the following two cases: the exchanger I is placed (1) between the exchangers II and III and (2) between the exchanger III and the feeding inlet. Which position is more profitable?

From a viewpoint of energy saving, the latent heat of the vapor leaving the top of the column is utilized in exchanger II to heat the feed mixture up to t_{F2} and the sensible heat of the bottom product discharged from the bottom reboiler is utilized in exchanger III to heat the feed mixture up to T_F. These methods can be regarded as the prerequisite utilization of energy. However it is more important to drastically reduce the heating duty of the reboiler and the cooling duty of the overhead condenser. We would like to consider whether or not the heat released by vapor condensation in the overhead condenser can be utilized for the heating duty for vaporization in the bottom reboiler. A problem is how to pump up the thermal energy from the low-temperature overhead condenser to the high-temperature bottom reboiler.

We shall study the principle of heat pump in the next section as another technology of effective energy saving.

In the latter half of this chapter, we will study a heat pump system only for the energy-saving technology of distillation and evaporation plants.

24.2 Heat Pump Technology

24.2-1 Principle of heat pump

There are various heat pump systems available depending on their purposes.

First of all, let us begin by considering the vapor-compression cycle as an example used by many refrigeration systems. We know well from the second law of thermodynamics that thermal energy cannot be freely transferred from a lower-temperature environment to a higher-temperature environment. It will become possible only if an external high-quality energy such as mechanical shaft work obtained by a compressor is applied from the outside to the system. We know that the temperature of gases can be raised by adiabatic compression due to a compressor. Therefore a standard room air conditioning system works by the vapor-compression cycle called “refrigeration cycle.”

Fig. 24.2-1 is a basic heat pump flow configuration using a refrigerant as the working fluid.

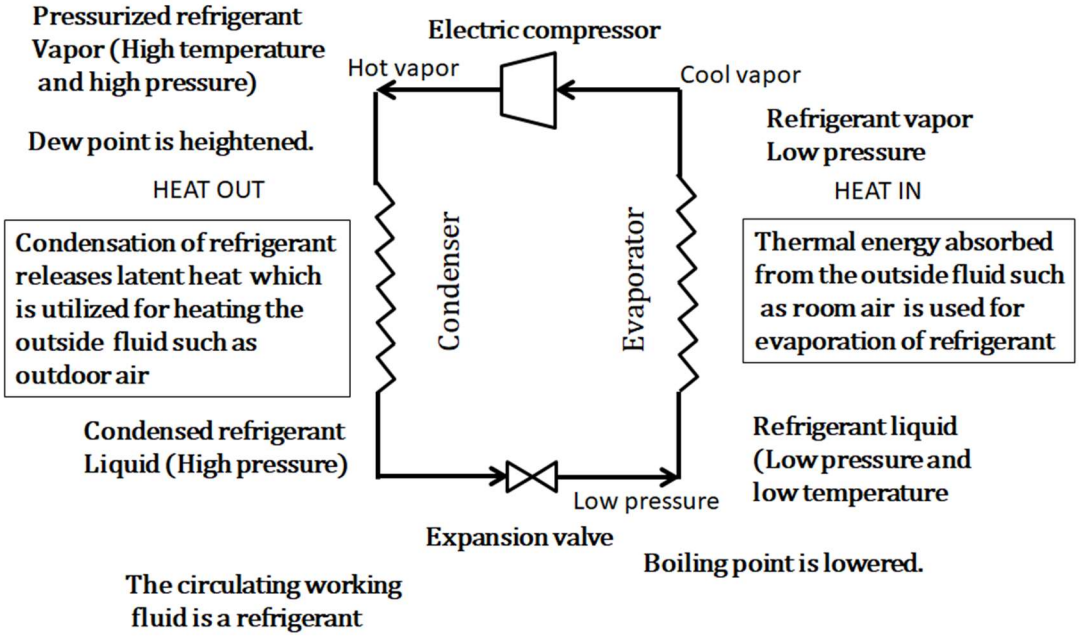

Fig. 24.2-1 Basic flow configuration of a heat pump air-conditioner

The amount of work W required to pump an amount of heat Q from a lower-temperature reservoir such as ambient outdoor air to a higher-temperature reservoir such as room air is given by

$$W = \frac{Q}{C_{op}} \tag{24.2-1}$$

where C_{op} is called as instantaneous coefficient of performance for the heat pump; a ratio of useful heating or cooling provided to work required.

Regarding the refrigeration cycle in cooling mode of Fig.24.2-1, the compressor sends the high-pressure and high-temperature refrigerant vapor to the condenser coil where it is converted to a liquid. In this condenser section, the latent heat is released for heating the outside air. Then by isenthalpic expansion traveling through the expansion valve, the refrigerant becomes low pressure and low temperature liquid with some flashed vapor. At the next evaporator section, the low-pressure and low-temperature refrigerant liquid is evaporated absorbing heat from the indoor air. A fan is necessary there to improve the efficiency of heat exchange with the condensing or evaporating refrigerant in the looped system. The fan blows the indoor air across the cold evaporator coil where the heat inside the room is absorbed into the refrigerant.

In this manner, the cooled air is then circulated throughout the room while the evaporated low-temperature refrigerant vapor is sent back to the compressor. There the low-pressure and low-temperature refrigerant vapor is adiabatically compressed to become high-pressure and high-temperature vapor.

This refrigeration cycle can be reversed; if the indoor evaporator coil switches roles, it becomes the condenser coil producing heat while the outdoor condenser unit also switches roles to serve as the evaporator discharging cold air.

That is, a usual sink or source for heat is the outdoor or room air, as used by an air-source heat pump.

A typical diagram of heat pumping by vapor-compression refrigeration is expressed as in Fig.24.2-2.

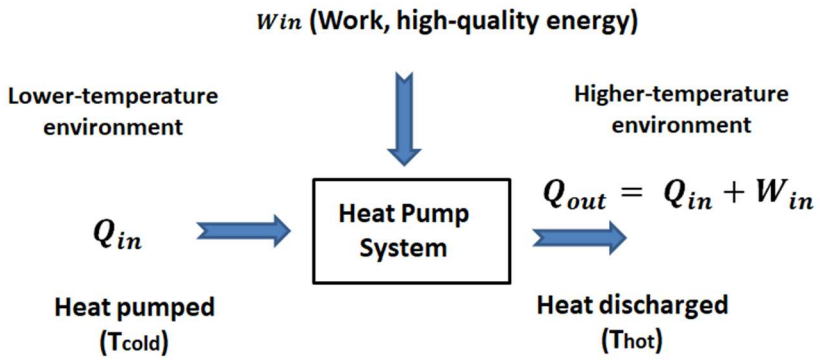

Fig.24.2-2 Principle of Reversed Heat Pumping

In the case of an ideal heat pump, the first law of thermodynamics gives

$$Q_{in} + W_{in} = Q_{out} \tag{24.2-2}$$

Its coefficient of performance is defined as

$$C_{op}\ (\text{refrigerator}) = Q_{in}/W_{in} = Q_{in}/(Q_{out} - Q_{in}) \tag{24.2-3}$$

If the heat transfers are reversible and isothermal at temperatures T_{hot} and T_{cold}, the COP is expressed as

$$C_{op}\ (\text{refrigerator}) = T_{cold}/(T_{hot} - T_{cold}) \tag{24.2-4}$$

$$C_{op}\ (\text{heat pump}) = Q_{out}/W_{in} = T_{hot}/(T_{hot} - T_{cold}) \tag{24.2-5}$$

Let us understand the principle of heat pump by using an ideal Carnot heat engine cycle schematically shown in the T-S diagram (Fig.24.2-3).

Consider the following ideal heat engine cycle using steam as an example vapor.

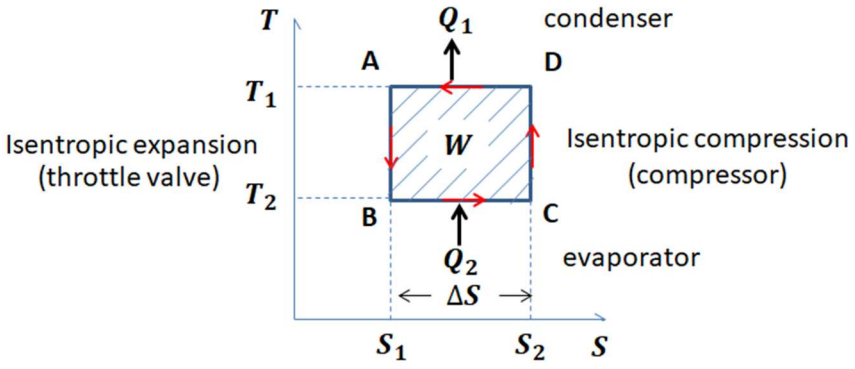

Fig. 24.2-3 Ideal heat engine cycle for heat pumping

Fig.24.2-3 indicates an ideal heat engine cycle for pumping thermal energy from the temperature T_2 of cool environment to the temperature T_1 of hot environment.

The basic loop consists of the following four sub-processes:

A→B Isentropic expansion (Throttle valve)

B→C Constant pressure heating (Evaporation)

C→D Isentropic compression

D→A Constant pressure cooling (Condensation)

Practically speaking, since it is difficult to compress wet vapor, the refrigerant is usually dried before compression. The vapor compressed by isentropic compression is usually somewhat superheated. The throttle does not produce a useful work. The enthalpies of the refrigerant vapor (or steam) before and after a throttle are the same. This is called "isenthalpic process" but the entropy increases over the throttle.

Fig.24.2-4 shows an actual Entropy-Temperature diagram of the heat pump system.

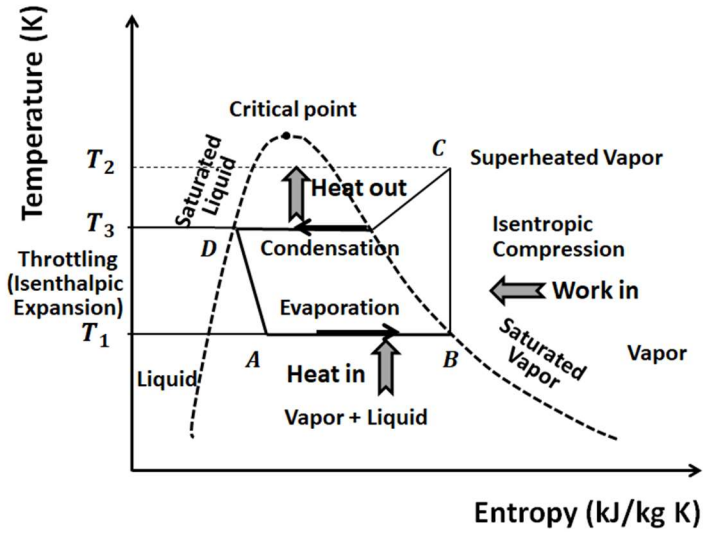

Fig. 24.2-4 S-T diagram for heat engine cycle for actual heat pumping

The purpose of this chapter is to provide a basic understanding of heat pump theory and a more practical approach to the solution of problems which may arise in conjunction with energy consumption of distillation processes.

By using Fig.24.2-4, an analysis would start at the evaporator (A→B) where cold liquid at low pressure is vaporized as it picks up heat from the room air passing over the coil of the exchanger. This sub-process is constant-pressure evaporation at its saturation temperature. Cool vapor from the

evaporator then flows to the electric compressor (B→C), where its pressure and temperature are elevated due to the isentropic compression. The hot refrigerant vapor containing heat of compression and latent heat of vaporization (superheated vapor) is pumped to the condenser (C→D) where heat is removed by the outdoor air passing over it.

Thus heat has been pumped up from the evaporator (room air) to the condenser (outdoor air). The refrigerant liquid (condensate) leaving the condenser passes through the throttle (D→A) accompanied with isenthalpic expansion and then goes back to the evaporator.

In this manner, the heat pump working principle is that a device transfers heat energy from a source of heat to the thermal reservoir. This implies a possibility that in a distillation column, the overhead condenser can be the source of heat and the bottom reboiler can be the thermal reservoir. In a usual situation, however, the overhead condenser is lower in temperature than the bottom reboiler. Therefore we need an electric compressor for the overhead condenser to become the heat source whereas the bottom reboiler serves as the heat sink. This method is also called “Vapor Recompression” or VRC method. However it should be kept in mind that the electric energy is much more valuable in quality than the thermal energy. From this point of view, therefore, we should compare how much the electric energy applied with how much the thermal energy saved.

24.2-2 Vapor recompression technology for distillation

An example of the VRC (vapor recompression) system for a distillation columns is given by Fig.24.2-5.

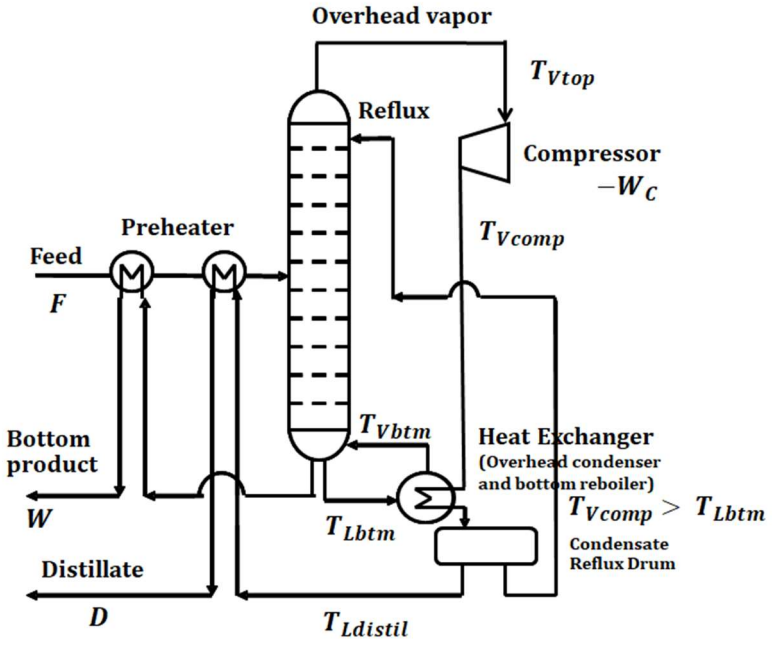

Fig. 24.2-5 VRC system of distillation column constructed by using heat pump technology

In this system, a heat exchanger plays a role of the condenser for the high-pressure overhead vapor as well as of the reboiler for the low-pressure bottom liquid. If we set up the energy balance over the area enclosed by the broken line in Fig.24.2-6, the following equation is obtained:

$$F\,H_F + (-W_c) = D\,H_D + W\,H_W \qquad (24.2\text{-}6)$$

This implies that we should consider the adiabatic work done by the electric compressor as the surplus energy from the outside. As a result, the heating duty for the bottom reboiler can be covered by the cooling duty for the overhead condenser by virtue of the additional energy input supplied by the electric compressor.

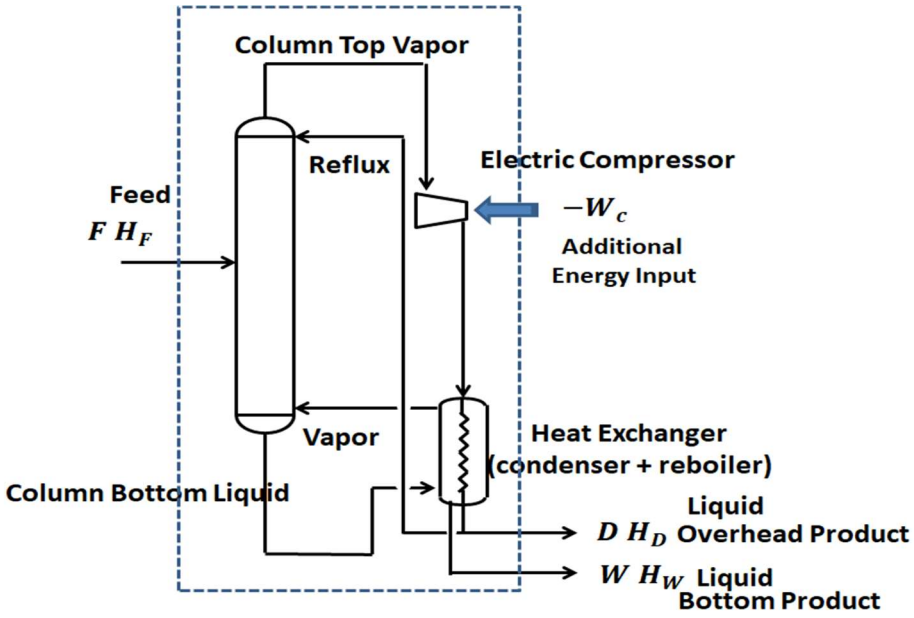

Fig. 24.2-6 Energy balance of VRC system of distillation column

For an ideal gas, the adiabatic compression work $(-W_c)$ is given from the outside by

$$(-W_c) = \int_{p_0}^{p_1} V\,dp = {p_0}^{1/\kappa} V_0 \int_{p_0}^{p_1} \frac{dp}{p^{1/\kappa}} = \frac{\kappa}{\kappa-1}\left[1 - \left(\frac{p_1}{p_0}\right)^{\frac{\kappa-1}{\kappa}}\right] \qquad (24.2\text{-}8)$$

This equation can be employed in case when steam used as the refrigerant with the volumetric flow rate V_0 is compressed from p_0 to p_1 by the compressor.

Here $\kappa = Cp/Cv$ is the specific heat ratio of the gas. For the case of steam, it can be assumed as $\kappa \cong 1.32$.

In this system, the more-volatile vapor (usually organic) must be directly compressed by an electric compressor. Practically speaking, we do not use a turbo-compressor which cannot give a high compression ratio. In order to get a high compression ratio, we very often employ a positive displacement compressor such as a screw-type compressor rather than a turbo-compressor. For safety, therefore we often utilize a steam compressor for the VRC system to be described in the following section.

[PROBLEM 24.2-1]

By using the VRC system shown in Fig.24.2-6, the overhead vapor of a distillation column having the following operation data is adiabatically compressed by a screw-type compressor.

Overhead vapor data:

Composition: ethanol 55.8 mol% and water 44.2 mol%, Temperature 82.3℃, Pressure 0.1 MPa,

Vapor rate $V_{top} = 4.5$ kmol/h

(1) Calculate the temperature of the vapor compressed with the compression ratio of 2.0.

Is the compressed vapor superheated?

(2) Calculate the theoretical work of the compressor.

(3) The liquid has the composition of ethanol 2.0 mol% and water 98 mol% in the bottom reboiler operated at 0.1 MPa and 95.5℃. Obtain the condition of the heat exchanger as the reboiler if using the compressed vapor as the VRC heating medium.

24.2-3 New heat-pumped distillation system

Let us consider how to pump up heat from low-temperature condensate of the overhead condenser to higher-temperature liquid of the bottom reboiler.

Fig.24.2-7 shows a standardized heat pump unit.

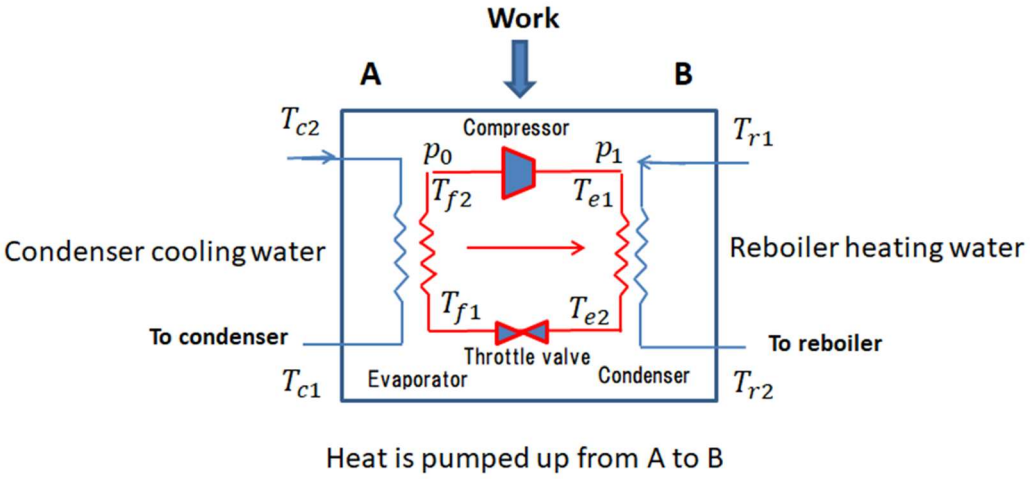

Fig. 24.2-7 Inside structure of a standard heat pump unit.

Consider the heat pump system using a refrigerant as the working fluid

This system has a heat engine cycle which consists of condenser section, evaporator section connected with a compressor and a throttle valve.

Regarding the red line loop shown in Fig.24.2-7, the high-pressure and high-temperature refrigerant vapor from the compressor (side B) is condensed in the condenser section operated at high pressure p_1, where the latent heat released is given to the hot water line for the reboiler. Usually the condensation takes place under the constant high temperature: $T_{e1} = T_{e2}$. Then isenthalpic expansion without energy input is conducted by a throttle valve, where the refrigerant temperature and pressure go down to T_{f1} and p_0 accompanied with some partial vaporization.

After the throttle valve, the two-phase fluid of the refrigerant is evaporated in the evaporator section (side A) operated at constant low temperature $T_{f1} = T_{f2}$ and low pressure p_0, where the latent heat for evaporation is obtained from the cooling water line for the overhead condenser. Downstream of the evaporator, it is usually necessary to get dry vapor for good operation of the compressor. The saturated vapor is adiabatically compressed from pressure p_0 to p_1 by the electric compressor.

This isentropic compression work $(-W_c)$ is put into the system by electricity from the outside environments.

Except for the heat input Q_c at the evaporator and the heat output Q_r at the condenser in the heat pump unit, the compression work should be treated as the additional energy input into the heat pump unit. In this manner, thermal energy can be pumped from the condenser cooling water to the reboiler heating water by adding the mechanical shaft work into the system.

Setting an energy balance over this heat pump unit

$$Q_c + (-W_c) = Q_r \qquad (24.2\text{-}7)$$

Fig.24.2-8 shows a distillation column system inside of which a heat pump unit is installed.

It should be kept in mind that the surplus energy, i.e. the work $-W_c$ given to the heat pump unit by the electric compressor needs to be cancelled by a cooler on the cooling water line shown in Fig.24.2-8.

Usually the heat duty of the bottom reboiler becomes slightly greater than the cooling duty of the overhead condenser. Therefore there is a possibility working without the surplus energy remover.

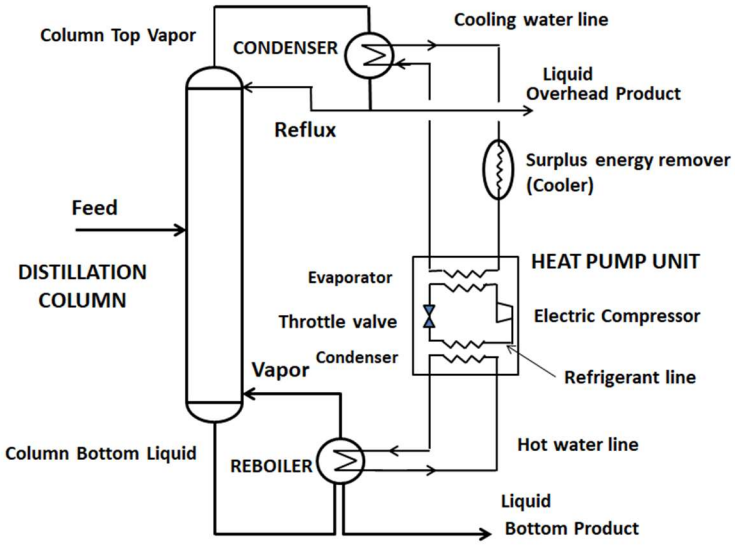

Fig. 24.2-8 Distillation column installed by a heat pump unit.

For the case of ideal solutions such as benzene-toluene binary system, the heating duty Q_r of the reboiler becomes approximately equal to the cooling duty Q_c of the condenser.

Therefore additional work is required in VRC distillation to pump up heat from the low temperature condenser to the higher temperature reboiler by using a heat pump unit.

The surplus energy is given as the compression work W_c by means of the compressor of the heat pump unit.

In the region enclosed by the red broken line as shown in Fig.24.2-9, the following energy balance can be obtained taking into account the work $(-W_c)$ by the compressor and the cooling duty Q'_c for the surplus energy.

$$Q_r + Q'_c = Q_c + (-W_c) \quad (24.2\text{-}9)$$

Roughly speaking, for an ideal system, the reboiler heating duty is approximately equal to the condenser cooling duty: $Q_r \cong Q_c$. The above equation indicates that the cooling device for removing the surplus energy Q'_c is necessary to keep the distillation system steady.

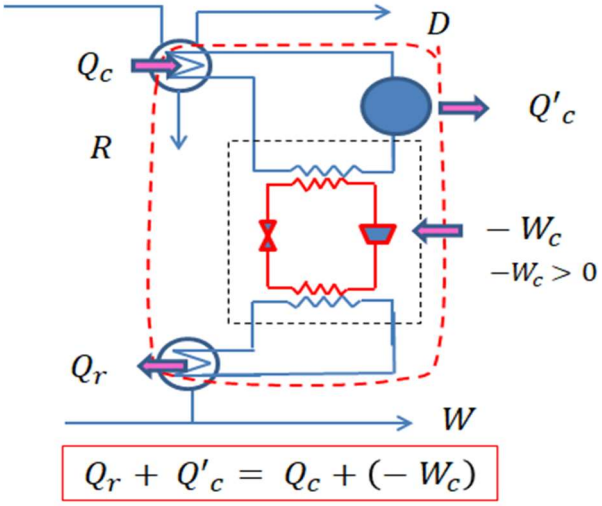

Fig. 24.2-9 Compensation for the surplus energy resulting from the heat pump unit.

24.3 Vapor Recompression Technology for a Jacketed Tank Evaporator

24.3-1 A new batch tank evaporator

By the way, we would like to introduce an effective batch evaporator shown below.

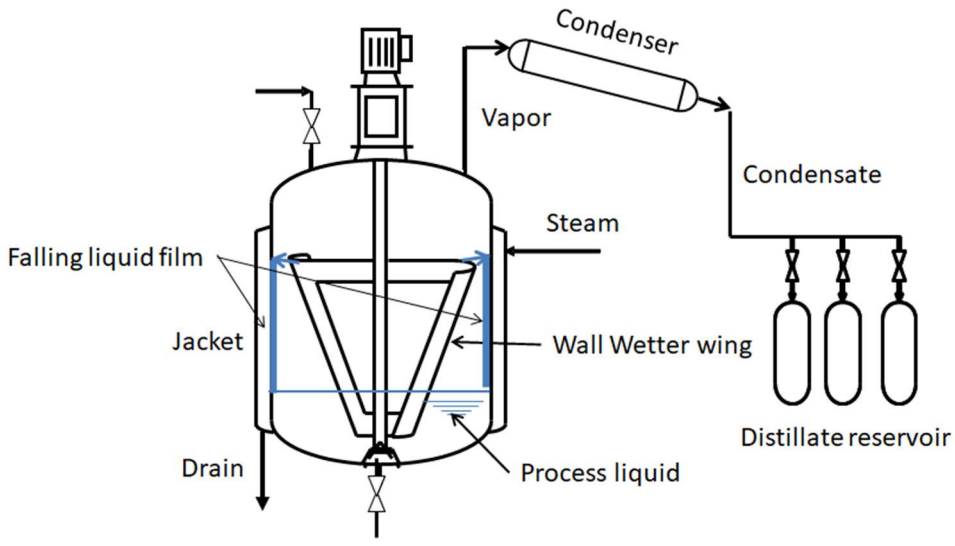

Fig.24.3-1 A batch system of Wall-Wetter evaporator

This is an our original “Wall-Wetter” batch evaporator consisting of two or four half-cut pipes (or gutters) which are fixed obliquely to the rotating shaft within a jacketed tank. (Kansai Chemical Engineering Co., Ltd)

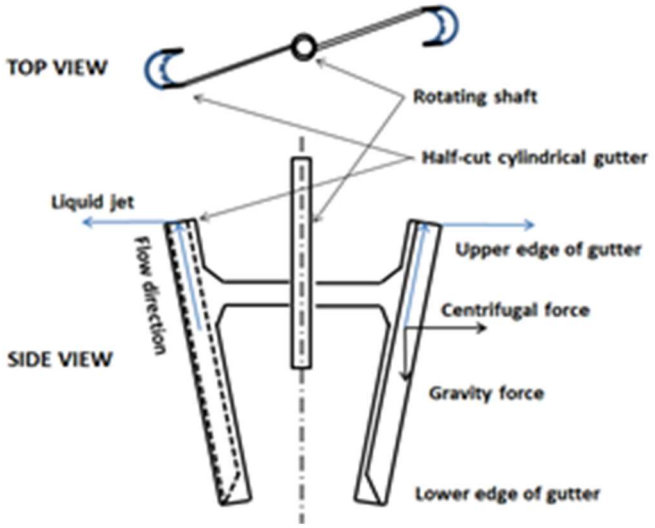

Fig.24.3-2 A configuration of two-wing Wall-Wetter.

The Wall-Wetter system has been devised noticing that the process liquid pooled in the tank bottom can be pumped up within the vessel due to the centrifugal effect of the rotating Wall-Wetter wings. As shown in Fig.24.3-2, the Wall Wetter wing has a form of inclined gutters (half-cut pipes), inside of which the process liquid crawls up toward their upper edges, and then the liquid jet issuing radially from the upper edges. It forms a liquid film falling on the inside wall of the evaporator tank.[1~4)]

Therefore the evaporating rate can be kept at a large constant value during the whole evaporation process time by maintaining the whole heat transfer surface constantly wet with the falling liquid film of the process liquid.

The process time required for attaining the request of evaporation is usually shortened very much.

The evaporative characteristics concerning the Wall Wetter can be obtained referring to the relevant literature.[1~4)]

---

1. Yamaji, H., Noda, H., and Kataoka, K., Proc. 6th World Congress of Chemical Engineering, (CD-ROM), Melbourne, Australia (2001)
2. Yamaji, H., Doctoral Dissertation, Kobe Univ. (2002)
3. Mukaida, T., Kataoka, K., Yamaji, H., Noda, H., and Ohmura, N., *Kagaku Kogaku Ronbunshu*, 44(2), pp.107-112 (2018)
4. Mukaida, T., Kataoka, K., Noda, H., and Yamaji, H., *Chem. Eng. Transactions*, **86**, (2021)

24.3-2 Saving energy by a vapor recompression technology

From a viewpoint of heat pump, we can consider the so-called vapor-recompression (VRC) method applied for this batch evaporator system shown in Fig. 24.3-3.

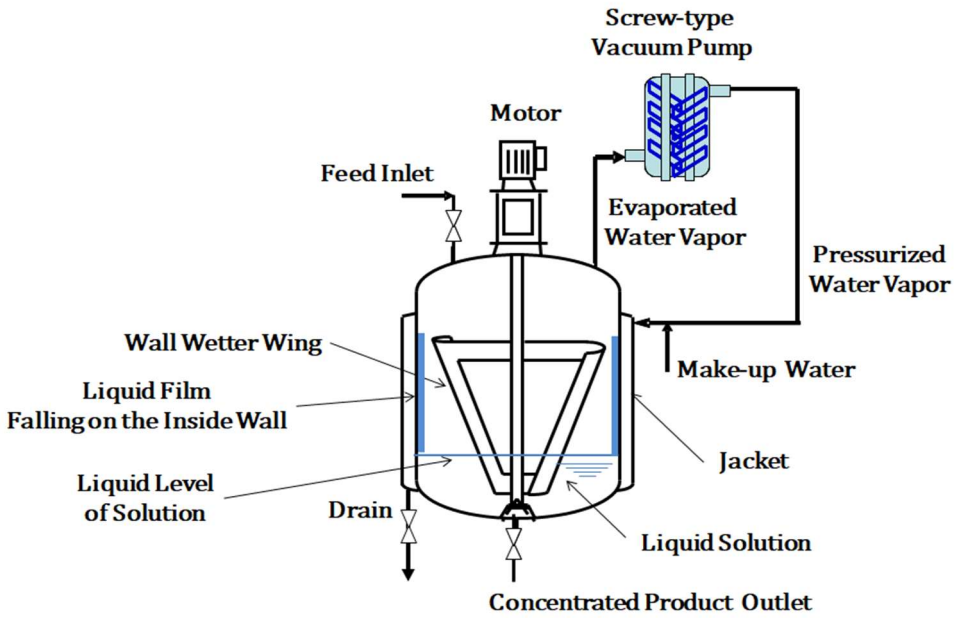

Fig.24.3-3 A batch system of Wall-Wetter evaporator arranged for VRC method.

Let us consider the case when water is evaporated for concentration of an aqueous solution of non-volatile substance such as salt and sugar.

The water vapor evaporated from the liquid film falling over the jacket wall as well as the liquid solution pooled in the bottom leaves the top of the evaporator and is compressed from P_V to P_C by an electric screw-type vacuum pump or compressor, so that the vapor temperature is raised from T_{sol} to T_{cond}.

The basic idea of VRC in this evaporator is expressed in Fig.24.3-4.

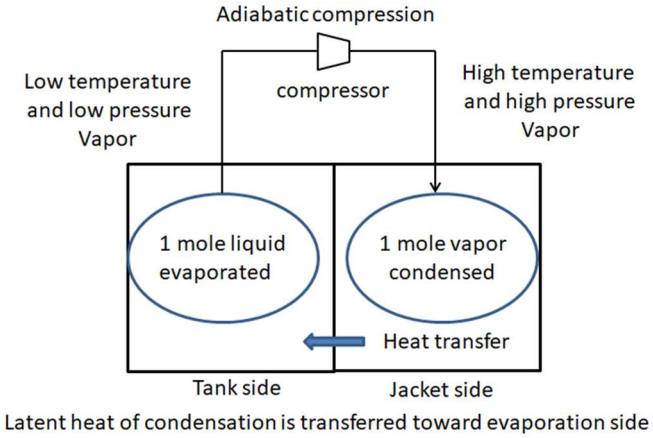

Fig.24.3-4 Basic idea of VRC for a Wall Wetter batch evaporator

Roughly speaking, the above figure states that one mole of evaporated water vapor can evaporate one mole of water of the same aqueous solution after the adiabatic compression. The energy requirement is the work of isentropic compression by the compressor only.

However it is usually necessary to utilize a cooling water system equipped inside a compressor or a vacuum pump. Otherwise the outlet vapor temperature raised due to the isentropic compression will become considerably higher than the saturation temperature at the compressor outlet pressure.

Because the latent heat of evaporation decreases in some degree with increasing pressure, the thermal energy for the evaporation cannot be covered with the thermal energy released by the condensation, that is, some extra steam or an auxiliary heater may be required.

Practically this pressurized water vapor a little higher than the saturation temperature is supplied into the jacket of the same evaporator for reuse as the heating medium.

Strictly speaking, owing to the effect of pressure on heat of evaporation, the thermal energy released by condensation of the pressurized vapor is a little less than the thermal energy required for evaporation of the solution. Therefore a very small auxiliary heater or an extra steam (make-up steam) should be utilized for compensating the energy deficit Q_c.

Fig.24.3-5 shows the temperature profile on both sides of the tank wall for heat exchange.

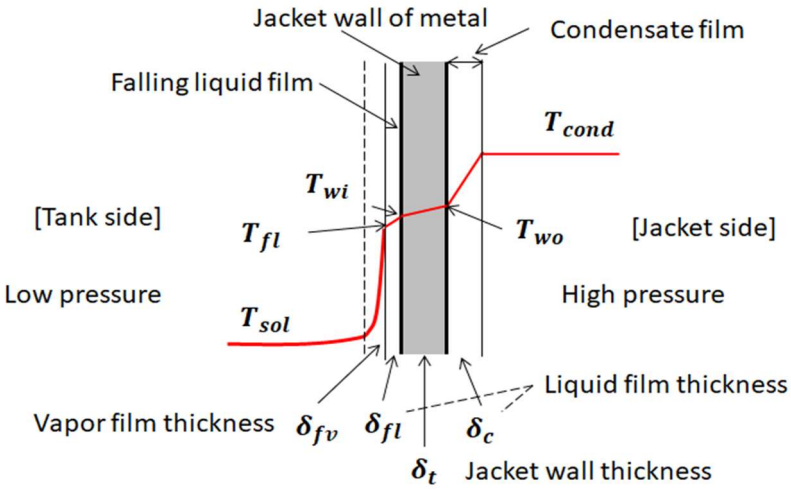

Fig.24.3-5 Schematic profile of the temperature distribution in the neighborhood of the jacket wall of the WW evaporator

For simplicity, the overall driving force for evaporating the process liquid is given by

$$\Delta T = T_{cond} - T_{sol} \tag{24.3-1}$$

Assuming no fouling effect, the overall heat transfer resistance $1/U_o$ can be expressed as the sum of the resistances lying in series:

$$\Delta R = \left(\frac{\delta_{fv}}{\kappa_v} + \frac{\delta_{fl}}{\kappa_f}\right) + \frac{\delta_t}{\kappa_t} + \frac{\delta_c}{\kappa_c} = \frac{1}{h_f} + \frac{\delta_t}{\kappa_t} + \frac{1}{h_c} = \frac{1}{U_o} \tag{24.3-2}$$

The evaporative heat transfer coefficient h_f is obtained from the resistance of the falling liquid film and the fictitious vapor film contacting the surface of the falling liquid film.

The thermal energy transferred from the jacket side to the tank side for evaporation of the process liquid is

$$Q_{ev} = U_o A_o \Delta T \quad (24.3\text{-}3)$$

In the case of non-volatile solute, the basic equation of evaporation by a batch WW evaporator can be expressed as

$$-\frac{dL}{dt} = \frac{Q_{ev}}{\lambda} \quad (24.3\text{-}4)$$

where L is the molar mass of the liquid solution contained in the evaporator tank, and λ the molar latent heat for vaporizing the solvent (i.e. water) in the tank.

The boiling point of the evaporating solution can be calculated at the operating pressure by Antoine equation

$$T = \frac{B}{A - log_{10}P} - C \quad (24.3\text{-}5)$$

where the units of temperature and pressure are t (℃) and P (mmHg).

The change in specific volume of the vapor by the adiabatic compression obeys the following perfect gas law:

$$v_1 = v_0 (P_0/P_1)^{1/\gamma} \quad (24.3\text{-}6)$$

The theoretical power requirement is calculated by the following adiabatic compression:

$$(-w_c) = \frac{-\kappa}{\kappa - 1} P_0 v_0 \left[1 - \left(\frac{P_1}{P_0} \right)^{\frac{\kappa-1}{\kappa}} \right] \quad (24.3\text{-}7)$$

where the specific heat ratio $\kappa = Cp/Cv$ becomes 1.4 for perfect gas or 1.32 for steam.

The vapor temperature raised by compression is given by

$$\frac{T_1}{T_0} = \left(\frac{P_1}{P_0} \right)^{\frac{\kappa-1}{\kappa}} \quad (24.3\text{-}8)$$

As aforementioned for ideal adiabatic compression by positive displacement compressors, this outlet temperature T_1 will usually become extremely higher than the saturation temperature.

In this example, a small amount of liquid water injected into the compressed water vapor line just before the entrance to the jacket is evaporated by the sensible heat above the saturation temperature of the compressed water vapor. That is, a proper amount of make-up water serves as the make-up water vapor.

As a result, the proper amount of water vapor in total is supplied at the saturation temperature into the jacket.

The condensation heat transfer occurs in the major part of the jacket. It is also possible to utilize the sensible heat of the condensate drain in the lower part of the jacket.

However the effect of condensate drainage are not so large. The heat capacity effect Q_{sys} of the evaporator construction system should also be considered.

In the practical system design, the heat loss Q_{loss} from the evaporator system to the surrounding atmosphere should also be taken into consideration. The evaluation of the energy saving should be done comparing with the heat duty of the original batch evaporator in the same operating condition.

In this case, the energy-saving rate can be considered as

$$Es\ (\%) = \left[1 - \frac{\text{energy requirement}}{\text{heat duty for evaporation}}\right] \times 100 = \frac{Q_{ev} - ((-W_c)/\eta_c + Q_{sys} + Q_{loss})}{Q_{ev}} \times 100 \quad (24.3\text{-}9)$$

where η_c is the overall efficiency of the compressor.

The consumption of electric energy of the compressor should take into consideration the generation efficiency of electric power besides its own efficiency.

[EXAMPLE 24.3-E1]

Let us consider the energy-saving problem of the Wall Wetter evaporator arranged for the VRC method shown in Fig.24.3-3. The cylindrical evaporator tank which can contain 60 litre of aqueous solution of non-volatile substance (ex. sugar) has the total effective heat transfer area $A = 0.34\text{m}^2$, the inside diameter $D_i = 400$ mm of the cylindrical tank and the thickness $\delta_t = 4$ mm of the tank wall, respectively. The construction material of the system is assumed as stainless steel (SUS304).

A screw-type dry vacuum pump belonging to a positive displacement vacuum pump is employed to control the operating pressure for evaporating water from aqueous solution of non-volatile solute. Owing to the given discharge rate of the vacuum pump, the evaporator tank pressure is raised a little bit gradually from 148 mmHg. The suction-side and discharge-side nozzles of the vacuum pump have 60 mm and 40 mm in inside diameter, respectively.

Actually the latent heat of evaporation decreases a little bit as the pressure is raised. The energy deficit due to the difference in latent heat of evaporation is compensated by the make-up water injected into the compressed water vapor line. Therefore the proper but small amount of make-up water added serves as the make-up saturated water vapor obtained by the sensible heat above the saturation temperature. The operation pressure is kept constantly about 148 mmHg so as to prevent the solute from becoming solidified.

In this way, the proper rate of the saturated water vapor is supplied into the jacket.

In this example, we shall deal with the batch evaporation required for the following specification. The aqueous solution of non-volatile solute is to be concentrated from 0.10 to 0.90 in mass fraction. The operation is begun by supplying the 60 kg (60℃) of the feed solution with the solute concentration of 10 wt% into the evaporator tank at the initial condition (temperature 60℃ and pressure 148 mmHg).

Because of a positive displacement type vacuum pump, the volumetric flow rate condition is automatically set to be $V_{vp} = 0.020\ \text{m}^3/\text{s}$ on the suction-side of the vacuum pump. This is equal to the rate of evaporation. The outlet pressure of the vacuum pump is also maintained as one atmospheric pressure. In the jacket maintained at 1 atm, the water vapor from the vacuum pump accompanied by the make-up water vapor is condensed to give the released energy to the tank for evaporation of aqueous solution.

In the case of a usual batch evaporator which does not have any VRC equipment, the total thermal energy requirement can be expressed as the sum of the latent heat Q_{ev} for evaporating the solution, the sensible heat Q_{sys} for heating the evaporator construction system, and the heat loss Q_{loss} through the outside surface of the equipment to the surrounding atmosphere:

$$Q_{total} = Q_{ev} + Q_{sys} + Q_{loss} \quad \text{(24.3-E1)}$$

The isentropic compression work $(-w)_c$ by the vacuum pump can be obtained by the following equation:

$$(-w)_c = \frac{-\kappa}{\kappa-1} P_0 v_0 \left[1 - \left(\frac{P_1}{P_0}\right)^{\frac{\kappa-1}{\kappa}}\right] \quad \text{(24.3-E2)}$$

The total efficiency of the vacuum pump is assumed as $\eta_c = 0.30$, which comes from the electric power generation efficiency as well as the vacuum pump efficiency.

The overall heat transfer coefficient is assumed to be kept at U_o =524 $\mathrm{W/m^2K}$ which is assumed taking into account our experimental data.

Only for simplicity, the boiling-point rise due to the non-volatile solute is assumed to be negligibly small in this example.

Obtain the temporal variations of energy saving rate, salt concentration, vacuum pump electricity requirement, and make-up water.

[Solution] The rate of evaporation in the tank is expressed in the form of decrease in mass of the liquid solution and the heat input from the jacket side:

$$-\frac{dL}{dt} = \frac{Q_{ev}}{\lambda_{ev}} \quad \text{(24.3-E3)}$$

Here the heat input Q_{ev} should include not only the condensation of the water vapor compressed by the vacuum pump but also an additional heat input from the make-up water vapor.

That is, the sensible heat Q_{ex} of the superheated vapor can be consumed for evaporation of the make-up water.

$$Q_{ex} = V_{com} Cp_{sv}(T_c - T_{con}) \quad \text{(24.3-E4)}$$

This effect is considered to be small (of order 10% or less).

The initial conditions are expressed as

$$L = L_0\ (= 60\ kg)\ , T = T_o (= 60℃), \text{and } x = x_0\ (= 0.10)\ \text{ at } t = 0 \quad \text{(24.3-E5)}$$

The initial tank pressure is assumed to be the saturation pressure (148 mmHg) for the initial solution.

The saturation temperature of water is calculated by the Antoine equation.

$$T = \frac{B}{A - log_{10} P} - C \quad \text{(24.3-E6)}$$

As the result of rough calculation, the overall heat capacity of the evaporator construction material is assumed to be 650 $\mathrm{kJ/kg\ ℃}$.

The overall heat transfer coefficient U_o is assumed to be constant at U_o = 524 $\mathrm{W/m^2K}$.

As the tank-side pressure or the boiling point rises gradually by the vacuum pump, the molar latent heat of water depending on the saturation temperature T_{sol} is evaluated by the approximate equation:

$$\lambda_{ev} = \lambda_0 + \lambda_1(T_{nbp} - T_{sol}) \quad (24.3\text{-E7})$$

where T_{sol} is the saturation temperature of the solution in the tank and T_{nbp} the normal boiling point.

The heat transfer area A_1 is allocated to the heat transfer due to the condensation and the remaining area A_2 to the heat transfer from the sensible heat of the drain: $A_1 + A_2 = A$.

For simplicity, the vapor density in the tank is evaluated by the perfect gas law.

$$\rho_v = M_w \frac{P}{R\,T(K)} \quad (24.3\text{-E8})$$

The evaporation rate $V_{ev} = \rho_v V_{vp}$ kg/s is automatically controlled by the volumetric suction rate $V_{vp} = 0.020$ m^3/s of the vacuum pump.

The specific heat ratio $\kappa = Cp/Cv$ is assumed to be 1.3 for steam in this condition.

Let us consider from here the calculation results of the process simulation analysis summarized in Figs.24.3-E1 to E5.

(1) Solute concentration, liquid solution temperature, tank pressure, and mass of liquid solution

Fig.24.3-E1 shows temporal variation of the pressure of the evaporator tank and the temperature of the liquid solution in the tank.

It has been found that owing to the inevitable small deviation between the vapor discharging rate of the vacuum pump employed and the evaporating rate of the WW evaporator, the liquid solution temperature is rising gradually with the tank pressure.

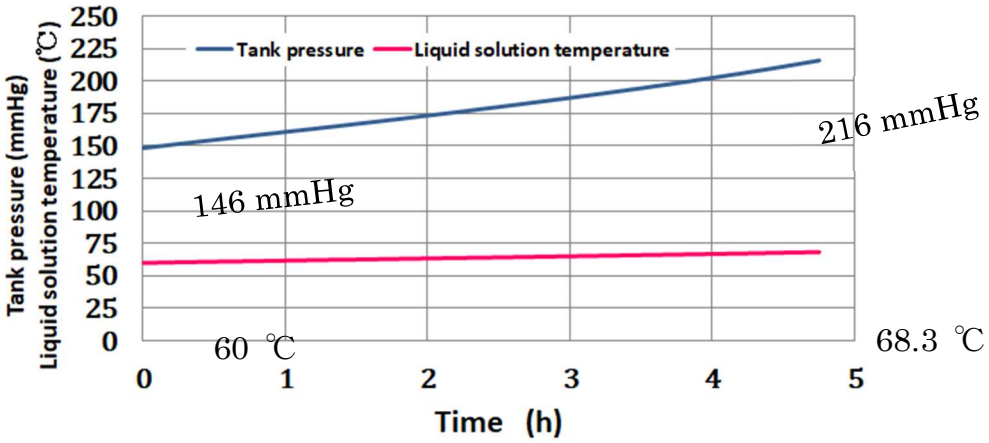

Fig.24.3-E1 Temporal variation of pressure and solution temperature in evaporator tank.

As shown in the figure, it has been found that the process time required for concentrating the solution from 10 to 90wt% is 4.75 h.

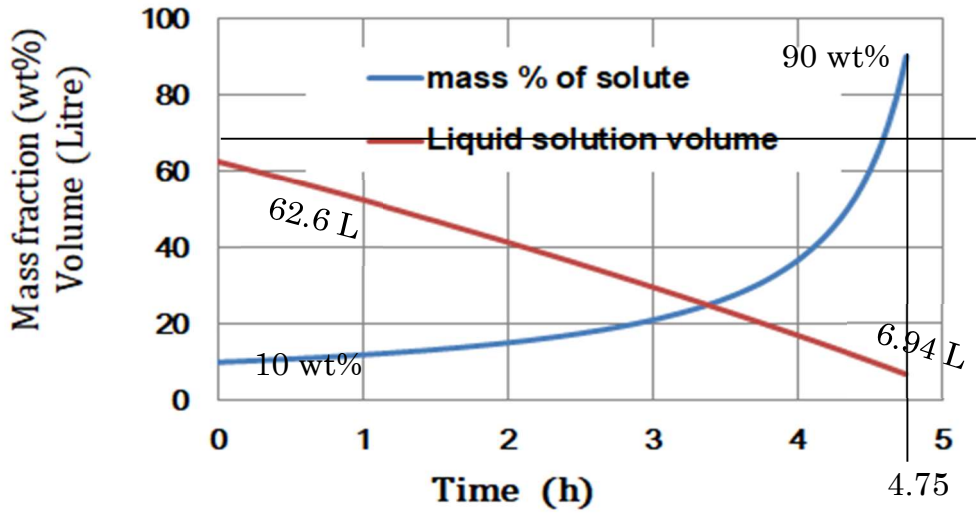

Fig.24.3-E2 Temporal variation of mass concentration and liquid solution volume.

The rate of energy saving is plotted taking into account the vacuum pump efficiency and the electric power generation efficiency in Fig.24.3-E3.

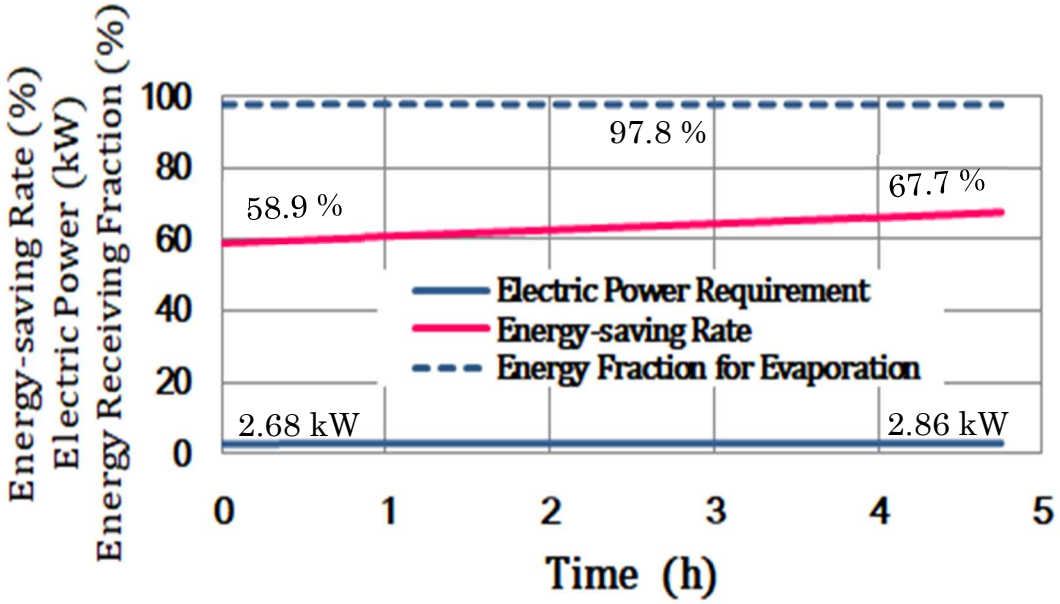

Fig.24.3-E3 Temporal variation of the energy-saving rate, the electric power requirement, and the energy fraction consumed for evaporation.

Under an assumption of 30% as the total efficiency of the vacuum pump, it has been found that the very large rate of energy saving by the VRC method is attained in between 58.9 and 67.7% for 4.75 h.

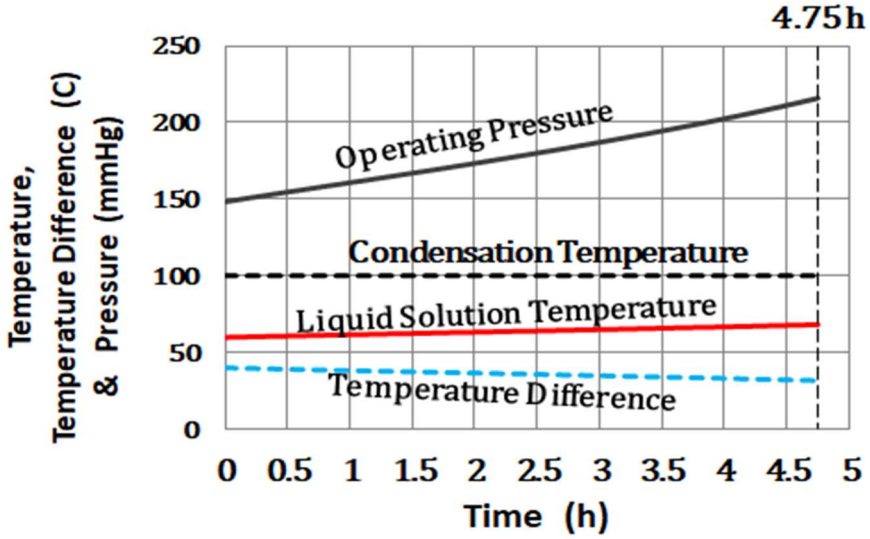

Fig.24.3-E4 Temporal variations of liquid solution in the tank, operation pressure, and the temperature difference as the driving force.

The condensation temperature in the jacket is kept at 100℃ at 1 atm.

The electric power required for the vacuum pump varies gradually from 2.68 to 2.86 kW during the process time (4.75 h).

The fraction of thermal energy consumed for evaporation is constantly maintained at 98% during the whole operation time. This implies that the remaining fraction comes from heat loss and heat requirement for the evaporator construction system.

As the operating pressure of the tank side is gradually raised by the vacuum pump, the boiling temperature of the liquid solution is very slowly raised.

It should be kept in mind that a small rate of makeup steam 0.846 kg/h is required for the energy deficit of evaporation latent heat.

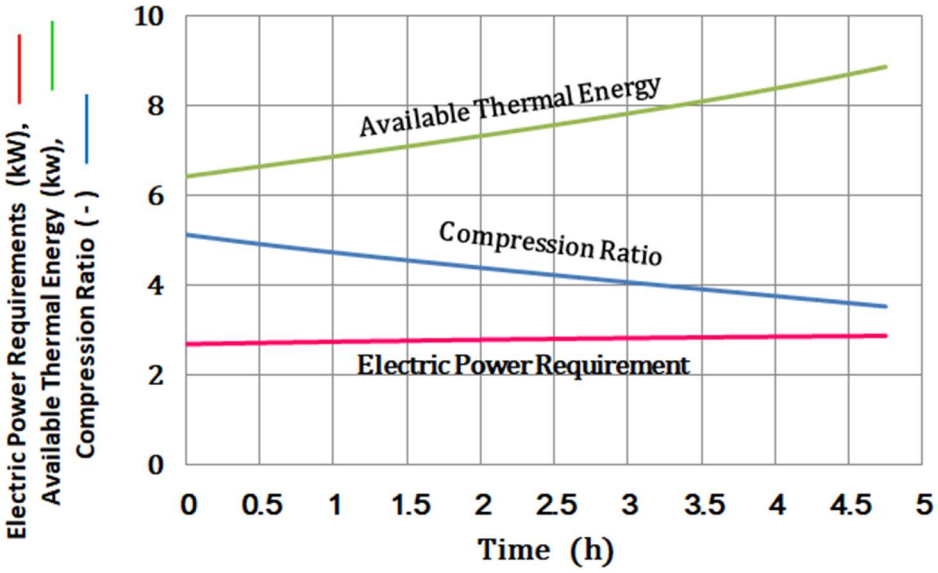

Fig.24.3-E5 Temporal variations of power requirement with available thermal energy

It is practically important to consider the fraction of the thermal energy used for evaporation of the liquid solution in the total thermal energy transferred from the jacket to the tank side.

Although no elevation of boiling point due to the concentrated solute in this condition is assumed, the rate of evaporation and the evaporation temperature are a little bit rising gradually with the operation pressure rise.

The theoretical work for isentropic compression of vapor by a screw-type vacuum pump varies slowly from 7.0 kW through 6.2 kW during the evaporation time.

The detailed explanation of calculation results is omitted here but the heat loss and the injected makeup water amount to 0.08% and 0.41%, respectively for the overall energy requirement.

The fraction of the energy saving rate amounts to 54.7 % if the efficiency of the vacuum pump is assumed to be 30%.

The contribution to the evaporation rate of the concentrated solution by the condensate drain in the jacket becomes 3.1% only.

You can understand that this is a good example for energy-saving of the batch evaporator by using a heat pump idea.

As the second law of thermodynamic law states, heat energy naturally transfers from warmer places to colder spaces. However, a heat pump can reverse this process, by absorbing heat from a cold space and releasing it to a warmer place. Therefore heat is not conserved in this process and requires some amount of energy such as electricity from the outside. In heating, ventilation and air conditioning (HVAC) systems, the term *heat pump* usually refers to vapor-compression refrigeration devices optimized for high efficiency in both directions of thermal energy transfer. These heat pumps can be reversible, and work in either direction to provide heating or cooling to the internal space. Most of the energy for heating comes from the external environment, only a fraction of which comes from electricity (or some other high-grade energy source required to run a compressor). In electrically-powered heat pumps, the heat transferred can be three or four times larger than the electrical power consumed, giving the system a coefficient of performance (COP) of 3 or 4, as opposed to a COP of 1 for a conventional electrical resistance heater, in which all heat is produced from input electrical energy.

Heat pumps use a refrigerant as an intermediate fluid to absorb heat where it vaporizes, in the evaporator, and then to release heat where the refrigerant condenses, in the condenser. The refrigerant flows through insulated pipes between the evaporator and the condenser, allowing for efficient thermal energy transfer at relatively long distances.

24.4 Energy Saving by Heat Integration in a Distillation System

24.4-1 Principle of internally heat integrated distillation column (HIDiC)

A configuration of internal heat integration method originally proposed by Mah et al.[1)] and Fitzmorris and Mar[2)] for the continuous distillation system of a single column is given by Fig.24.4-1.

The concentric double-tubed HIDiC system consists of an inner column serving as the rectifying section and a concentric outer column serving as the stripping section. The vapor from the top of the stripping section is compressed into the bottom of the rectifying section by a compressor.
The internal heat integration takes place as the transfer of heat from the high-pressure and high-temperature rectifying section to the low-pressure and low-temperature stripping section. Therefore the liquid flow rate in the stripping section is decreased in the downward direction by partial vaporization of the internal reflux liquid flowing down due to the heat input from the rectifying section. This effect results in the big decrease in the heat duty of the bottom reboiler. At the same time, the vapor flow rate in the rectifying section is decreased in the upward direction by partial condensation of the internal vapor flowing upward due to the heat transfer to the stripping section. This effect results in the big decrease in the cooling duty of the overhead condenser. This suggests the great reduction of the external reflux.

One advantage of HIDiC is that HIDiC can be operated at significantly low compression ratio (pressure ratio of the rectifying to stripping sections) as compared to a conventional heat pump system such as the vapor recompression. In addition, if the thermal design is improved, the HIDiC column could be made much lower in column height than normal columns.[3)]

1) Mah, R. S. H., Nicholas, Jr., J. J., Wodnik, R. B.: Distillation with Secondary Reflux and Vaporization. A Comparative Evaluation, *AIChE Journal*, Vol.23, 6521-658 (1977).
2) Fitzmorris, R. E. and Mar, R. S. H.: Improving Distillation Column Design Using Thermodynamic Availability Analysis, *AIChE Journal*, Vol.26, 265-273 (1980).

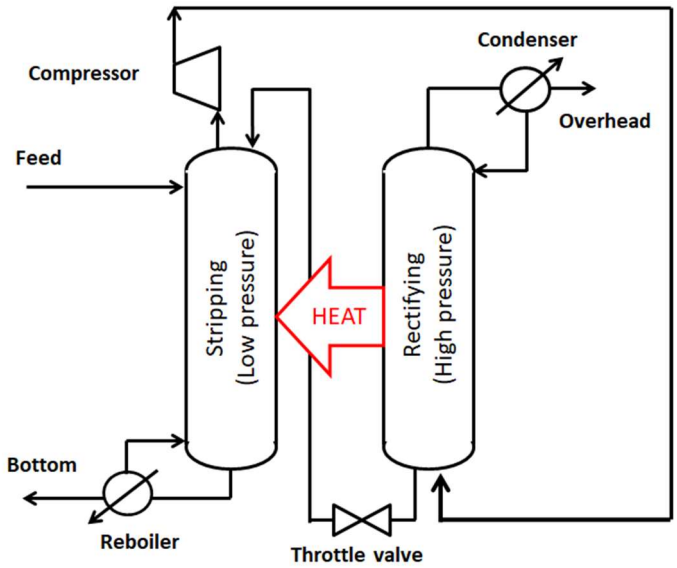

Fig. 24.4-1 Basic configuration of a single column HIDiC system

The partial condensation of the vapor flowing upward occurs at temperature T_{Rj} at the jth stage of the rectifying section, whereas the partial vaporization of the liquid flowing downward occurs at temperature T_{Si} at the ith stage of the stripping section.

The overall heat transfer coefficient can be defined as shown in Fig.24.4-2. For convenience, the fictitious heat transfer area A_i is defined as the surface area of the partition wall corresponding to one tray-to-tray spacing. However it is very difficult to estimate the area of the partition wall that causes vapor condensation in the rectifying section and liquid vaporization in the stripping section. In addition, usually for effective effect of heat transfer, the stages of the rectifying section and the stripping section are piled up in stagger arrangement: the condensing area on the jth stage of the

rectifying section is located at the same height with the evaporating bubbling layer on the i[th] stage of the stripping section.

3. De Rijke, A., Development of a concentric internally heat integrated distillation column (HIDiC), Ph.D. Dissertation, (2007)

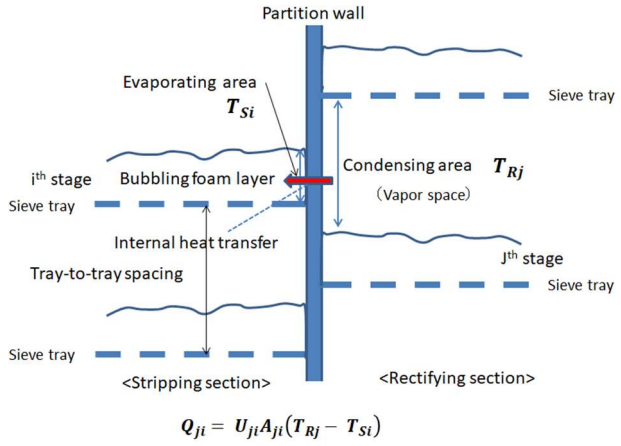

Fig.24.4-2 Internal heat exchange between the rectifying and stripping sections in a HIDiC trayed distillation column

24.4-2 Operation modes of HIDiC

The internal heat transfer is controlled by the pressure ratio P_R/P_S between the rectifying and stripping sections. In relation to the boiling points of volatile components for distillation, as shown by Fig.24.4-3, there are two operation modes possible: (1) Pressurized mode and (2) Depressurized mode.

(1) Pressurized mode ($P_R > 1$ atm & $P_S = 1$ atm) is operated by a compressor while (2) Depressurized mode ($P_R = 1$ atm & $P_S < 1$ atm) is operated by a dry vacuum pump.

In particular, a fouling problem may arise in the stripping section as well as in the bottom reboiler. Therefore if it is necessary to lower the boiling points, the depressurized mode is recommendable.

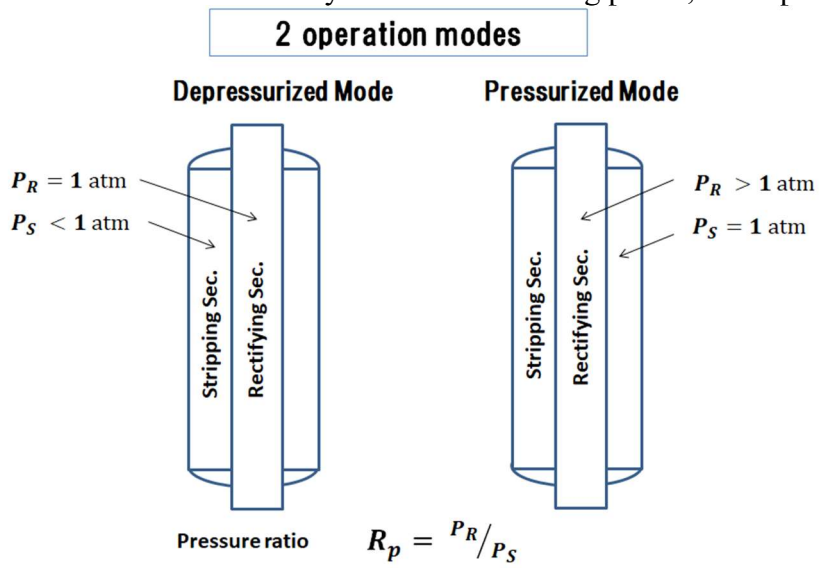

Fig.24.4-3 Two operation modes for single column HIDiC systems

24.4-3 Heat transfer characteristics of a trayed-column HIDiC system

For reference, some experimental data of internal heat transfer characteristics observed by a single concentric HIDiC column are introduced here.

Fig.24.4-4 shows the experimental distillation column consisting of concentric double-tube trayed column.

The column structure with dimensions was given as follows:

Inner column diameter = 508 mm OD, outer column diameter = 800 mm ID

Tray: Lift Tray

The tray-to-tray spacing was 400 mm

Heat transfer area $3.97\ m^2$

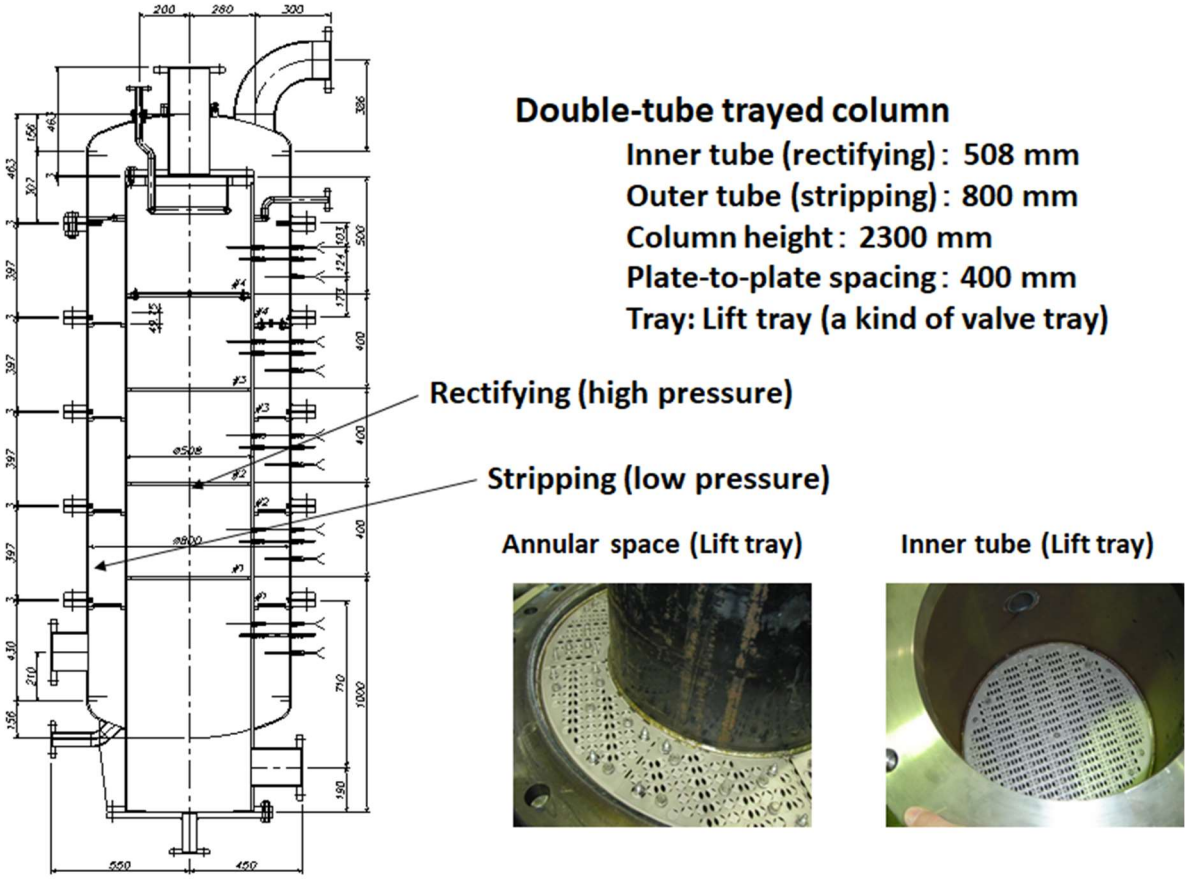

Fig.24.4-4 Experimental apparatus obtaining HIDiC heat transfer data

As can be seen from Fig.24.4-2, because of very complicated phenomena occurring on both sides, it is not easy to determine the internal heat transfer from the rectifying section to the stripping section.

Only for simplicity, the overall heat transfer coefficient is defined as

$$U_{ji} = \frac{Q_{ji}}{A_{ji}(T_{Rj} - T_{Si})} \qquad (24.4\text{-}1)$$

where the heat transfer area A_{ji} is defined as the cylindrical surface area of the inner tube given by one plate-to-plate spacing L_{pp} :

$$A_{ji} = \pi D_{io} L_{pp} \qquad (24.4\text{-}2)$$

The distillation experiment for the pressurized and depressurized modes was conducted by using two kinds of binary systems: (1) benzene-toluene system and (2) ethanol-water system.

Both experiments were conducted under the following two conditions: (1) $P_R > 1$ atm & $P_S = 1$ atm for the pressurized mode and (2) $P_R = 1$ atm & $P_S < 1$ atm for the depressurized mode.

The experimental data of internal heat transfer are shown for benzene-toluene binary system in Figs. 24.4-5 & 24.4-6 and for ethanol-water system in Figs.24.4-7& 24.4-8, respectively.

The temperature differences between the rectifying to the stripping section averaged over the column height increases linearly with the pressure ratio. This must be due to the boiling point rise with pressure.

The overall heat transfer coefficients averaged over the column height slightly decrease with the pressure ratio. This can be considered to be due to the change in the physical properties such as viscosity and thermal conductivity of the two countercurrent flows in the rectifying and stripping sections.

The heat flux between the rectifying and stripping sections also increases almost linearly with the pressure ratio P_R/P_S mainly owing to the boiling point rise with the increasing pressure.

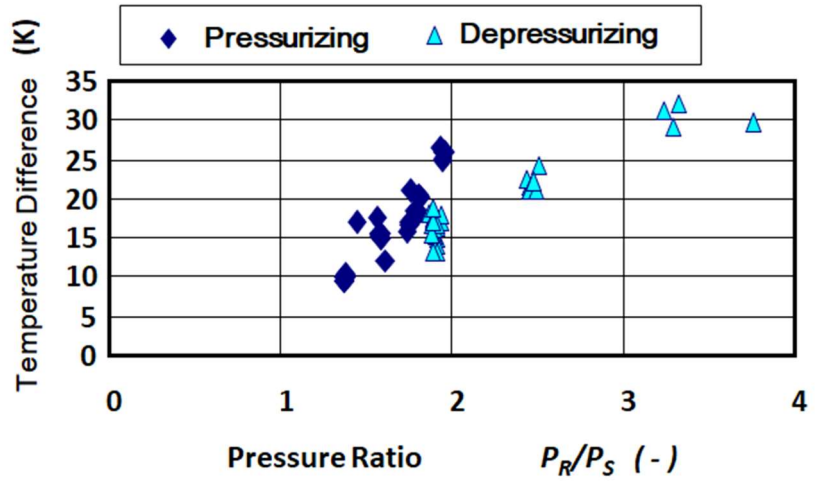

Fig.24.4-5 Variation of experimental temperature difference with pressure ratio for benzene-toluene system

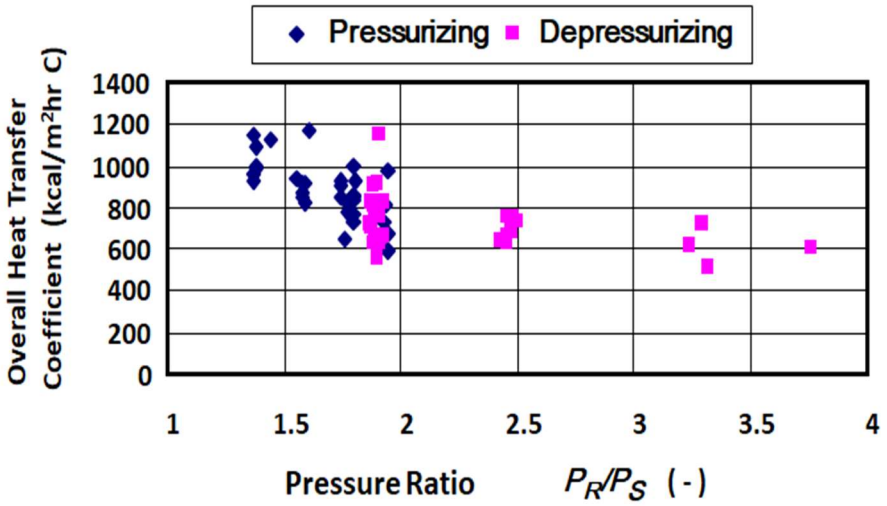

Fig.24.4-6 Variation of overall heat transfer coefficient with pressure ratio for benzene-toluene system

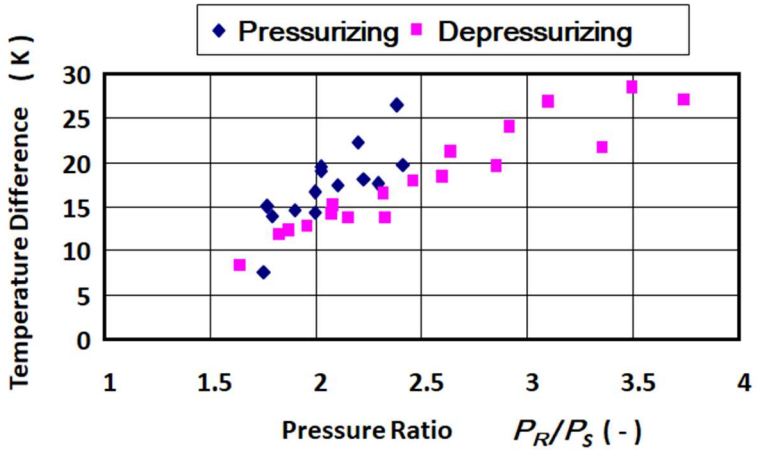

Fig.24.4-7 Variation of experimental temperature difference with pressure ratio for ethanol-water system

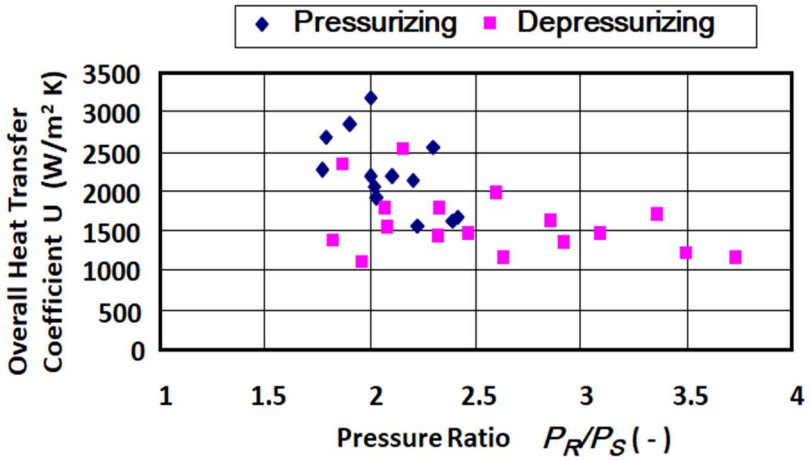

Fig.24.4-8 Variation of overall heat transfer coefficient with pressure ratio for ethanol-water system

It can be considered that the overall heat transfer coefficients are larger for ethanol-water system than for benzene-toluene system.

24.5 Application of HIDiC Technology

24.5-1 HIDiC system applied for a bioethanol distillation process[1)]

A concentric HIDiC system of a single trayed column was developed for dehydration process in the production process of ethanol from non-food biomass. It is very serious problem that the fermented mash liquid (6 wt% ethanol) to be fed still contains various fouling substances such as proteins and carbohydrates even after filtration. Therefore in order to prevent the stripping section and bottom reboiler from becoming fouled, this bench plant places the stripping section inside as the inner column and the rectifying section outside as the outer column. In addition to that, the operating pressure of the stripping section is lowered to 225 mmHg by a dry vacuum pump while the rectifying section is

operated at normal pressure. If the stripping section temperature is raised above 100 ℃, the deposition of solidified substances by Maillard reaction occurs on the inside heat transfer surface of the stripping section. For easy cleaning and maintenance, an actual double-tube HIDiC plant should have the stripping section placed inside as the inner column.
From the same reason, the steam distillation supplying live steam should be used instead of a bottom reboiler. Taking into account that non-volatile substances do not usually invade the rectifying section, which is equipped with structured packings.

On the basis of the process simulation results obtained by a commercial simulator package based on an algorithm of equilibrium-stage model, a HIDiC bench plant was designed for producing an overhead product of > 90 wt% ethanol from 50 kg/h of fermented mash (5 wt % ethanol).

The flow sheet is shown in Fig.24.5-1.

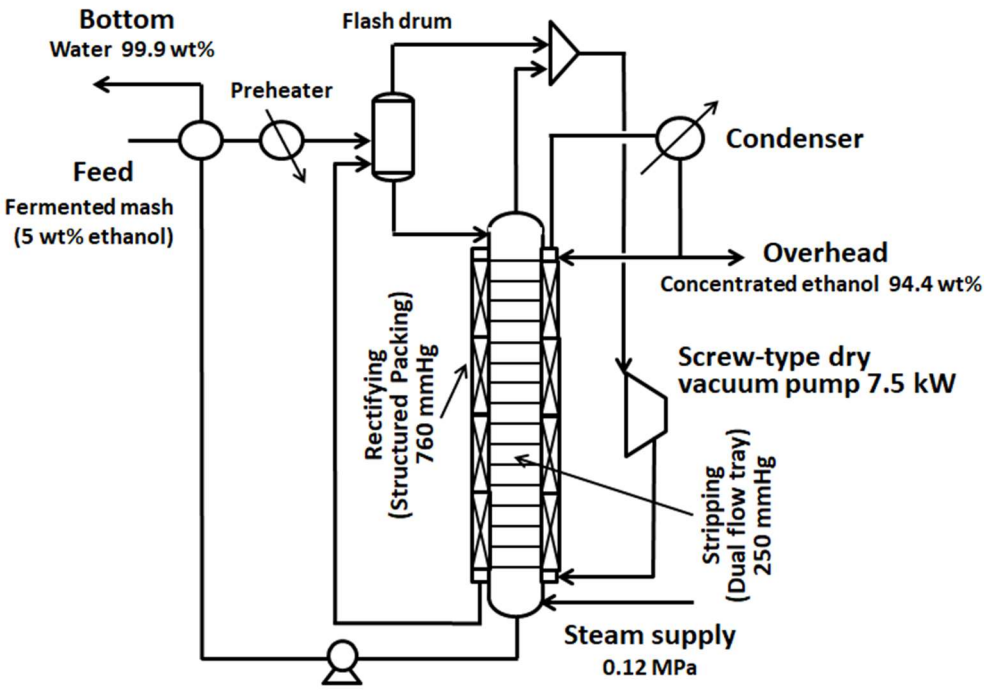

Fig.24.5-1 Flow sheet of the HIDiC bench plant

The rectifying section is kept at normal pressure. A dry vacuum pump is necessary to keep the pressure of the stripping section lower than 250 mmHg. The stripping section is equipped with dual-flow Lift Trays inside with no downcomer while the rectifying section is filled with structured packing. To avoid fouling, the bottom of the stripping section has a nozzle for live steam supply instead of a bottom reboiler.

24.5-2 Test operation of a HIDiC bench plant

This bench plant successfully recovered 95.4 % of the ethanol in the feed, gave an ethanol concentration in the overhead product of 94.4 wt%, and left only 0.024 wt% ethanol in the bottom of the stripping section. Owing to the azeotropic solution, the ethanol concentration of the overhead product amounted to 94.4 wt% a little bit lower than the azeotropic concentration 95.5 wt%.

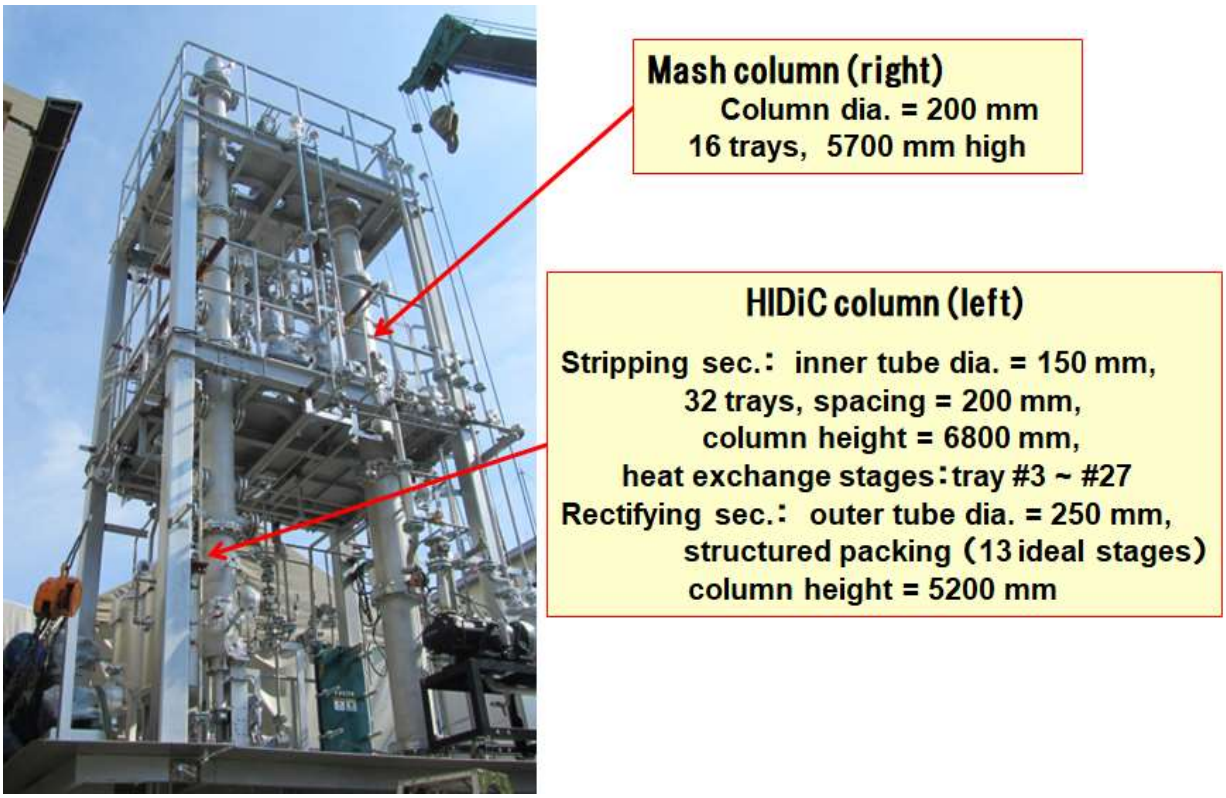

Fig.24.5-2 HIDiC distillation bench plant for bio-ethanol dehydration

1) Kataoka, K/., Noda, H., Mukaida, T., Nishimura, G., and Yamaji, H.: Boost to Bioethanol Distillation by Internal Heat-Integrated Distillation Column (HIDiC), *Advanced Chemical Engineering Research*, Vol.3, 48-57 (2014).

The depressurizing mode of operation should be used to prevent the stripping section from becoming fouled due to the Maillard reaction. In addition, the bottom reboiler also has the same problem.

The fouling test shown in Fig. 24.5-3 suggests that when the stripping section is operated at normal pressure (0.1 MPa), the boiling point goes beyond 100℃ and the fermented mash is scorched due to Maillard reaction. As can be seen from the right photo, the Maillard reaction can be suppressed if operated at 235 mmHg.

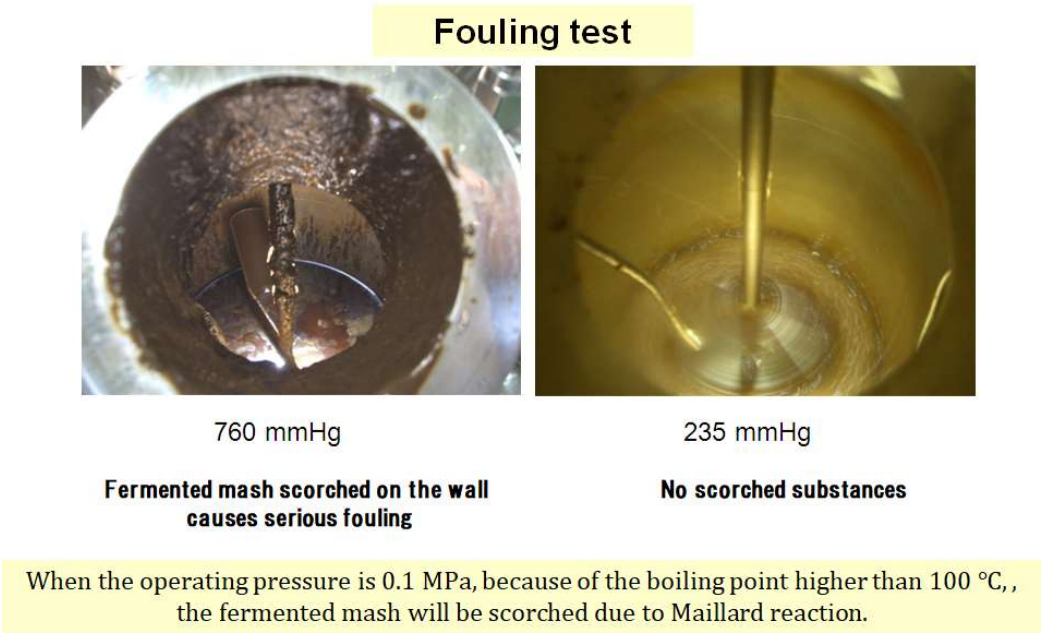

Fig.24.5-3 Fouling test examining the fermented mash scorching due to Maillard reaction

A live steam is supplied into the bottom of the stripping section instead of a bottom reboiler for a prevention against fouling. Fortunately, there was no need for supplying live steam under the condition of optimal operation for energy saving. This means that the total energy consumed by the HIDiC distillation plant amounts to the work requirement of the dry vacuum pump only.

Fig.24.5-4 is a test operation result of the HIDiC bench plant designed for dehydration process of the fermented bio-ethanol liquid mash which is filtrated in advance.

The energy rate 2.86 MJ/L- ethanol consumed in the dehydration process for producing 1 L ethanol can be considered to be sufficiently small in comparison with the thermal energy for combustion of 1 L ethanol 23.4 MJ/L-ethanol.

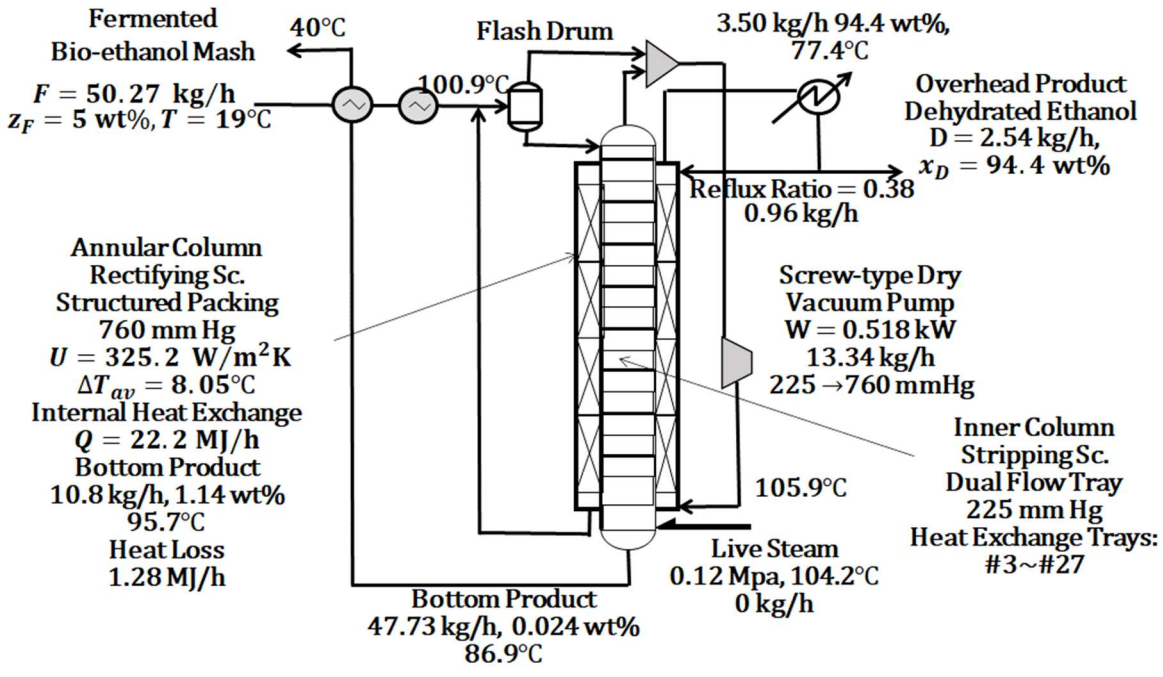

Fig.24.5-4 Test operation result of HIDiC bench plant for dehydration of fermented bio-ethanol mash

It is necessary to take into account the practical electric generation efficiency in power plant in order to evaluate the energy requirement of the compressor.

If we compare this HIDiC system in energy requirement with a conventional dehydration system in the same condition, we obtain by calculation as

$$E_s = \frac{E_{con} - E_{HIDiC}}{E_{con}} \times 100 = 68\ \%$$

[PROBLEM 24.5-1]

Explain qualitatively in the above HIDiC bench plant how the energy consumption rate changes if the ethanol concentration z_F of the fermented bio-ethanol mash becomes higher than 5 wt%.

Nomenclature

A	heat transfer area, [m^2]
A, B,C	Antoine constant
C_{op}	coefficient of performance, [-]
Cp	heat capacity, [J/kmol K]
D	overhead product, [kmol/s]
E_s	energy saving rate, [%]
F	feed rate, [kmol/s]
$H_X,\ H_Y$	specific enthalpy, [J/kmol]
h	heat transfer coefficient, [W/m^{2}K]
L	mass of solution, [kg]
Lpp	tray-to-tray spacing for trayed column, [m]
m	slope of equilibrium curve, dy/dx,
P_R	pressure ratio, [-]
Q	heat input, [J] or [W]
Q'	surplus energy by heat pump, [W]
r	reflux ratio, [-]
R	resistance to heat flow, [m^{2}K/W]
Re	Reynolds number, [-]
Sc	Schmidt number, [-]
T	temperature, [K]
t	time, [s]
U	overall heat transfer coefficient, [W/m^{2}K]
v	specific volume, [m^3/kg] or [m^3/kmol]
$-W_C$	theoretical work of compressor, [W]
x_A, y_A	mole fraction of more-volatile component A, liquid- and vapor-phase, [-]
δ	film thicknesses for heat transfer, [m]
λ	latent heat of evaporation, [J/kg]
κ	thermal conductivity. [w/m K]
μ	viscosity, [kg/m s]

Subscripts

B	bottom
c	condenser or condensation
D	overhead
ev	evaporation
F	feed
fl	vapor film
o	outside surface
r	rectifying sec. or reboiler
s	stripping sec.
sol	solution

CHAPTER 25
TRANSFER MODEL FOR DESIGN OF PACKED DISTILLATION COLUMNS

We know that distillation is by far the most applied but the most energy-consuming separation technology. It is of great significance to reconsider the practical design of a real packed distillation column from a viewpoint of the characteristics of simultaneous energy and mass transfer.

There are two modeling concepts available for analyzing the packed column distillation[1)]: the ideal-stage (or equilibrium-stage) model and the rate-based transfer model. As described in Chapter 11 of Volume 1, the ideal-stage model, e.g. the McCabe-Thiele model is very simple and convenient to apply to various column design calculations. However the ideal-stage model still remains to be extended to the real interphase mass transfer in packed column distillation processes. A generalized model for distillation efficiency has not yet been constructed.

On the other hand, the rate-based model[2, 3, 4, 5)] based on the very strict nonequilibrium thermodynamic concept has to make the theoretical approach solving the differential transport equations, which rely heavily on empirical correlation data of heat and mass transfer coefficients as well as the counter-current two-phase flow conditions for various boundary conditions of the differential governing equations. Owing to the complicatedness of packed column distillation phenomena, the rate-based model is not yet so fruitful for analyzing the practical packed column distillation phenomena. In this chapter, we study the modeling of a real packed distillation column by applying the control volume method from a viewpoint of interphase mass and enthalpy transfer. In other words, we would like to construct the design concept for a real packed distillation column based not only on the equilibrium model but also on the interphase mass and enthalpy transfer model.

25.1 Modeling Concept by Control Volume Method[1,2)]

25.1-1 Definition of control volume

The control volume method[1)] is a very convenient tool for bridging the gap between the ideal column and the real column. We already studied it a little bit in Chapter 12.2 ~ 3 of PART II.

The control volume can be defined taking into consideration the interphase mass and enthalpy transfer occurring within it. As in Fig.25.1-1, the equilibrium stage of an ideal column is converted into the corresponding control volume of a real column where local HETP (i.e. the reciprocal of distillation efficiency) can be utilized as the control volume height.

You can review the definition of HETP for packed distillation columns in Chapter 12.2-2.

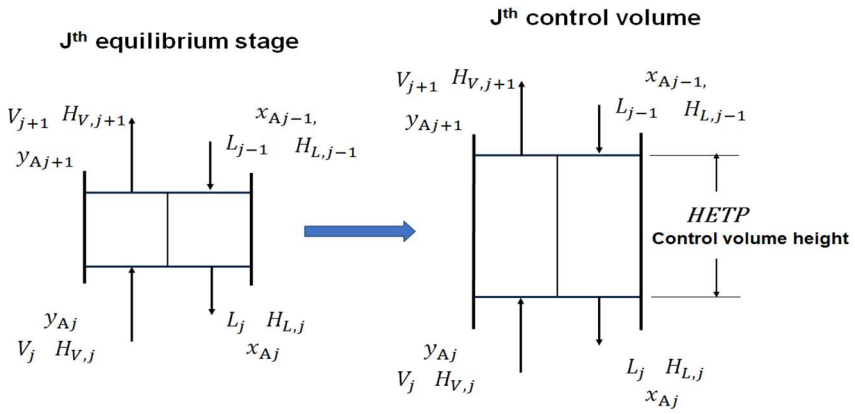

Fig.25.1-1 jth control volume corresponding to jth equilibrium stage

Figure 25.1-2 gives how to define a control volume taking into account the composition profiles within the control volume. The bulk and interface compositions should vary in the vertical direction within the control volume. From the control volume definition, the bulk compositions of the vapor and liquid y_{Aj} and $x_{Aj,}$ respectively leaving the control volume should have the equilibrium relationship: $y_{Aj} = K_{Aj}x_{Aj}$ because the jth control volume also corresponds to jth equilibrium stage having local *HETP* as the height.

The more-volatile component A gives rise to the mass transfer from liquid-phase to vapor-phase with the concentration profile of $y_A^* > y_{Ai} = m\,x_{Ai} > y_A$. The simulation analysis based on the equilibrium stage model can give the interfacial composition y_{Aij}, x_{Aij} and temperature T_j of jth control volume. In addition, as in Fig.25.1-2, we can also assume that the vapor bulk concentrations at the top and bottom of the jth control volume become respectively:

$y_{Ajtop} = y_{Aj} = y_{Aij}$ and $y_{Ajbottom} = y_{Aj+1} = y_{Aij+1}$

Therefore at the central height $z = (h_{top} + h_{btm})/2$, the vapor bulk concentration $y_{Aavj} = (y_{Aj} + y_{Aj+1})/2$ and the vapor-phase driving force of component A $y_{Aij} - y_{Aavj}$ are given for mass transfer analysis. Similarly the liquid-phase driving force becomes $x_{Aavj} - x_{Aij}$.

Then the film coefficient of mass transfer $k_{Aj}a_j$ can be calculated within the jth control volume.

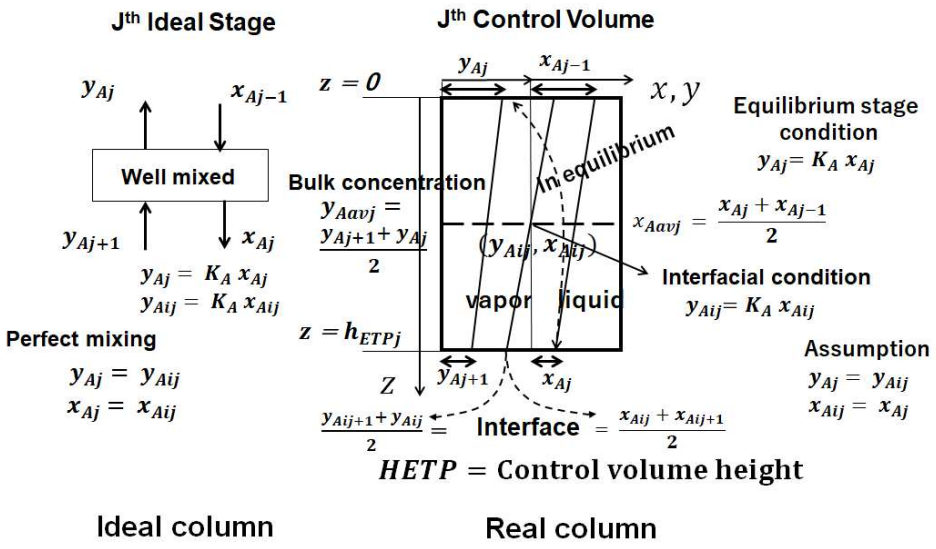

Fig.25.1-2 Definition of control volume and HETP for a packed distillation column

25.1-2 Allocation of theoretical profiles of temperature and composition

The theoretical profiles pf temperature and composition are obtained by the process simulation calculation (see Chapter 25.1-4) based on the equilibrium-stage model.

Considering similarly to the McCabe-Thiele method, as shown in Fig.25.1-3, the temperatures of the vapor phase, liquid phase, and interface T_{Vj}, T_{Lj}, T_{ij} calculated on j^{th} equilibrium stage are assigned step-by-step by the control volume method.

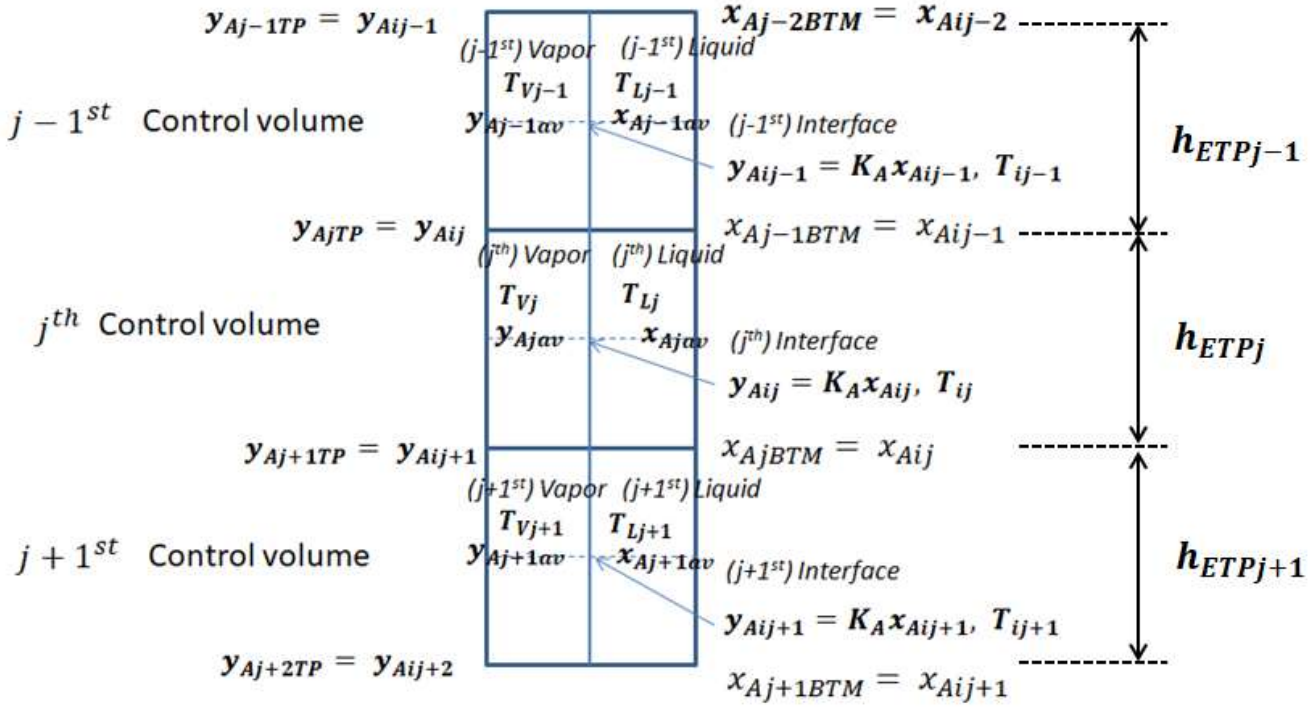

Fig.25.1-3 Allocation of vertical variation in temperature with vapor and liquid compositions

For example, at the top and bottom of the j[th] control volume corresponding to the j[th] equilibrium stage, the vapor and liquid bulk concentrations can be considered as follows:

$y_{Ajtop} = y_{Aj} = y_{Aij}$ $\quad y_{Abottom} = y_{Aj+1} = y_{Aij+1}$

$x_{Ajtop} = x_{Aj-1} = x_{Aij-1}$ $\quad x_{Abottom} = x_{Aj} = x_{Aij}$

1) Kataoka, K., Transport Process Chemical Engineering (2021), https://doi.org/10.24546/90008260
2) Nishimura, G., Kataoka, K., Noda, H., and Ohmura, N., Control Volume Approach for Modeling the Interphase Mass Transfer in a Packed Column Distillation, *J. Adv. Chem. Eng*., Vol.11, Issue 2, 1-14 (2021)

25.1-3 Definition of local film coefficients of mass and enthalpy transfer

As can be seen from the definition of j[th] control volume in Fig.25.1-4, the vapor-phase film coefficients of enthalpy and more-volatile component A accompanied with the effective vapor-liquid contacting interfacial area can be expressed as follows:

$$E_j = V_{j+1}H_{Vj+1} - V_jH_{Vj} = (h_V a)_j \left(\frac{T_{ij+1} - T_{ij}}{2}\right) h_{ETPj} \quad (25.1\text{-}1)$$

$$N_{Aj} = V_j y_{Aj} - V_{j+1} y_{Aj+1} = (k_y a)_j \left(\frac{y_{Aij} - y_{Aij+1}}{2}\right) h_{ETPj} \quad (25.1\text{-}2)$$

These equations suggest that as long as the information of a generalized correlation of HETP is available,

both the film coefficients can be determined with the calculation results of temperature and vapor composition based on the equilibrium-stage model.

Mass Transfer Coefficient of Component A

$$N_{Aj} = V_j y_{Aj} - V_{j+1} y_{Aj+1}$$
$$= (k_V a)_j (y_{Aij} - y_{Aavj})\, h_{ETPj}$$
$$= (k_j a)_j ((y_{Aij} - y_{Aij+1})/2) h_{ETPj}$$
$$y_{Aavj} = \frac{y_{Aij+1} + y_{Aij}}{2}$$

Enthalpy Transfer Coefficient

$$E_j = H_{Vj+1} V_{j+1} - H_{Vj} V_j$$
$$= (h_V a)_j (T_{Vavj} - T_{ij})\, h_{ETPj}$$
$$= (h_{Vj} a)_j ((T_{ij+1} - T_{ij})/2) h_{ETPj}$$
$$T_{Vavj} = \frac{T_{ij+1} + T_{ij}}{2}$$

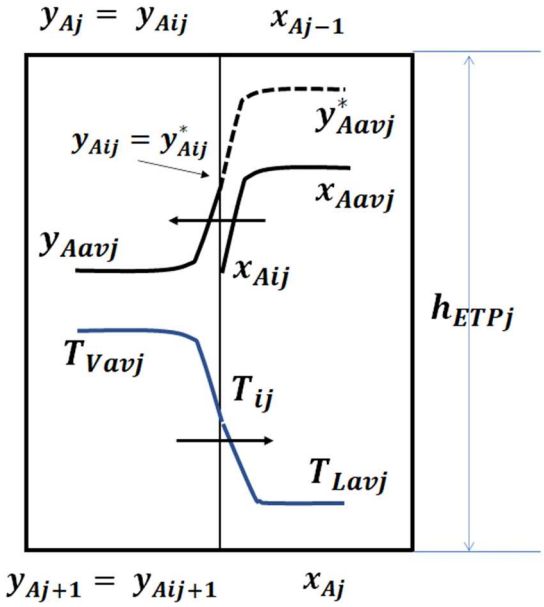

Fig.25.1-4 Definition of vapor-phase film coefficients of mass and enthalpy transfer

This indicates that the evaluation of local film coefficients of mass and enthalpy transfer needs local variation of HETPs for defining a control volume.

25.1-4 Process simulation based on equilibrium-stage model

The practical evaluation of HETP as the reciprocal of distillation efficiency is usually conducted by the distillation experiment under the total-reflux condition.

For determining local HETPs, the real column distillation experiment is collaborated with the following process simulation analysis based on the ideal-stage model. Its algorithm is consisted with the following set of equations.

Mass and enthalpy balance around j^{th} equilibrium stage under the total-reflux condition

$$M_{jk} = V_j y_{j,k} + L_j x_{j,k} - V_{j+1} y_{j+1,k} - L_{j-1} x_{j-1,k} = 0 \quad (25.1\text{-}3)$$
$$E_j = V_j H_{V,j} + L_j H_{L,j} - V_{j+1} H_{V,j+1} - L_{j-1} H_{L,j-1} = 0 \quad (25.1\text{-}4)$$

Overhead condenser (stage 1)

$$M_{1k} = L_1 x_{1,k} - V_2 y_{2,k} = 0 \quad (25.1\text{-}5)$$

Cooling duty: $Q_1 = L_1 H_{L1} - V_2 H_{V2}$ (25.1-6)

Bottom reboiler (stage N)

$$M_{Nk} = V_N y_{N,k} - L_{N-1} x_{N-1,k} = 0 \quad (25.1\text{-}7)$$

Heating duty: $Q_N = V_N H_{VN} - L_{N-1} H_{LN-1}$ (25.1-8)

Equilibrium relation

$$K_{j,k} = p_{k,sat}(T_j)/P \quad (25.1\text{-}9)$$

Vapor-liquid equilibrium condition

$$S_{j,k} = K_{j,k} x_{j,k} - y_{j,k} = 0 \quad (25.1\text{-}10)$$

Mole fraction condition of liquid composition

$$W_{x_j} = \sum_{k=1}^{m} x_{j,k} - 1 = 0 \quad (25.1\text{-}11)$$

Mole fraction of vapor composition

$$W_{y_j} = \sum_{k=1}^{m} y_{j,k} - 1 = 0 \quad (25.1\text{-}12)$$

In this calculation, the NRTL model is used to evaluate activity coefficients and physical properties of vapor and liquid of a ternary mixture ($m = 3$) such as methanol-ethanol-iso-propanol system. The specification and the operating conditions used for the process simulation are given from the experimental condition and the distillation performance data obtained.

Usually a commercial process simulator package is employed. This process simulation analysis will give local values of temperature, enthalpy, flowrate and concentration of vapor and liquid at each equilibrium stage.

1) Nishimura, G., Kataoka, K., Noda, H., and Ohmura, N., Proc. 30th European Symposium on Computer Aided Process Engineering (ESCAPE30), 1 – 6, May 24-27, Italy (2020)

25.2 Experiment of a Packed Column Distillation

25.2-1 Test column and experimental method[1)]

A generalized data base of HETPs or distillation efficiency of packed distillation columns has not yet been constructed. The distillation experiment under the total-reflux condition should be usually enforced with a test column for the practical design of a packed distillation column.

The experimental method and result of ternary system[1)] are introduced here to understand the new design concept. The packed column distillation data and calculated result introduced in this chapter come from the experimental and theoretical investigation of total-reflux distillation for a ternary system of methanol-ethanol-iso-propanol[1)].

Flow channel of structured packing (see Chapter 7.4-3)

In a packed column distillation, the liquid flows down the channel in counterflow to the vapor and spreads into thin liquid film. Therefore the vapor velocity is much larger than the liquid velocity.

It is necessary to define an equivalent diameter of a flow channel. For example, the hydraulic equivalent diameter of a structured packing of triangular cross section is defined as

(triangular cross section)

d_{eq} = 4 flow cross-sectional area/wetted perimeter $= 2B\,h/(2S + B)$ (25.2-1)

(diamond cross section)

$d_{eq} = B\,h/S$ (25.2-2)

For the structured packing having the corrugated mixed structure of triangular and diamond cross sections, the following arithmetic mean can be adopted[2)]:

$d_{eq} = B\,h/[1/(B + 2S) + 1/2S]$ (25.2-3)

where S = channel side length, h = crimp height, and B = channel base length

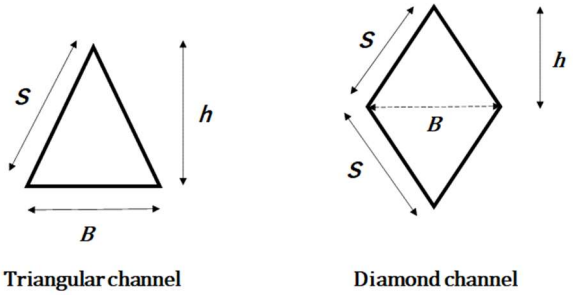

Triangular channel Diamond channel

1) Nishimura, G., Kataoka, K., Noda, H., and Ohmura, N., Control Volume Approach for Modeling the Interphase Mass Transfer in a Packed Column Distillation, *J. Adv. Chem. Eng.*, Vol.11, Issue 2, 1-14 (2021)

2) Bravo, J. L., Rocha, J. A., and Fair, J. R., Mass Transfer in Gauze Packings, *Hydrocarbon Processing*, Jan. 91-95 (1985)

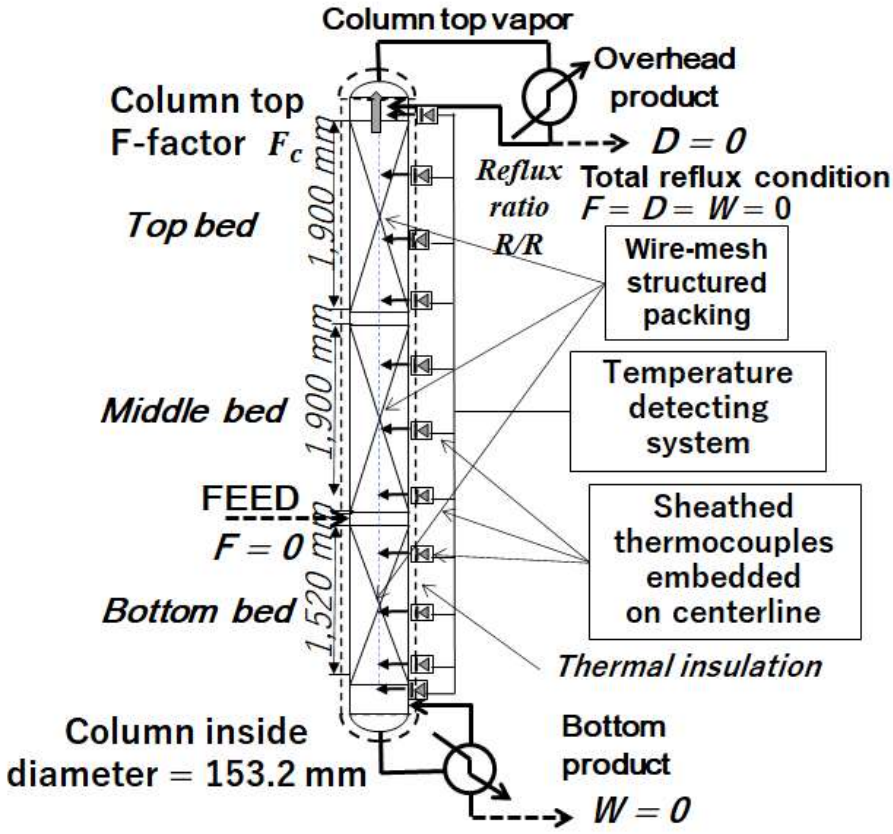

Fig.25.2-1 Experimental packed distillation column for determining local variation of HETP

Figure 25.2-1 shows an experimental packed distillation column equipped with three beds of wire-mesh corrugated structured packing stacked up in series. Those packing sections are 1,900 mm, 1,900 mm, and 1,520 mm in vertical height. The mesh-type corrugated structured packing has the hydraulic equivalent diameter $d_{eq} = 0.00625$ mm and the specific surface area $a_p = 500\ \mathrm{m^2/m^3}$.
The two empty spaces between those three beds are installed with a funnel-type liquid collector and a channel-type liquid distributor in order to avoid maldistribution of liquid stream. In the empty space above the upper edge of the top packing section, the channel-type distributor is also equipped for the reflux liquid.
The ternary system of methanol, ethanol and iso-propanol was selected as an ideal mixture. The key component methanol (the most volatile component A) was adjusted high in concentration compared with the remaining two components (component B: ethanol and C: iso-propanol). The performance data obtained by the total-reflux distillation experiment were used for the specification of the process simulation analysis. The reason why the total-reflux condition was adopted is that in a usual way for the practical design of packed columns, the HETP measurement makes it a rule to conduct the total-reflux distillation.

The primary purpose of the distillation experiment is to observe local variation of HETPs under the total-reflux condition. For that purpose, nine sets of sheathed thermocouples (wire dia.=1 mm OD) were embedded so as to locate their hot junctions just on the column centerline at an equal interval (every 475 mm in the top and middle beds and every 380 mm in the bottom bed). It was assumed that those thermocouples could measure local temperatures of internal reflux liquid because of its heat capacity much larger than the flowing up vapor. The distillation experiment was performed at normal pressure under the total-reflux conditions accompanied with 4 variables of F-factor ($F = 0.5, 1.0, 1.5, \text{and } 2.0$), i.e. by changing the heating duty of the bottom reboiler. The representative F-factors based on the superficial vapor velocity were defined at the top stage of the experimental column.

Fig.25.2-2 indicates the vertical variations in the equilibrium coefficient for each component and liquid temperature calculated by the process simulator when $F = 2.0$. All the data tend to decrease hyperbolically toward the column top.

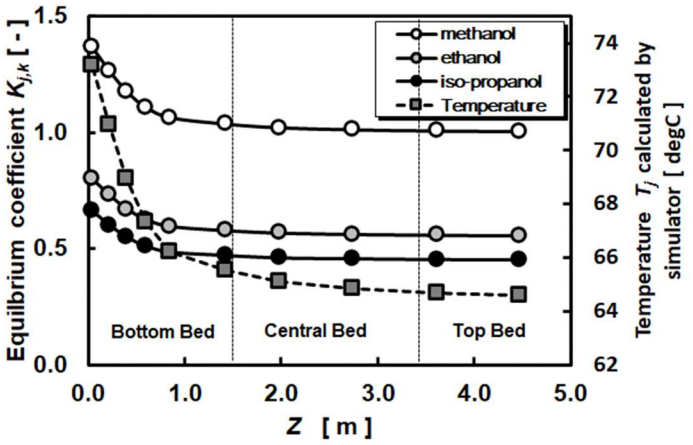

Fig.25.2-2 Vertical variations of equilibrium coefficients of ternary system and liquid temperature

25.2-2 Determination of local HETPs

It is a little bit difficult to measure local values of HETP.[1)]

Fig.25.2-3 indicates the liquid temperature measured by the embedded thermocouples compared with the liquid temperature calculated by the process simulation based on the equilibrium-stage model. Since the locations of the embedded thermocouples in the test column are known, local values of HETPs can be evaluated comparing step-by-step the theoretical temperature profiles T_n^{th} at theoretical stage n calculated for an ideal column with the experimental temperature profiles T_m^{ex} at a vertical position Z_m observed by the embedded thermocouples in a real column. The local HETP of each control volume is determined by the following equation:

$$h_{ETPj} = \frac{T_{n+1}^{th} - T_n^{th}}{T_{m+1}^{ex} - T_m^{ex}} \times (Z_m - Z_{m+1}) \qquad (25.2\text{-}1)$$

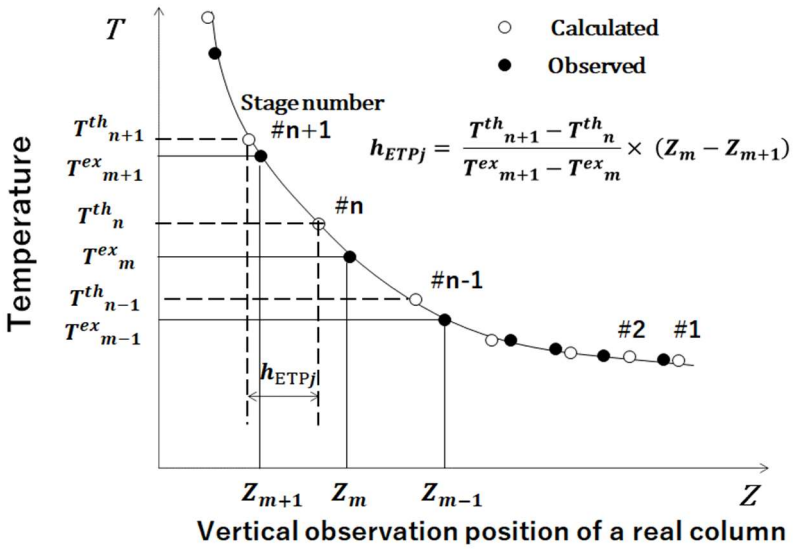

Fig.25.2-3 Comparison of the temperatures observed by thermocouples with the temperatures calculated by the process simulation based on the equilibrium stage model for determination of local HETPs

It is very important to obtain a generalized correlation model of HETPs for the practical design of packed distillation columns.

Local variation of HETPs

Fig.25.2-4 shows the experimental result of HETP obtained for the ternary system, where the observed HETPs are plotted against the dimensionless vertical height divided by equivalent diameter of test structured packing. In this figure, each run of the experiment is specified by the F-factor defined as the column top vapor flow rate.

Local values of HETP as the distillation efficiency vary largely in the vertical direction. Actually the local HETPs in a real column tend to give very large values in the upper region of the packing section, especially near the column top in the rectifying section. This suggests the necessity of observing local variation in distillation efficiency, i.e. HETP in a real packed column.

Therefore the practical design of real packed distillation columns should be constructed taking into account the local variation of distillation efficiency.

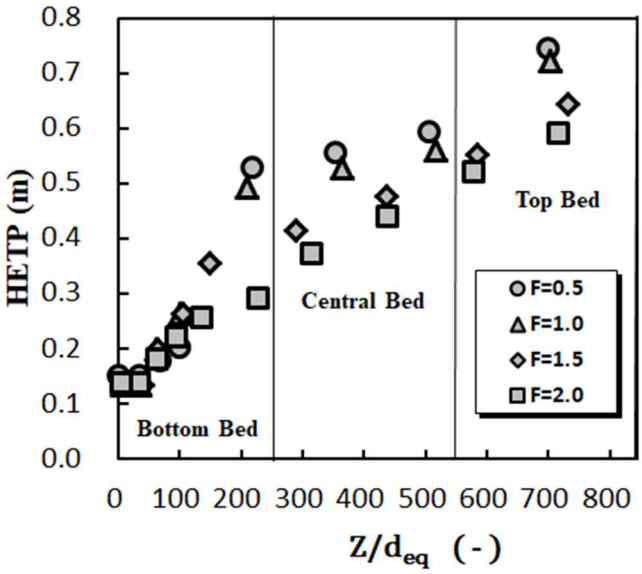

Fig.25.2-4 Vertical variation of local HETPs for ternary system

It has been found that the distillation efficiency (i.e., the reciprocal of HETP) remarkably goes down vertically upward in the packing section. This result suggests that it is possible to analyze local variation of mass and enthalpy transfer in a real packed column by utilizing those HETP data as the height of each control volume. The figure indicates that we should be careful of very low distillation efficiency near the column top in the rectifying section where the HETP becomes very large.

Variation of HETPs with vapor velocity

Judging from the correlation of Reynolds number dependency on interphase mass transfer resistance, we can conjecture that the HETPs usually decrease with increasing F-factor. Therefore for the correlation analysis of HETPs, we should consider that the HETPs are related not only with the distribution function in vertical variation but also with the F-factor defined at the leading edge (i.e. bottom) of the packing section. Here we regard the bottom edge of the packing section as the leading edge of boundary layer flow along a flat plate.

Our distillation experiment of the ternary system of methanol, ethanol, and iso-propanol gives the experimental HETPs plotted against local F-factor in Fig.25.2-5, which indicates the local variation of HETPs from bottom to top of the packing section. If these data are divided by a distribution function,

they will converge on the correlation curve obtained at the leading edge. For an example, those converged HETPs denoted by hmin (EXP) can be correlated with the F-factor at the leading edge by the following equation:

$$h_{ETP0} = \frac{0.03}{{F_0}^{0.3}+0.05} \qquad (25.2\text{-}2)$$

where F_0 is the F-factor defined at the leading edge (bottom) of the packing section.

If the h_{ETP0} is calculated by the above equation, local values of HETP can be obtained by using the following distribution function:

$$f(\zeta) = 1 + 0.7\,(\zeta + 4)^{1/2} \qquad (25.2\text{-}3)$$

where $\zeta = z/d_{eq}$ is vertical distance from the bottom of the packing section. The number 4 in the parenthesis indicates the deviation of a virtual origin of the vertical development from the leading edge.

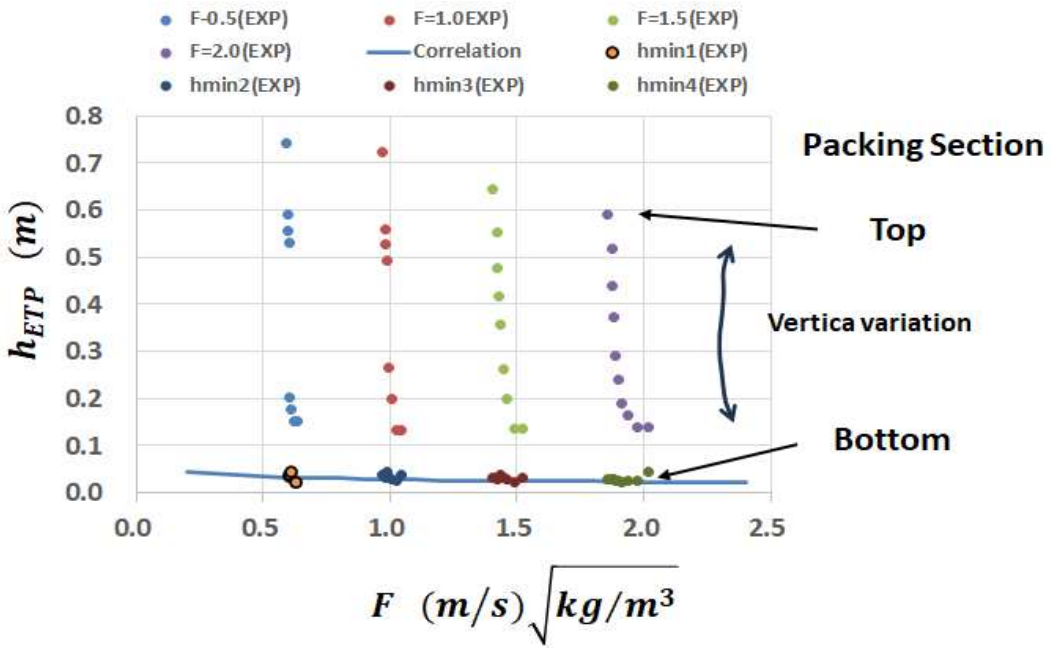

Fig.25.2-5 Experimental data of local HETPs and the HETP data converged on the correlation curve defined at bottom of packing section

As a result, local HETPs can be estimated by the following correlation equation:

$$h_{ETP} = h_{ETP0} \times f(\zeta) \qquad (25.2\text{-}4)$$

If the F-factor is given at the leading edge of the packing section, local values of HETP can be calculated by this equation. Then by means of the control volume method, we can estimate local values of vapor rate and composition, interphase mass and enthalpy transfer coefficients, and vapor and liquid temperatures and enthalpies necessary for the practical design of packed distillation columns.

If the local HETPs estimated by Eq.25.2-4 are plotted against the dimensionless vertical distance from the bottom of the packing section in Fig.25.2-6, it has been found that the vertical variation of local HETPs is similar to the streamwise variation of laminar boundary layer along a flat plate.

For this kind of conceptual consideration, we had better review the boundary layer theory in Chapter 18 (see Chapter 18.2 from page 212).

If the HETP correlation curve is expressed similarly to the boundary layer flow type functional form, the following equation can be obtained:

$h_{ETP} = 0.05 + 0.02\,\zeta^{1/2}$ (25.2-5)

This equation can be derived from streamwise development of the boundary layer thickness expressed by Eq.18.2-21 of Chapter 18.2 in PART II.

The mass transfer in the boundary layer flow indicates the similar functional form:

$Sh_x = 0.343\,Re_x{}^{1/2} Sc^{1/3}$ (18.2-38)

Here since $Sh_x = \frac{c\,k_x\,x}{D_{AB}}$ and $Re_x = \frac{v_\infty\,x}{\nu}$, $1/k_x$ becomes proportional to $x^{1/2}$.

The Reynolds number is called "length Reynolds number" which means the streamwise distance from the leading edge of the flat plate. (see Chapter 18.2)

The exponent 1/2 indicates the laminar boundary layer.

This kind of conceptual consideration is also done in Chapter 12.3 of PART II. (see on Fig.12.3-3 on p.150).

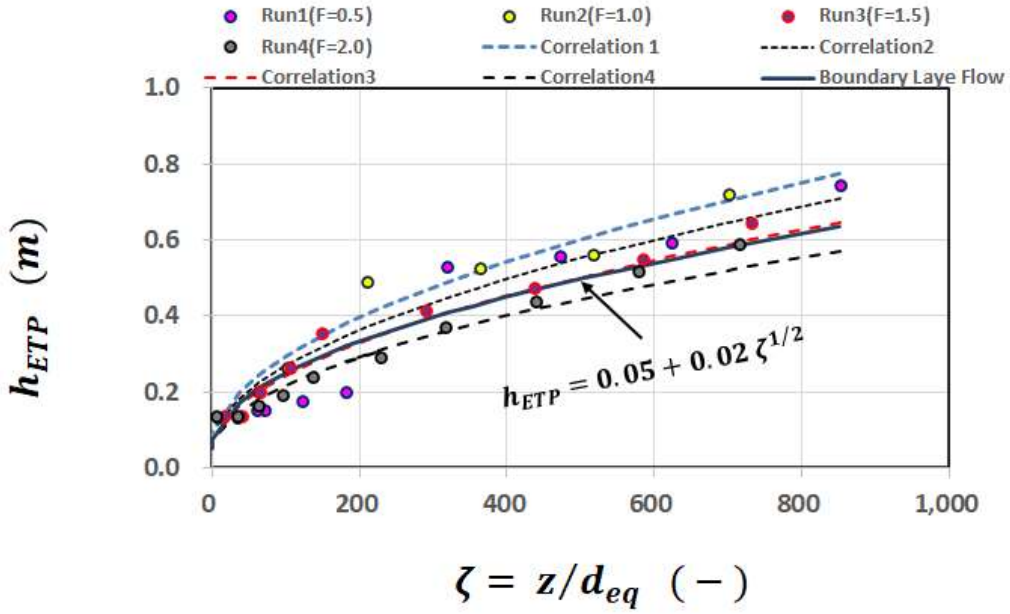

Fig.25.2-6 Boundary layer plots of local HETPs in comparison with interphase mass transfer resistance of the boundary layer flow along a flat plate.

The comparison of the packed column distillation with the boundary layer flow along a flat plate is shown in Fig.25.2-7.

The bulk vapor-phase velocity (superficial velocity) is kept almost constant similarly to the free stream uniform velocity of boundary layer flow along a heated flat plate. However as distinct from the free stream temperature of the boundary layer flow, the bulk vapor-phase temperature and composition vary in the vertical direction.

For simplified modeling the packed distillation column, we consider by separating the counter-current two-phase flow in the packing section into the vapor-phase section and the liquid-phase section. It is marvelously interesting that the inter-phase mass transfer of the simplified counter-current flow in the packing section is similar in the streamwise development to the laminar boundary layer flow along a flat plate.

1) Lockett, M. J., Easily predict structured-packing HETP, *Chem. Eng. Prog.*, Jan., 60-66 (1998)

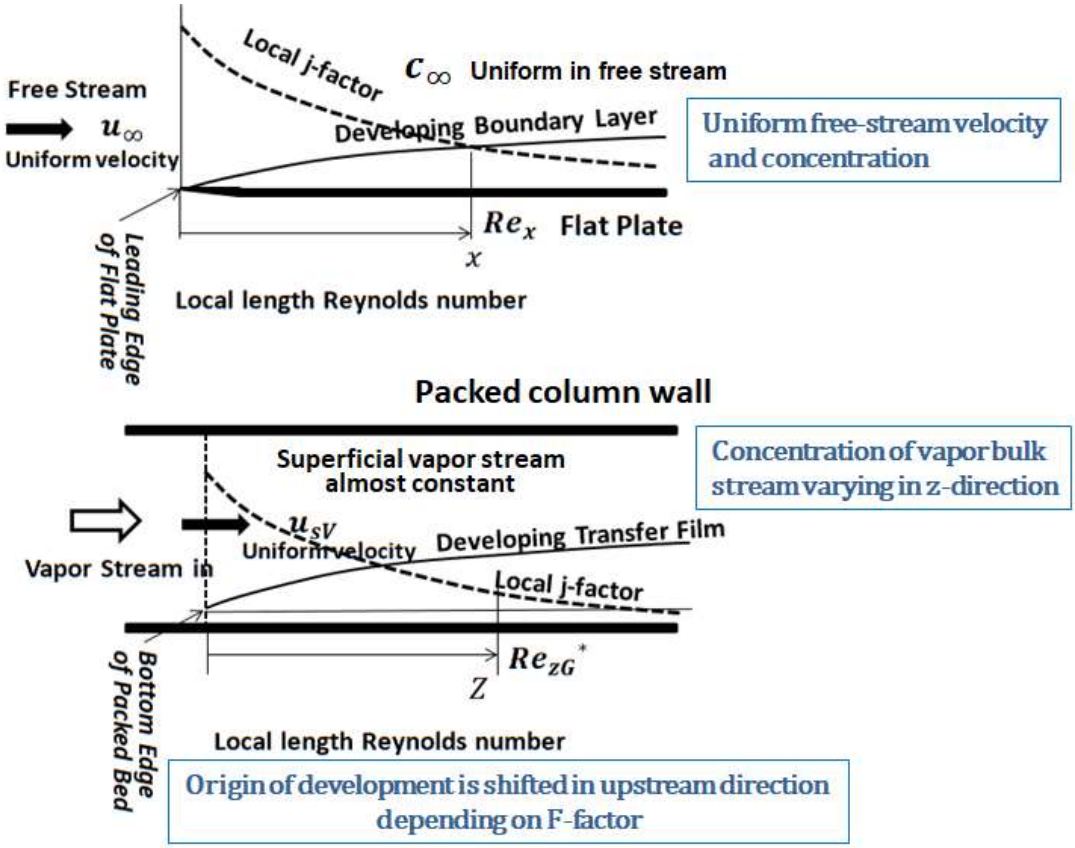

Fig.25.2-7 Comparison of packed column distillation with boundary layer flow along a flat plate.

Total height of packing section for practical design of a real packed distillation column

As indicated in Fig.25.2-8, if a generalized form of the HETP correlations is given separately in the rectifying and stripping sections, we can calculate the total height of the packed distillation column as

$$Z_T = \sum_{j=1}^{N_{REC}} h_{ETPj} + \sum_{k=1}^{N_{str}} h_{ETPk} \qquad (25.2\text{-}2)$$

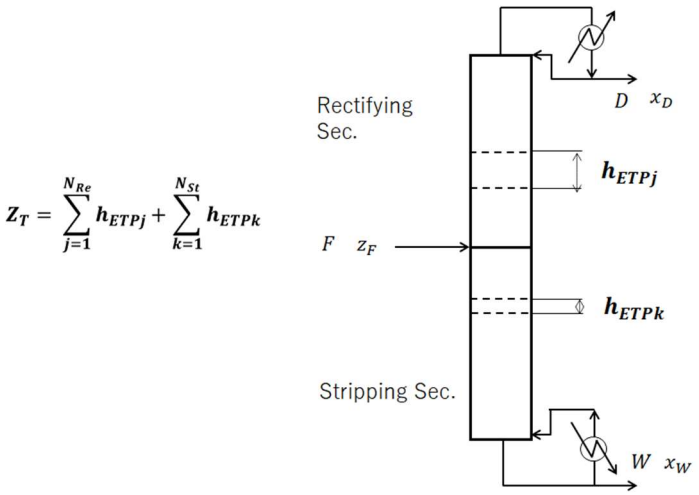

Fig.25.2-8 Calculation of total height of packing section in a real packed distillation column

For a continuous distillation process feeding the liquid mixture, the rate of the internal reflux liquid is different between the rectifying and stripping sections. Therefore, for the practical design of a real packed column operated by continuous distillation, we will have to evaluate the HETPs separately in the rectifying and stripping sections, respectively.

25.3 Correlation of Mass and Enthalpy Transfer

25.3-1 Local variation of mass and enthalpy transfer

Fig.25.3-1 shows the vertical variation in molar fluxes of the three components. For convenience, the distillation experiment of this study was conducted using the following mass balance based on the condition of equimolar counter-diffusion:

$$N_A = N_B + N_C \tag{25.3-1}$$

In this condition, the two components B and C transfer in a direction opposite to component A.

In the experimental range of three components $(x_A \gg x_B > x_C)$, the ethanol and iso-propanol components transfer together from the vapor bulk toward the interface for condensation whereas the methanol component vaporized at the position near the interface of the liquid phase transfers in the opposite direction in the vapor stream.

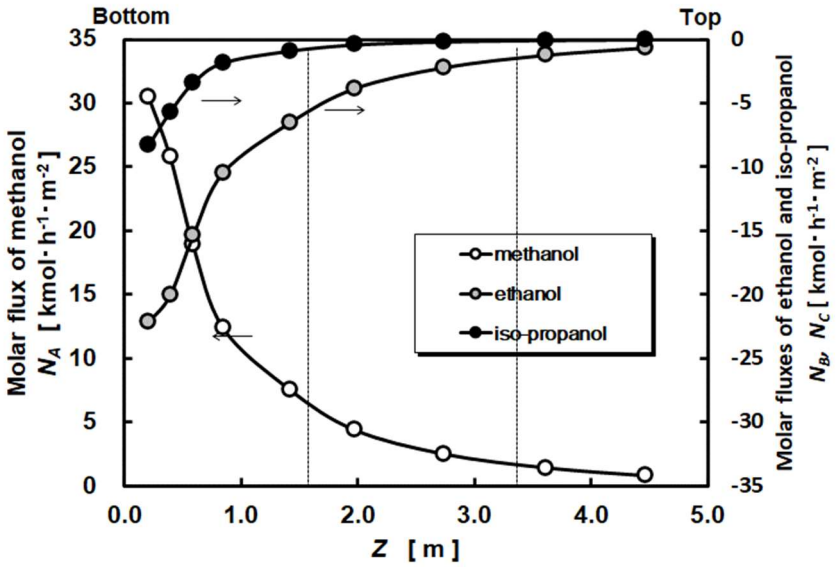

Fig.25.3-1 Vertical variation of molar fluxes of methanol, ethanol, and iso-propanol. (F = 2.0)

Fig.25.3-2 shows the overall, vapor-phase film, and liquid-phase film coefficient evaluated by the control volume analysis. This suggests that these vertical distributions can be expressed in the hyperbolic function form.

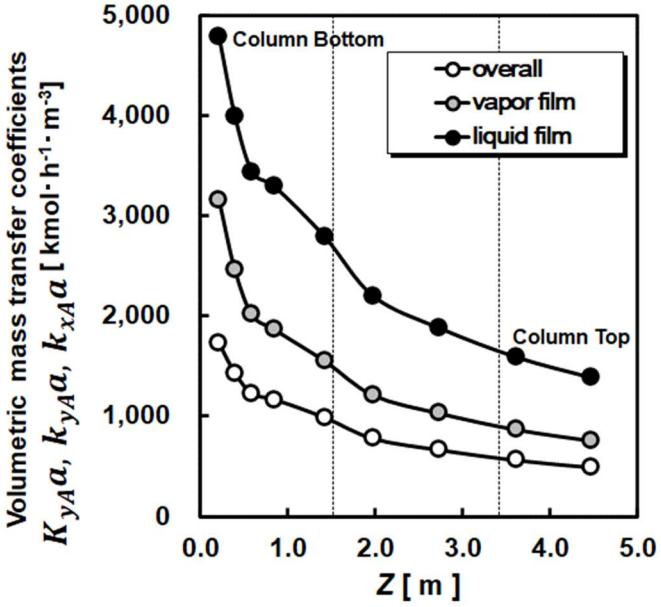

Fig.25.3-2 Vertical distribution of the overall, vapor-film, and liquid-film volumetric mass transfer coefficients ($F = 2.0$)

Similarly to the correlation analysis of local HETPs in Chapter 25.2-2, this suggests that it is necessary to construct the correlative model dividing the mass and enthalpy transfer data into the two following groups: Reynolds number dependency and vertical variation.
There are not so many experimental investigations on mass transfer in packed distillation columns.[1,2)]

1) Bravo, J. L., Rocha, J. A., and Fair, J. R., Mass transfer in gauze packings, *Hydrocarb. Process*. Jan. 91-95 (1985)
2) Kosuge, H., Matsudaira, J., and Asano, K., Ternary mass transfer in packed distillation column, *J. Chem. Eng. Jaspan*, Vol.24, 455-460 (1991)

25.3-2 Generalization of mass and enthalpy transfer correlations

We can conjecture that distillation process should make progress under the analogy between simultaneous mass and enthalpy transfers.

The following dimensionless groups are defined as

$$Nu_V = \frac{(h_V a)d_{eq}}{a_p \kappa_V} \quad \text{and} \quad Nu_L = \frac{(h_L a)d_{eq}}{a_p \kappa_L} \tag{25.3-2}$$

$$Sh_V = \frac{(k_{yA} a)d_{eq}}{a_p \rho_{mV} D_{VAB}} \quad \text{and} \quad Sh_L = \frac{(k_{xA} a)d_{eq}}{a_p \rho_{mL} D_{LAB}} \tag{25.3-3}$$

$$Re_V = \frac{\rho_V (u_{SV} - u_{SL})d_{eq}}{\mu_V} \quad \text{and} \quad Re_L = \frac{\rho_L (u_{SV} - u_{SL})d_{eq}}{\mu_L} \tag{25.3-4}$$

Here the superficial velocity difference $u_{SV} - u_{SL}$ between vapor and liquid streams can be approximated as u_{SV} because $u_{SV} \gg u_{SL}$.

In the interphase transfer of this process, the vapor-phase film exerts the rate-controlling contribution to the interphase enthalpy and mass transfer.
Therefore the generalized correlation of transfer coefficients will be described focusing the mass and enthalpy transfer through the vapor-phase film.
If you desire, the liquid-phase mass and enthalpy transfer could be treated in a similar manner.

In order to construct a simplified transfer model, all the experimental and theoretical data should be ordered separating the correlative equations into the two parts: local variation effect and the Reynolds number dependency.

$$Nu_V = a_e {Re_V}^{b_e} {Pr_V}^{c_e} f_e(\zeta_e) \quad (25.3\text{-}5)$$

$$Sh_V = a_m {Re_V}^{b_m} {Sc_m}^{c_m} f_m(\zeta_m) \quad (25.3\text{-}6)$$

where the two distribution functions $f_e(\zeta_e)$ and $f_m(\zeta_m)$ are expressed as a dimensionless vertical position from the bottom edge of the packing section in the upward direction: $\zeta = Z/d_{eq}$.

The Reynolds number dependency was analyzed as the dimensionless correlation functions giving the maximal coefficients when $f_e(\zeta) = 1$ and $f_m(\zeta) = 1$

This position should have corresponded to the bottom edge $\zeta_e = \zeta_m = 0$ of the packing section. However the leading edge position deviates to some degree ζ_0 from the bottom edge of the packing section.

Vertical distribution function of vapor-phase mass and enthalpy transfer

Fig.25.3-3and 4 indicate the two distribution functions expressed as $Sh_V/a_m {Re_V}^{b_m} {Sc_m}^{c_m}$ vs. ζ_m and $Nu_V/a_e {Re_V}^{b_e} {Pr_V}^{c_e}$ vs. ζ_e For simplification of modeling concept, we may consider one common distribution function curve indicated by dotted line.

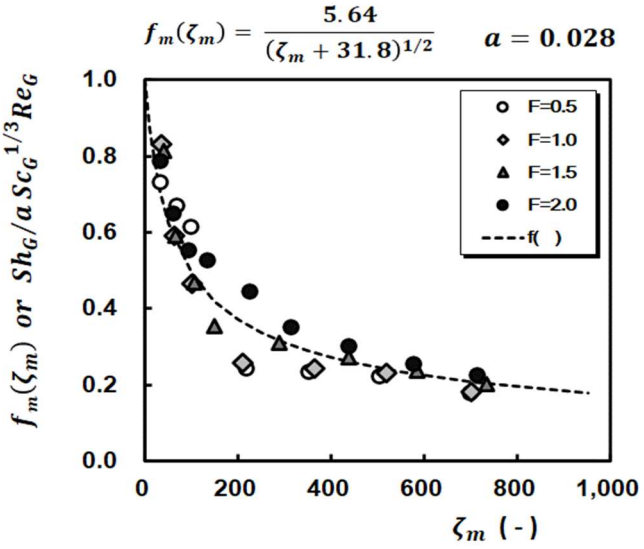

Fig.25.3-3 Distribution function for mass transfer through vapor-phase film

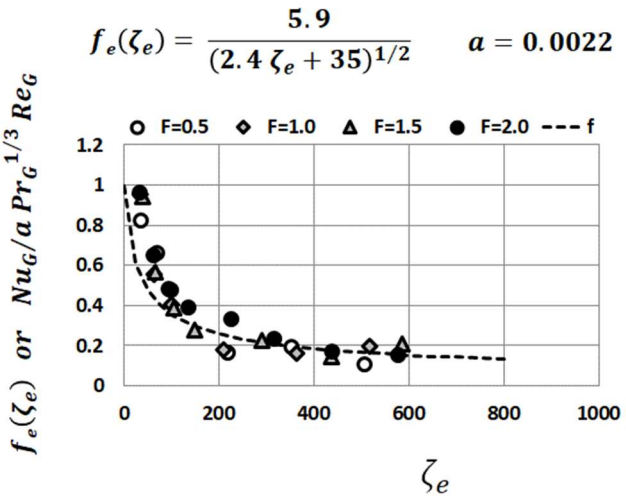

Fig.25.3-4 Distribution function for enthalpy transfer through vapor-phase film

After making trial-and-error calculations using a parameter fitting method, the following distribution functions are obtained:

$$f_m(\zeta) = \frac{5.64}{(\zeta + \zeta_0)^{1/2}} \qquad \zeta_0 = 31.8 \tag{25.3-7}$$

$$f_e(\zeta) = \frac{5.9}{(2.4\,\zeta + \zeta_0)^{1/2}} \qquad \zeta_0 = 35 \tag{25.3-8}$$

Here ζ_0 means that the fictitious origin of vertical distribution deviates downward from the lowest edge of the packing section.

It should be noticed that the local variation in HETPs (see Eq.25-2-59) is also similar to these distribution functions.

In the case of enthalpy transfer, the effect of thermal conduction going back toward vapor-upstream side below the lowest edge of the packing section seems considerably larger than expected.

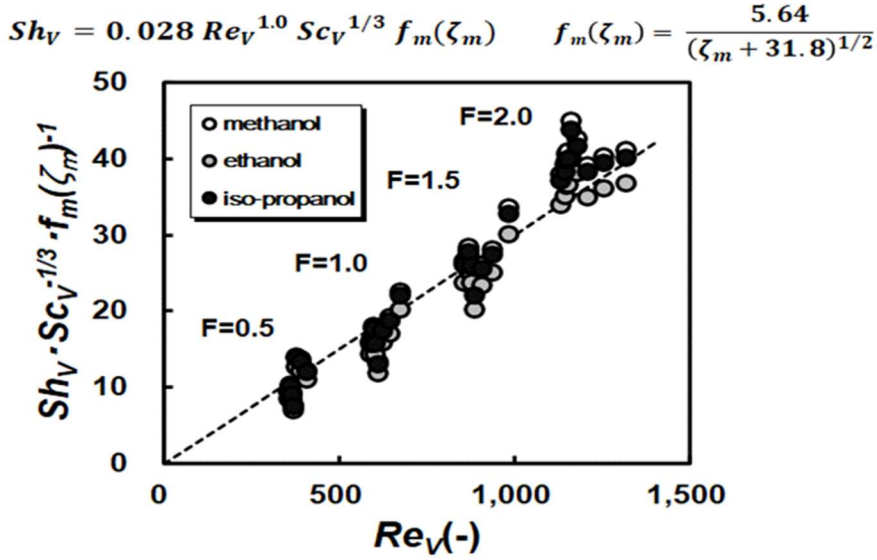

Fig.25.3-5 Reynolds number dependency of mass transfer

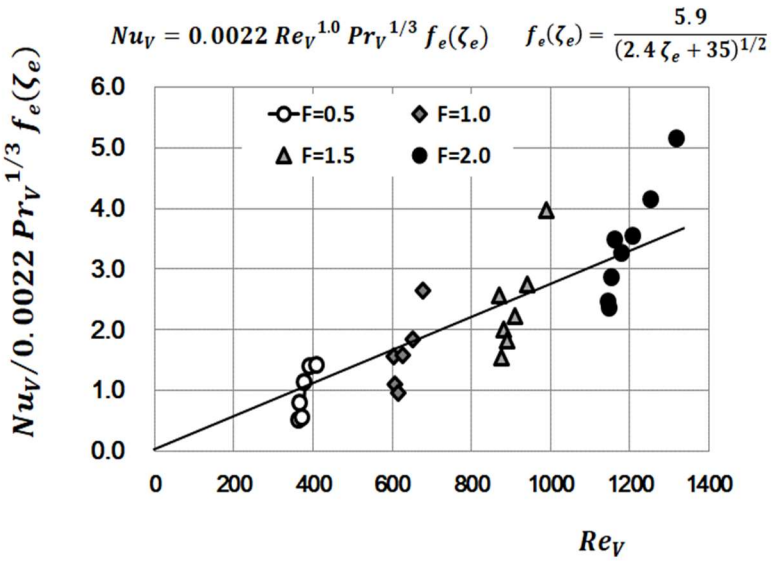

Fig.25.3-6 Reynolds number dependency of enthalpy transfer

Reynolds number dependency

Finally the following correlation equations are obtained from Figs.24.3~6 analyzing the Reynolds number dependency:

$$Nu_V = 0.0022\, {Re_V}^{1.0}\, {Pr_V}^{1/3}\, f_e(\zeta) \quad (25.3\text{-}9)$$

$$Sh_V = 0.028\, {Re_V}^{1.0}\, {Sc_V}^{1/3} f_m(\zeta) \quad (25.3\text{-}10)$$

Both the exponents of the Reynolds number given by b_m and $b_e = 1.0$ are the same as for random packings.

Regarding the vertical distribution functions, the term ζ_0 implies that the vertical origin deviates on the downside below the lowest edge of the packing section. For energy transfer, in particular, it is very difficult to prevent the leading edge of the vertical development from going up a vapor stream below the lowest edge of the packing section.

As in Chapter 12.3, the j-factor for enthalpy and mass transfer in the vapor-phaser are defined as

$$j_{HG} = \frac{Nu_V}{Re_V {Pr_V}^{1/3}} \quad (25.3\text{-}11)$$

$$j_{DG} = \frac{Sh_V}{Re_V {Sc_V}^{1/3}} \quad (25.3\text{-}12)$$

As can be seen from the functional form of the above equations, the j-factor analogy comes to existence between the simultaneous mass and enthalpy transfers. It can be interpreted as the analogy that except for conductive energy transfer, this packed column distillation makes progress with the vapor-phase mass transfer of the less--volatile component accompanied with the enthalpy transfer.

If the distillation conditions necessary for the design are given, we can start with (1) the process simulation based on the equilibrium stage model. At the next step, we determine (2) HETP variation from the generalized HETP correlation and evaluate (3) the Reynolds number dependency accompanied with the vertical distribution functions. (4) The packed column height required can be calculated by Eq.(25.2-2). (5) Local distribution of temperature, compositions, and mass and enthalpy transfer coefficients can be calculated for a real packed column.

At any rate, as a result, the practical design concept based on the control volume model expressed as Eq.(25.3-7) through Eq.(25.3-10) has been constructed. Still for that purpose, we will have to construct a generalized data bank accumulating very many experimental investigations.

For generalizing the control volume method for practical design of various packed distillation columns, systematic accumulation of many experimental data on HETP for various packings is hoped. As in Lockett article[3], there is no doubt about the dependency of the HETPs on the vapor velocity, i.e. F-factor.

3. Lockett, M. J., Easily predict structured-packing HETP, *Chem. Eng. Prog.*, Jan. 60-66 (1998)

[PROBLEM 25.3-1]

Discuss the similarity between the vertical development of simultaneous mass and enthalpy transfer in a packed column distillation and the streamwise development of the heat and mass boundary layer along a flat plate which plays a role of the mass and energy source. Assume that in the free stream outside the boundary layer, the profiles of velocity, temperature, and concentration are kept uniform.

[PROBLEM 25.3-2]

We would like to construct a test packed distillation column and treat an experiment of distillation under a total-reflux condition operated at normal pressure by using a binary system of benzene and toluene. The distillation performance data expected are: (a) operating pressure $p_{op} = 0.1$ MPa, (b) rate of the column top vapor rate is $V_{TOP} = 2.6$ kmol/h, (c) desirable F-factor based on column top vapor is

$F_{TOP} = 1.2$, and (d) benzene concentrations of the overhead product and the bottom product $x_D = 0.99$ and $x_W = 0.97$. The specific surface area and equivalent diameter of the structured packing are given by $a_p = 400\ \mathrm{m^2/m^3}$, $d_{eq} = 0.02$ m. For simplicity, the internal reflux liquid is assumed to be equal to the vapor flow rate, i.e. $L = 2.6$ kmol/h.

As the preliminary test, the vertical variation of local HETPs is given by the following distribution function:

$$HETP = \frac{h_{ETP0}}{\left(0.1 \times Z/d_{eq} + 1.0\right)^{1/2}} \qquad \text{(25.3-P1)}$$

where h_{ETP0} is the maximum HETP $h_{ETP0} = 1.1$ m evaluated at the column top $z = 0$.

(1) Determine the inside diameter of the test column.
(2) Calculate the Reynolds number and the Schmidt number assuming that the vapor rate is kept constant over the total height of the column.
(3) Calculate by using the McCabe-Thiele step-by-step method how many ideal stages are necessary.
(4) Obtain the vapor composition profile within each control volume from the above graphical calculation.
(5) Calculate vapor-phase film coefficient of more-volatile component at each control volume
(6) Give a result of the required total height of the test packed column.

Nomenclature

a, a_p	effective interfacial area per unit packed volume, [m^2/m^3]
Cp	heat capacity, [J/kmol K]
d_{eq}	hydraulic equivalent diameter of packing, [m]
D_G, D_L	diffusivity in gas- and liquid-phase, [m^2/s]
E_j	Enthalpy transfer rate, [W]
F	F-factor, [(m/s)(kg/m^3)$^{0.5}$]
F_0	F-factor specified at leading edge of packing section, [(m/s)(kg/m^3)$^{0.5}$]
f	distribution function, [-]
G_M	superficial molar gas-mass velocity, [kmol/m^2s]
$H_L,\ H_V$	specific enthalpy of liquid and vapor, [J/kmol]
h_{ETP}	HETP (Height Equivalent to a Theoretical Plate), [m]
h_{ETP0}	HETP evaluated at leading edge of packing section, [m]
j	stage number, or j-factor, [-]
K	vapor-liquid equilibrium constant or coefficient, [-]
K_x, K_y	overall mass transfer coefficients defined by vapor-phase and liquid-phase concentrations [kmol/m^2s]
k_x, k_y	mass transfer coefficients of vapor-phase and liquid-phase film [kmol/m^2s]
L	liquid flow rate, [kmol/s]
m	slope of equilibrium curve, dy/dx,
N_{Aj}	mass transfer rate, [kmol/s]
n	theoretical plate/stage number, [-]
Pr	Prandtl number, [-]
Re	Reynolds number, [-]
Sc	Schmidt number, [-]
Sh	Sherwood number, [-]
T	temperature, [K]
u	velocity, [m/s]
V	vapor flow rate, [kmol/s]
x_A, y_A	mole fraction of component A, liquid- and vapor-phase, [-]
z	vertical height of packing section, [m]
ζ	dimensionless vertical distance, [-]
μ	viscosity, [kg/m s]

Subscripts

A	component A
i	interface
sv	superficial
L	liquid
V	vapor
∞	free stream

Superscripts

*	equilibrium

Chapter 26

Thermodynamic Approach for Thermal Engineering Processes

Historically speaking, "Thermodynamics," the basic structure of which was constructed about 100 years earlier than Transport Science, still continues to exercise its authority over extensive scientific and technological fields. In particular, the first law of thermodynamics is serving as the basic concept of various sciences. In this course, we learned the first law of thermodynamics in Chapter 4 of PART I as the fundamental idea of the conservation of energy. You can go back to Chapter 4 whenever you want to know the fundamentals of thermodynamics.

26.1 Fundamental Laws of Thermodynamics

We begin by reviewing the first law of thermodynamics for total energy given by

$$\frac{d}{dt}\int_V \rho E_T \, dV = -\Delta\left[H_e + E_k + E_p\right] + Q - W \qquad (4.4\text{-}5)$$

You can see the derivation procedure in the macroscopic energy balance in Chapter 4.4 of PART I .

A simple steady-state form of the mechanical energy balance can be obtained for incompressible fluid flows with no heat input $(Q = 0)$ into the flow system:

$$\frac{p_2 - p_1}{\rho} + \Delta\frac{1}{2}\langle v\rangle^2 + g\,\Delta h = -Fr_m - W_m \qquad (4.5\text{-}5)$$

A steady-state form of thermal energy balance for non-isothermal system is given by

$$-\Delta\left(H_m + \frac{1}{2}\langle v\rangle^2 + g\,h\right) + Q_m - W_m = 0 \qquad (4.6\text{-E13})$$

In moderate non-isothermal conditions, the kinetic and potential energy terms in the first term of Eq. (4.6-E13) $\frac{1}{2}\langle v\rangle^2 + g\,h$ and the work term W_m are much smaller than the heat input term Q_m for the case of thermal energy systems such as heat exchangers, evaporator, condenser and so on,

Finally Eq.(4.6-E13) reduces to

$Q_m = \Delta H_m$ (26.1-1)

For a heat exchanger without phase transformation, this equation gives the following heat balance expressed with heat flux:

$Q = w\,Q_c = w\,Cp\,(T_{in} - T_{out})$ (26.1-2)

The heat exchange rate is proportional to the change in temperature of the flowing fluid between the inlet and outlet of the heat transfer pipe.

The variables of these equations can be referred to the Notation of Chapter 4.

In Chapter 4, the loss of energy by irreversible viscous dissipation such as $-Fr_m$ was taken into consideration in the energy balance. The friction loss is an important factor for determining the power requirement of the pump transporting the fluid through a pipeline.

However the friction loss is too difficult to theoretically analyze for complicated flow systems. We have already studied that the friction loss and heat loss should be evaluated along the route of fluid stream over the boundary wall between the system and the surroundings. This chapter will study the role of thermodynamics in complicated flow phenomena from a viewpoint of quasi-static change in the ideal condition.

26.2 Thermodynamic Diagram

In thermodynamics, there are various convenient diagrams available which represent many thermodynamic states of materials at the condition of thermodynamic variables such as temperature, pressure, specific volume, enthalpy, entropy, etc. A thermodynamic diagram illustrates the change or relation between two or more thermodynamic variables during a thermodynamic process. One of the thermodynamic diagram is shown Fig.26.2-1. This is also called "Mollier diagram", where the vertical axis gives specific enthalpy while the horizontal axis gives specific entropy.

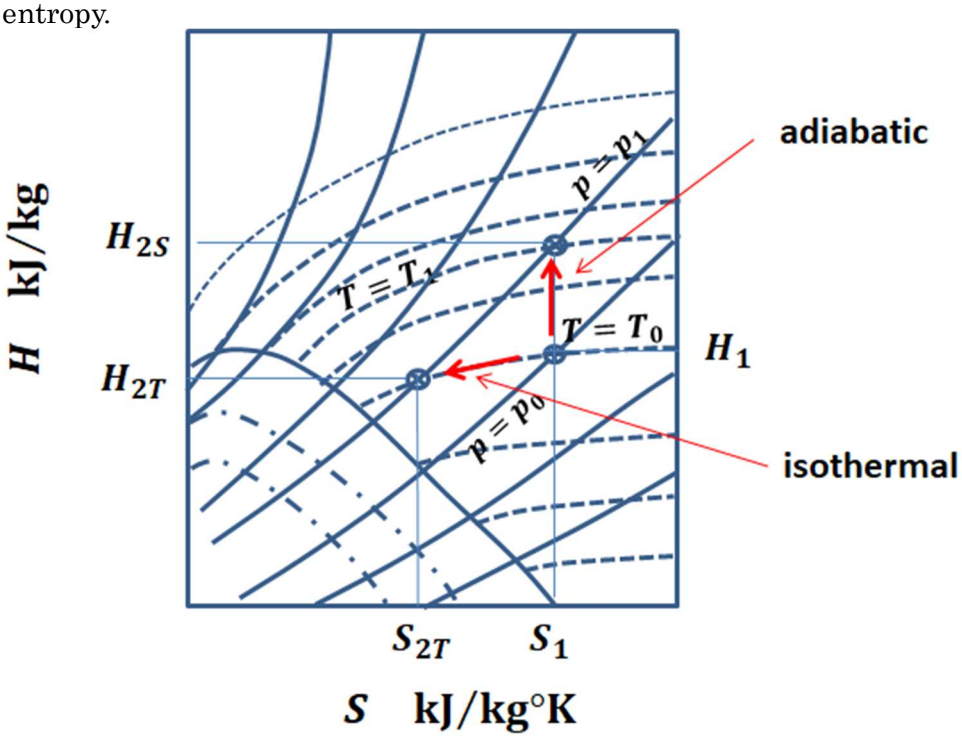

Fig.26.2-1 Mollier diagram indicating an adiabatic change and an isothermal change.

An isentropic change from p_0 to p_1 is indicated as the adiabatic (constant-entropy) compression by the vertical arrow. During this compression, the enthalpy change is given by $H_{2S} - H_1$. An isothermal change from p_0 to p_1 is indicated as the isothermal (constant-temperature) compression by the arrow along the isotherm of T_0. During the compression, the enthalpy change is given by $H_{2T} - H_1$. These two evaluations of enthalpy change are done under an assumption of quasi-static change with neither heat loss nor friction loss.

26.3 Joule-Thomson Expansion

Let us consider adiabatic abrupt expansion through a horizontal flow system shown in Fig.26.3-1, where a real gas flowing at high pressure p_1 in the region A is released into the region B of low pressure p_2 without significant change in kinetic energy. This is called "Joule-Thomson expansion". Throttling is done through a throttling valve or a porous plug where no kinetic energy loss is assumed.. This is one of the quasi-static processes treated as the thermodynamic approach. In the quasi-static process, no loss is assumed in the route from state 1 to state 2.

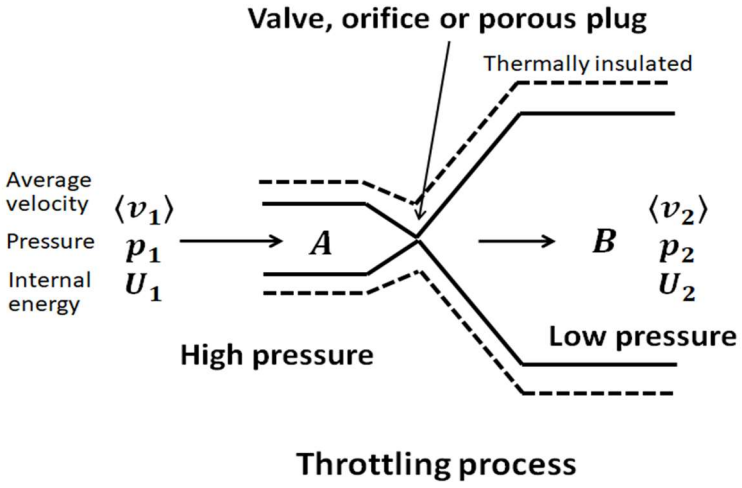

Fig.26.3-1 Throttling flow system for Joule-Thomson expansion

The expansion is inherently irreversible. During this expansion, enthalpy remains unchanged (see below). Unlike a free expansion, work is done, causing a change in internal energy. Whether the internal energy increases or decreases is determined by whether work is done on or by the fluid; that is determined by the initial and final states of the expansion and the properties of the fluid.

Applying the thermodynamic law to this expansion,

$$U_1 + p_1 v_1 + \langle v_1 \rangle^2/2 + g\,Z_1 + q = U_2 + p_2 v_2 + \langle v_2 \rangle^2/2 + g\,Z_2 + W \qquad (26.3\text{-}1)$$

You may notice that the frictional loss term Fr vanishes from the above equation. This is the thermodynamic consideration.

In this flow system,
$Z_1 = Z_2$, i.e. negligible potential energy effect.

$q = 0$, i.e. no heat input and output from the insulated wall. In thermodynamic consideration, no heat loss is assumed.
$w = 0$, i.e. no shaft work such as pumps, turbines and impellers.
The above equation reduces to

$$H_1 + \langle v_1 \rangle^2/2 = H_2 + \langle v_2 \rangle^2/2 \quad (26.3\text{-}2)$$

Since $p_1 \gg p_2$, $\langle v_1 \rangle \ll \langle v_2 \rangle$.
In this flow system dealing with the enthalpy change, $H_1, H_2 \gg \langle v_2 \rangle^2/2$.
As a result,

$$H_1 \cong H_2 \quad (26.3\text{-}3)$$

It has been found that the Joule-Thomson expansion is done by the equi-enthalpy (Isenthalpic) change. Thermodynamic approach can consider a change in the physical state between the starting point and the reaching point. What route traced from the start to the goal is not taken into account. It is necessary to consider the friction loss and heat loss along the route.
For this Joule-Thomson expansion,

$$H_1 \cong H_2$$

Therefore

$$\int_1^2 dH = H_2 - H_1 = (H_2 - H_3) + (H_3 - H_1) = 0 \quad (26.3\text{-}4)$$

Generally the enthalpy change can be expressed by the following formula based on the change in temperature and pressure:

$$dH = Cp\, dT + \left[V - T\left(\frac{\partial V}{\partial T}\right)_p\right] dp \quad (26.3\text{-}5)$$

As shown in Fig.26.3-2, from a thermodynamic viewpoint, the change from 1 to2 directly is equivalent to the change from 1 through 2 via 3.

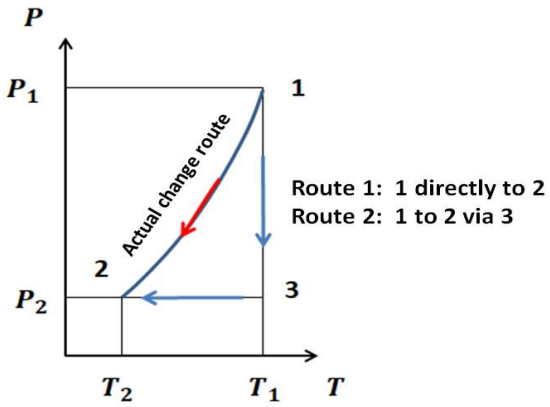

Fig.26.3-2 Two routes for enthalpy change calculation in Joule-Thomson expansion

We can calculate the enthalpy change separately:

$$H_3 - H_1 = \int_{p_1}^{p_2}\left[V - T_1\left(\frac{\partial V}{\partial T}\right)_p\right] dp \quad \text{(constant temperature)}$$

$$H_2 - H_3 = \int_{T_1}^{T_2}(Cp)_{p_2}\, dT = (Cp_{av})_{p_2}(T_2 - T_1) \quad \text{(constant pressure)}$$

Therefore

$$H_2 - H_1 = \int_{p_1}^{p_2}\left[V - T_1\left(\frac{\partial V}{\partial T}\right)_p\right] dp + (Cp_{av})_{p_2}(T_2 - T_1) = 0 \quad (26.3\text{-}6)$$

From this equation, we obtain the following relation:

$$T_2 - T_1 = \frac{-\int_{p_1}^{p_2}\left[V - T_1\left(\frac{\partial V}{\partial T}\right)_p\right] dp}{(Cp_{av})_{p_2}} = \frac{H_1(p_1, T_1) - H_3(p_2, T_1)}{(Cp_{av})_{p_2}} \quad (26.3\text{-}7)$$

where $(Cp_{av})_{p_2}$ is the specific heat averaged over the range of T_1 and T_2.
This result indicates that the gas temperature is lowered or raised by the Joule-Thomson expansion depending upon the pV work.
The enthalpy is defined as $H = U + p\,V$.
Under the condition of a Joule-Thomson expansion, the change in pV represents the work done by the fluid. This is called "flow work". (see Chapter 4.4) If $p\,V$ increases doing the work on its surroundings, U should decrease to keep H constant. This means the cooling effect. However for an ideal gas, pV does not change during a Joule-Thomson expansion. That is, there is no change in internal energy. The numerator of the above equation reduces to zero if the perfect gas law is substituted.

The adiabatic cooling which occurs by the Joule-Thomson expansion when a compressed gas at p_1 is suddenly allowed to expand into a low pressure space in the condition of no external work done. This indicates that the Joule-Thomson expansion can produce larger heating or cooling than observed in a free expansion.
The Joule-Thomson coefficient is defined as

$$\mu_{JT} = \left(\frac{\partial T}{\partial p}\right)_H \qquad (26.3\text{-}8)$$

This coefficient may be either positive or negative.

Fig.26.3-3 shows a schematic picture of *T-p* mapping diagram of Joule-Thomson coefficients for N_2 gas.

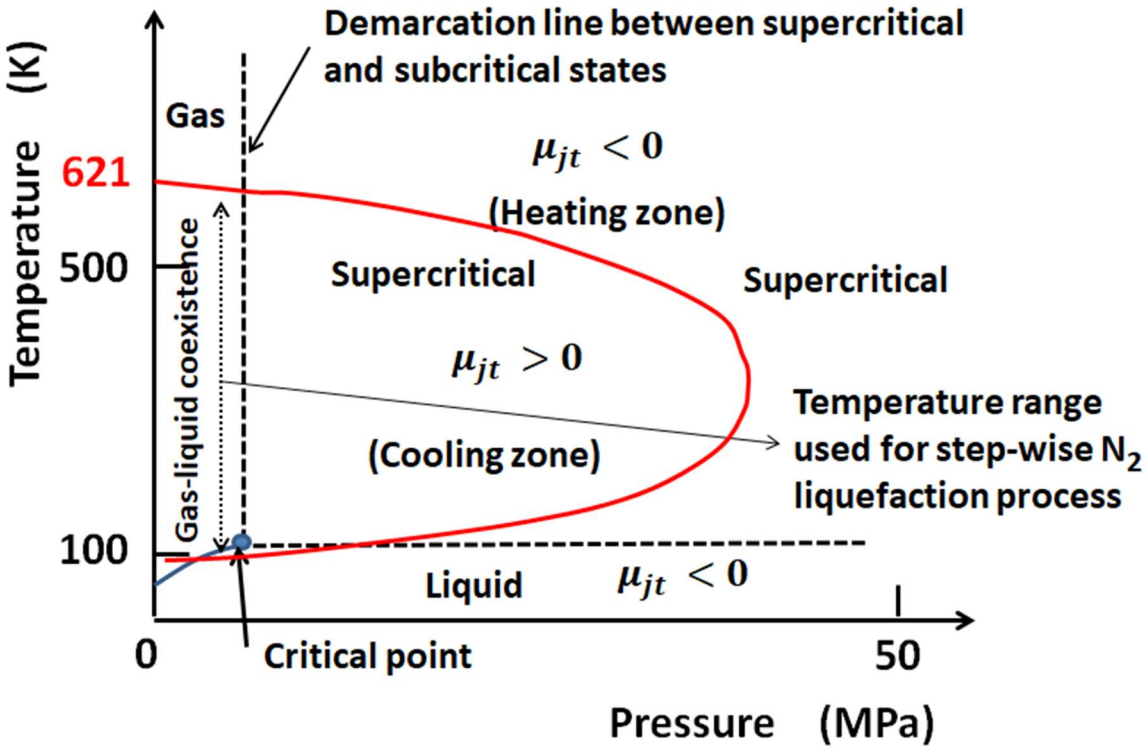

Fig.26.3-3 *T-p* mapping diagram of Joule-Thomson coefficients (N_2 gas)

The coefficient μ_{JT} is negative in the region of very high and very low temperatures. At temperatures below the gas-liquid coexistence curve, N_2 condenses to form a liquid and μ_{JT} becomes negative. Within the region bounded by the red line, $\mu_{JT} > 0$. This means cooling effect.

Outside the bounded region, all regions indicate $\mu_{JT} < 0$. This implies that the adiabatic expansion causes heating effect. The dashed line indicates the demarcation line for becoming a supercritical fluid (see Fig,23.1-1). All gases have an inversion point at which the μ_{JT} value changes sign. For example, N_2 gas has inversion temperature of 621 K as shown in Fig.26.1-3.

[EXAMPLE 26.3-1]

In the flow system shown in Fig.26.3-E1 , a steam stream A ($p_1 = 5$ MPa, $T_1 = 280$ ℃) undergoes a Joule-Thomson expansion with pressure change from p_1 to $p_2 = 0.1$ MPa. Calculate the temperature change.

Solution:

Fig.26.3-E1 is a thermodynamic diagram (p-H diagram), where a Joule-Thomson expansion is indicated by an arrow from the point of $p_1 = 5$ MPa and $T_1 = 280$℃ to a pressure line of $p_2 = 0.1$ MPa. Since this is an adiabatic expansion with *H* constant, the arrow reaches an isotherm of 230℃. Therefore the temperature drop reduces to 50℃. (It may be somewhat difficult to precisely find the correct isotherm from this entangled diagram.)

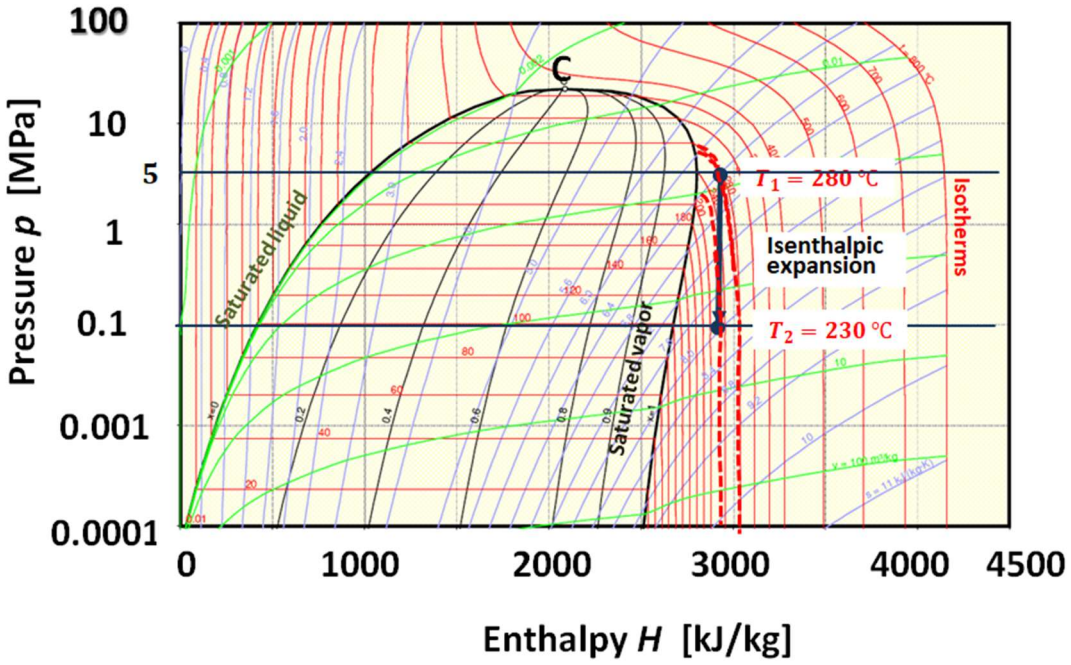

Fig.26.3-E1 Calculation of Joule-Thomson expansion by means of a thermodynamic diagram

Let us reconsider a similar problem by another diagram (Mollier diagram).
A steam stream ($p_1 = 1$ MPa, $T_1 = 250$ ℃) undergoes a Joule-Thomson expansion with pressure change from p_1 to $p_2 = 0.1$ MPa. We will calculate the temperature change.
The constant-pressure heat capacity averaged at p_2 is given by
$Cp_{av} = 1.96$ kJ/kg K.

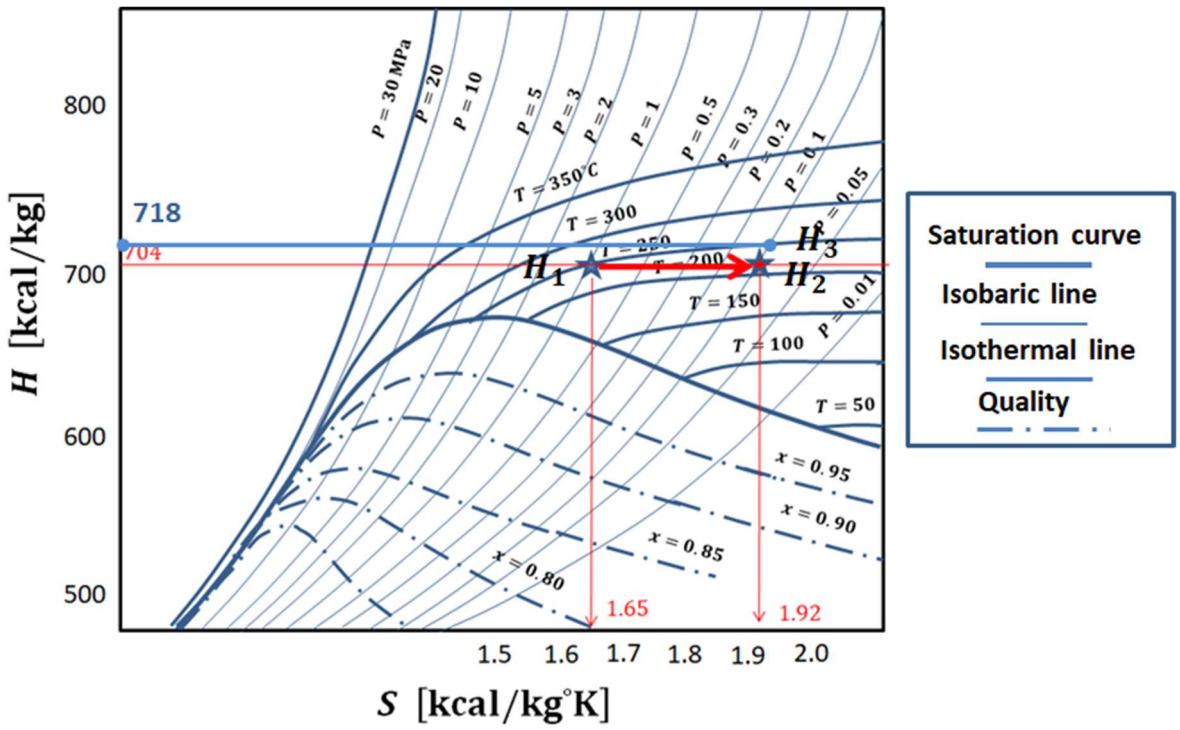

Fig.26.3-E2 Calculation of Joule-Thomson expansion using a Mollier diagram.

The initial state ($p_1 = 1$ MPa, $T_1 = 250$ ℃) is located at the star indicated in Fig.26.3-E2. The red horizontal line implying the Joule-Thomson expansion with constant enthalpy crosses the isobaric line of $p_2 = 0.1$ MPa. We can consider that an isotherm of 220℃ should pass through that crossing point. That is, the temperature of the steam stream at the final state is 220℃. The temperature drop is $T_2 - T_1 = -30$℃.

Another solution: From the above Mollier diagram, the specific enthalpy of the steam stream ($p_1 = 1$ MPa, $T_1 = 250$ ℃) is $H_1 = 704$ kcal/kg.

From a thermodynamic viewpoint, the route $1 \rightarrow 3 \rightarrow 2$ gives the same result of isenthalpic change as the direct route $1 \rightarrow 2$.

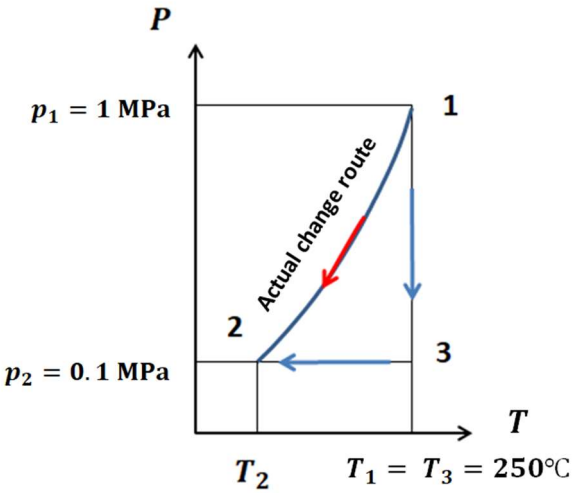

Fig.26.3-E3 Two routes of isenthalpic change from 1 to 2 for a Joule-Thomson expansion.

As shown in the Mollier diagram, the specific enthalpy at the fictitious condition ($p_2 = 0.1$ MPa, $T_3 = 250$ ℃) is given by

$H_3 = 718$ kcal/kg.

The constant-pressure heat capacity averaged is given by $Cp_{av} = 1.96$ kJ/kgK $= 0.47$ kcal/kg℃.

Therefore

$$T_2 - T_1 = \frac{-\int_{p_1}^{p_2}\left[V - T_1\left(\frac{\partial V}{\partial T}\right)_p\right]dp}{(Cp_{av})_{p_2}} = \frac{H_1(p_1, T_1) - H_3(p_2,\ T_1)}{(Cp_{av})_{p_2}} = \frac{704-718}{0.47} = -29.8℃ \quad \text{(26.3-E1)}$$

This solution with the aid of the $(Cp_{av})_{p_2}$ value seems to be somewhat easier than the first one.

Derivation of Joule-Thomson coefficient

Let us study using the laws of thermodynamics about what the Joule-Thomson coefficient is. The isenthalpic condition of a Joule-Thomson expansion is applied in the defining equation of enthalpy

$$dH = dU + d(pV) = T\,dS + V\,dp = 0 \quad \text{for} \quad dU = Q - p\,dV = T\,dS - p\,dV \quad \text{(26.3-E2)}$$

From the above equation we obtain

$$dS/dp = -V/T \quad \text{(26.3-E3)}$$

The following relation could be obtained by somewhat difficult derivation.

$$\left(\frac{\partial S}{\partial p}\right)_T = -\left(\frac{\partial V}{\partial T}\right)_p \quad \text{(26.3-E4)}$$

Only for simplification, we will omit the derivation process.

Since $dH = T\,dS$ in the constant pressure condition, the definition of constant-pressure heat capacity is given by

$$Cp = \left(\frac{\partial H}{\partial T}\right)_p = \left(\frac{\partial H}{\partial S}\right)_p \left(\frac{\partial S}{\partial T}\right)_p \quad \text{(26.3-E5)}$$

Therefore

$$\left(\frac{\partial S}{\partial T}\right)_p = \frac{Cp}{T} \quad \text{(26.3-E6)}$$

Differentiating the relation $dH = T\,dS + V\,dp$ with respect to p in the condition of constant T gives

$$\left(\frac{\partial H}{\partial p}\right)_T = T\left(\frac{\partial S}{\partial p}\right)_T + V = -T\left(\frac{\partial V}{\partial T}\right)_p + V \quad \text{(26.3-E7)}$$

Using this relation, the enthalpy change can be expressed as

$$dH = \left(\frac{\partial H}{\partial T}\right)_p dT + \left(\frac{\partial H}{\partial p}\right)_T dp = Cp\,dT + \left[V - T\left(\frac{\partial V}{\partial T}\right)_p\right] dp \quad \text{(26.3-E8)}$$

Differentiating with respect to p in the condition of $dH = 0$, the Joule-Thomson coefficient is obtained:

$$\mu_{JT} = \left(\frac{\partial T}{\partial p}\right)_H = \frac{-\left[V - T\left(\frac{\partial V}{\partial T}\right)_p\right]}{Cp} \quad \text{(26.3-E9)}$$

This coefficient indicates the rate of temperature change with the pressure for an isenthalpic condition. For perfect gases ($p\,V = n\,R\,T$),

$$\left(\frac{\partial V}{\partial T}\right)_p = \frac{n\,R}{p} = \frac{V}{T} \quad \text{(26.3-E10)}$$

Therefore the numerator of the defining formula becomes zero for perfect gases

$\mu_{JT} = 0$ (perfect gas)

It has been demonstrated that even if the Joule-Thomson expansion process is performed with a perfect gas, the fluid temperature would not change.

26.4 Actual Issues of Joule-Thomson Expansion Process

According to the macroscopic energy balance obtained from the first law of thermodynamics in Chapter 4.6:

$$-\Delta\left(H_m+\frac{1}{2}\langle v\rangle^2+g\,h\right)+Q_m-W_m=0 \qquad (4.6\text{-E13})$$

For the case of Joule-Thomson expansion from p_1 to p_2, the flow system exhibits the following isenthalpic change

$$H_1=H_2$$

In the thermodynamic diagram shown in Fig. 26.4-1, the initial state and the final state are indicated. The route between the initial and final states for the Joule-Thomson expansion is not taken into account except the condition of isenthalpic change.

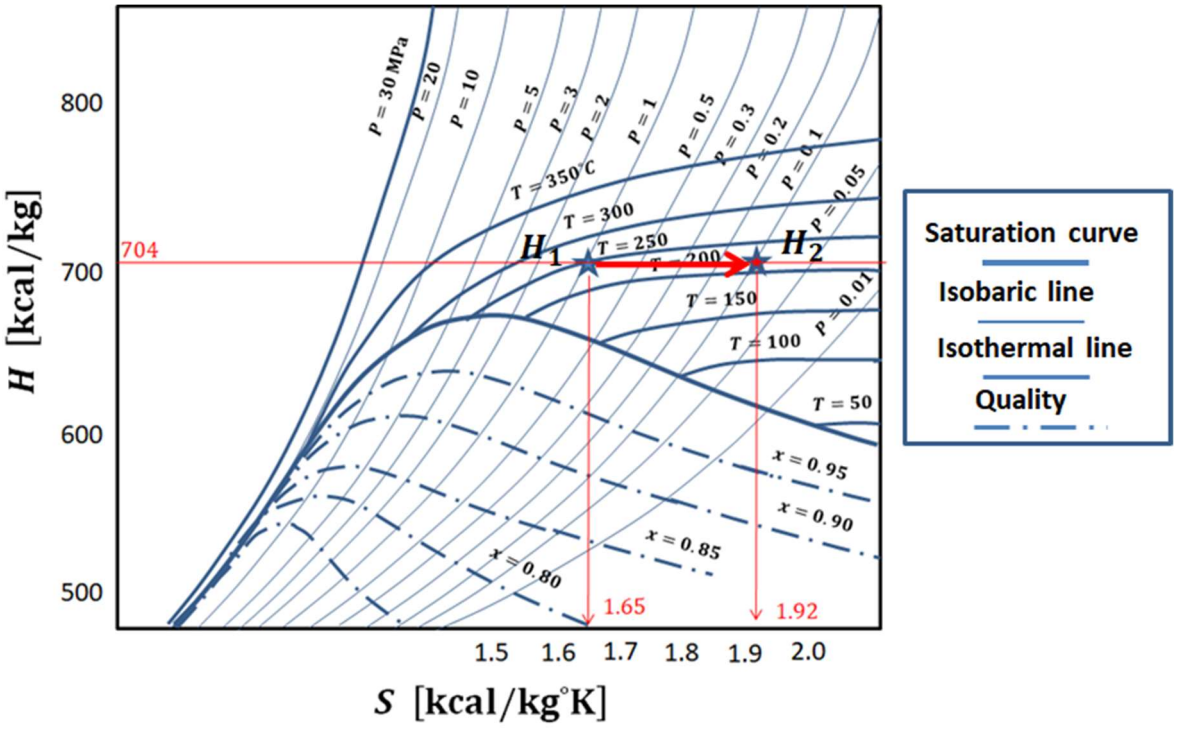

Fig.26.4-1 Mollier diagram indicating an isenthalpic Joule-Thomson expansion process.

This means an ideal isenthalpic process due to the quasi-static change which can be analyzed by a simple calculation method assuming neither friction loss nor heat loss. This is one of the thermodynamic approaches.

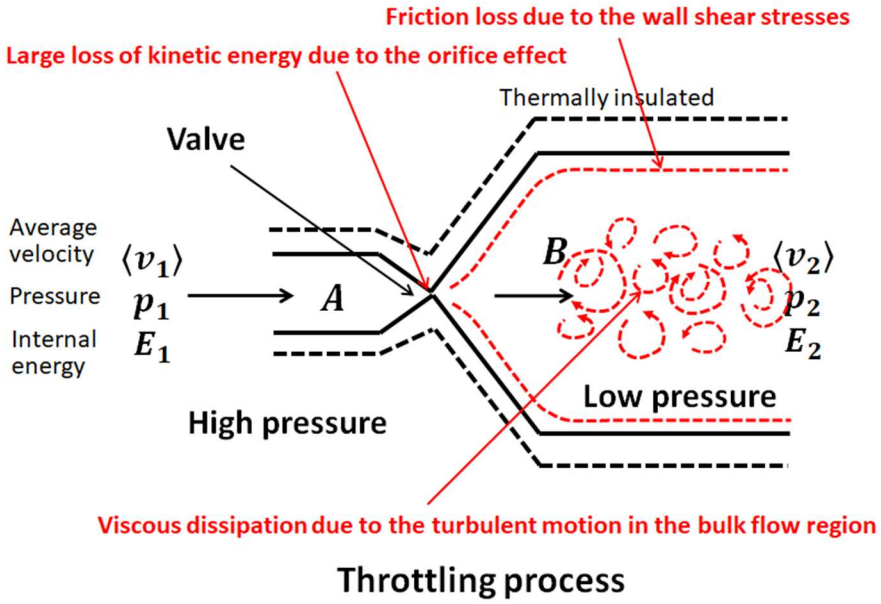

Fig.26.4-2 Friction losses in an actual Joule-Thomson expansion process

However these irreversible losses should be evaluated along the flow direction. The heat loss from the outside surface of the system to the surroundings should be reduced as much as possible by a thermal insulation. On the other hand, the friction losses occur not only due to the shear stress acting on the inside surface of the flow system but also due to the viscous dissipation of turbulent flow in the bulk flow region. The latter effect is very difficult to evaluate except by experiment.
In particular, the fluid stream undergoes very large loss of kinetic energy due to the orifice effect at the throttling valve.

Strictly speaking, an actual Joule-Thomson process should proceed accompanied with some degree of enthalpy loss, i.e. $H_2 < H_1$. The friction loss is converted to the generation of internal energy.

For a flow system without heat exchange ($Q_m = 0$), The enthalpy change reduces to

$$\Delta H_e = \Delta E_h + \Delta(p\, V_s) = T\, \Delta S + V_s\, \Delta p \qquad (4.5\text{-}1)$$

The friction loss renders the process irreversible owing to the frictional heating. Therefore

$$T\, \Delta S = Q_m + Fr_m \qquad \text{That is,} \quad \Delta H_e = Q_m + Fr_m + V_s\, \Delta p \qquad (4.5\text{-}2)$$

As a result, the mechanical energy balance equation reduces to

$$\int_{p_1}^{p_2} V_s\, dp + \Delta \frac{1}{2} \langle v \rangle^2 + g\, \Delta h = -Fr_m - W_m \qquad (4.5\text{-}3)$$

This generalized Bernoulli equation should be used for a strict analysis of practical Joule-Thomson expansion processes. If the flow system does not have any shaft work, $W_m = 0$.
The friction loss can be evaluated by experiment with the aid of Eq. (4.5-3).

[PROBLEM 26.4-P1]

Fig.26.4-P1 is a p-H diagram of carbon dioxide.
A compressed carbon dioxide gas ($p_1 = 12$ MPa, $T_1 = 80$°C) undergoes the first step of Joule-Thomson expansion from $p_1 = 12$ MPa to $p_2 = 3$ MPa. Obtain the temperature drop.

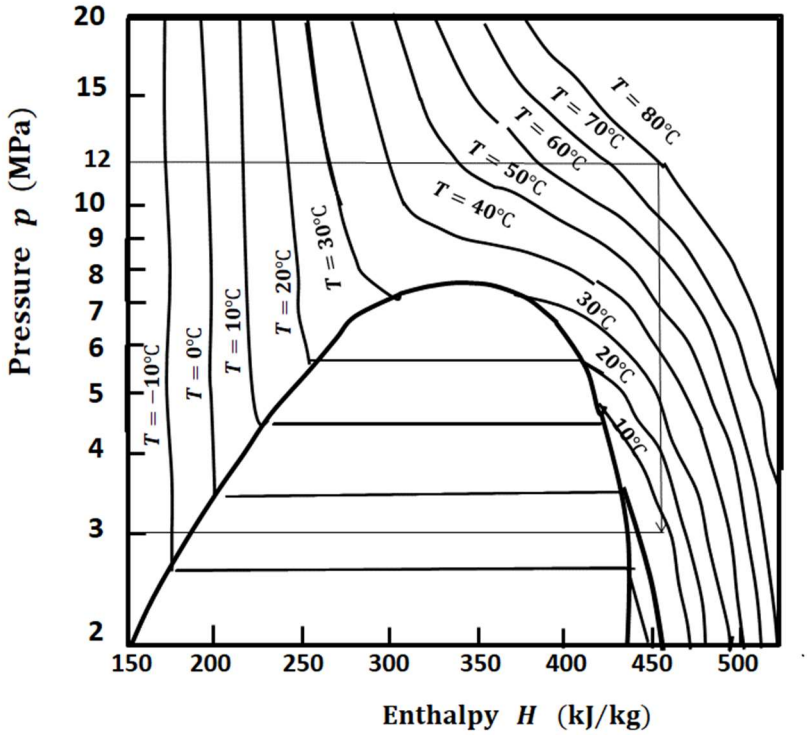

Fig.26.4-P1 P-H diagram of carbon dioxide

26.5 Ejector Engineering

26.5-1 Working principle of ejectors

There are various kinds of ejectors available for many chemical engineering purposes: (1) water ejector or aspirator, (2) air ejector, (3) vacuum ejector, (4) steam ejector, etc.
An ejector is constituted of a suction chamber, a jet nozzle section, and a diffuser section.

As shown in Fig.26.5-1, a working fluid A (motive fluid) flows through a jet nozzle into a suction chamber with high velocity where another fluid B is drawn in due to a low pressure (obtained by Bernoulli principle). Then the mixed fluid A+B entering the diffuser section is very much accelerated due to the convergent section. Then the velocity of the mixed fluid becomes maximum at the diffuser throat. They undergo an adiabatic expansion after passing through the throat. In the next divergent section, they are decelerated with the recovery of pressure up to the outlet pressure.

The strength of the vacuum depends on the working fluid velocity and pressure, the shape of the jet nozzle, and the shape of the construction and mixing section.

Water ejector (aspirator) is commonly used when not strong vacuum is needed in chemistry and biology laboratories. If a liquid is used as the working fluid like an aspirator, the strength of the vacuum is limited by the vapor pressure of the liquid. Therefore steam ejectors are the most effectively utilized for industrial processes. In this chapter, we will study mainly the steam ejector behavior and design method from a thermodynamic viewpoint.

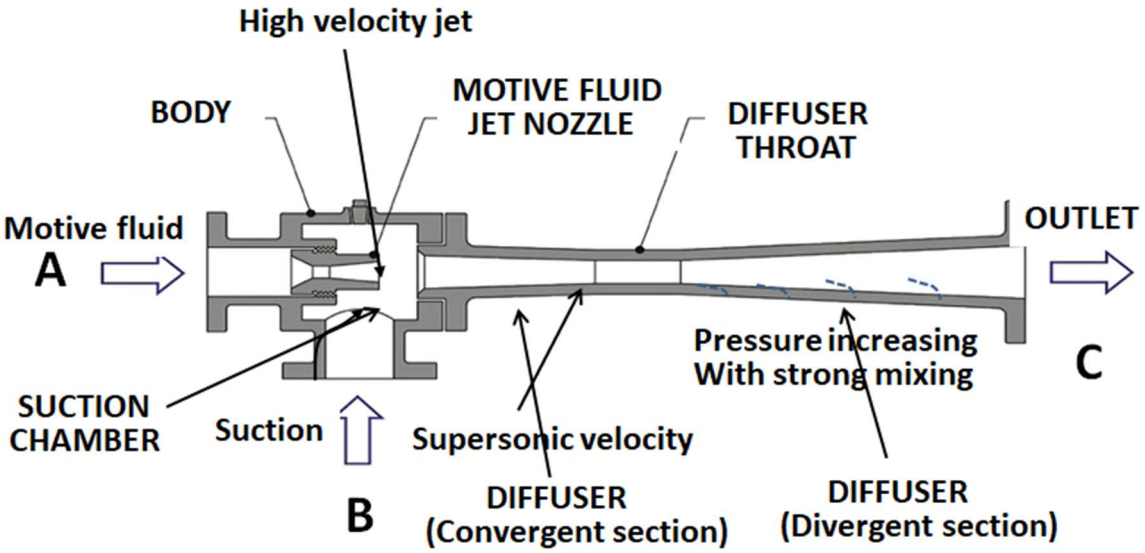

Fig.26.5-1 Standard structure of ejectors

Steam ejectors using high-pressure steam as the working fluid A have a simple structure with no moving part such as rotating machinery. In addition, they have sufficient durability with advantages of easy maintenance and cheap price.

The steam ejector operates by utilizing the pressure energy of a motive steam A, converting it to the kinetic energy, and then ejecting the high-velocity jet from a jet nozzle. As a result, another fluid B (usually low-pressure steam) is drawn in into a suction chamber by Bernoulli principle. Then the mixed fluid A+B flowing into the downstream tube called “diffuser” is accelerated in the convergent section, and reaches the maximum velocity at the diffuser throat. After the throat, the mixed fluid A+B is decelerated in the divergent section with increasing pressure. Steam ejectors can be regarded not only as a vacuum pump but also as a compressor recovering low-pressure steam to medium-pressure steam.

26.5-2 Usage of steam ejectors

As shown in Fig.26.5-2, usually a steam ejector has two purposes for usage except for depressurization as a vacuum pump. Generally speaking, low-pressure or low-temperature steam implies thermally low effectiveness for thermal engineering. One purpose is to compress a low-pressure steam up to a medium-pressure steam. The pressure of the motive steam is lowered down to the medium pressure instead. It should be considered that we can obtain thermally valuable steam $w_1 + w_0$. The second purpose is to use the medium-pressure steam produced by an ejector as an effective heating medium.

Steam ejectors are very often used in a variety of applications. Typical duties involve distillation, filtration, mixing, vacuum packaging, freeze drying, etc. Steam ejectors are very simple and reliable with low cost in that there are no moving parts such as rotating machinery and in that ejectors can be made highly resistant to corrosion and erosion.

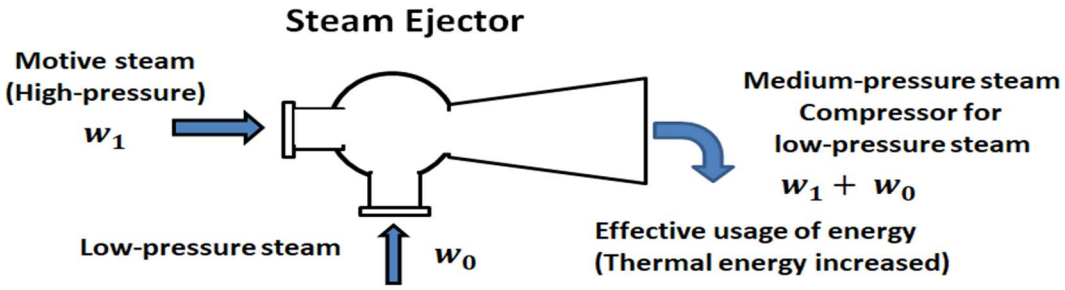

Fig.26.5-2 Usage of a steam ejector

26.5-3 Thermodynamic consideration of steam ejectors

It is very difficult to theoretically analyze the flow behavior in a steam ejector. In particular, the loss of mechanical energy generated within the flow passage of the ejector and the loss of thermal energy from the surface of the ejector system to the surroundings are complicated engineering issues. As treated in Joule-Thomson expansion processes, the thermodynamic approach has a very simple and convenient concept (Fig.26.5-3): A change 1 to 2 in thermodynamic variables such as enthalpy, entropy, specific volume, pressure, and temperature is given by a difference only between the initial state and the final state, regardless of the tracing routes from 1 to 2.

Regarding an ejector shown in Fig.26.5-1, the initial state corresponds to A and B whereas the final state corresponds to C. For example, a change in enthalpy becomes $H_C - (H_A + H_B)$.

A Mollier H-S diagram shown in Fig.26.5-4 is very convenient to use for consideration of thermodynamic behavior of ejectors.

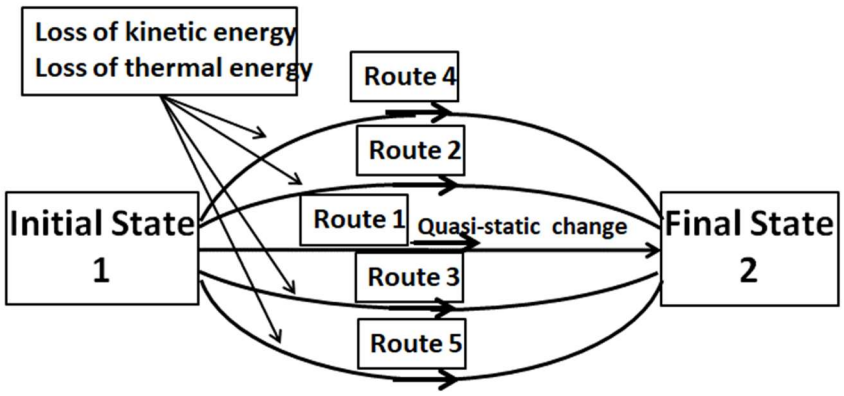

Fig.26.5-3 Thermodynamic concept of change 1 to 2 of thermodynamic variables

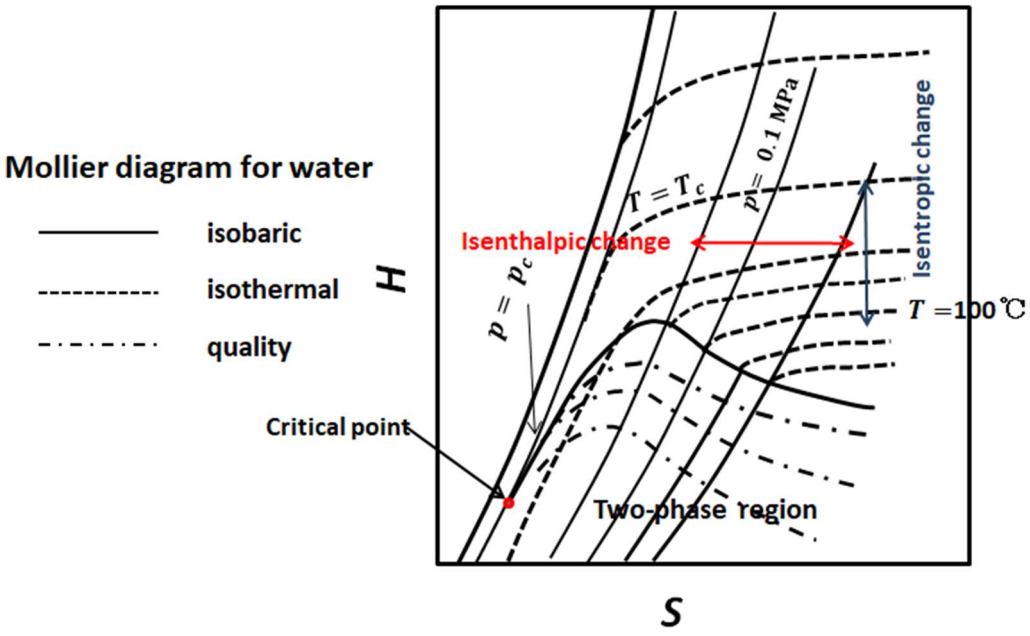

Fig.26.5-4 Schematic picture of Mollier diagram for calculating a thermodynamic change

26.6 Steam Ejectors for Effective Energy Conservation

26.6-1 Effective application of a steam ejector for evaporation processes

Let us consider about the utilization of a steam ejector for effective energy conservation of steam lines in a factory. Fig.26.6-1 shows a continuous evaporator supported by a steam ejector. The evaporator is one of our original Wall Wetter evaporators (see Chapter 24.3-1&2). The water vapor produced by evaporation of aqueous solution of non-volatile substance is recompressed by a steam ejector which works with the aid of a motive steam taken from the steam line of another plant.

In a usual condition of the evaporator operated without any ejector, the evaporator needs the heating duty $Q = 5{,}390$ kcal/h which is covered with $w_{ST} = 10.1$ kg/h of saturated water vapor (1 atm) in the jacket. The motive steam requirement $w_1 = 28.0$ kg/h is calculated by the trial-and-error method to be described in the later section. At this stage, $w_1 = 28.0$ kg/h can be regarded as an assumed value.

$w_1 = 28.0$ kg/h of motive steam ($p_1 = 0.7$ MPa, $T_1 = 166$℃) and $w_0 = 10$ kg/h of water vapor ($p_0 = 0.04$ MPa, $T_0 = 75$℃) are mixed inside the ejector and comes out as the medium-pressure steam $w_1 + w_0 = 38.0$ kg/h in the condition of $p_4 = 0.1$ MPa, $T_4 = 100$℃, and quality $x_4 = 100\%$ (saturated steam). Strictly speaking, the outlet steam is obtained in the somewhat superheated condition.

Only for simplicity, we ignore the boiling point elevation due to the solute of the aqueous solution in the evaporator and the heat loss from the outside surface of the steam jacket.

The $w_{ST} = 10.1$ kg/h of the outlet steam can be reused for the heating duty of the evaporator. This can be considered as a kind of vapor-recompression method (VRC). As a result, the remaining steam $w_3 = 27.9$ kg/h at 1 atm can be used for another purpose. Finally only the thermal energy due to the pressure change of the motive steam from 0.7 to 0.1 MPa is utilized for evaporation without consumption in mass quantity. In addition, the pressure $p_0 = 0.04$ MPa of the evaporator is controlled by the sucking strength of the ejector.

For the low-pressure steam to be sucked into the ejector, the compression ratio is

$\beta = p_4/p_0 = 0.1/0.04 = 2.5$.

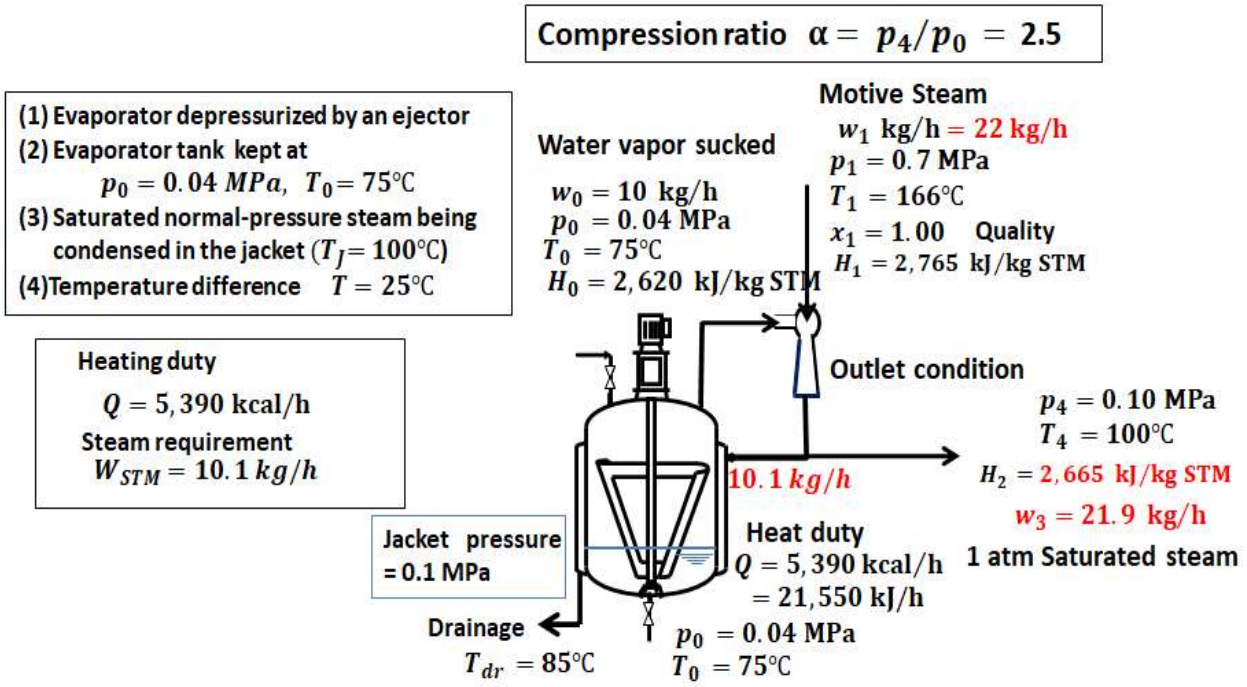

Fig.26.6-1 Energy saving method of an evaporator depressurized by a steam ejector

Practically the necessary supplying rate of the motive steam should be calculated in advance by the trial-and-error method to attain the appropriate condition of the ejector outlet. The practical design calculation method will be described later.

From now, let us study first the thermodynamic calculation based on unit mass.

According to the H-S diagram, the enthalpies of the motive steam and the water vapor from the evaporator are obtained by $H_1 = 2{,}765$ kJ/kg and $H_0 = 2{,}620$ kJ/kg, respectively.

As aforementioned, the following enthalpy balance can be used with neither friction loss nor heat loss:

$$w_1 H_1 + w_0 H_0 = (w_1 + w_0) H_2 \tag{26.6-1}$$

This indicates the enthalpy balance of the ejector between the initial state A+B and the final state C.

From the above equation, the enthalpy at the ejector outlet is calculated as

$$(28.0)(2{,}765) + (10)(2{,}620) = (28.0 + 10) H_2 \tag{26.6-2}$$

The enthalpy of the outlet steam is obtained as $H_2 = 2{,}726.8$ kJ/kg.

If w_1 becomes a different quantity as a result of the practical design calculation, the above calculation should be revised with a new value.

The 10.1 kg/h of the mixed steam obtained from the ejector outlet $w_1 + w_0 = 38.0$ kg/h can be reused as the heating medium for the evaporator and the remaining steam 27.9 kg/h can be used as the effective steam for another usage. This suggests that the evaporator can be operated by using the water vapor obtained by itself as the necessary steam for the jacket.

26.6-2 Thermodynamic calculation model for steam ejectors

Let us consider how to calculate the enthalpy change in a steam ejector.

As aforementioned, it is one of the great advantages of the thermodynamics to calculate a change of thermodynamic variables from the initial and final state without considering any routes.

We introduce “Two-flow-passage model” for the calculation of enthalpy change for a steam ejector.

The two-flow-passage model shown in Fig.26.6-2 assumes that two streams A and B are separately flowing without interaction between them. Therefore we can consider that the stream A related with the motive steam undergoes adiabatic (isentropic) expansion with the pressure change from p_1 to p_2 whereas the stream B undergoes adiabatic (isentropic) compression with the pressure change from p_0 to p_2.

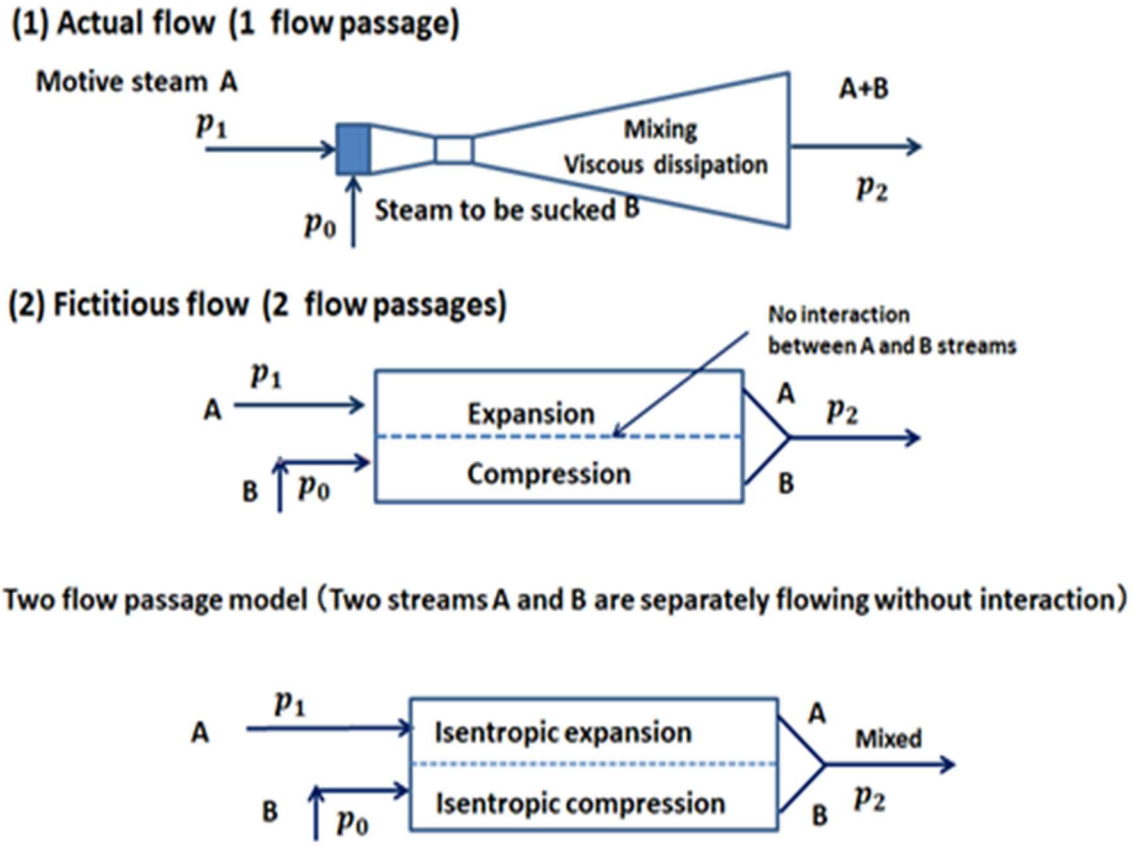

Fig.26.6-2 Two-flow-passage model for thermodynamic calculation of a steam ejector

If we adopt the two-flow-passage model for this problem, we can calculate the enthalpy change on the following Mollier diagram.

The stream B experiences isentropic change from p_0= 0.04 MPa to $p_4 = 0.10$ MPa. Therefore the stream B requires the enthalpy change $H_4 - H_0 = 2{,}800 - 2{,}620 = 180$ kJ/kg.

However in Fig.26.6-3, the stream A has available energy $H_1 - H_2 = 2{,}765 - 2{,}285 = 480$ kJ/kg. Be careful about $H_1 - H_2$ as the available energy based on the 0.04 MPa water vapor although the stream A also experiences isentropic change from p_1 to p_3.

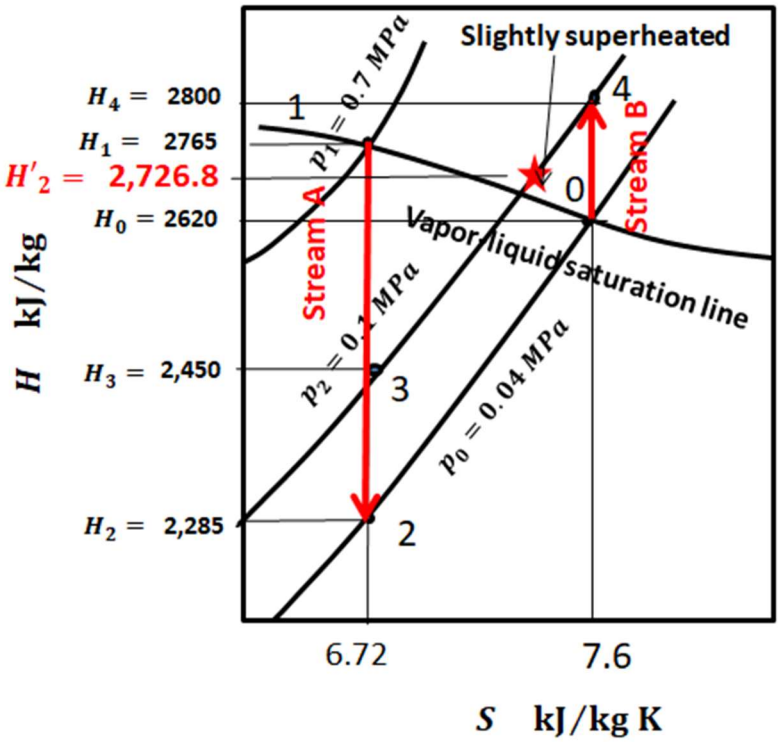

Fig.26.6-3 Thermodynamic enthalpy calculation on Mollier diagram

From here, let us consider the practical method determining the rate of the motive steam w_1 kg/h.

The flow and energy behaviors inside the ejector are so complicated that we cannot but rely on the empirically constructed data base.

26.7 Diffuser Efficiency of a Steam Ejector

The capacity of a steam ejector must be investigated by experiment.

In a practical design procedure, the diffuser efficiency empirically correlated with the suction pressure shown below is usually used.

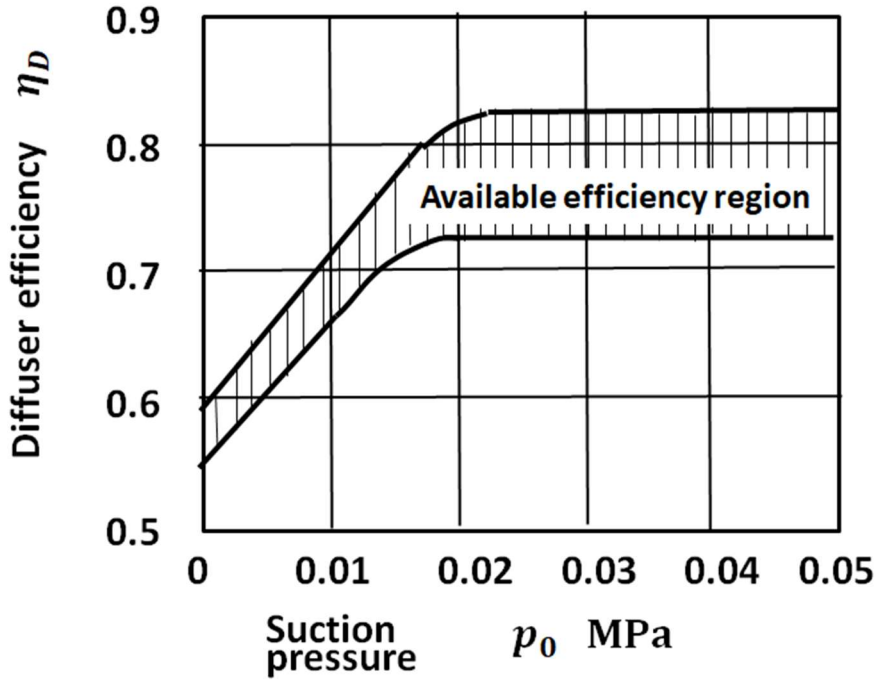

Fig.26.7-1 Empirical correlation of diffuser efficiency with suction pressure

The diffuser efficiency of a steam ejector depends on the structural design of an individual ejector. We should have our own correlation data accumulated by experiment.

In the problem of interest, the suction pressure is given as $p_0 = 0.04$ MPa. Therefore the diffuser efficiency lies between 0.725 and 0.83.

As shown in Fig.26.7-1, the diffuser efficiency can be interpreted in a relation with the friction loss factor ς as follows.

The diffuser efficiency is defined as

$$\eta_D = \frac{p_2 - p_1}{(1/2)\,\rho v^2}\,(1 - (A_1/A_2)^2) \tag{26.7-1}$$

This implies how to convert the kinetic energy $(1/2)\,\rho v^2$ into the pressure energy $p_2 - p_1$.

For the case of suddenly enlarged flow passage (see Chapter 7.4-2), the pressure change based on the friction loss can be expressed as

$$p_2 - p_1 = \rho\, Fr_m = \varsigma\, \frac{1}{2}\,\rho\langle v_1\rangle^2 \tag{26.7-2}$$

where the friction loss factor is given by $\varsigma = \left(1 - \frac{A_1}{A_2}\right)^2$

Therefore we can consider that the friction loss factor of the diffuser can be expressed as

$$\varsigma = \frac{\eta_D}{1 - (A_1/A_2)^2} \tag{26.7-3}$$

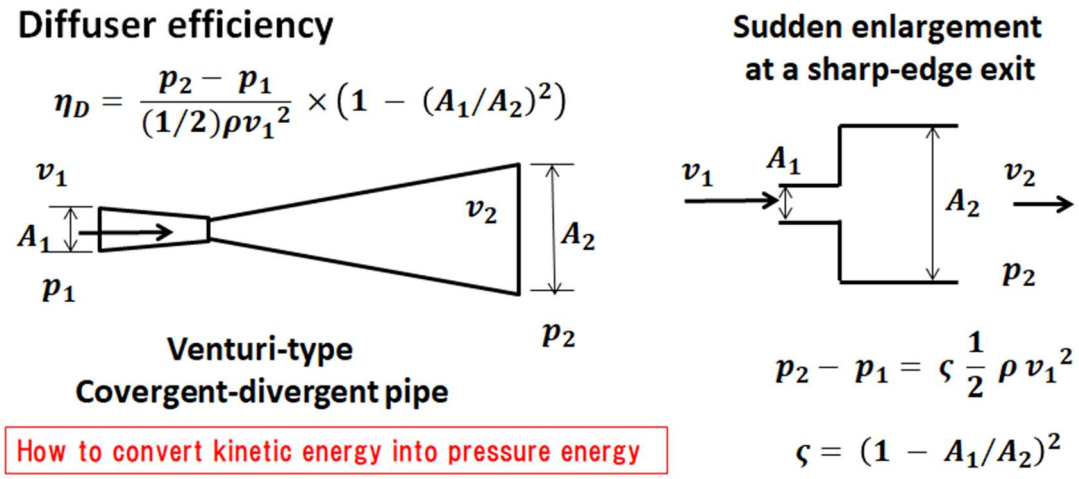

Fig.26.7-2 Physical meaning of diffuser efficiency

26.8 Motive Steam Required for a Steam Ejector

In order to obtain the necessary motive steam rate w_1, it is necessary to consider a relation with the ejector efficiency based on the enthalpy change ratio defined as

$$\eta_e = \frac{\Delta H_0}{\Delta H_1} = \frac{H_4 - H_0}{H_1 - H_2} \tag{26.8-1}$$

Here the denominator should be $H_1 - H_2$ from a viewpoint of available energy (enthalpy difference) higher than the steam with pressure p_0 to be sucked.

Fig.26.8-1 indicates an empirical correlation of the necessary motive steam rate w_1/w_0 with the ejector efficiency (enthalpy efficiency) η_e, where each correlative curve designates the diffuser efficiency η_D as the parameter.

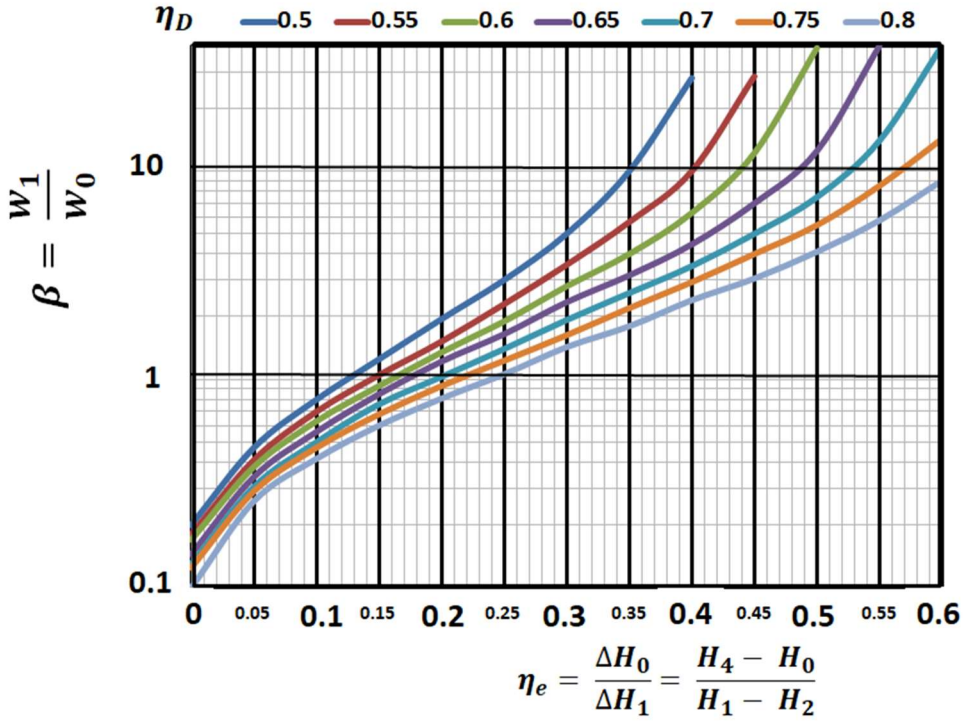

Fig.26.8-1 Empirical correlation of motive steam rate with ejector efficiency

These two correlation data should be empirically provided as the data bank for practical design work. (Figs. 26.7-1 & 26.8-1)

Let us try to determine the necessary motive steam rate from these correlation data.

[EXAMPLE 26.8-E1]

Regarding the problem treated above, we will determine the necessary rate of the motive steam.

The suction pressure is given by $p_0 = 0.04$ MPa from the operating condition of the evaporator. According to Fig.26.7-1, the diffuser efficiency lies between 0.725 and 0.83.

We will adopt $\eta_D = 0.725$ for our safe-side design principle.

The ejector efficiency is given by

$$\eta_D = \frac{2{,}800-2{,}620}{2{,}765 \quad ,285} = 0.375 \qquad (26.8\text{-E1})$$

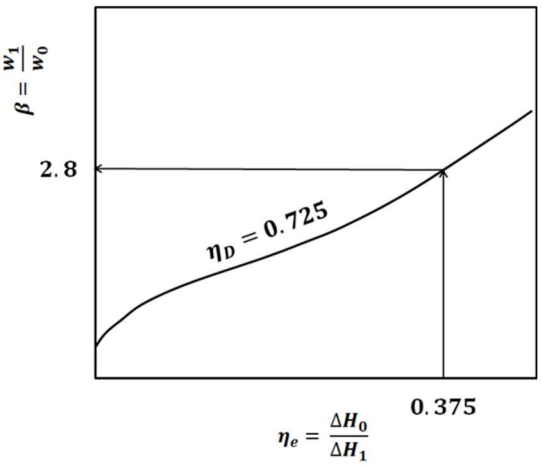

Fig.26.8-E1 Determination of necessary motive steam rate

Using Fig.26.8-1, the necessary motive steam rate can be obtained as $\beta = 2.8$, as shown in the above diagram. Therefore

$$w_1 = \beta\, w_0 = 2.8 \times 10.0 = 28.0 \text{ kg/h} \quad \text{(26.8-E2)}$$

The motive steam rate $w_1 = 28.0$ kg/h assumed at the beginning has been confirmed to be valid.

Usually the obtained motive steam rate is very large owing to the energy efficiency of steam ejectors.

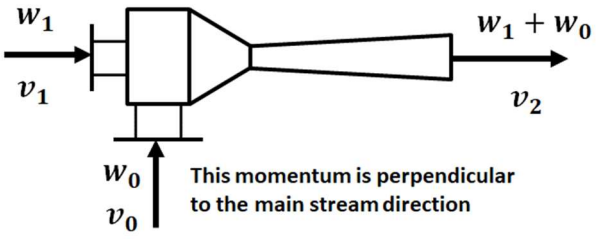

Fig.26.8-E2 Momentum balance around the ejector

The following momentum balance check can also be tested:

$$w_1 v_1 = \gamma(w_1 + w_0)v_2 \quad \text{(26.8-E3)}$$

When the constant (a kind of correction factor) $\gamma = 1.0$, the momentum balance is completely kept. However usually $\gamma = 0.8 \sim 0.9$ owing to the kinetic energy loss.

[EXAMPLE 26.8-E2]

Fig.26.8-E3 shows a continuous evaporating system equipped with a steam ejector for producing distilled water from the city water (20℃). A motive steam ($p_1 = 1.2$ MPa) with quality 98% can be utilized for the steam ejector. The evaporator is operated at normal pressure. A portion of the medium-pressure steam ($p_2 = 0.15$ MPa) issuing from the ejector is supplied into the coil for evaporation of the city water. Roughly speaking, from a viewpoint of VRC, the water vapor evaporated can be used after compression by the ejector as the heating medium for the same evaporator. Actually the latent heat of vaporization decreases with increasing pressure. For example, the heat of evaporation is 540 kcal/kg at 0.1 MPa and 532.7 kcal//kg at 0.15 MPa.

This is a problem how to determine the rate of the motive steam appropriate for compression by the ejector. As shown in the figure, the water (saturation temperature 110℃) condensed in the coil is used for preheating the city water up to 100℃ by the preheater.

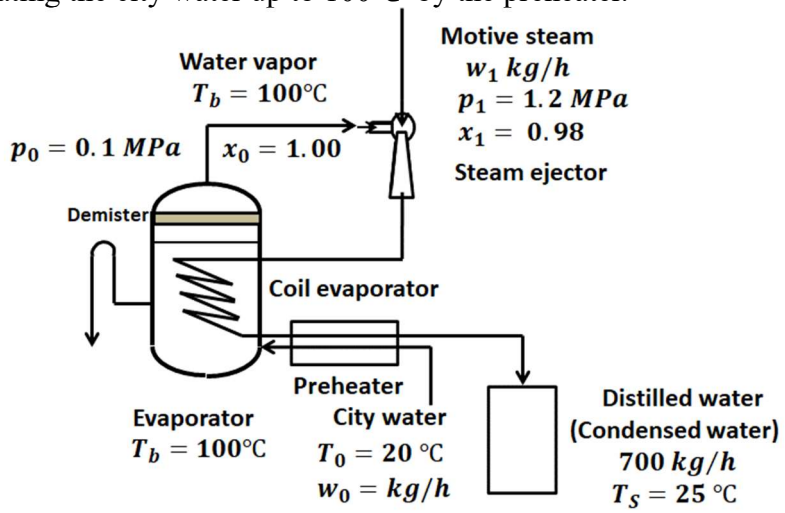

Fig.26.8-E3 Coil evaporator equipped with a steam ejector producing distilled water

Heat balance

This project is planning how efficiently to produce distilled water from $w_0 =$ 200 kg/h of the city water with the aid of the ejector.

The heat duty for the evaporator producing 200 kg/h of water vapor (0.1 MPa) is given by

$Q_{ev} = \lambda_{ev} w_0 = (540)(200) = 108{,}000$ kcal/h. (26.8-E4)

We can firstly calculate how much the steam (0.15 MPa) compressed by the ejector is necessary for the evaporator:

$w_s = Q_{ev}/\lambda_s = 108{,}000/532.7 = 202.7$ kg/h (26.8-E5)

The 202.7 kg/h of hot water (100℃) condensed in the coil is used to preheat the 200 kg/h of city water from 20℃ to 100 ℃ in the preheater. The heat exchange rate is given by

$Q_{II} = w_s Cp_s (T_s - T_{ds}) = w_0 Cp_0 (T_{bp} - T_{cw})$ (26.8-E6)

The outlet temperature of the distilled water is calculated as

$T_{ds} = T_s - \frac{w_0 Cp_0}{w_s Cp_s}(T_{bp} - T_{cw}) = 110 - \frac{(200)}{202.7}(100 - 20) = 31.1$ ℃ (26.8-E7)

Enthalpy calculation for determining the rate of motive steam w_1

The water vapor discharged from the evaporator is compressed by the ejector using w_1 kg/h of the motive steam ($p_1 = 1.2$ MPa). The compression ratio of the ejector is $\alpha = p_4/p_0 = 1.5$. Determine how much motive steam is required for this purpose.

The Mollier diagram shown below expresses the isentropic enthalpy change in the two-flow-passage model.

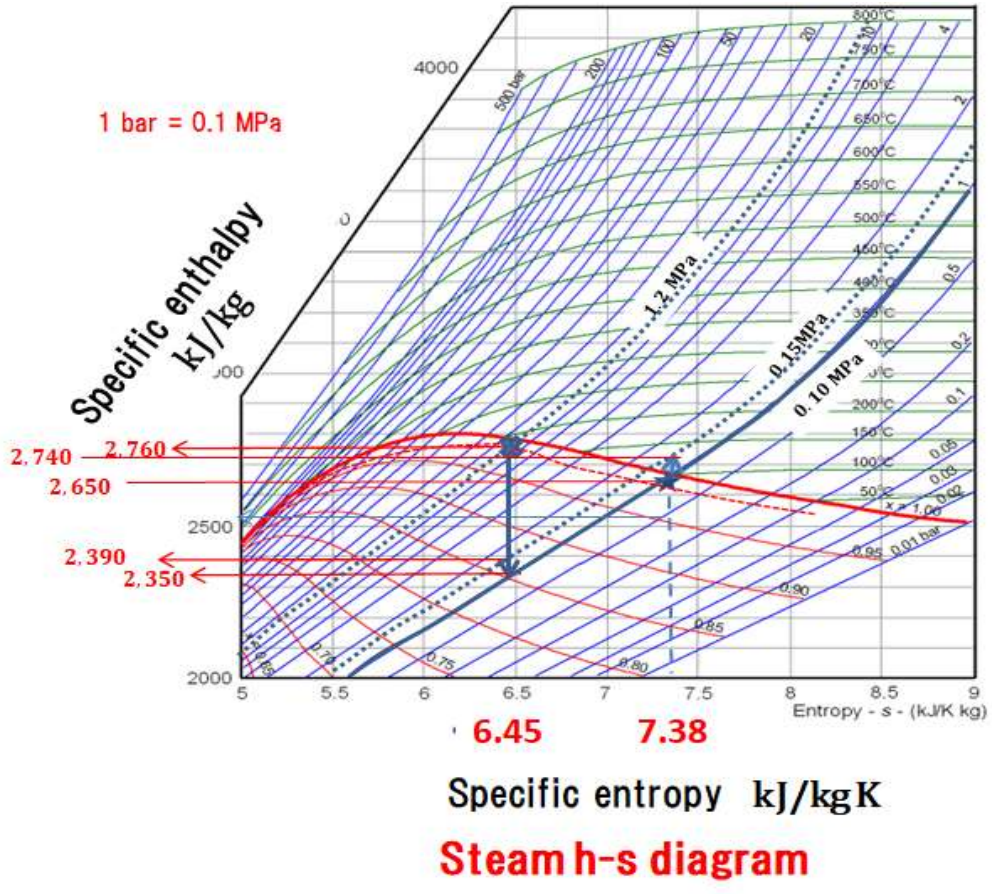

Fig.26.8-E4 Mollier diagram of an enthalpy change of a steam ejector for a process producing distilled water from the city water

The available energy of the motive steam (1.2 MPa) based on the water vapor (0.1 MPa) from the evaporator is given by

$H_1 - H_2 = 2{,}760 - 2{,}350 = 410$ kJ/kg (26.8-E8)

On the other hand, the isentropic enthalpy change of the stream B from p_0 to p_4 is given in the Mollier diagram:

$H_4 - H_0 = 2{,}740 - 2{,}650 = 90$ kJ/kg (26.8-E9)

For convenience, the enthalpy calculation can be schematically redrawn as Fig.26.8-E3.
According to TheFig.26.7-1, the diffuser efficiency is selected as $\eta_D = 0.725$ for the safe-side design.
The ejector efficiency is given by

$\eta_e = \frac{H_4 - H_0}{H_1 - H_2} = \frac{90}{410} = 0.22$ (26.8-E10)

Fig.25.7-1 gives the following steam flow ratio β for $\eta_D = 0.725$:

$\beta = w_1/w_0 = 1.1$ (26.8-E11)

Therefore the rate of the motive steam is determined as

$w_1 = 1.1\, w_0 = 1.1 \times 200 = 220$ kg/h (26.8-E12)

As a result, $w_0 + w_1 = 420$ kg/h of mixed steam (0.15 MPa) issues from the ejector.
From the heat balance calculation, 202.7 kg/h of the mixed steam should be supplied into the coil.
Finally the 202.7 kg/h of distilled water (31.1℃) is produced.
The 2.7 kg/h of the motive steam is consumed for producing the 202.7 kg/h of the distilled water.
For this condition, it should be kept in mind that the motive steam should also be pure enough.

Since the remaining mixed steam 217.3 kg/h still has 0.15 MPa, it can be utilized for another purpose.

The specific enthalpy H'_2 of the mixed steam issuing from the ejector exit can be calculated as

$w_1 H_1 + w_0 H_0 = (w_1 + w_0) H'_2$ (26.8-E13)

$(220)(2{,}760) + (200)(2{,}650) = (220 + 200) H'_2$

As a result, $H'_2 = 2{,}708$ kJ/kg.
This value lies a little bit above the vapor-liquid saturation curve. This suggests that the mixed steam is slightly superheated.

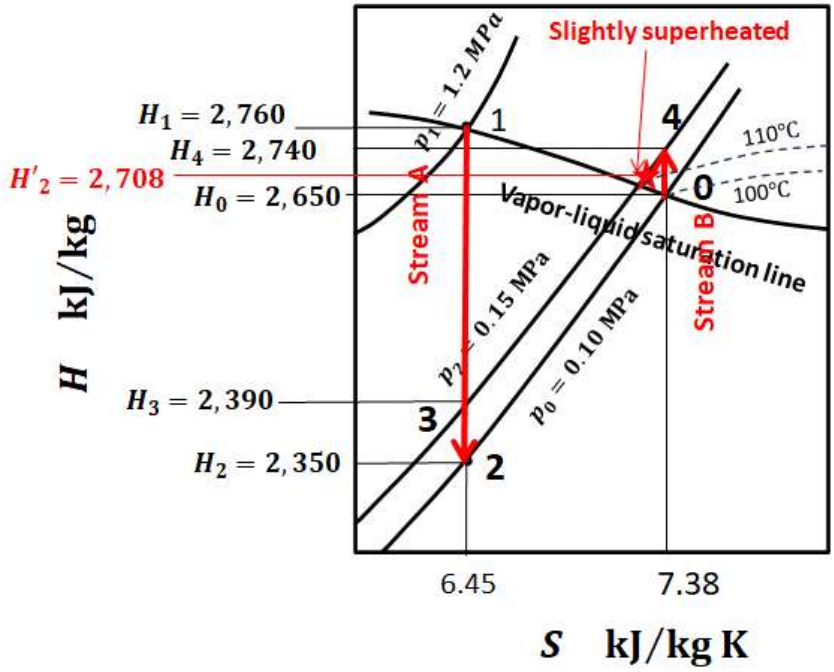

Fig.26.8-E5 Schematical picture of enthalpy change calculation on Mollier diagram

[PROBLEM 26.8-P1]

Fig.26.8-P1 shows a continuous evaporating system of coil evaporator accompanied with a steam ejector. An aqueous dilute solution of non-volatile organic substance ($w_f = 20$ kg/h, $C_f = 10$ wt%) is fed into the coil evaporator after preheating it from 25℃ to 81.6℃ (= boiling point at 0.05 MPa) by the steam w_c obtained from the ejector. In order to avoid thermal decomposition of the organic substance (solute), the evaporator is operated at $T_{ev} =$ 81.6℃ and $p_{ev} = 0.05$ MPa by condensing the steam w_c supplied into the coil from the steam ejector. Only for simplification, the elevation of the boiling point due to the solute can be neglected. A motive steam w_1 ($p_1 = 1.0$ MPa, quality $x_s = 1.0$) is utilized for the ejector. The concentrated product w_e is continuously withdrawn with the concentration of $C_e =$ 50 wt% from the bottom nozzle. Therefore $w_{ev} = 16$ kg/h of water should be evaporated, and then a part of w_{ev}, w_{cd} kg/h is condensed in an overhead condenser in order to save the rate of motive steam. The remaining water vapor w_0 kg/h is sucked into the ejector.

The latent heat of evaporation is assumed to be 550 kcal/kg at 0.05 MPa. The outlet pressure of the ejector should be set at the same as the pressure inside the coil, i.e. 0.10 MPa. The operating pressure inside the coil can be assumed to be 0.1 MPa constant. The latent heat of evaporation is 539 kcal/kg at 0.1 MPa. The compression ration p_2/p_0 is given by 2.0. The mixed steam w_c issuing from the ejector is consumed in the coil of the evaporator, and then its condensate is used in the preheater for heating the feed solution up to 81.6℃. The residual steam shown in Fig.26.8-P1) should be controlled to zero.

(1) What is the heat duty Q_{ev} of the evaporator?
(2) Calculate the necessary steam w_c issuing from the ejector for evaporation.
(3) Calculate the rate w_{cd} of water vapor condensed in the overhead condenser.
(4) Determine the diffuser efficiency η_D.
(5) Complete the Mollier H-S diagram (shown below) for determining the steam enthalpies H_4, H_0, H_1, H_2.
(6) Calculate of the enthalpy efficiency $\eta_e = (H_4 - H_0)/(H_1 - H_2)$.
(7) Determine the rate of the motive steam w_1
(8) Set up a heat balance of the preheater between the hot water issuing from the evaporator and the supplying stream of the aqueous solution feed. Then obtain the outlet temperature of the hot water issuing from the preheater.

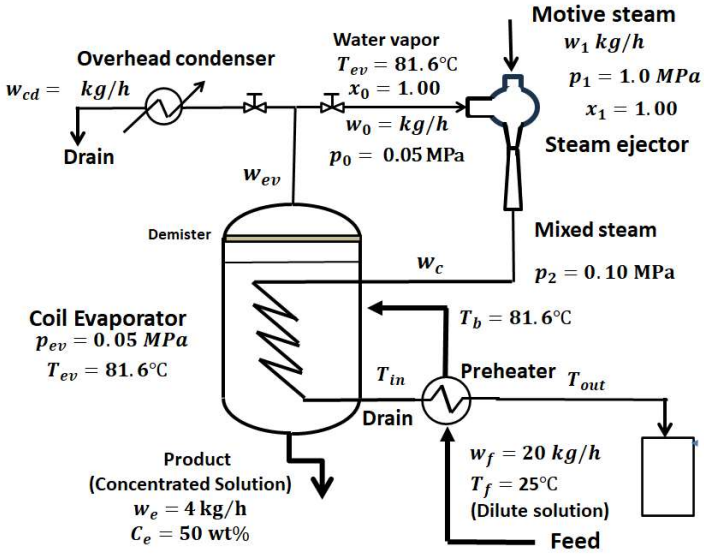

Fig.26.8-P1 Continuous evaporation system of coil evaporator accompanied with a steam ejector.

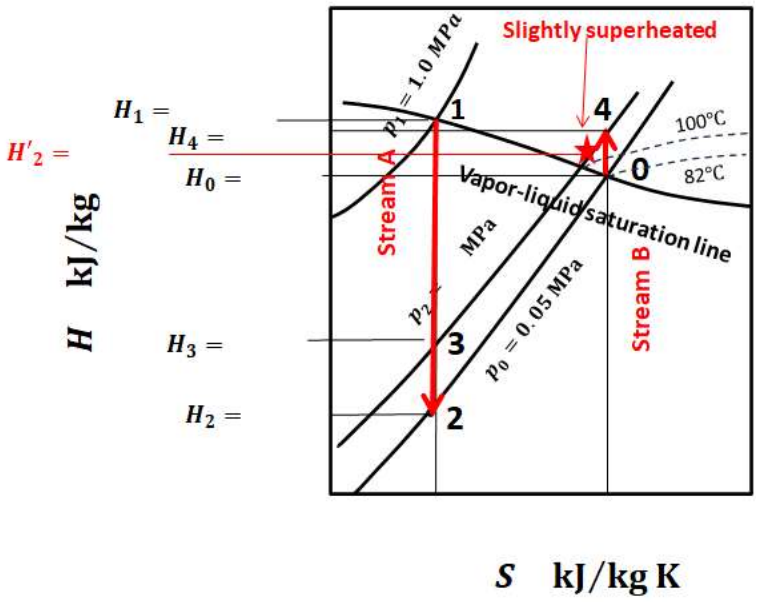

Fig.26.8-P2 Mollier diagram to be completed for PROBLEM 25.8-P1

26.9 Multi-stage Ejector System

Staging of steam ejectors becomes necessary for economical operation as the absolute suction pressure decreases since there is an upper limit for compression ratio of a single ejector system.

Fig.26.9-1 shows a standard system of two-stage steam ejector.

The two-stage ejectors comprise a primary high-vacuum ejector and a secondary low-vacuum ejector. The general operating range of two-stage steam ejector usually lies between 3 mmHg and 130 mmHg. The calculation method of two-stage steam ejector is the same as for a single steam ejector.

The mixed steam from the outlet of the primary ejector should be treated as the steam to be sucked into the secondary ejector. The same motive steam is usually supplied into both of the ejectors.

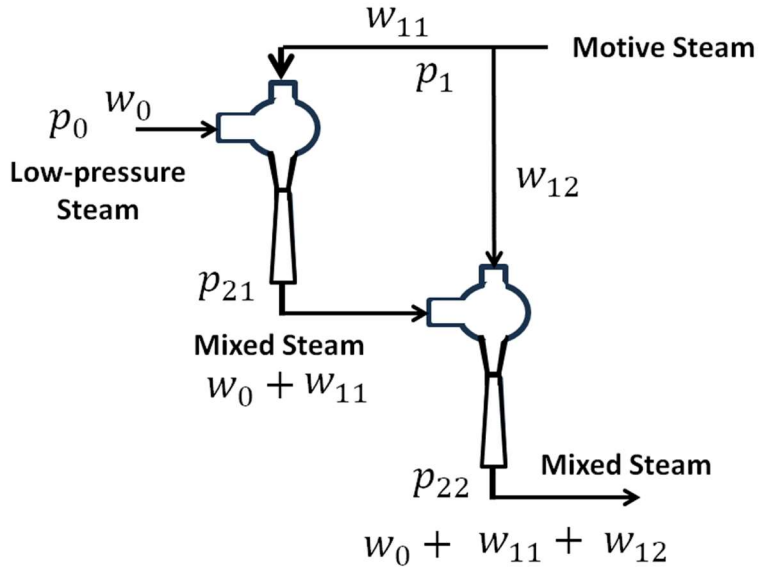

Fig.26.9-1 Standard type of two-stage ejector

[EXAMPLE 26.9-E1]

Fig.26.9-E1 shows a two-stage steam ejector for keeping the operating pressure of an evaporator at $p_0 = 3.0$ mmHg. The compression ratio is divided into two ejectors, i.e. α_1 and α_2 are given to be 3.0 and 5.0, respectively. The primary ejector is made smaller in the compression ratio α than the secondary ejector.

A high-pressure steam of 0.7 MPa can be utilized as the motive steam w_{11} and w_{12} for the two ejectors. The water vapor $w_0 = 15$ kg/h which is generated at 3 mmHg in the evaporator should be sucked by the #1 ejector using the motive steam w_{11}. The mixed steam $w_0 + w_{11}$ discharging from the outlet of the #1 ejector is supplied into the inlet of the #2 ejector. Calculate the necessary rate of the motive steam $w_{11} + w_{12}$ assuming no heat loss from the system to the surroundings.

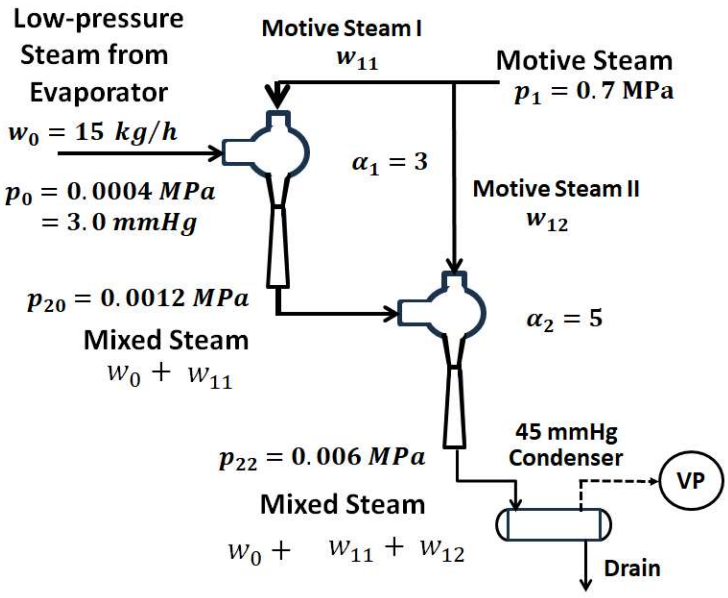

Fig.26.9-E1 Two-stage ejector for depressurizing an evaporator

Solution:

[Primary ejector]

A thermodynamic enthalpy-entropy diagram (Mollier H-S diagram) for water vapor is given by Fig.26.9-E2.

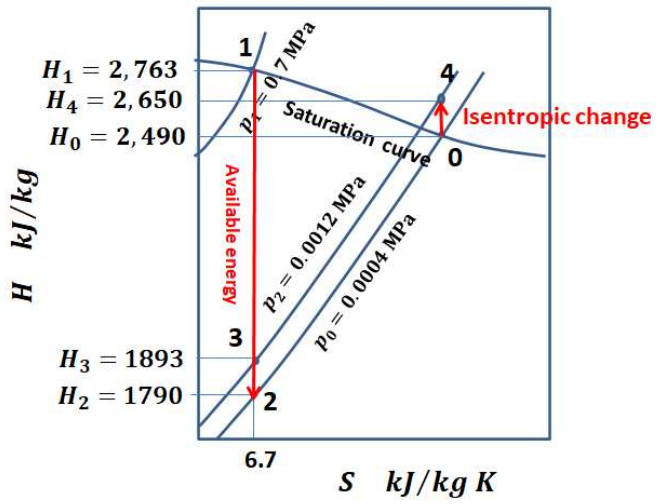

Fig.26.9-E2 Thermodynamic H-S diagram for enthalpy calculation of primary ejector

Following the two-flow-passage model introduced in Chapter 26.6-2, the isentropic change in the motive steam indicates the downward arrow from state 1 to 2. Regarding this stream A, the motive steam enthalpy becomes $H_1 = 2{,}763$ kJ/kg at $p_1 = 0.7$ MPa and $H_2 = 1{,}790$ kJ/kg at $p_2 = 0.0004$ MPa . Regarding stream B, the isentropic change is expressed as the upward arrow from state 0 to 4. The vapor enthalpy of stream B becomes $H_0 = 2{,}490$ kJ/kg at $p_1 = 0.0004$ MPa and $H_4 = 2{,}650$ kJ/kg at $p_2 = 0.0012$ MPa .
The isentropic enthalpy difference of the stream A meaning the available energy for stream B becomes $H_1 - H_2 = 2{,}763 - 1{,}790 = 973$ kJ/kg.
The isentropic enthalpy change of the stream B from p_0 to p_4 is given in the Mollier diagram: $H_4 - H_0 = 2{,}650 - 2{,}490 = 160$ kJ/kg.

According to Fig.26.7-1, since the suction pressure is 0.0004 MPa, the diffuser efficiency can be assumed as $\eta_{D1} = 0.55$ for the safe-side design.
The ejector efficiency defined by Eq.(26.8-1) is calculated as

$$\eta_e = \frac{H_4 - H_0}{H_1 - H_2} = 0.164$$

From the curve of $\eta_{D1} = 0.55$ in Fig.26.8-1, the ratio of motive steam to water vapor is obtained as $\beta = w_{11}/w_0 = 1.1$. Then the motive steam for the primary ejector amounts to
$w_{11} = \beta\, w_0 = 1.1 \times 15 = 16.5$ kg/h

The enthalpy of the mixed steam $w_0 + w_{11}$ is obtained by the following enthalpy balance:

$$w_0 H_0 + w_{11} H_1 = (w_0 + w_{11}) H'_0$$

That is

$$H'_0 = \frac{w_0 H_0 + w_{11} H_1}{w_0 + w_{11}} = 2{,}633 \text{ kJ/kg K}$$

In this condition, $T'_0 = 65$ ℃ (superheated steam)

[Secondary ejector]

The next enthalpy-entropy diagram (Mollier H-S diagram) for water vapor is given by Fig.26.9-E3.

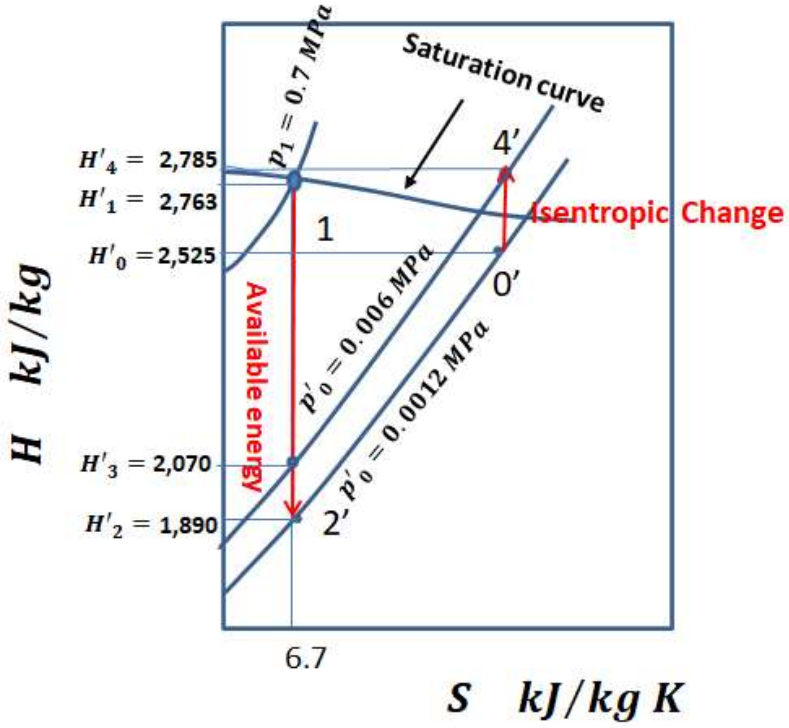

Fig.26.9-E3 Thermodynamic H-S diagram for enthalpy calculation for secondary ejector

The vapor to be sucked into the secondary ejector is

$w'_0 = w_0 + w_{11} = 31.5$ kg/h

The compression ratio is $\alpha_2 = 5$.

Since $p_{20} = 0.0012$ MPa, the diffuser efficiency can be assumed as $\eta_{D2} = 0.57$ for the safe-side design.

The isentropic enthalpy difference of the stream A of the secondary ejector is given by

$H_1 - H'_2 = 2{,}763 - 1{,}890 = 873$ kJ/kg.

The isentropic enthalpy change of the stream B from p_0 to p_4 is given in the Mollier diagram:

$H'_4 - H'_0 = 2{,}785 - 2{,}525 = 260$ kJ/kg.

$$\eta'_e = \frac{H\prime_4 - H\prime_0}{H_1 - H\prime_2} = 0.30$$

From Fig.26.8-1, $\beta' = w'_1/w'_0 = 3.0$. Therefore $w_{12} = \beta' w'_0 = 94.5$ kg/h.

The total motive steam necessary for the two ejectors amounts to

$w_{12} = 16.5 + 94.5 = 111$ kg/h,

The mixed steam issuing from the secondary ejector has

$p'_2 = 0.006$ MPa $= 45$ mmHg, $H''_2 = 2{,}730.5$ kJ/kg,

Its outlet temperature $T_{out} = 120$ ℃ implies a superheated steam but its saturation temperature reduces to 37℃ at 45 mmHg.

It can be considered that this steam temperature is appropriate for the condenser using the city water (25℃) as the cooling water. As a result, the condenser can be compact as the work required of the vacuum pump is reduced very much.

The vacuum pump to be used for the 45 mmHg condenser can be made very much profitable in the work requirement as compared with the vacuum pump originally used for the evaporator.

Fig.26.9-E4 gives the summary of calculation results.

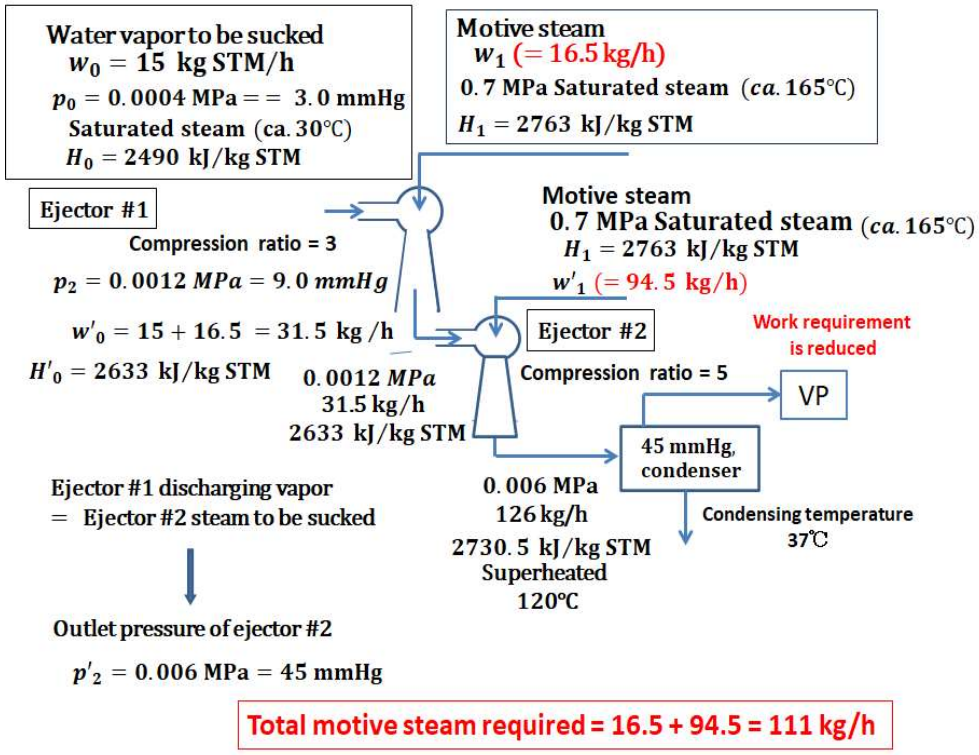

Fig.26.9-E4 Summary of calculation results

26.10 Special Matters of Heed to Ejector Engineering

We have been studying the engineering aspect of steam ejectors by the thermodynamic consideration. Let us consider why a steam ejector cannot be considered by the fundamental laws of momentum and enthalpy conservations.

The behavior of the flow and enthalpy transfer in a steam ejector is actually so difficult to analyze by theory that we have to rely on the empirical investigations.

Fig.26.7-1 of the diffuser efficiency and Fig.26.8-1 of the calculation of the rate of motive steam are an example of empirical databases.

In particular, Fig.26.8-1 is worthy to reconsider.

According to the two-flow-passage model, as shown in Fig.26.10-1, a steam ejector can be regarded as a double-tube exchanger shown below:

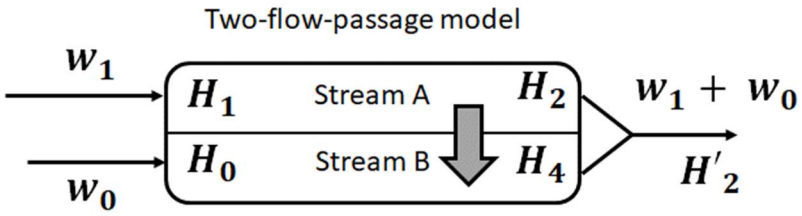

Similarly to the exchange rate of enthalpy in a double tube exchanger,
the exchange rate of enthalpy between streams A and B without any losses is given as

$$w_1(H_1 - H_2) = w_0(H_4 - H_0)$$

$$\frac{w_1}{w_0} = \frac{H_4 - H_0}{H_1 - H_2}$$

Fig.26.10-1 Exchange of enthalpy between stream A and stream B in an ideal state

The two-flow-passage model gives the enthalpy balance between the stream A (motive steam) and stream B (low-pressure steam):

$$w_1(H_1 - H_2) = w_0\,(H_4 - H_0) \tag{26.10-1}$$

The following relation is obtained:

$$\frac{w_1}{w_0} = \frac{H_4 - H_0}{H_1 - H_2} \tag{26.10-2}$$

This relation implies that the ratio $\beta = w_1/w_0$ of motive steam to low-pressure steam to be sucked is proportional to the enthalpy efficiency η_e.

As shown in Fig.26.10-2, for comparison with the empirical data, the above relation can be plotted in the schematic picture of Fig.26.8-1 which is usually employed for the practical design procedure in industry.

From a fundamental consideration, the above enthalpy balance should have been done with H_3 instead of H_2.

In addition, the two-flow-passage model does not take into account the interactions such as mixing and friction loss/viscous dissipation between the two streams.

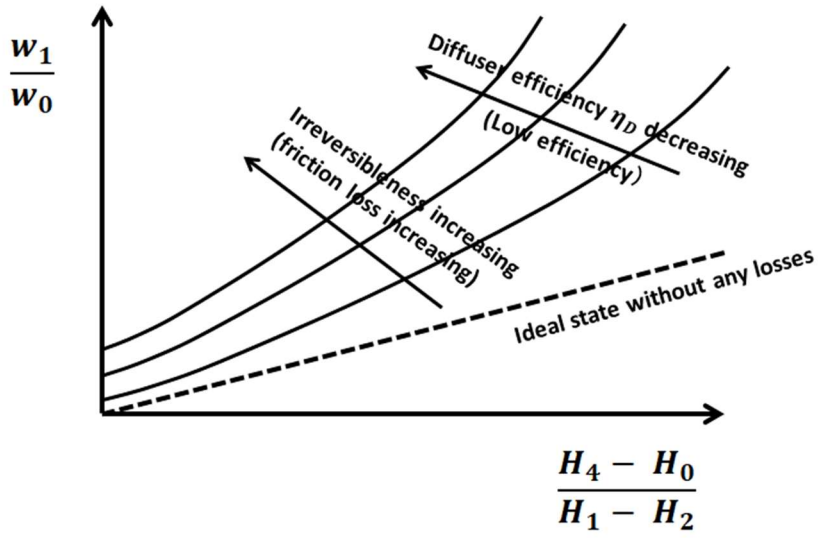

Fig.26.10-2 Comparison of empirical data on ejector efficiency with ideal state variation

At any rate, it has been confirmed from the figure that a steam ejector is usually operated with an efficiency much lower than the ideal operating condition without any losses.

It should be kept in mind that ejectors still have various advantages of low cost, easy maintenance, safe operation, simple structure, and sufficient durability.

Still much remains to be done for improving the ejector efficiency.

26.11 Macroscopic Momentum Balance for Steam Ejectors

It is worthy to reconsider the above steam ejector problems by means of macroscopic momentum balance. (see Chapter 4.3 of PART I)

According to Eq.(4.3-7) of Chapter 4.3 of PATRT I, the macroscopic momentum balance set up over a steam ejector can be expressed as

$$-\vec{F}_f = w_1\langle\overrightarrow{v_1}\rangle + w_0\langle\vec{v}_0\rangle - w_2\langle\overrightarrow{v_2}\rangle - p_1S_1\overrightarrow{n_1} - p_0S_0\overrightarrow{n_0} - p_2S_2\overrightarrow{n_2} + \mathrm{m}\vec{\mathrm{g}} \quad (26.11\text{-}1)$$

Here $\vec{F}_f$ means the total holding force against steam stream including the frictional force acting on the fluid stream.

As can be seen from the figure, the remaining variables w_i, $\langle\overrightarrow{v_i}\rangle$, p_i, $\overrightarrow{n_i}$, S_i, are mass flow rate of steam, velocity vector, pressure, unit vector, and cross-sectional area of inlet and outlet, respectively.

The outlet mass flow rate is

$$w_2 = w_1 + w_0 \quad (26.11\text{-}2)$$

The gravitational effect $\mathrm{m}\vec{\mathrm{g}}$ can be neglected because the steam ejector is placed horizontally.

With respect to the main stream direction, the equation is simplified as

$$-F_D = w_1v_1 - w_2v_2 + p_1S_1 - p_2S_2 \quad (26.11\text{-}3)$$

$$v_1 = w_1/\rho_1S_1 \text{ and } v_2 = (w_1 + w_0)/\rho_2S_2 \quad (26.11\text{-}4)$$

If the total holding force is known, the mass flow rate of the motive steam required can be determined.

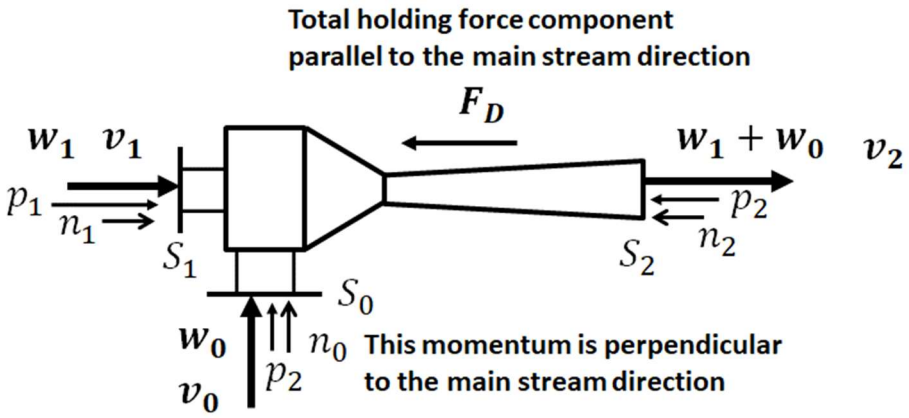

Fig.26.11-1 Macroscopic momentum balance set up around a steam ejector

Nomenclature

a	effective interfacial area per unit packed volume, [m^2/m^3]
Cp	heat capacity, [J/kmol K]
D	overhead product, [kmol/s]
D_G, D_L	diffusivity in gas- and liquid-phase, [m^2/s]
F	feed rate, [kmol/s] or F-factor [$(m/s)(kg/m^3)^{0.5}$]
G_M	superficial molar gas-mass velocity, [$kmol/m^2s$]
$H_X,\ H_Y$	latent heat (enthalpy) of x- and y- component, [J/kmol]
h_{ETP}	HETP (Height Equivalent to a Theoretical Plate), [m]
K	vapor-liquid equilibrium constant, [-]
K_x, K_y	overall mass transfer coefficients defined by vapor-phase and liquid-phase concentrations [$kmol/m^2s$]
k_x, k_y	mass transfer coefficients of vapor-phase and liquid-phase film [$kmol/m^2s$]
m	slope of equilibrium curve, dy/dx,
n	theoretical plate/stage number, [-]
Re	Reynolds number, [-]
Sc	Schmidt number, [-]
T, t	temperature, [K]
x_A, y_A	mole fraction of component A, liquid- and vapor-phase, [-]
z	height of packing section, [m]
α_{AB}	relative volatility, [-]
δ_G, δ_L	thicknesses of gas-phase and liquid-phase film, [m]
λ	stripping factor, [-]
μ	viscosity, [kg/m s]
μ_{JT}	Joule-Thomson coefficient, [-]

Subscripts

A, B	component A, B
G, L	gas-phase, liquid-phase
i	interface

CHAPTER 27
VISUALIZATION OF DYNAMIC TRANSPORT PHENOMENA

27.1 Observation of an Organized Structure of Stirred Tank Reactor[1,2)]

In any kinds of liquid-phase chemical reactions, any reactants participating in a reaction must be transferred to collide with each other. This implies that any chemical reaction makes progress with micro-mixing due to the coupling of two or more nonlinear dynamics. In particular, complex reactions are apt to become hysteretically unstable depending upon the degree of micro-mixing.

We have an experience in observing nonlinear dynamical structure of chaotic mixing motion at very low Reynolds numbers in a disk-turbine stirred tank reactor with the aid of flow-visualization technique.[1)]

The Reynolds number is defined using the rotation number of the disk turbine impeller as

$$Re = \frac{\rho d^2 N}{\mu} \qquad (27.1\text{-}1)$$

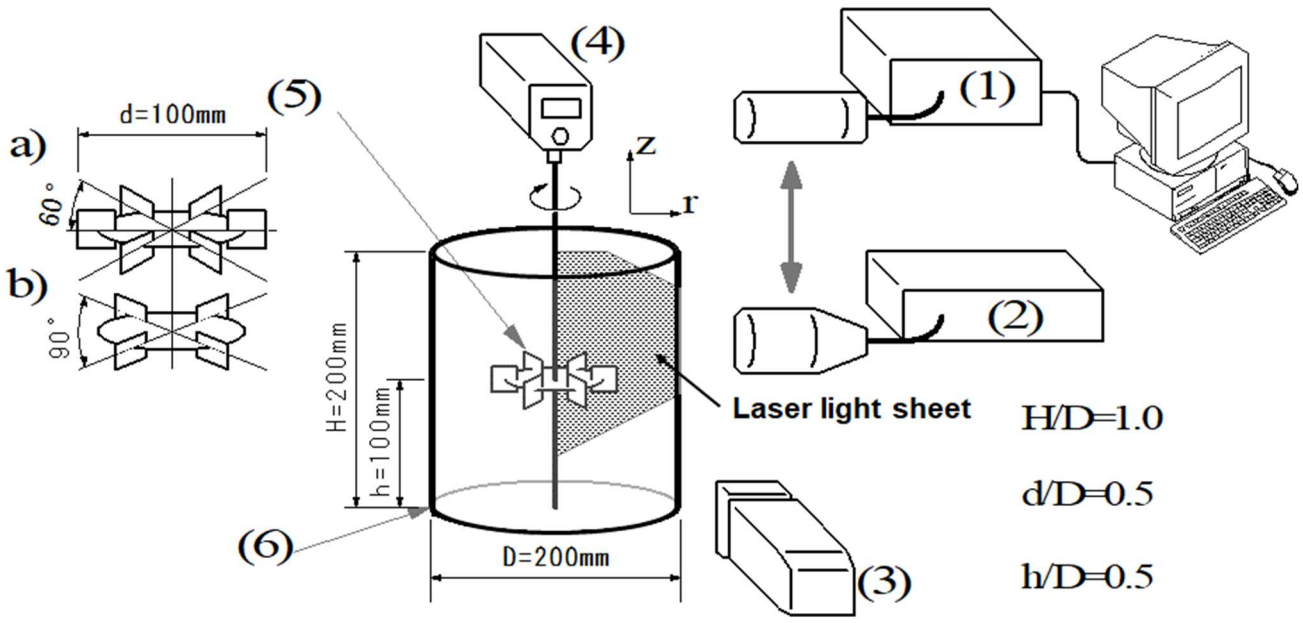

Fig.27.1-1 Experimental apparatus for visualization of a stirred tank flow
(1) LDV measuring system, (2) Ar-laser system, (3) Digital video camera, (4) Motor control system, (5) Disk turbine impeller (a: six-bladed, b: four-bladed), (6) Cylindrical test vessel

The experimental apparatus shown in Fig.27.1-1 consists of a transparent cylindrical vessel (200 mm ID) with no baffle plates which is equipped with four-bladed or six-bladed disk turbine impeller. The upper end of liquid solution is fixed with a flat plate, so that the ratio of the liquid height to the inner diameter of the vessel is fixed at unity and the impeller is placed at height $h = 100$ mm, i.e. $h/D = 0.5$. An aqueous glycerin solution ($\mu = 0.85 \sim 1.5\ \mathrm{Pa \cdot s}$) which contains a small amount of basic solution (0.5 N-NaOH + glycerin) is colored with fluorescent green dye. (Laser fluorescent method)

After the basic solution filled in the vessel reaches a certain steady flow state, a small amount of acidic solution (0.5 N-HCl + glycerin) is poured from the top of the vessel, so that the fluid region locally neutralized due to the mixing of acidic and basic solutions can be decolored. The cross-section of the flow field is illuminated by a plane sheet of Ar-laser light.

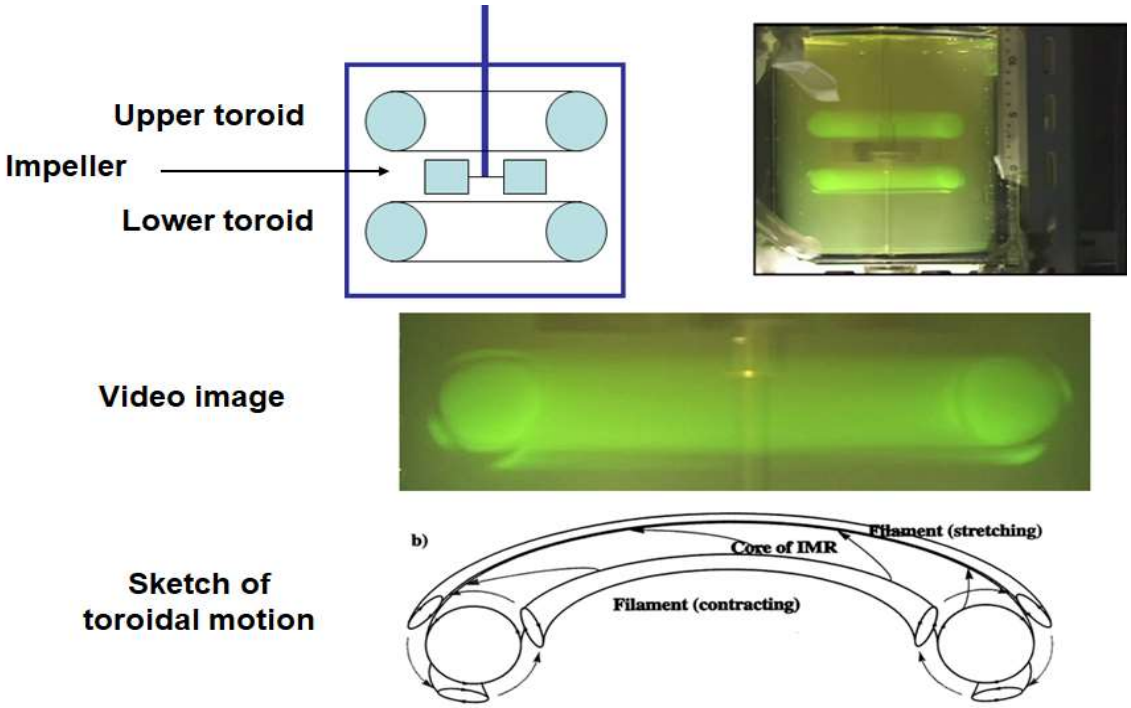

Fig.27.1-2 Ring-doughnut-shaped mixing regions appearing above and below the rotating impeller

Fig.27.1-2 shows two ring-doughnut-shaped toroidal regions accompanied by three satellites (named "isolated mixing region") appearing respectively above and below the rotating impeller when $Re < 100$. From the video images, the toroidal motion can be observed.

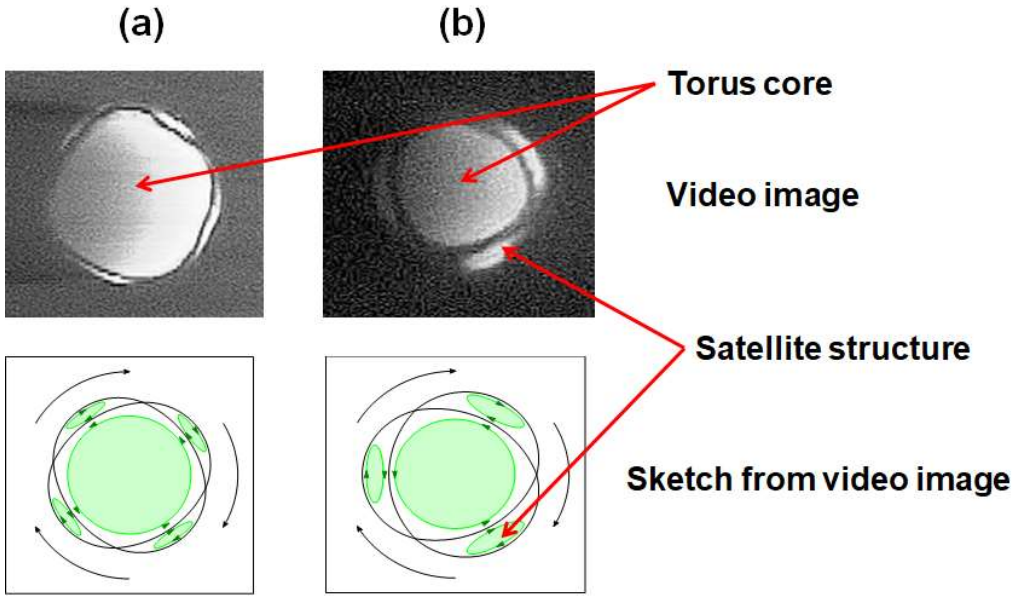

Fig.27.1-3 Cross-sectional views of the lower isolated mixing regions observed with four-bladed and six-bladed turbine impellers.

Fig.27.1-3 shows two cross-sectional views of the lower isolated mixing region observed with the six-bladed and four-bladed turbine impellers. The torus structure depends on the number of turbine blades. Four satellite-like filaments go around the central core for the case of four-bladed turbine ($Re = 29$). Three filaments can be seen to go around the central core for the case of six-bladed turbine ($Re = 31$).

A set of stable satellite islands circulate around the torus with a constant period depending on the period of the impeller rotation. It can be conjectured that this filament-torus structure depends on the periodical perturbation produced by the rotating turbine blades.

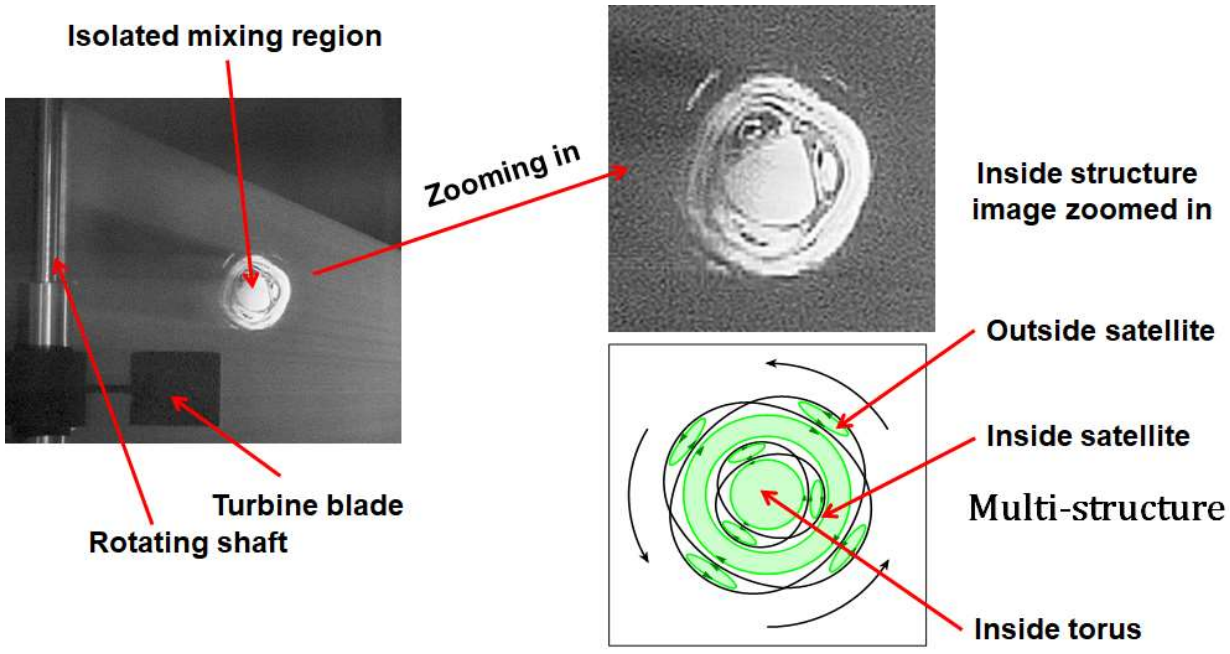

Fig.27.1-4 Multi-structure inside an isolated mixing region (six-bladed turbine impeller)

Another set of islands have been found inside the core region in the case of six-bladed turbine ($Re = 29$). This flow structure is formed by unsteady zigzag startup operation ($Re: 29 \rightarrow 0 \rightarrow 29$). This suggests that the isolated mixing region has a complex multi-structure consisting of various KAM tori.

Fig.27.1-5 shows the streak lines of the circulating flow surrounding the isolated mixing region visualized by suspending small MMA particles. This picture is taken at the same time by suspending small MMA particles in the stream of the basic solution.

The trajectories of the tracer particles show the streak lines of the outer circulating flow.
It can be considered that the primary effect of mixing is controlled in the main flow region outside the isolated mixing region.

The isolated mixing region surrounded by the circulating flow shows a turnstile-lobe like structure generated by each stroke of the passing turbine blades, which causes the chaotic mixing (alternate stretching-folding) mixing at the boundary between the circulating flow region and the isolated mixing region. This implies that the dynamically-chaotic micro-mixing occurs even in a very complex fractal-/multi-structure. The streak lines near the outer edge of turbine blades are oscillating with the fluid ejected by the turbine blades.

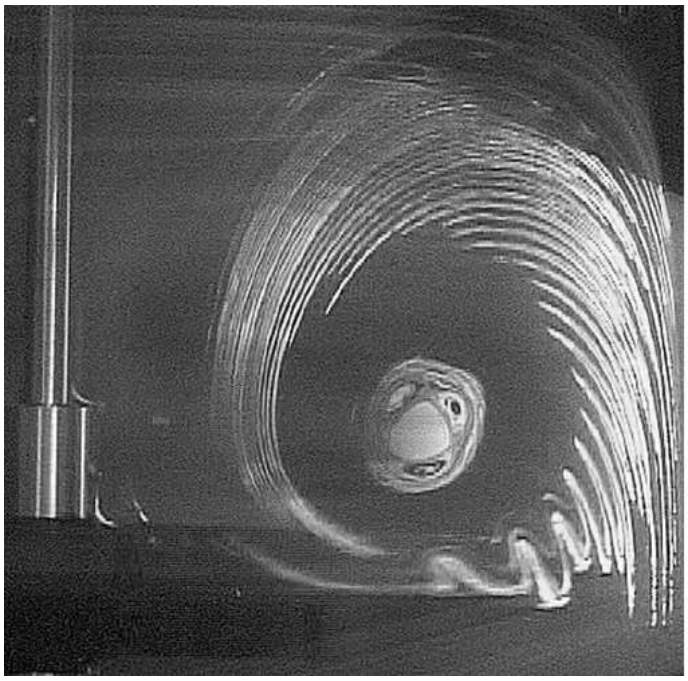

Fig.27.1-5 Streak lines of circulating flow surrounding an isolated mixing region (six-bladed turbine impeller)

Much remains to be done for observing at higher Reynolds numbers.

1) Makino, T., Kaise, T., Ohmura, N., and Kataoka, K., Lase-optical observation of chaotic mixing structure in a stirred vessel, Proc. of 10th Int. Symp. on Application of Laser Techniques to Fluid Mechanics, July 10-13, Lisbon, CD-ROM (Session 21-2) (2000)
2) Makino, T., Ohmura, N., and Kataoka, K., Observation of Isolated Mixing Regions in a Stirred Vessel, *J. Chem. Eng. Japan*, Vol.34(5), 574 (2001)

27.2 Transitional Route of Laminar to Chaotic Flow[3)]

27.2-1 Instability of circular Taylor-Couette flow

If the degree of flow intensity goes beyond a critical point, many kinds of shear flow generally become unstable due to non-linear dynamic phenomena. We know that a laminar flow in a straight circular tube becomes unstable when the Reynolds number reaches $Re_{cr} = 2{,}100$. We study in Chapter 3.2 of PART I that when the flow rate is increased enough, the velocity gradient near the tube wall becomes so steep that an unstable rotating motion due to the moment effect of shear stress occurs to generate turbulent eddy motions.

In the case of the straight tube flow, there is a transitional region in between $2{,}100 < Re < 10{,}000$. The width of the transitional region depends on various conditions such as pipe roughness, tube length from its entrance, and perturbation superimposed in the approaching stream. The micro-structures in the transitional region are so complicated that the route to turbulence generation has not yet realized enough.

At any rate, in this kind of parallel flow, the Reynolds number can be considered as a universal dimensionless parameter indicating the flow states.

Shear flow between two concentric cylinders with the inner one rotating is a very interesting shear flow for investigation of the transitional scenario to chaos in the pure physical science. This flow is firstly introduced at page 51 of Chapter 6.2. In this flow system, the Reynolds number is defined for this flow system as

$$Re = \frac{\rho R_i \omega d}{\mu} \qquad (27.2\text{-}1)$$

Here the annular gap width *d* is a very important controlling parameter when the flow condition is specified because there is a distinction in flow structure between the wide-gap and small-gap systems.

Therefore the flow problem is considered by separating into a wide-gap problem and a small-gap problem.

Fig.27.2-1 gives a schematic picture of time-independent laminar Taylor vortex flow and time-dependent wavy Taylor vortex flow.

When the rotation speed of the inner cylinder, i.e. the Reynolds number goes beyond a certain critical point ($Re^* = Re/Re_{cr} = 1$), the basic laminar shear flow in the annulus between the concentric cylinders becomes unstable to lead to the transition to a laminar cellular vortex flow, referred to as Taylor vortex flow.[4)]

This time-independent flow regime is drawn on the left side of Fig.27.2-1.

As the rotation speed is further raised, this flow system exhibits a sequence of distinct time-independent followed by time-dependent flow regimes until chaotic turbulence occurs.

The first time-dependent wavy vortex flow is drawn on the right side of Fig.27.2-1.

This transitional scenario is of great importance for the fundamental concept of non-linear mechanics in physics.

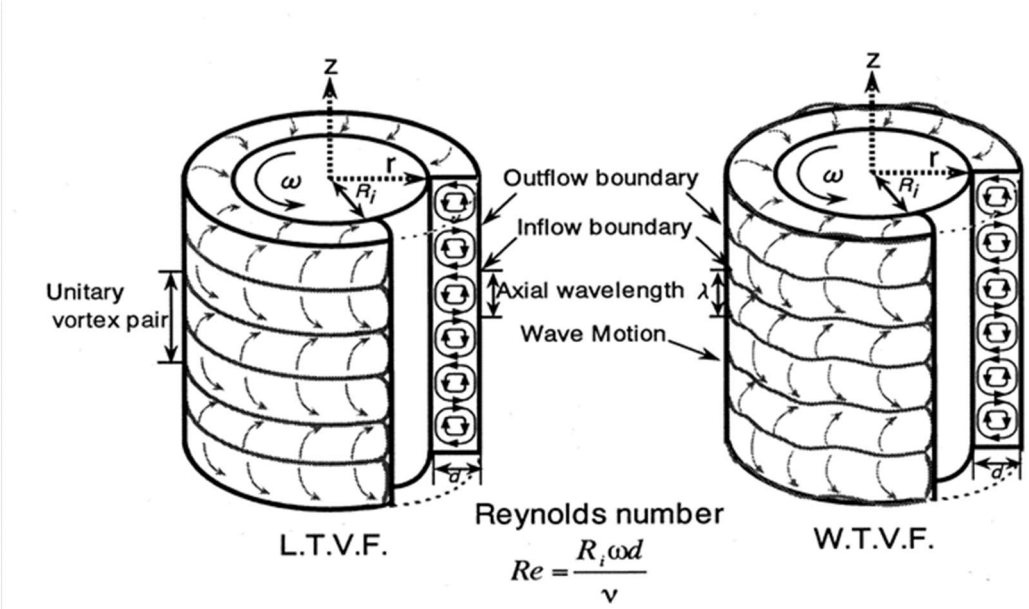

Fig.27.2-1 Schematic pictures of time-independent and time-dependent Taylor vortex flows

27.2-2 Visualization of time-independent and time-dependent vortex flows[3)]

For observing such time-dependent vortical structures, the flow visualization technique suspending fine aluminum platelets in the viscous test fluid is very often utilized. The flow behavior can be observed clearly as variations in the transmitted or reflected intensity from the scattered light of the suspending aluminum platelets aligned with the stream. We can observe dynamic behaviors of the outside surfaces of flow structure. (Aluminum platelet flow visualization method)

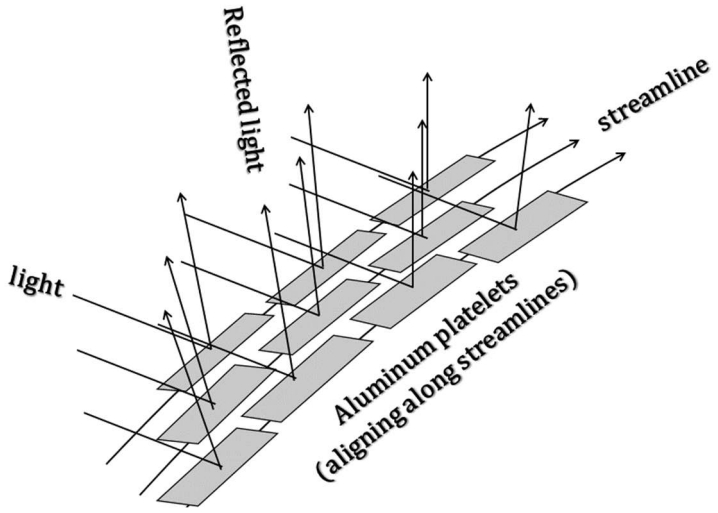

Fig.27.2-2 Flow visualization by suspending fine aluminum platelets in a stream

All the following photographs[3)] of Taylor vortex flows visualized by fine aluminum platelets are taken in a wide annular gap between two concentric rotating cylinders. The radius ratio of the inner cylinder to the outer cylinder is $\eta = R_i/R_o = 0.68$.

(1) Laminar Taylor vortex flow

The Taylor-Couette flow system has the first instability from purely laminar Couette flow to a stable laminar cellular vortex flow called “Taylor vortex flow.”

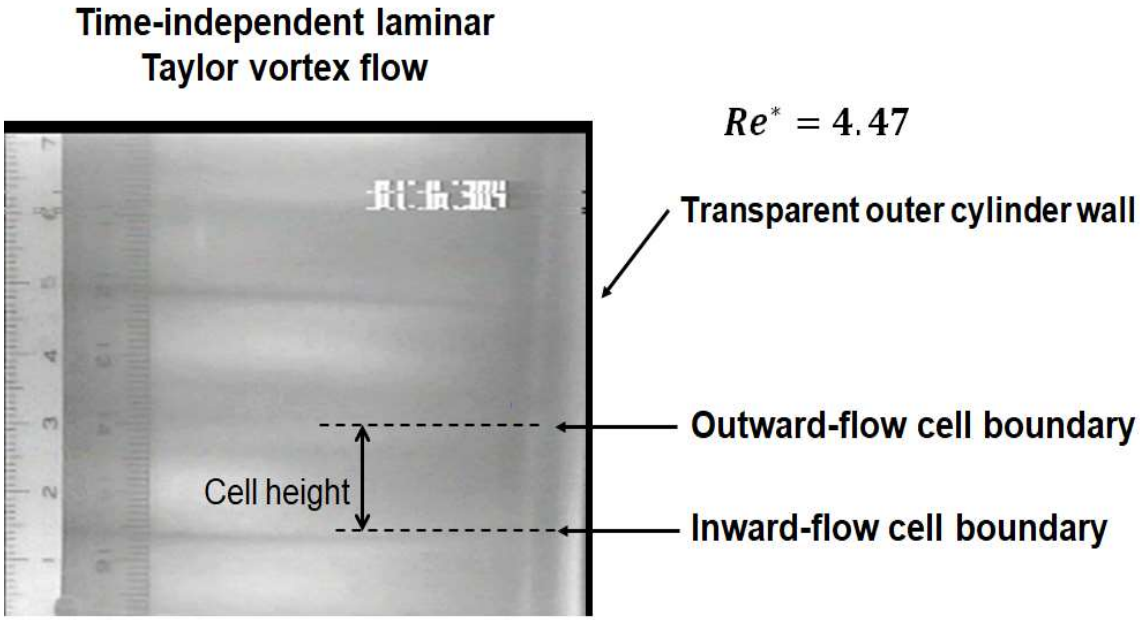

Fig.27.2-3 Time-independent laminar Taylor vortex flow visualized by suspending fine aluminum platelets

The dark horizontal lines indicate the boundary between the neighboring two vortices. Ring-doughnut-shaped counter-rotating vortices are arrayed along the cylinder axis. The first transition to a time-independent laminar vortex flow called “Taylor instability”[4] depends upon the radii R_i/R_o of the two cylinders, the critical rotation speed of the inner cylinder and the kinematic viscosity of fluid.

As distinct from the Reynolds number for straight pipe flows, the critical Reynolds number cannot easily be determined for the Taylor-Couette flow system.

Thus it is very difficult to uniquely define the flow system since the Reynolds number still depends on d/R_i.

Usually we consider this flow problem by separating into small-gap and large-gap problems.

The critical Reynolds number for small annular gap is given by

$$Re_{cr}\sqrt{d/R_i} = 41.2 \quad \text{if} \quad d/R_i \ll 1 \tag{27.2-2}$$

This critical Reynolds number group $Re_{cr}\sqrt{d/R_i}$ for the small gap problem can be predicted by the linear theory of hydrodynamic stability.

We observe for the present equipment with $\eta = R_i/R_o = 0.68$ that the critical Reynolds number becomes $Re_{cr} = 86.2$, i.e. $Re^*_{cr} = 1$.

Since the critical Reynolds number still varies with the annular gap, the Reynolds number ratio $Re^* = Re/Re_{cr}$ is used as the dimensionless flow parameter.

The axisymmetric laminar vortex flow continues to keep the stabile structure over some range of the Reynolds number above the critical point. All the flow properties such as local pressure and velocity components are kept time-independent everywhere in this flow regime.

3. Kataoka, K., "Taylor vortices and instabilities in circular Couette flows," Encyclopedia of Fluid Mechanics, Gulf Pub., Houston, ed. By N.P. Cheremisinoff, Chap.9, 236-274 (1986)
4. Taylor, G. I., *Phil. Trans.,* **A223,** 289 (1923), *Proc. Roy. Soc.* (London), **A151**. 494 (1935)

(b) Singly-periodic wavy vortex flow

As the rotation speed is increased further, the axisymmetric Taylor vortex flow becomes unstable and the instability leads to a new time-dependent vortex flow called "wavy vortex flow."

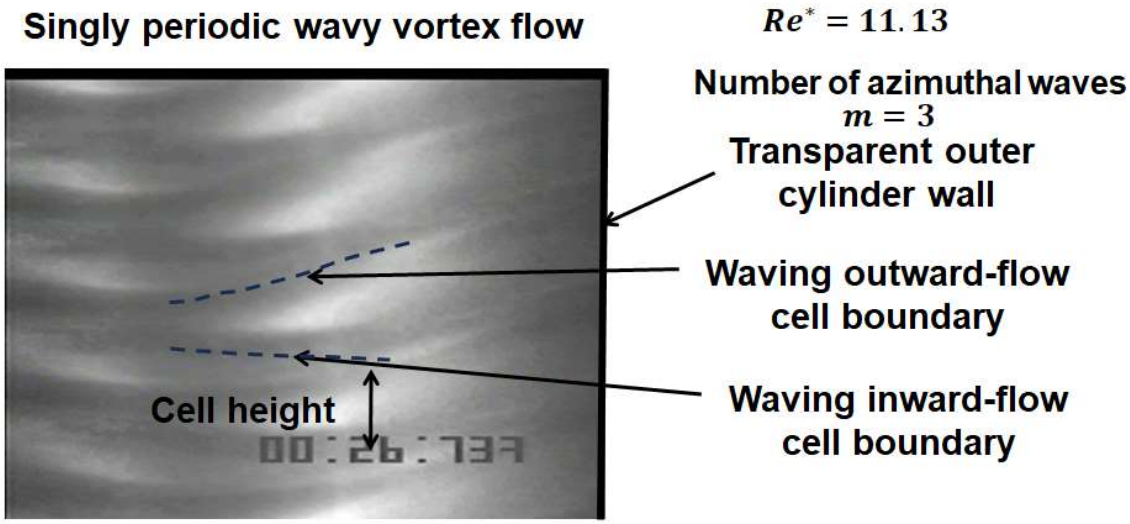

Fig.27.2-4 Time-dependent singly periodic wavy vortex flow (m= 3)

Fig.27.2-4 shows time-dependent wavy vortex flow observed when $Re^* > {Re_{w1}}^*$
The number of azimuthal waves is 3.

As can be seen in the photograph of Fig.27.2-4, the vortex boundaries show time-dependent S-shaped sinusoidal waves. This instability is known as wave instability. The second critical Reynolds number Re_{w1} depends on the ratio of the gap to the inner cylinder diameters. The wavy vortex flow with m waves in the azimuthal direction shows many stable states at a given Reynolds number. The time-dependent wavy vortex flow having a single fundamental frequency and its harmonics is called "singly periodic wavy vortex flow."

The fundamental frequency corresponds to the frequency of traveling azimuthal waves passing a point of observation.

(c) **Doubly-periodic wavy vortex flow**

As the Reynolds number is raised further, the wavy vortex flow becomes more complex at Re_{w2}, where the amplitude of the azimuthal waves varies periodically with time.

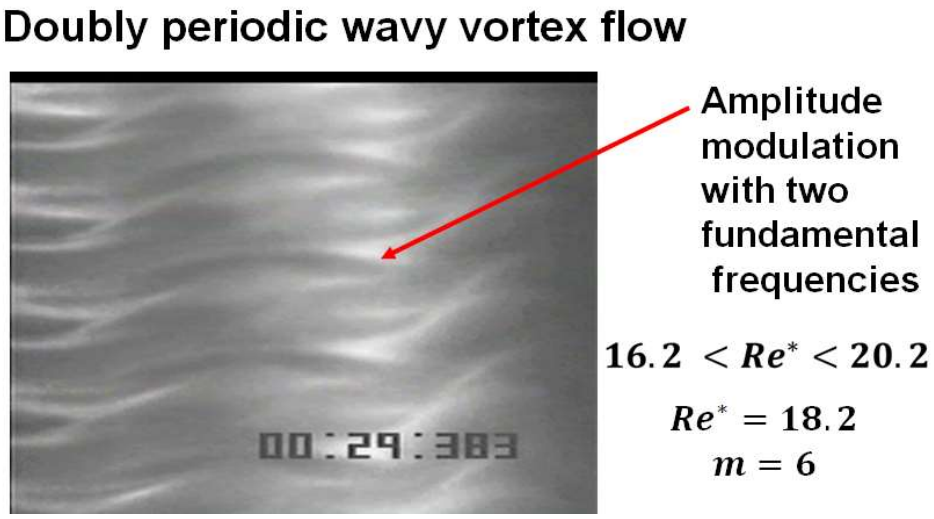

Fig.27.2-5 Doubly periodic wavy vortex flow

This amplitude-modulated wavy vortex flow called "doubly periodic wavy vortex flow" has two fundamental frequencies; the first fundamental frequency comes from the basic wave motion and the second fundamental frequency from the periodicity of amplitude-modulation. This transition appears at about $Re^*_{w2} = 16$.

These quasi-periodic wavy vortex flow regimes exhibit various bifurcation properties depending not only upon the equipment dimensions such as the annular gap width and height but also upon the start-up operation as to how to reach a steady state.

(d) **Weakly turbulent wavy vortex flow**

Then when $Re > Re_{ch1}$, the doubly periodic vortex flow undergoes the next transition to weakly turbulent wavy vortex flow where chaotic turbulence is superimposed on the wavy vortex structure.

It can be considered that this transition implies the generation of chaotic turbulence.

It is still a question as to whether or not the generation of chaos results from nonlinear interaction of fundamental frequencies and their harmonics of azimuthal wave motion.

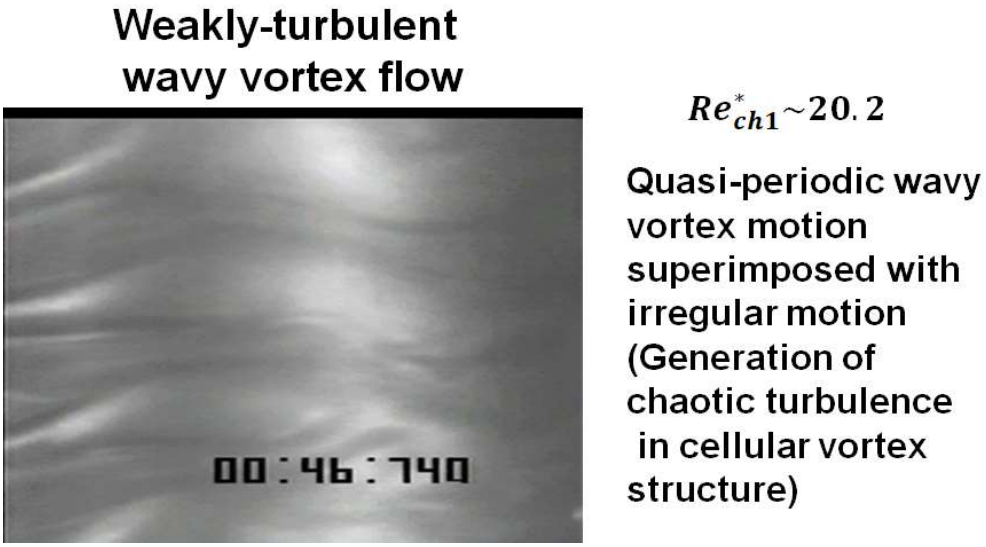

Fig.27.2-6 Weakly turbulent wavy vortex flow (m = 6)

(e) Fully turbulent Taylor vortex flow

As the Reynolds number goes beyond a critical value Re_{ch2}, the azimuthal waves disappear but the cellular vortex structure is still preserved.

The author obtained a triply-periodic like spectrum from an electrochemical method but its existence remains denied.

For the present, it is generally considered that no triply periodic wavy vortex flow has yet confirmed.

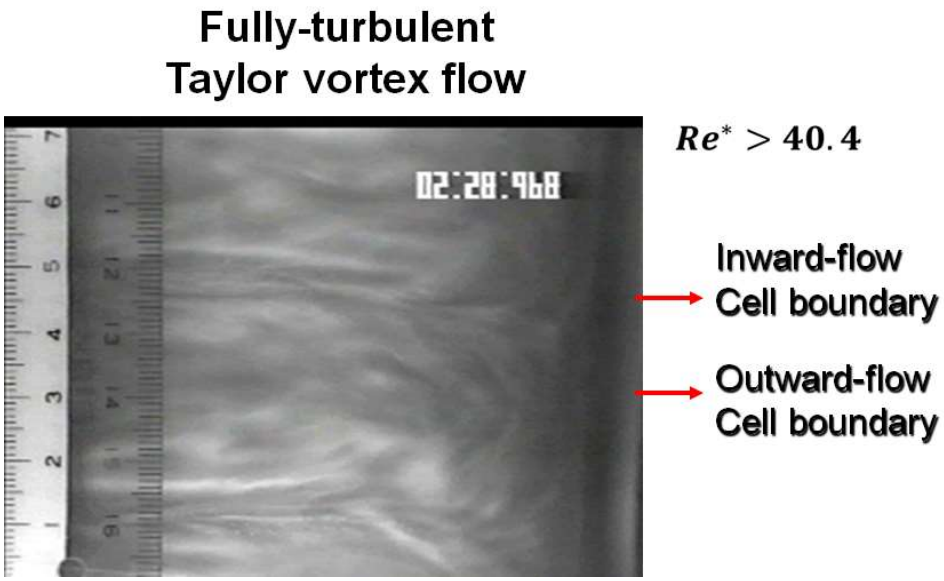

Fig.27.2-7 Fully turbulent Taylor vortex flow

27.2-3 Transitional scenario to generation of chaos in Taylor-Couette flow[1,3)]

For the present, as indicated in Fig.27.2-8, the following scenario of transition to chaos is approved from many investigations observed by various observation techniques:

The axisymmetric circular shear flow (Couette shear flow) becomes unstable to form a time-independent cellular vortex flow (Taylor vortex flow) when the Reynolds number reaches its critical value Re_{cr}.[2)] This first transition to the time-independent Taylor vortex flow can be analyzed by the linear instability model. For very small gap width system ($d/R_i \ll 1$), the critical Reynolds number Re_{cr} is given by Eq.(27.2-2). The Reynolds number is further raised beyond $R^* \geq Re_w/Re_{cr}$, the Taylor vortex flow changes into a time-dependent vortex flow called "Singly-periodic wavy vortex flow." A regularly periodical wavy motion appears with a characteristic frequency in the cellular structure.

The second transition to the wavy vortex flow is analyzed by the supercritical non-linear analysis. The characteristic wave frequency and the number of azimuthal waves are investigated by very many researchers from the bifurcation problem.[3)] The next transition occurs when $R^* \geq Re_{w2}/Re_{cr}$. This transition from the singly- to the doubly-periodic wavy vortex flow can be interpreted by the non-linear interaction of two independent frequencies of wave motion. In this quasi-periodic flow regime, the cellular vortical motion exhibits more complicated wave motion amplitude-modulated with two independent characteristic frequencies f_1 and f_2: the first one comes from the basic azimuthal wave motion and the other one from the periodicity of amplitude-modulation.

However regarding the next transition, there is still a question as to whether the triply-periodic wavy vortex flow exists or not. This fourth transition which this author observed by the electrochemical method is not approved. The physics researchers are wondering that it seems a very long transitional state. When $R^* \geq Re_{ch1}/Re_{cr}$, the quasi-periodic wavy vortex flow exhibits not so large irregular disturbances inside the stable wavy vortex structure.

That can be considered as the generation of chaotic turbulence. For the present, they think that the chaotic turbulence appears after the doubly-periodic wavy vortex flow has become unstable. When $R^* \geq Re_{ch2}/Re_{cr}$, the weakly-turbulent wavy vortex flow changes into the fully-turbulent vortex flow where the cellular structure is still alive but the azimuthal wave motion cannot clearly be detected.

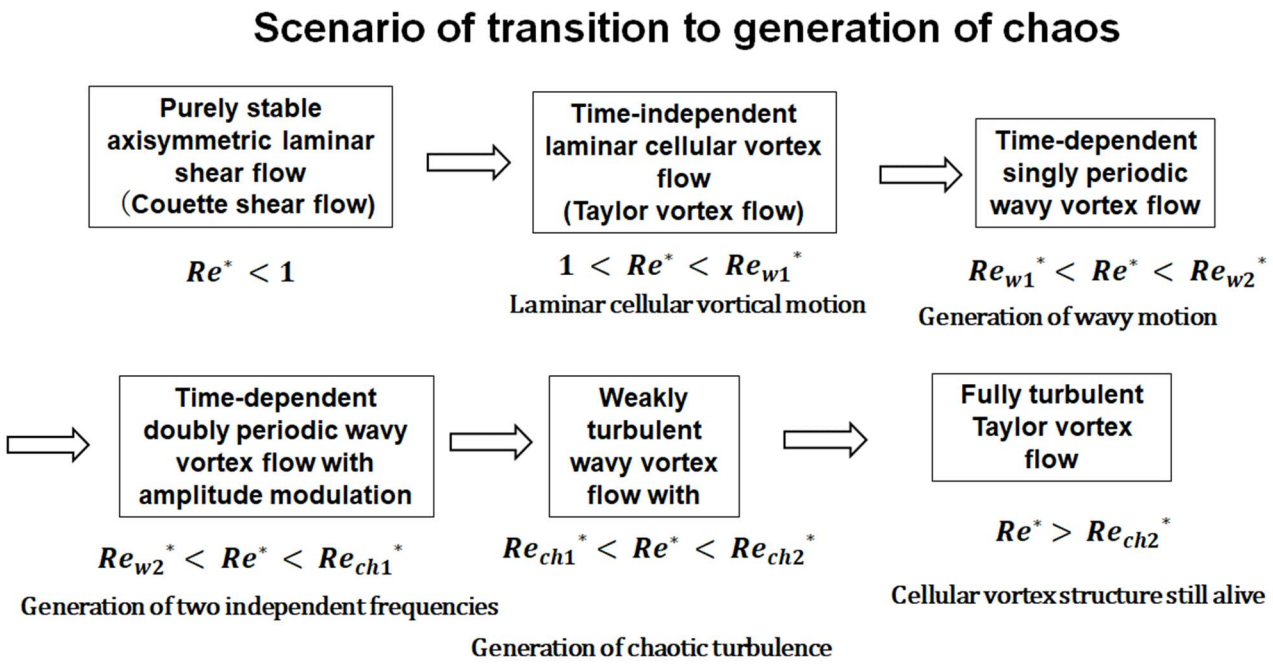

Fig.27.2-8 Scenario of transition to chaos for Taylor-Couette flow

1. Kataoka, K., Chapter 9 Taylor Vortices and Instabilities in Circular Couette Flows, Encyclopedia of Fluid Mechanics, Vol.1, 236-274, Gulf Pub., Houston (1986)
2. Taylor, G.I., *Phil. Trans. Roy. Soc. London*, **A223**, 289 (1923)
3. Coles, D., *J. Fluid Mech.*, Vol.14, 385 (1965).

27.3 Visualization of Mass Transfer Distribution

27.3-1 Mass transfer distribution in Taylor-Couette flow[1)]

Chapter 14.4 introduces that the electrochemical reaction can be made use of for measuring local and time-dependent mass transfer under the limiting current condition. Fig.27.3-1 indicates the electrochemical method measuring the axial distribution of mass transfer in a Taylor-Couette flow system. The inner rotating copper cylinder served as the anode and the outer stationary copper cylinder serves as the main cathode. In the main cathode wall, many isolated cathodes are embedded for observing local mass transfer of copper ions.
The following electrolytic reaction is utilized for observing axial distribution of mass transfer on the inner wall of the outer stationary cylinder in a Taylor vortex flow.

(anode) $\quad Cu - 2\ e^- \rightarrow Cu^{++}$

(cathode) $\quad Cu^{++} + 2\ e^- \rightarrow Cu$

The principle of this ionic mass transfer method is explained in Chapter 14.2.

As shown in Fig.27.3-1, a circular copper wire is inserted into the hole drilled in the main cathode, and fixed with resin adhesive used as the electric insulator, and then the electrode surface is smoothly flattened.

By making isolated point cathode at the same potential (voltage) as the main cathode, we can observe local film coefficients of mass transfer on the inner wall of the outer cylinder.
Fig.27.3-2 is the experimental apparatus for measuring local mass transfer of Cu^{++} ions to the inner wall surface of the outer cylinder at rest.

The working fluid is an aqueous solution of $CuSO_4$ (1.15~1.75 mol/m^3) which contains 2×10^3 mol/m3 H_2SO_4 as the supporting electrolyte.
An appropriate quantity of glycerol is added to adjust the fluid viscosity.
The mass flux on the wall of the outer cylinder wall is measured at the limiting current condition by using the following equation:

$$N_w = I_w/(F\ S) = k_w C_b$$

where C_b at tis the bulk fluid concentration he limiting current condition, the concentration of copper ion becomes zero
The viscosity of the working solution is adjusted by adding glycerine in thw range of Sc = 3,000 to 7.7 $\times$ 10^5

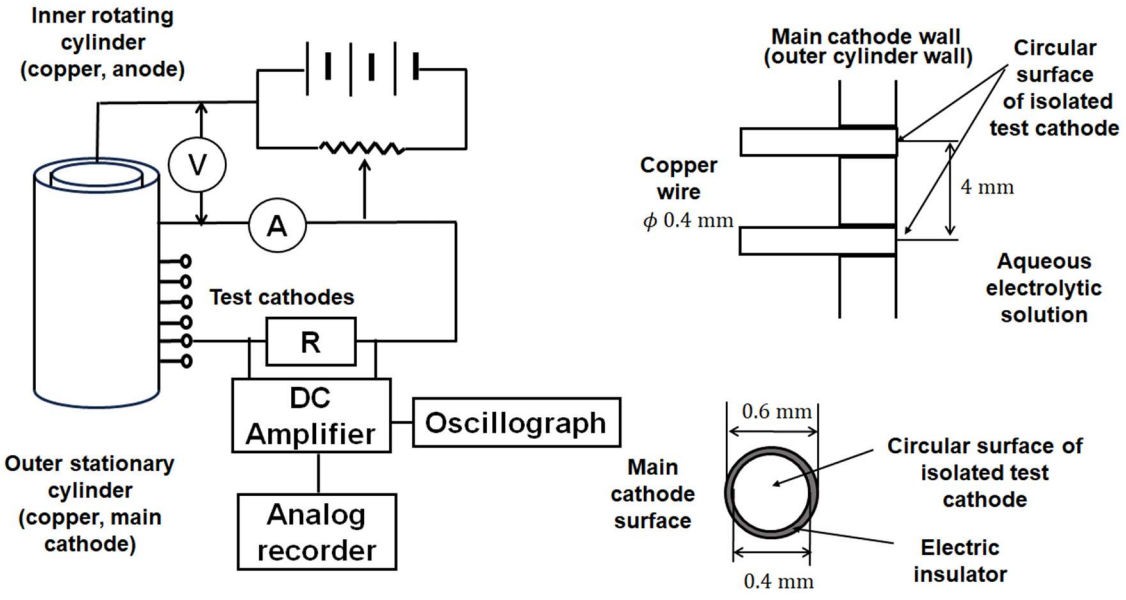

Fig.27.3-1 Electrochemical measuring system for two concentric copper cylinders with the inner one rotating[1)]

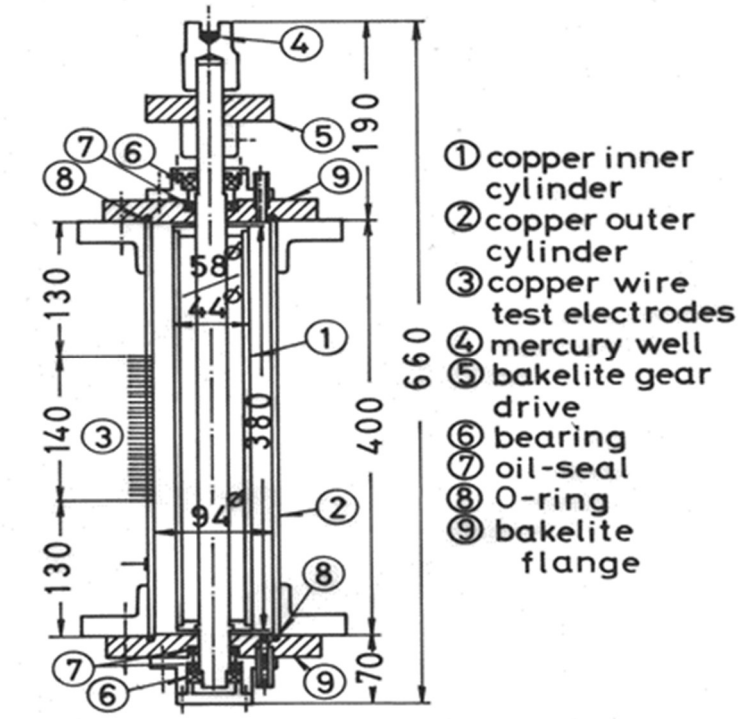

Fig.27.3-2 Experimental apparatus of electrochemical method for two concentric cylinders with the inner one rotating.[1)]

1) Kataoka, K., Doi, H., and Komai, T., Heat/mass transfer in Taylor vortex flow with constant axial flow rates, *Int. J. Heat Mass Transfer,* Vol.20, 57-63 (1977)

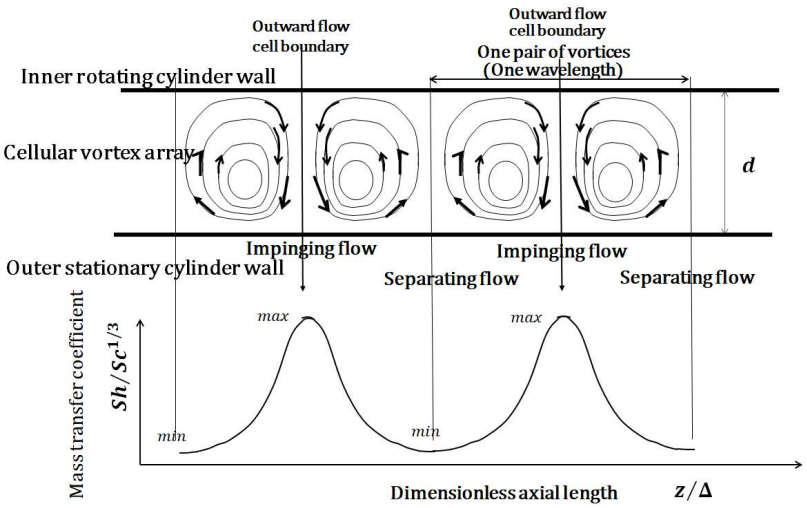

Fig.27.3-3 Axial variation of mass transfer corresponding to cellular vortex array

As shown in Fig.27.3-3, the axial distribution of the mass transfer coefficient on the outer cylinder corresponds to the axially periodic array of Taylor vortices. The maximal position of mass transfer corresponds to the vortex outflow cell boundary while the minimal position corresponds to the inflow cell boundary. The peak-to-peak distance is equal to the axial spacing of a couple of vortices. The wavelength Δ is defined as the axial length of a pair of Taylor vortices.

Fig.27.3-4 shows time-dependency and local variation of Cu^{++} ionic mass transfer observed by electrochemical methos.[1,2)]

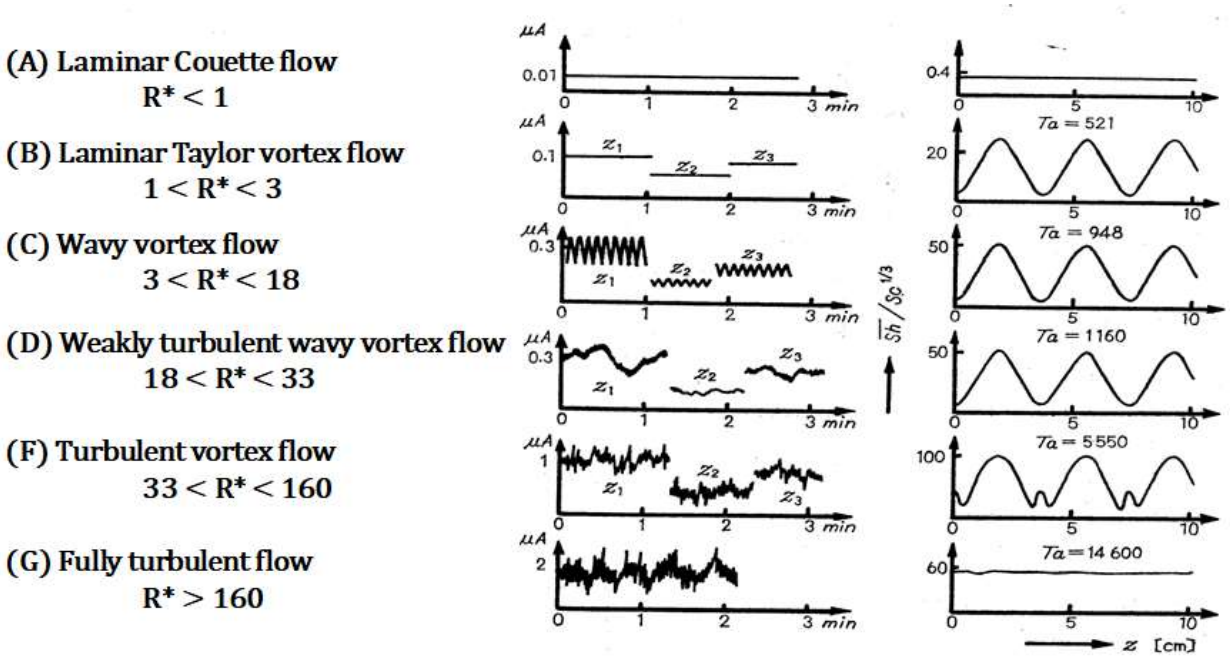

Fig.27.3-4 Time-dependent limiting current and time-averaged local mass transfer coefficient observed by electrochemical method[2)]

In this experiment, we could not notice the transition from singly-periodic to doubly-periodic wavy vortex flow regimes.

2. Kataoka, K., Chapter 9 Taylor Vortices and Instabilities in Circular Couette Flows, Encyclopedia of Fluid Mechanics, Vol.1, 236-274, Gulf Pub., Houston (1986)

27.4 Visualization of Dynamically Organized Jet Flows

27.4-1 Hydrogen bubble method for a free jet development[1)]

The hydrogen bubble method is a convenient visualization technique making use of an electrolysis of water. A small amount of NaOH is added for increasing the electrical conductivity of water. Owing to the buoyancy effect of hydrogen bubbles, this visualization technique is limited to the slow velocity flow condition.

A round free jet issuing from a convergent nozzle into quiescent surroundings of the same fluid exhibits a beautiful structural development accompanied with dynamically organized structures generated due to the shear forces between the jet flow and the surrounding fluid at rest.

Fig.27.4-1 is a photograph of an isothermal submerged water jet visualized by a hydrogen-bubble technique. The white streaklines of hydrogen bubbles are produced by applying a 40-60 V d.c. potential to a nickel zigzag-wire electrode (100 μm diameter, zigzag pitch = 1.73 mm). The hydrogen-bubble timelines are simultaneously produced by applying 140 V pulse potential at a chosen frequency (30-50 Hz) to a platinum straight-wire electrode (50 μm diameter). The anode plate generating oxygen bubbles is placed far downstream of the main flow region.

From the successive photographs of the visualized flow pattern, we can draw a schematic picture of developing jet with organized structures shown on the right of the figure.
In the well-designed convergent nozzle, close to the jet exit, there is a potential core region in the center where the centerline velocity remains unchanged from the initial value. Then the core diminishes in width in the downstream direction. The instability of the initial shear layer near the nozzle lip results in a migration of vorticity to form periodic axisymmetric coherent concentrations and leads to the physical appearance of the rolling-up of the laminar shear layer. That results in the periodic street of ring-shaped vortices. In this manner, large-scale eddies are produced in the late-transitional region as a result of disintegration of line- or ring-vortices.

The free jet development in the axial direction is a very important problem for the convective heat transfer where a free jet impinges normally on a flat plate. The flow structure in the jet impingement region depends on the flow structure of the approaching free jet.

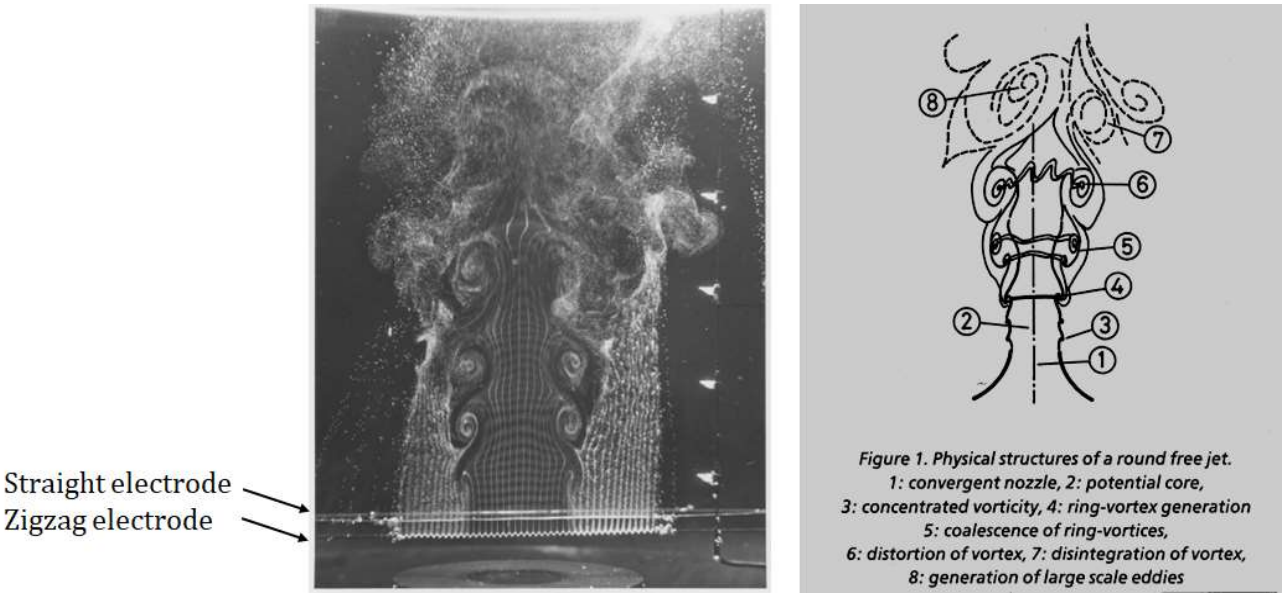

Fig.27.4-1 Cross-sectional view of a free jet flow pattern visualized by the hydrogen-bubble method

It is considered that jet impingement heat transfer is largely controlled by unsteady large-scale coherent structures of the approaching free jet.
Many convective heat transfer researchers paid attention to the role of large-scale eddies in the enhancement of the jet impingement heat transfer. Therefore it is important to observe dynamic change in the coherent structures in the developing region of a free jet.
As a similar technique, a smoke wire method is available for visualization of slow gas flows.

1. Kataoka, K., Mihata, I., Maruo, M., Suguro, M., and Chigusa, T., Quasi-periodic large-scale structure responsible for the selective enhancement of impinging jet heat transfer, Proc. 8th Int. Heat Transfer Conf., vol.3, 1193-1198 (1986)

27.4-2 Hydrogen bubble method for a two-dimensional impinging jet[2)]

If a convergent slot nozzle is employed for convective heat transfer processes, jet development accompanied by instability of the free shear layer downstream of the nozzle mouth is a very important

factor to control the stagnation point flow behavior. By using the same hydrogen-bubble method, we can observe the downstream instability of an intermittently generated large-scale vortex structure in the near-field of the free jet.

It is known that the stagnation-point heat transfer usually becomes maximal when a heat transfer surface (impingement plate) is placed at 6-8 nozzle widths, i.e. H/D = 6-8 downstream of a nozzle mouth. As shown in Fig.27.4-2, we would like to pay attention to the unsteady coherent structures intermittently appearing in the stagnant region of the impingement plate.

It is necessary to observe how unsteady coherent structures appear in the jet impingement region from a viewpoint of the heat transfer enhancement in such an impinging flow.

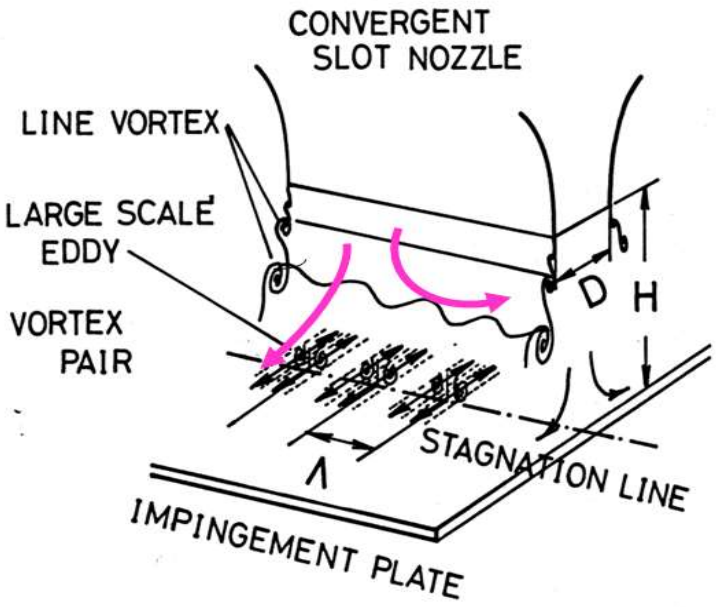

Fig.27.4-2 Impinging jet arrangement and generation of large-scale eddies in stagnation region

A two-dimensional jet issuing from a well-designed convergent slow nozzle (exit width *D*) impinges normally on the impingement plate. The nozzle-to-plate distance *H* is an important jet development parameter. A zigzag Pt wire is placed 50 mm upstream in parallel to the impingement plate.

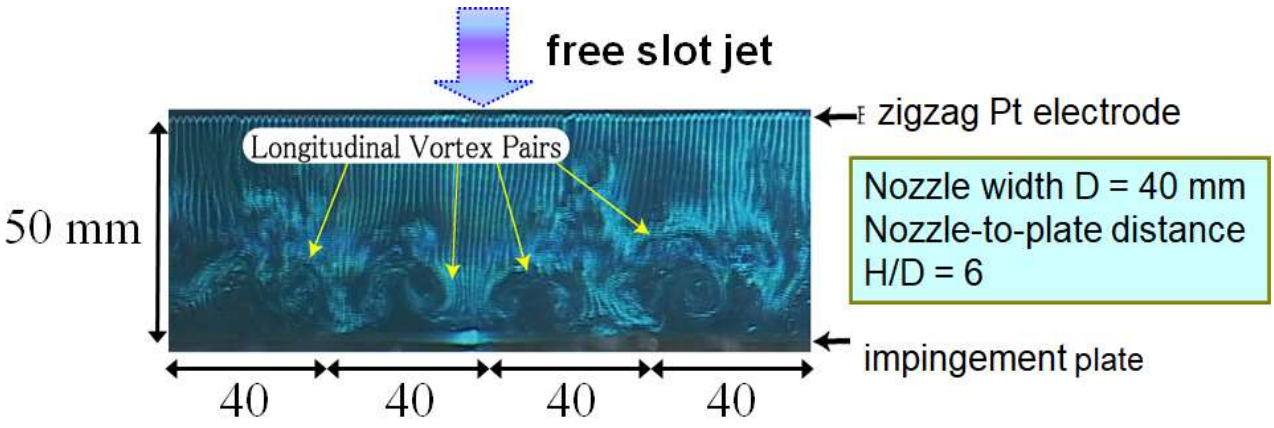

Fig.27.4-3 Intermittently formed longitudinal vortex pairs visualized by the streaklines of hydrogen bubbles when *H/D* = 6

Fig.27.4-3 is a photograph of organized vortical motions intermittently appearing across the stagnation line.

Note: Impinging jet heat transfer is dealt with a little in Chapter 18.5 of the previous volume.

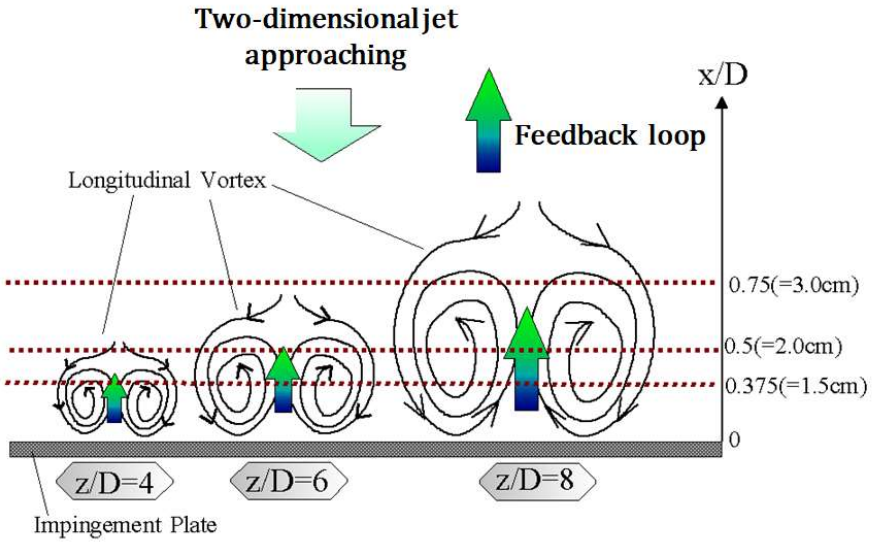

Fig.27.4-4 Schematic picture of cross-sectional view of longitudinal vortex pairs

As shown in Fig.27.4-2, when the impingement plate is in the late-transitional region ($4 \leq z/D \leq 8$)) of a two-dimensional free jet, longitudinal vortex pairs intermittently appear across of the stagnation line. The schematic picture of vortex pairs is indicated by Fig.27.4-4. The size of the vortex pairs tends to become large with the development length z from the jet exit. It can be conjectured that the augmentation of stagnation point heat transfer is controlled by these intermittent large-scale vortical motion.

1. Kataoka, K., Kawasaki, H., Tsujimoto, M., and Ohmura, N., Effect of longitudinal vortices on heat transfer surfaces a two-dimensional jet strikes against, Proc. 10th Int. Heat Transfer Conf., Vol.3, 31-36 (1994)
2. Kataoka, K., Ochi, T., Uyama, K., and Ohmura, N., Time-dependent structures of a two-dimensional turbulent impinging jet accompanied by longitudinal vortex pairs, *J. Chem. Eng. Japan*, Vol.37(2), 299-303 (2004)

27.4-3 Local time-dependent wall shear stresses in jet impingement region[1,2,3)]

It was considered to be very difficult to observe local distribution of shear stresses acting on a flat plate. The electrochemical method is also utilized to measure local and time-dependent behaviors occurring on a flat plate on which a free round jet impinges perpendicularly. The measuring principle is introduced in Chapter 14.4.

Fig.27.4-5 shows that a free jet issuing from a convergent nozzle impinges normally on a flat plate. Fig.27.4-6 is layout of two kinds of test cathodes where dimensions given are in mm. The U-electrode is used or velocity measurement similarly to the hot-wire anemometry.

Local measurement of the mass transfer coefficient k (m/s) is accomplished using circular point cathodes (K-electrode) which are fabricated by inserting 0.3 mm diameter nickel wires into 0.5 mm diameter holes drilled in the main cathode wall. The K-electrodes electrically isolated from the main cathode are held at the same potential as the main cathode for the following electrode reaction under the diffusion-controlling condition:

Cathode: $Fe(CN)_6^{3-} + e^- = Fe(CN)_6^{4-}$
Anode: $Fe(CN)_6^{4-} = Fe(CN)_6^{3-} + e-$

Local measurement of local, time-dependent velocity gradient on the impingement plate is also accomplished using small rectangular cathodes (S-electrode) which are fabricated by inserting 0.2 mm thick nickel sheets into 0.7 mm long slits normally to the radial main flow direction in the wall of the main cathode.

$$k = i_d/Fa\ C_A \quad (14.3\text{-}2)$$

The velocity gradient measurement is carried out by measuring the limiting current between each S-electrode and the anode under the condition of the main cathode inactive.

Local velocity gradient on the impingement flat plate can be obtained as the limiting current density i_d on each S-electrode:

$$s = 1.90\ (i_d/Fa\ C_A)^3 (L/D_{AB}^2) \quad (14.4\text{-}1)$$

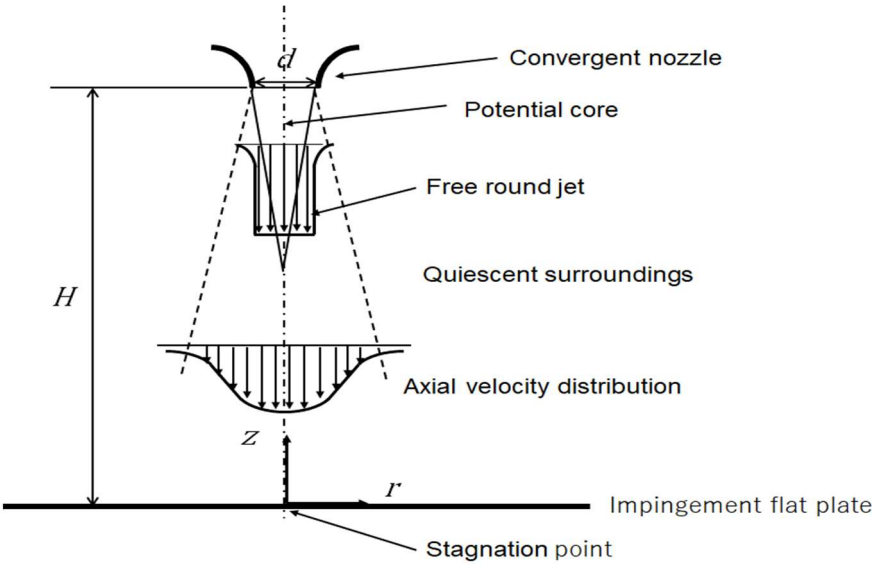

Fig.27.4-5 Schematic picture of a free round jet impinging normally on a flat plate

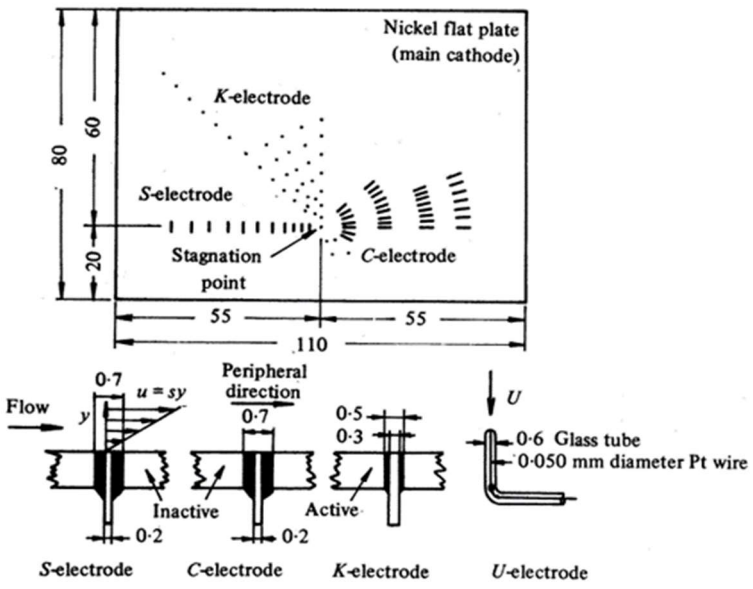

Fig.27.4-6 Layout of test cathodes for measuring local velocity-gradients and mass transfer coefficients on jet impingement plate[1)]

The heat or mass transfer at the stagnation point becomes maximal when the jet exit-to-impingement plate distance H/d is $H/d = 6 \sim 8$. Some experimental results when $H/d = 6$ are shown here.

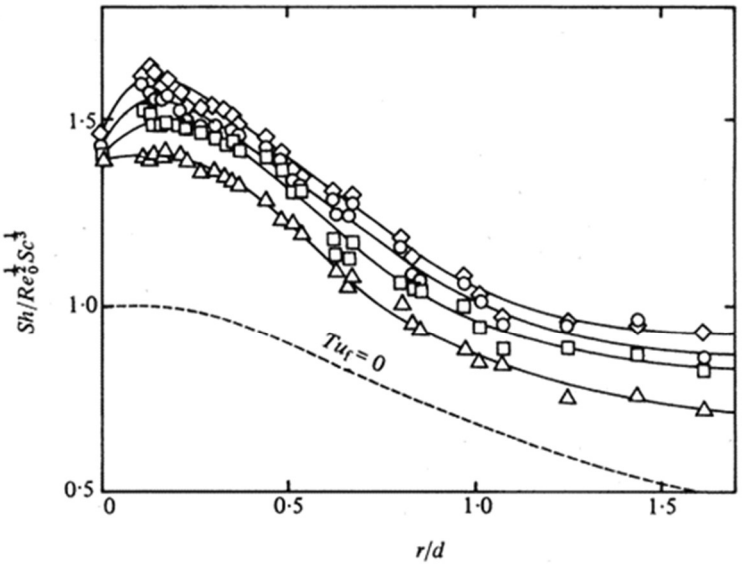

Lateral variation of mass-transfer coefficients when $H/d = 6$.
△, $Re_0 = 4000$; □, 6000; ○, 10000, ◇, 15000.

Fig.27.4-7 Lateral variation of mass transfer coefficients when *H/d* = 6[1)]

Fig.27.4-7 is lateral distribution of mass transfer coefficient in the form of Sherwood number. This indicates a typical bell-shaped distribution but the mass transfer coefficient seems to have a small dent at the stagnation point. This behavior is still a question for discussion. As distinct from the two-dimensional impinging jet, it has been not yet elucidated well for the circular impinging jet what intermittent organized motion is formed in the stagnant region. It is observed that when $H/d > 4$, instantaneous stagnation point hastily moves around the geometrical stagnation point.

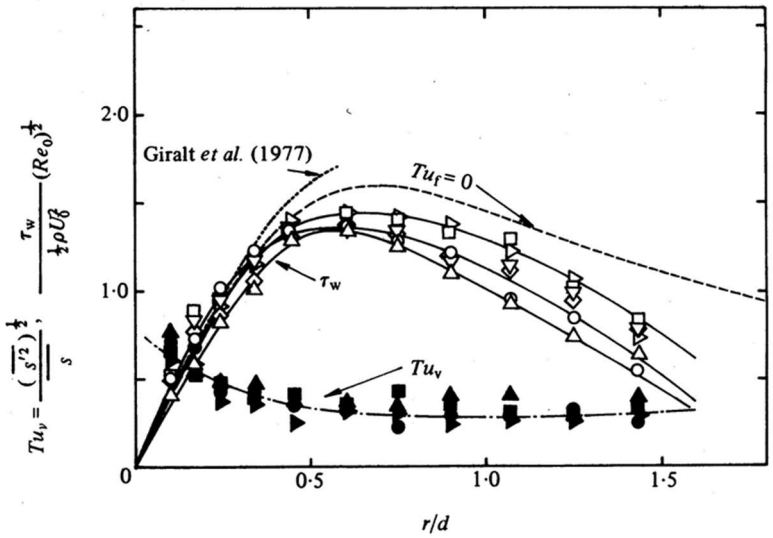

Lateral variation of skin friction and the relative intensity of velocity-gradient fluctuations at the wall when $H/d = 6$. △, ▲, $Re_0 = 4000$; □, ■, 6000; ▽, 8000; ○, ●, 2000; ▷, ▶, 15000.

Fig.27.4-8 Lateral variation of time-averaged wall shear stress and the relative turbulence intensity[1)]

In the impingement region, the velocity gradient increases almost linearly due to the accelerating lateral flow along the impingement plate. In the outside region of the impingement region (r/d > 0.5) with no static pressure change, the lateral velocity is decelerated owing to the widely developing boundary layer.

3. Kataoka, K., Kamiyama, Y., Hashimoto, S., and Komai, T., Mass transfer between a plane surface and an impinging turbulent jet: the influence of surface-pressure fluctuations, *J. Fluid Mech.*, vol.119, 91-105 (1982)

Note: The principle of the electrochemical method is also treated in Chapter 14 of the previous volume.

27.5 Local convective heat transfer on the wall of jet impingement plate[4,5)]

An isothermal air jet, issuing vertically upward from a well-designed convergent nozzle, impinges normally on a horizontal, circular flat plate. The jet exit has a uniform velocity distribution with low initial turbulence (<0.5%). The circular flat plate made of copper (420 mm dia. 10 mm thick) has a hot water jacket on the backside so as to keep it at a constant uniform temperature T_w (about 52°C).

The heat transfer distribution in the jet impingement region can be measured by a heat-flux sensor when the circular flat plate is cooled by the impinging air jet.

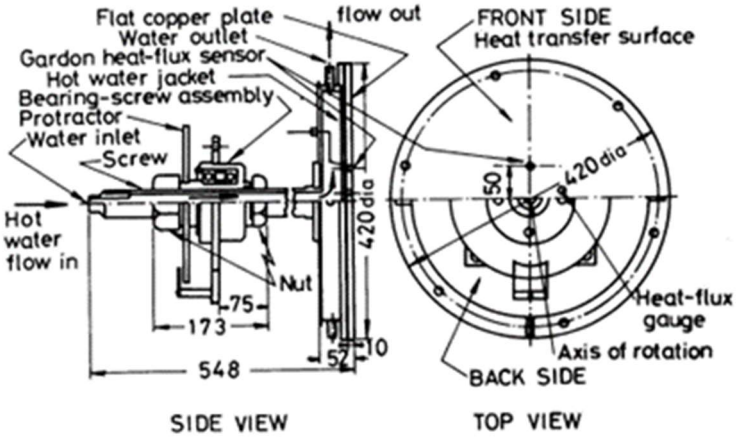

Circular flat plate. Dimensions in mm.

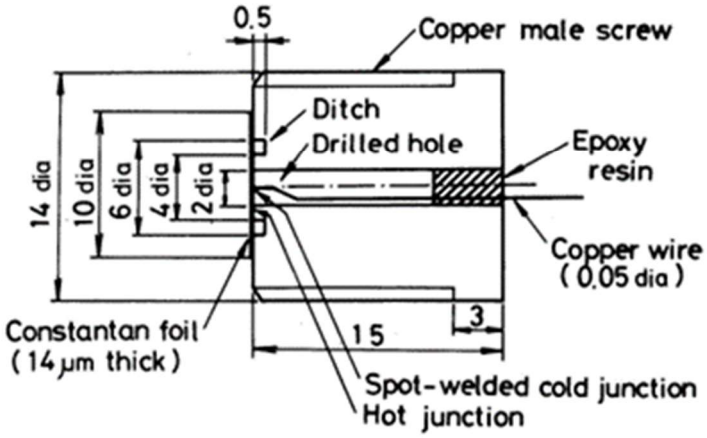

Gardon-type heat-flux sensor. Dimensions in mm.

Fig.27.5-1 Circular copper flat plate for convective heat transfer measurement and the embedded plug-type heat-flux sensor

Gardon Heat-flux Sensor

A plug-type heat-flux sensor constituted by thermocouples shown in Fig.27.5-2 is available to measure local values of convective heat transfer coefficient.

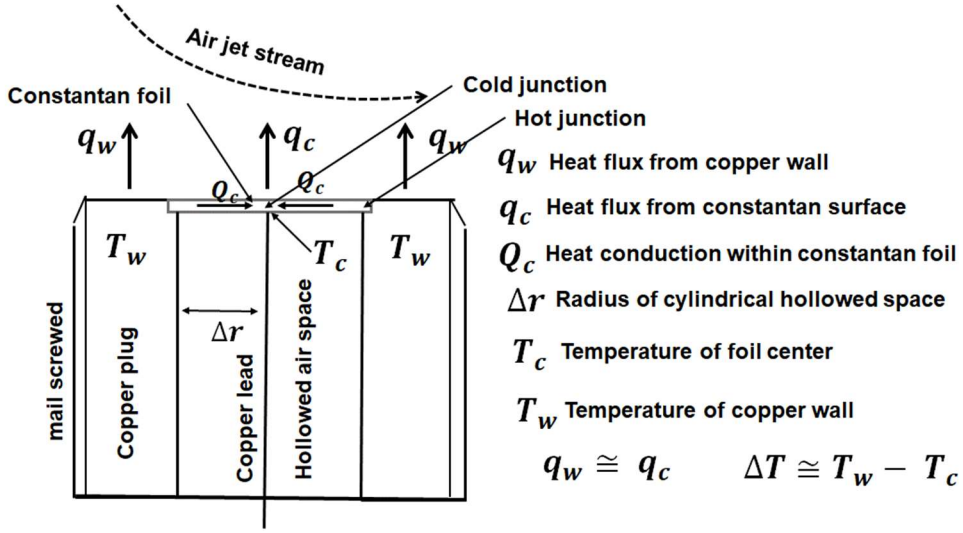

Fig.27.5-2 Measurement of local heat transfer coefficient by wall heat-flux sensor

The hot junction (i.e. the periphery of the constantan foil) is kept at the same temperature T_w as the flat copper plate. The cold junction (i.e. the spot welded with copper lead at the center of the constantan foil) is cooled by air jet (temperature T_∞). The temperature difference between these two junctions is proportional to local coefficient of heat transfer:

$$h = K_1 \Delta T \quad (27.5\text{-}1)$$

Local wall heat-fluxes at the periphery and center of the constantan foil are respectively expressed as

$$q_w = h\,(T_w - T_\infty) \quad (27.5\text{-}2)$$

$$q_c = h\,(T_c - T_\infty) \quad (27.5\text{-}3)$$

The rate of heat conduction occurring within the foil from the periphery to the center is given by

$$Q_c = \kappa_c \frac{\Delta T}{\Delta r} S_c \quad (27.5\text{-}4)$$

Since the heat loss q_c is rapidly compensated by the heat conduction,

$$\kappa_c \frac{\Delta T}{\Delta r} S_c = h\,S\,(T_c - T_\infty) \quad (27.5\text{-}5)$$

In the operating condition, $\Delta T = (T_w - T_c) \ll T_w - T_\infty$.

Therefore time-dependent wall heat-flux and heat transfer coefficient have the following linear relationship with ΔT:

$$h = K_1 \Delta T \quad (27.5\text{-}6)$$

$$q_w = K_2 \Delta T \quad (27.5\text{-}7)$$

where

$$K_1 = \frac{\kappa S_c}{(T_w - T_\infty)\Delta r\, S} \quad (27.5\text{-}8)$$

$$K_2 = \frac{\kappa S_c}{\Delta r\, S} \quad (27.5\text{-}9)$$

These two constants are determined by experiment.

Local heat-flux on the surface of the flat plate can be measured by means of a Gardon-type heat-flux sensor[5]. The sensor consists of a copper hollow male-screw as a heat sink and a circular constantan foil (14μm thick) which has a spot-welded thermocouple junction of 50μm dia. copper lead at its center. The other thermocouple junction is formed at the periphery of the constantan foil. This sensor is embedded in the copper flat plate, 50 mm from the rotation axis.

Another copper plug heat-flux sensor is also embedded in the same flat plate.

The axis of the convergent nozzle is fixed 50 mm away from the rotation axis of the flat plate so that the heat-flux sensor can be placed at an arbitrary radial position from the geometrical stagnation point. The turbulent velocities of the approaching air jet are measured by a constant-temperature X-probe hot-wire anemometry.

The radial distribution of wall heat-flux measured by experiment is shown in Fig.27.5-3.

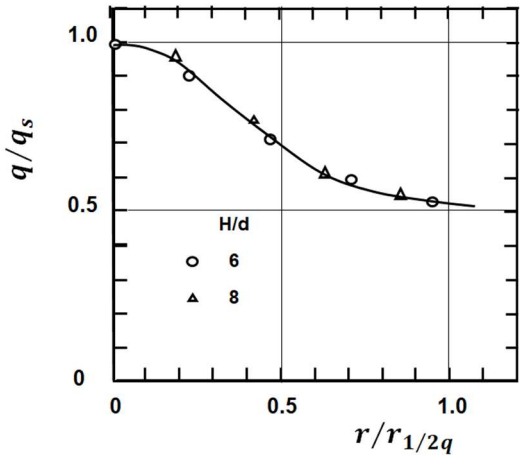

Fig.27.5-3 Lateral variation of wall heat-flux with lateral distance from geometrical stagnation point normalized by stagnation-point heat-flux and half-radius of wall heat-flux.[5)]

Fig.27.5-3 suggests that the radial distribution of the normalized heat transfer coefficient normalized with the stagnation point heat-flux becomes similar when $H/d \geq 6$ if the radial coordinate is made dimensionless with respect to the radius $r_{1/2q_s}$ where the wall heat -flux becomes 1/2 q_s.

The summarized correlations of stagnation point heat transfer coefficients are given by Fig.27.5-4. It can be confirmed that the stagnation point heat transfer coefficient becomes maximal when $H/d = 6 \sim 8$.

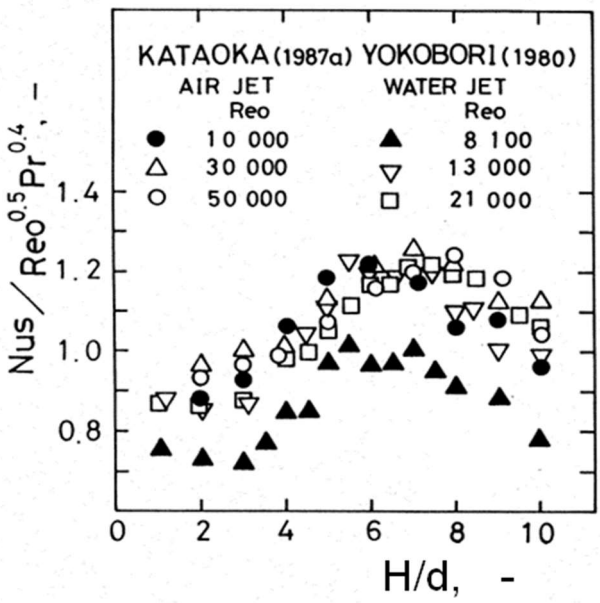

Fig.27.5-4 Correlations of stagnation-point heat transfer coefficients with nozzle-to- jet impingement plate distances

4. Kataoka, K., Sahara, R., Ase, H., and Harada, T., Role of large-scale coherent structures in impinging jet heat transfer, *J. Chem. Eng. Japan*, Vol.20(1), 71-76 (1987)
5. Kataoka, K., Harada, T., and Sahara, R., Mechanism of heat transfer in turbulent impinging jets, Current Research in Heat and Mass Transfer, A compendium and a Festschrift for Professor A. Ramachandran, ed. M.V. Krishna Murthy et al., Hemisphere, 81-95 (1986)

Nomenclature

a	effective interfacial area per unit packed volume, [m^2/m^3]
Cp	heat capacity, [J/kmol K]
D	overhead product, [kmol/s]
D_G, D_L	diffusivity in gas- and liquid-phase, [m^2/s]
E_{MG}	Murphree plate efficiency, [-]
E_{PG}, E_{PL}	point efficiency for vapor- and liquid-phase, [-]
F	feed rate, [kmol/s] or F-factor [$(m/s)(kg/m^3)^{0.5}$]
G_M	superficial molar gas-mass velocity, [$kmol/m^2s$]
$H_X,\ H_Y$	latent heat (enthalpy) of x- and y- component, [J/kmol]
h_{ETP}	HETP (Height Equivalent to a Theoretical Plate), [m]
h_w	outlet weir height, [m]
K	vapor-liquid equilibrium constant, [-]
K_x, K_y	overall mass transfer coefficients defined by vapor-phase and liquid-phase concentrations [$kmol/m^2s$]
k_x, k_y	mass transfer coefficients of vapor-phase and liquid-phase film [$kmol/m^2s$]
m	slope of equilibrium curve, dy/dx,
N_{OG}, N_G, N_L	number of transfer unit, OG:overall, G:gas phase, L:liquid phase, [-]
n	theoretical plate/stage number, [-]
Re	Reynolds number, [-]
Sc	Schmidt number, [-]
T, t	temperature, [K]
x_A, y_A	mole fraction of component A, liquid- and vapor-phase, [-]
z	height of packing section, [m]
α_{AB}	relative volatility, [-]
δ_G, δ_L	thicknesses of gas-phase and liquid-phase film, [m]
λ	stripping factor, [-]
μ	viscosity, [kg/m s]

Subscripts

A, B	component A, B
G, L	gas-phase, liquid-phase
i	interface

CHAPTER 28
NONLINEAR BEHAVIORS IN COMPLEX CHEMICAL PROCESSES

28.1 Why Do We Study Nonlinear Dynamics in Complex Chemical Processes?

In general, chemical processes proceed under an effect of coupling between chemical dynamics and mass transport controlled by fluid dynamics. In any kinds of liquid-phase chemical reactions, any reactant solution should be mixed for increasing the frequency of collision of reactant molecules. In industrial chemical processes. if elementary reaction steps are taken into account for reaction mechanism, most of chemical reactions can often become difficult to control. Nonlinear dynamics of complex chemical processes in an open system (i.e. flow system) is so complicated that we will study a little about its simple examples in this Chapter for the design methodology of system and operation.

Any chemical reaction cannot proceed without the coupling of two or more nonlinear dynamics such as the complex interaction of elementary reaction steps with micro-mixing of reactant solution. This Chapter brings up the necessity of operation design as well as system design from a viewpoint of nonlinearity in chemical dynamics coupled with fluid mixing.

28.1-1 A simplified chemical model

The Brusselator model[1,2] is very interesting as a model of nonlinear chemical reactions. This model is given by an irreversible reaction of the following form:

$$A + B \rightarrow C + D \tag{28.1-1}$$

The elementary steps including two intermediates X and Y are expressed as

$$A \rightarrow X$$
$$B + X \rightarrow D + Y$$
$$Y + 2X \rightarrow 3X$$
$$X \rightarrow E \tag{28.1-2}$$

The third elementary step can be considered to be autocatalytic. The intermediate component X is produced from 2 to 3 moles by itself.

Assuming that the concentrations of A and B are almost constant since the reactant components A and B are supplied sufficiently, the reaction rate equations for a batch system can be given by

$$\frac{dx}{dt} = k_1 C_{A0} - k_2 C_{B0} x + k_3 x^2 y - k_4 x \tag{28.1-3}$$

$$\frac{dy}{dt} = k_2 C_{B0} x - k_3 x^2 y \tag{28.1-4}$$

Only for simplification, the following quantities are given to those rate constants.

$$k_1 C_{A0} = 1, \quad k_2 C_{B0} = 3, \quad k_3 = k_4 = 1$$

The dynamic equations of this reaction model for a continuous stirred tank reactor (CSTR) as an open system can be expressed as

$$\frac{dx}{dt} = 1 - 4x + x^2y - fx \quad (28.1\text{-}5)$$

$$\frac{dy}{dt} = 3x - x^2y - fy \quad (28.1\text{-}6)$$

where $f = F/V$ denotes a space velocity of efflux from the CSTR shown in Fig.28.1-1.

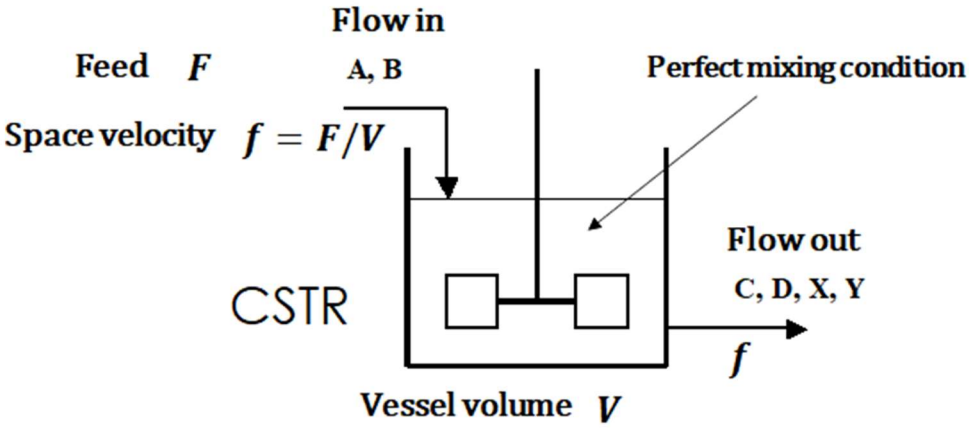

Fig.28.1-1 Open system of perfect mixing tank reactor

The space velocity can be adopted as a bifurcation parameter. Such a kind of open system can be assumed to be in a perfect mixing condition.

28.1-2 Phase space analysis

The nonlinear behavior of the ordinary differential equations can be analyzed in phase space if time-dependent concentrations of the intermediate components X and Y are drawn as a trajectory in phase space.

Firstly solving the governing equations for a batch system ($f = 0$) under the initial conditions $x(0) = y(0) = 0$, a limit cycle attractor can be obtained in Fig.28.1-2. This indicates that both intermediates have a singly-periodic oscillation in concentration. It should be noted that the trajectory of the dynamic solution never converges on the stationary-state solution: $x_{ss} = 1$ and $y_{ss} = 3$.
It has been confirmed that this chemical dynamics gives the same attractor regardless of the initial condition.

What is an attractor?

Attractors are subsets of the phase space of a dynamical system. As its simple examples, attractors are thought as being simple geometric subsets of the phase space, like points, lines, and surfaces (e.g. tori) as simple regions of three-dimensional space. For example, a limit cycle is a periodic orbit of a continuous dynamical system. As shown below, a trajectory can be obtained in the dynamical phase space by a temporal variation plotting the X concentration against the Y concentration.

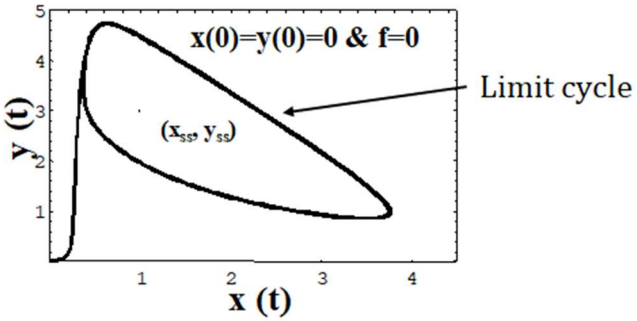

Fir.28.1-2 Attractor of Brusselator model in a batch system.

28.2 Nonlinearity of Brusselator Model

28.2-1 Bifurcation analysis of Brusselator model for a CSTR

The governing equations for an open system Eqs (28.1-5 and 6) can be solved for various space velocities under the common initial condition: $x(0) = y(0) = 0$. The space velocity $f = 0.1$ implies that 10% of the reacting fluid in the reactor is exchanged for the fresh feed fluid every unit time. Fig.28.2-1 shows the temporal variation in concentration of those two intermediates X and Y.
Both intermediates seem to converge on the stationary-state point attenuating the oscillating behavior.

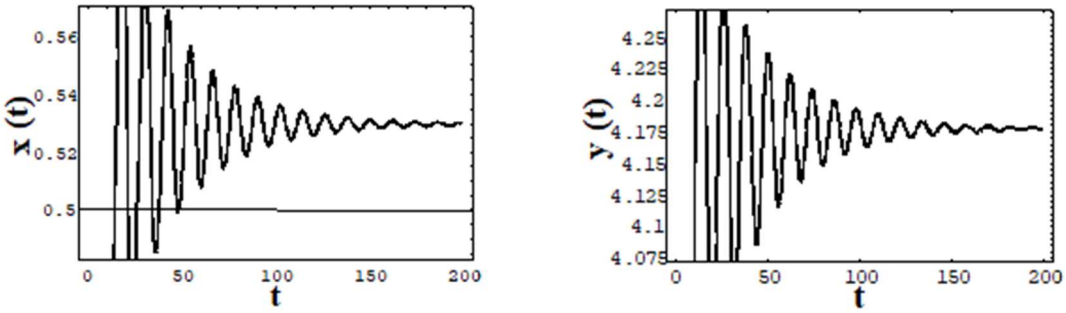

Fig.28.2-1 Temporal variation of concentration of two intermediate components X and Y.

Figure 28.2-2a indicates that when f =0.100, the trajectory converges attenuating its own original oscillation towards the stationary-state solution point. It has, however, been confirmed that if the space velocity is increased to 0.11, the trajectory converges very fast and directly towards the stationary-state point without oscillation. Figure 28.2-2b shows the trajectory converges on the stationary-state point after very small oscillations. This suggests that there is a bifurcation point between f = 0.105 and 0.11. This implies that only 5% deviation from the feed rate in this region gives rise to quite a big difference in transient phenomenon.

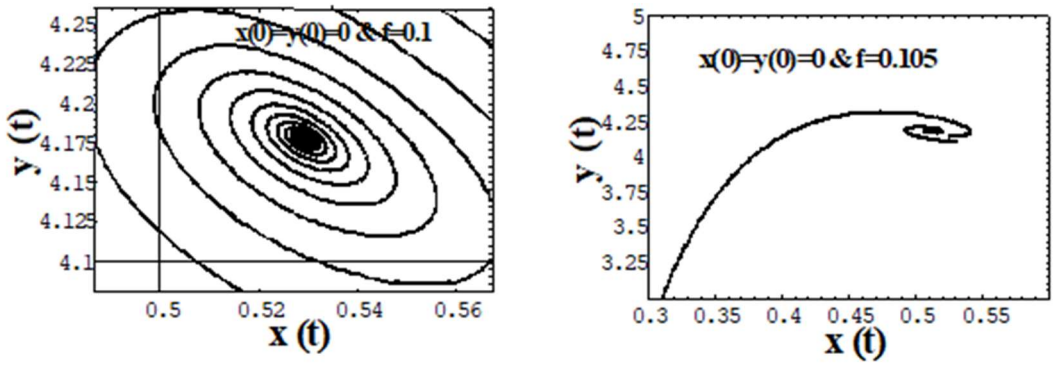

Fig.28.2-2 Attractor of an open system when (a) f = 0.1 and (b) 0.105.

On the other hand, if f is a little bit less than 0.1, the convergence of the oscillating trajectory towards the stationary-state point is decelerated, as shown in Fig.28.2-3a.
This diagram does not show the further trajectory towards the stationary-state point owing to very slow convergence. Figure 28.2-3b indicates that the trajectory shows a limit cycle when $f = 0.095$. This suggests that the other bifurcation point lies between $f = 0.095$ and 0.098. For the case of practical commercial-size reaction systems, there very often appear disturbances superimposed on the feed rate.

Stable operation mode should be considered taking into account the effect of the periodical disturbances superimposed on the space velocity from a viewpoint of such a delicate bifurcation behavior.

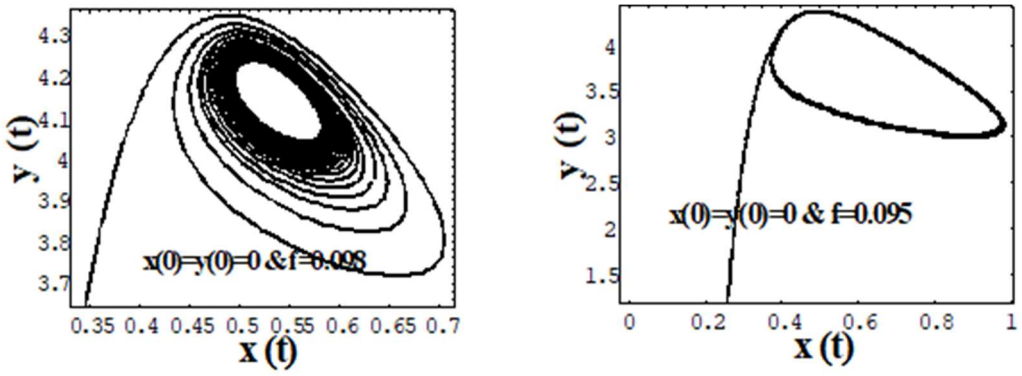

Fig.28.2-3 Attractor of an open system when (a) f = 0.098 and (b) 0.095.

The dynamic equation can also be solved for the case when a certain amplitude (fraction) f_a of periodical disturbances are superimposed on the space velocity $f = 0.1$:

$$f = 0.1(1 + f_a \sin 2\pi t) \qquad (28.2\text{-}1)$$

The results calculated for $f_a = 0.05$ and 0.02 are shown in Fig.28.2-4.

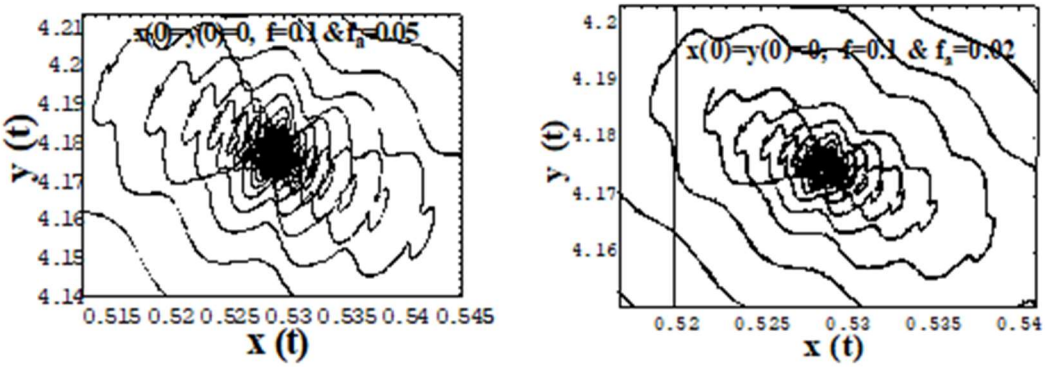

Fig.28.2-4 Doubly-periodic attractor with periodical disturbances in space velocity.

Both diagrams show that the trajectory of doubly-periodic oscillation is gradually attenuated but the oscillation coming from the forced oscillation of the feed rate would not disappear.

28.2-2 Bifurcation scenario of Brusselator model

Table 28.2-1 gives a bifurcation scenario depending on space velocity as a control parameter. It has been found that the limit cycle oscillation occurs only in the limited range of space velocity. In order to guarantee a very stable stationary-state, the space velocity should be set at a considerably high value without disturbance for this process.

Table 28.2-1 Bifurcation Scenario of an Open System of Brusselator

Space Velocity : f = F/V	Type of Trajectory
0	A
0.08	A
0.095	A
0.098	B
0.1	B
0.105	B
0.11	C
0.2	C

A: Singly-periodic oscillation (Limit cycle) without attenuation
B: Singly-periodic attenuating oscillation converging on the stationary-state fixed point
C: Transient trajectory without oscillation converging directly on the stationary-state fixed point

1. Prigogine, I., Thermodynamic Theory of Structure, Stability, Fluctuations, Wiley-Interscience, London (1971)
2. Scott, S. K., Chemical Chaos, Clarendon, Oxford Chapter 3, p.60 (1991)

28.3 Instability of a Complex Reaction in a CSTR

28.3-1 Belousov-Zhabotinskii reaction

As an example of complex reactions, the following Belousov-Zhabotinskii (B-Z) reaction are investigated by many researchers.

Elementary Steps of Belousov-Zhabotinskii reaction (FKN scheme)

$Br^- + HOBr + H^+ \leftrightarrow Br_2 + H_2O$ (R1)
$HBrO_2 + Br^- + H^+ \leftrightarrow 2HOBr$ (R2)
$BrO_3^- + Br^- + 2\,H^+ \leftrightarrow HBrO_2 + HOBr$ (R3)
$2\,HBrO_2 \leftrightarrow HOBr + BrO_3^- + H^+$ (R4)
$BrO_3^- + HBrO_2 + H^+ \leftrightarrow 2\,BrO_2\cdot + H_2O$ (R5)
$Ce^{3+} + BrO_2\cdot + H^+ \leftrightarrow Ce^{4+} + HBrO_2$ (R6)
$Ce^{4+} + BrO_2\cdot + H_2O \leftrightarrow Ce^{3+} + BrO_3^- + 2\,H^+$ (R7)
$Br_2 + CH_2(COOH)_2 \leftrightarrow BrCH(COOH)_2 + Br^- + H^+$ (R8)
$6\,Ce^{4+} + CH_2(COOH)_2 + 2\,H_2O \leftrightarrow 6\,Ce^{3+} + HCOOH + 2\,CO_2 + 6\,H^+$ (R9)
$4\,Ce^{4+} + BrCH(COOH)_2 + 2\,H_2O \leftrightarrow 4\,Ce^{3+} + HCOOH + Br^- + 2\,CO_2 + 5\,H^+$ (R10)

This reaction involves the following autocatalytic step:
$2\,Ce^{3+} + BrO_3^- + HBrO_2 + 3\,H^+ \leftrightarrow 2\,Ce^{4+} + 2\,HBrO_2 + H_2O$ (R5+2R6)
This autocatalytic step switches on or accelerates the overall rate of reaction.
We are interested in an experimental work from a viewpoint of reactor design and operation.

Fig.28.3-1 shows an experimental setup. Three kinds of CSTRs different in volume but similar in shape are used for examining the effect of reactor volume. Their effective volumes are 49 ml, 99 ml, and 159 ml, respectively.

As described in the Brusselator model (28.2), this kind of complex reaction is so sensitive to the initial condition that the reaction starts from the condition of empty reactor filled with nitrogen gas only. Four kinds of feed solutions shown in Table 28.3-1 are supplied separately at a specified feed rate into the reactor by a common peristaltic pump. The reaction temperature is kept at 25℃. The mean residence time based on the total rate of the four feeding streams is changed as a controlling parameter. Each CSTR used is well mixed with a three-bladed propeller rotating at 2,300 rpm.

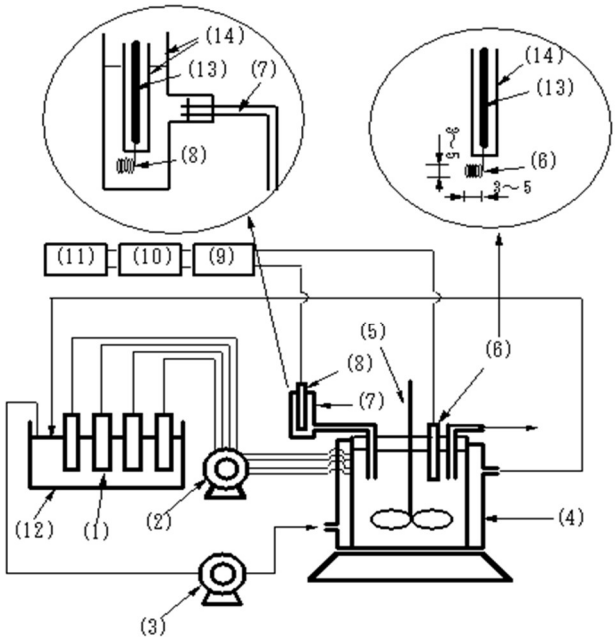

(1) Feed containers (2) Peristaltic pump (3) Magnetic pump (4) Cylindrical glass reactor , (5) Stirrer (6) Pt-electrode (7) Saturated KNO_3 agar bridge (8) Ag-AgCl electrode (9) DC amplifier (10) Disc recorder (11) mV recorder (12) Constant temperature water bath (13) Cu-wire (14) Glass tube

Fig.28.3-1 Experimental setup for observing dynamic chemical oscillations of BZ reaction

The redox potential based on the activity ratio of Ce4+/Ce3+ is measured as the dynamical signal of the reaction with a platinum electrode. At very small mean residence times (large space velocity) , the reaction state becomes steadily dynamically-balanced, so that any chemical oscillations do not occur. At very large mean residence times, the reaction field becomes in chemical equilibrium. In a relatively wide range of mean residence time between these two limits of reaction state, there appear two types of oscillations depending upon the mean residence time: (1) single-peak periodic and (2) chaotic oscillations. Some of the sustained chemical oscillations experimentally observed are shown in Figs.28.3-2~4. Any CSTR shows chaotic oscillations when the mean residence time becomes large.

Table 28.3-1 Four feed solutions supplied separately into CSTRs

Feed	Reagent	Concentration (kmol/m$^{3)}$
Feed 1	Malonic acid $CH_2(COOH)_2$	1.20
Feed 2	Sodium bromate $NaBrO_3$	0.56
Feed 3	Sulphuric acid H_2SO_4	0.80
Feed 4	Potassium bromide KBr Cerium sulphate $Ce_2(SO_4)_3$	1.4×10^{-5} 0.40×10^{-2}

28.3-2 Chemical oscillations sustained in a continuous B-Z reaction

It can be seen from Figures 28.3-2 to 4 that the temporal variation of the redox potential measured by the platinum electrode exhibits three-different chemical oscillations at the respective mean residence times.

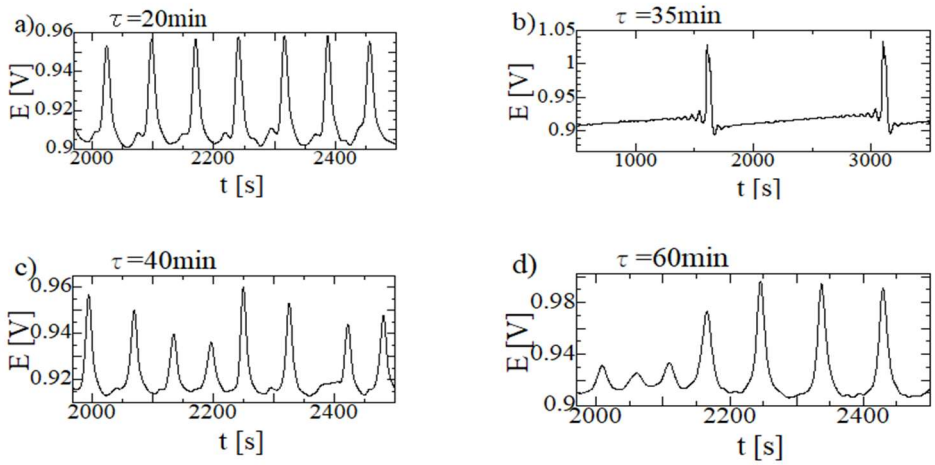

Fig.28.3-2 Chemical oscillations sustained in a small CSTR (V = 39 ml)

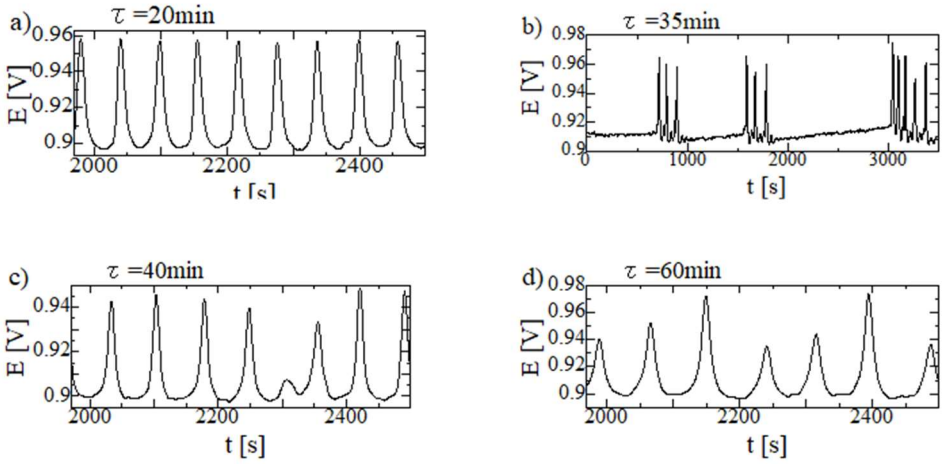

Fig.28.3-3 Chemical oscillations sustained in a middle-sized CSTR (V = 99 ml)

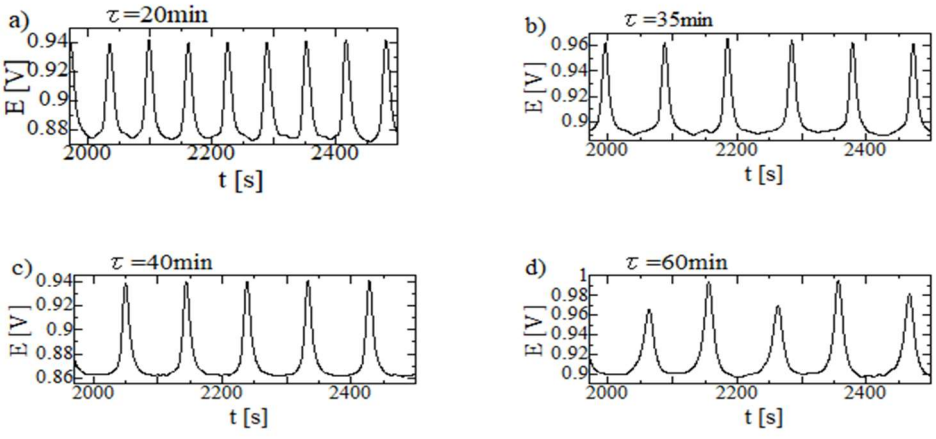

Fig.28.3-4 Chemical oscillations sustained in a large CSTR (V = 159 ml)

When $\tau = 35$ min in the two smaller reactors, there appears an intermittent oscillation between the single-peak and chaotic oscillations.
In the case of the largest reactor (V = 159 ml), the stable single-peak chemical oscillations survive to some larger region of the mean residence time.

Table 28.3-2 Bifurcation scenario of chemical oscillations depending upon reactor volume

Mean Residence Time	Reacting Liquid Volume V (ml) in CSTR		
τ (min)	49 ml	99 ml	159 ml
20	Single Peak	Single Peak	Single Peak
30	Single Peak	Single Peak	Single Peak
35	Intermittent	Intermittent	Single Peak
40	Chaotic	Chaotic	Single Peak
45	Chaotic	Chaotic	Single Peak
50	Chaotic	Chaotic	Chaotic
60	Chaotic	Chaotic	Chaotic

Table 28.3-2 shows the bifurcation scenario of chemical oscillations obtained with the three different-sized CSTRs. The largest reactor indicates a transition point different from the other two smaller ones.

It should be considered that there is a narrow transition window having peculiar bursting-like intermittent oscillation between the single peak and chaotic chemical oscillations. Since the reciprocal of mean residence time means space velocity, this bifurcation scenario may be contrasted with that of the Brusselator model (Table 28.2-1). We can conjecture that any complex chemical reactions tend to have chaotic chemical oscillations when the mean residence time becomes large.

Apart from temperature control, what reaction state should be attained by steady operation depends upon the following various mixing conditions: (1) initial condition and start-up operation, (2) degree of mixing/micromixing, and (3) way and position for feeding and effluxing.

1. Kataoka, K., Ohmura, N., Watanabe, S., Sumida, K., and DEki, S., Electrochemical observation of instabilities of the Belousov-Zhabotinskii reaction in CSTR, *J. Appl. Electrochem.,* vol.24, 647-651 (1994)
2. Kataoka, K., Plenary Lecture , 2000 Annual Meeting AIChE, Los Angeles, Nov.12-17 (2000)

28.4 Dynamical Behavior of an Emulsion Polymerization Process

Nonlinear dynamics such as self-sustained chemical oscillations is also encountered in continuous emulsion polymerization processes. Usually in order to stabilize an emulsion polymerization process, a single CSTR is very often employed in industrial large-scale productions.

Even at steady operation, there can appear self-sustained oscillations in the elementary steps.

It is known in the process of emulsion polymerization that self-sustained oscillations observed in time-dependent monomer conversion result from intermittent nucleation of primary polymer particles.

As distinct from water-insoluble monomer such as styrene, an emulsion polymerization of vinyl acetate exhibits an interesting mechanism owing to solubility in aqueous phase. The self-sustained oscillations observed in time-dependent monomer conversion can be considered to result from intermittent nucleation of the primary polymer particles. The main interest in this section is focused on the instability of continuous polymerization of water-soluble monomer due to the water-soluble emulsifier below CMC (Critical Micelle Concentration, see Chapter 21.2).

Reaction Scheme of Emulsion Polymerization

Decomposition of water-soluble initiator: $I \rightarrow 2R\cdot$ (S1)
Initial step of propagation: $R\cdot + M \rightarrow P_1\cdot$ (S2)
Subsequent propagation: $P_n\cdot + M \rightarrow P_{n+1}\cdot$ (S3)
Termination (1): $P_m\cdot + P_n\cdot \rightarrow P_{m+n}$ (S4)
Termination (2): $P_m\cdot + P_n\cdot \rightarrow P_m + P_n$ (S4)'
Entry: P_z + latex particle → entry (S5)

28.4-1 Experimental method of continuous emulsion polymerization

The recipe of the continuous emulsion polymerization in a CSTR is indicated in Table 28.3-1.

Table 28.4-1 Recipe of continuous emulsion polymerization

	Reagent	Quantity
(A) Initial contents of reactor	Distilled water Vinyl acetate monomer Sodium dodecyl sulfate	164 ml 22 ml 0.131 g
(B) Initiator solution	Ammonium peroxodisulfate	0.218 g/10 ml water
(C) Initiator & emulsifier In solution tank	Distilled water Ammonium peroxodisulfate Sodium dodecyl sulfate	4,000 ml 5 g 3 g
(D) Monomer tank	Vinyl acetate monomer	600 ml

Fig.28.4-1 shows an experimental setup for the continuous emulsion polymerization. The CSTR (effective volume = 196 ml) (1) consists of a cylindrical glass vessel with water jacket and a stirrer (2) made of Teflon. Firstly the monomer is fed directly into the CSTR and emulsified by adding the emulsifier. After the initial operation adding the initiator, the monomer and the emulsifier and initiator solution are continuously supplied from the monomer tank (6) and the solution tank (7), respectively.

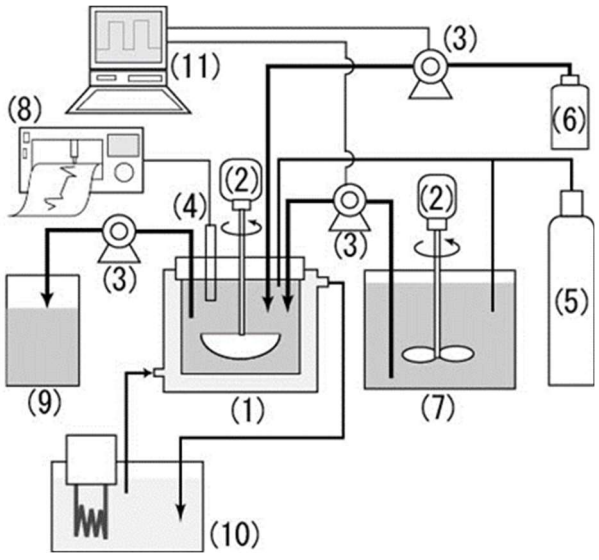

Fig.28.4-1 Experimental setup for continuous emulsion polymerization of water-soluble monomer.
(1) CSTR, (2) Stirrer, (3) Pump, (4) Thermocouple, (5) Nitrogen gas, (6) Monomer, (7) Aqueous solution of emulsifier and initiator, (8) mV recorder, (9) Sampling collector, (10) Temperature-controlled water, (11) Computer

Since this reaction is very sensitive to the initial condition, the following operation procedure is fulfilled. Initially the reactor is filled with an emulsified mixture (A) and then the reaction is started with adding the initiator solution (B) into the reactor. Ammonium peroxodisulfate **$(NH_4)_2S_2O_8$** (water-soluble initiator) and sodium dodecyl sulfate **$CH_3(CH_2)_{11}OSO_3Na$** (emulsifier) are premixed at 50℃ in another stirred tank (7). The vinyl acetate monomer **$CH_3COOCH{:}CH_2$** (D) and the aqueous solution of initiator and emulsifier (C) are fed separately and continuously into the reactor at a constant ratio of feed rates, i.e. C/D = 8. The mean residence time is defined from the total feed rate of these two streams. The reaction temperature is kept at 55℃.

Figure 28.4-2 is a PSD of monomer droplets emulsified in an initial solution of the reactor at 800 rpm. The PSD is obtained by use of the laser diffraction particle size analyzer. This gives the mean droplet diameter to be 2.712 μm.

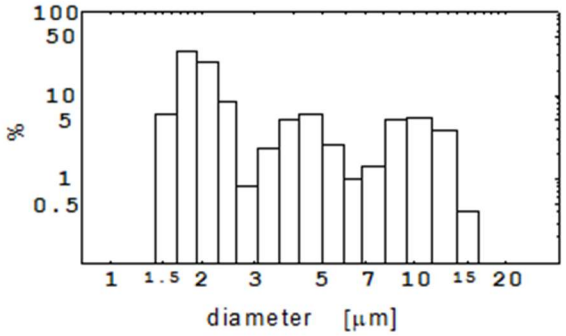

Fig.28.4-2 Particle size distribution of monomer droplets emulsified in the initial solution at 800 rpm. (Mean size = 2.712μm)

28.4-2 Dynamical behavior of continuous emulsion polymerization processes

Figure 28.3-3 shows temporal variation of monomer conversion obtained at the same mean residence time ($\tau = 27.2$min) with various revolution numbers of the stirrer and the corresponding mean diameters of monomer droplets (given in the brackets) of the initial emulsified solution measured by the laser-diffraction particle-size analyzer.

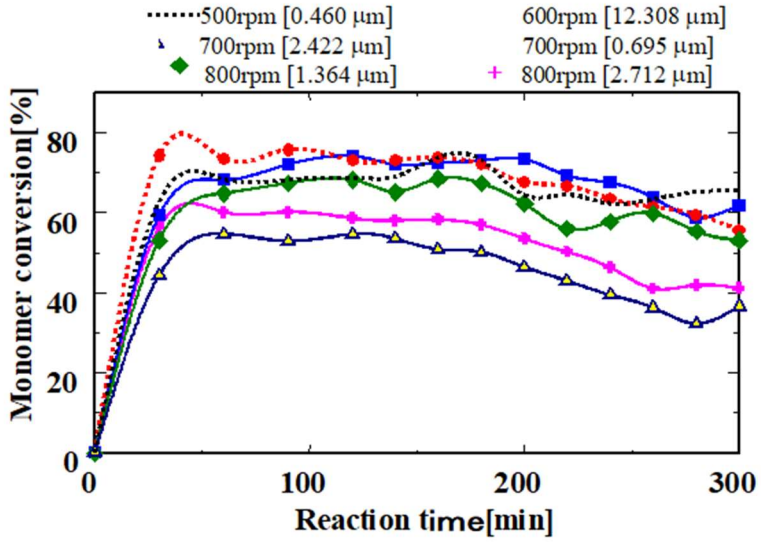

Fig.28.4-3 Temporal variation of monomer conversion observed at various stirrer revolutions. The number given in bracket means initial mean diameter of emulsified monomer droplets.

The monomer conversion attained at steady operation depends neither on the stirrer revolution number nor on the mean diameter of emulsified monomer droplets. This implies that the total surface area of monomer droplets does not influence very much the overall reaction rate. It can be considered that the elementary process for dissolving monomer molecules into the aqueous phase is not a rate-controlling step and that the aqueous phase is saturated with monomer. The homogeneous nucleation begins with the radical reaction of dissolved monomer with water-soluble initiator radicals. When the oligomeric radicals become hydrophobic because of their increased molecular weight, primary solid polymer particles appear due to precipitation. The primary particles grow by the further propagation reaction. If the mass transfer process of the dissolved monomer and oligomer toward the primary growing particles were a rate-controlling step, the monomer conversion should have become high owing to the large mixing effect when the revolution number is high.

As can be seen from Fig28.4-4, the emulsion polymerization reaction would not occur at the reaction temperatures below 53℃.

28.4-3 Temporal variation in particle size distribution of polymer particles

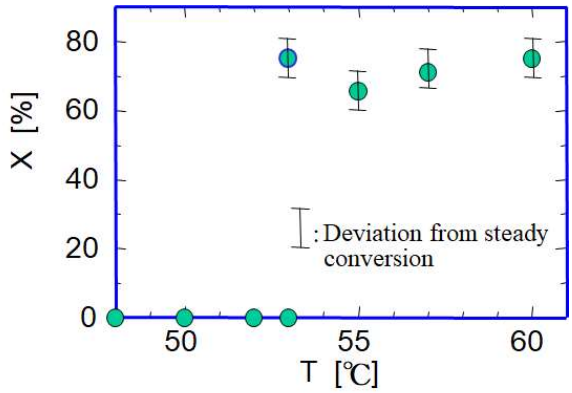

Fig.28.4-4 Variation of time-averaged monomer conversion with reaction temperature. (mean residence time = 24.2 min, stirrer revolution = 600 rpm)

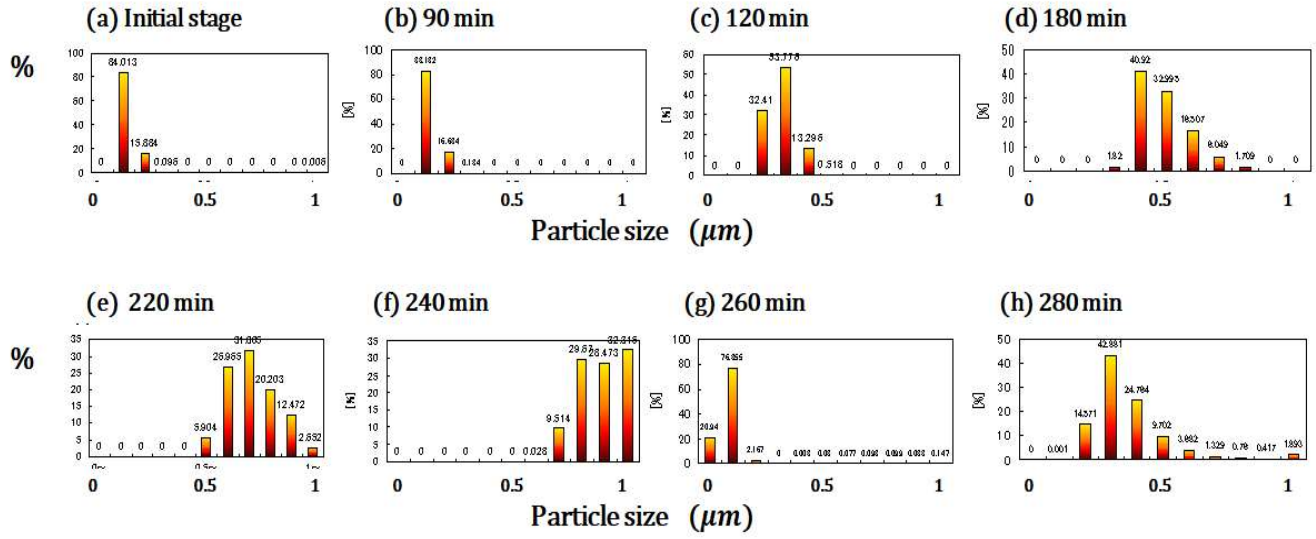

Fig.28.4-5 Latex particle size distributions sampled in efflux solutions observed by laser diffraction particle size analyzer. (Revolution = 800 rpm, mean residence time τ = 27.2 min.)

Fig.28.4-5 shows temporal variation in the PSDs of latex particles sampled at various times. It can be considered that the PSDs indicate a kind of cyclic behavior in the continuous emulsion polymerization.

The PSDs from b to f indicate the continuous growth of secondary particles due to selective precipitation of hydrophobic nuclei to the surfaces of the secondary particles. The number of the growing secondary particles decreases owing to the continuous discharge of the reacting solution from the CSTR. The process seems to end at the critical particle size of about 1 μm. For 90 min in the first term, a steady PSD is maintained with the primary particles only growing due to polymerization reaction. For the next 3 hours, unsteady PSDs appear. This indicates a process of selective agglomerative precipitation combined with continuous nucleation due to polymerization reaction. In such a manner, agglomerative precipitation process is repeated.

It can be considered that the following cyclic process begins with the first initiation of homogeneous nucleation under the condition below the CMC of free emulsifier:

1) Initiator radicals are produced by decomposition in the aqueous phase
2) Polymerization starts with making oligomeric radicals due to the initial propagation reaction of the water-soluble initiator radicals with the monomer dissolved in the aqueous phase. The homogeneous nucleation step is controlled by free emulsifier in the aqueous phase when its concentration is relatively high.
3) When the growing oligomeric radicals become hydrophobic, a large number of primary particles are formed via nucleation due to the precipitation of hydrophobic oligomeric radicals.
4) As the primary particles grow, i.e. as the total surface area of the particles increases rapidly, the consumption rate of free emulsifier for covering over the particle surfaces becomes larger than the net feed rate of emulsifier. At this stage, the reaction rate reaches a local maximum and the PSD becomes very narrow and has a very small average diameter.
5) When the concentration of free emulsifier becomes extremely low, the homogeneous nucleation is suppressed while the agglomeration of the primary grown-up particles occurs very actively to become very large secondary particles owing to the shortage of emulsifier covering over the primary particle surfaces. At this stage, the reaction rate goes down to a local minimum and the PSD is expanded with its peak shifting toward a large diameter. At the end of this stage, the average particle size becomes maximum.
6) Most of the secondary particles are discharged with the continuous efflux of the CSTR reactor. When the net feed rate of emulsifier becomes larger than the consumption rate of free emulsifier, the homogeneous nucleation becomes active again. At the beginning of this stage, the PSD becomes bimodal because of the mixture of the newly-produced primary particles and the remaining old secondary particles owing to the effect of residence time distribution in the CSTR.

This result suggests that the PSD of polymer particles can be controlled by controlling the intermittent nucleation and agglomeration, i.e. the concentration of the free emulsifier in the aqueous phase.

TEM (transmission electron microscope) photographs of polymer particles are shown in Fig.28.4-6.

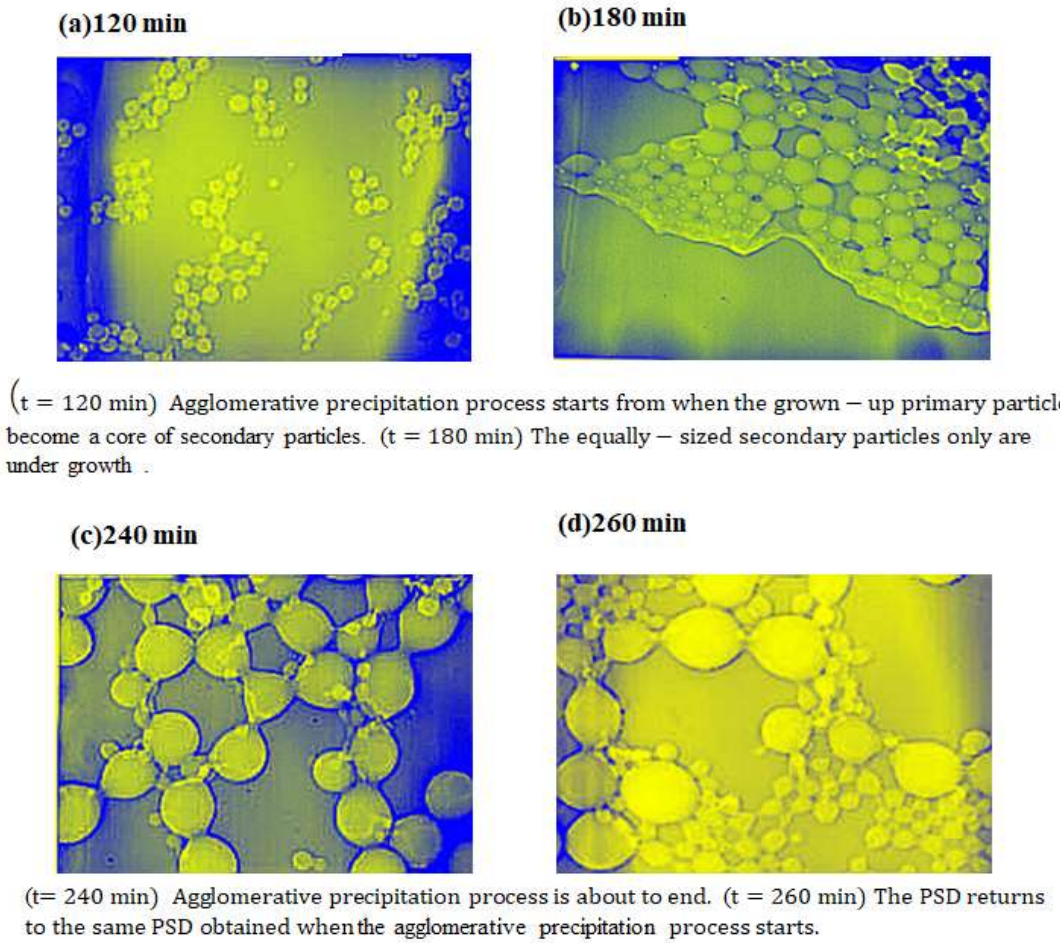

Fig.28.4-6 TEM photographs of latex particles sampled at 120, 180, 240, and 280 min. (Revolution = 800 rpm, mean residence time τ = 27.2 min.)

The TEM photographs indicate a cyclic change controlled by the agglomerative precipitation process. After 260 min, the large secondary particles are discharged from the CSTR and then the PSD returns to the state of 120 min containing secondary particle cores only. This time period (from 120 to 260 min) implies the second stage of secondary particle growth.

From τ = 280 min, the next agglomerative precipitation proceeds, but some grown-up secondary particles (largest particles) are still left behind. After the first stage of primary particles production, the second stage of complex process combined between homogeneous nucleation and agglomerative precipitation is repeated with a large time scale of 3 hr. The selective agglomerative precipitation regarded as a kind of mass transfer influenced by an electrostatic effect in a diffusion electric double layer. The electrostatic attraction and repulsion occur unbalanced in an electrostatic charge due to the adsorption of ionic emulsifier.

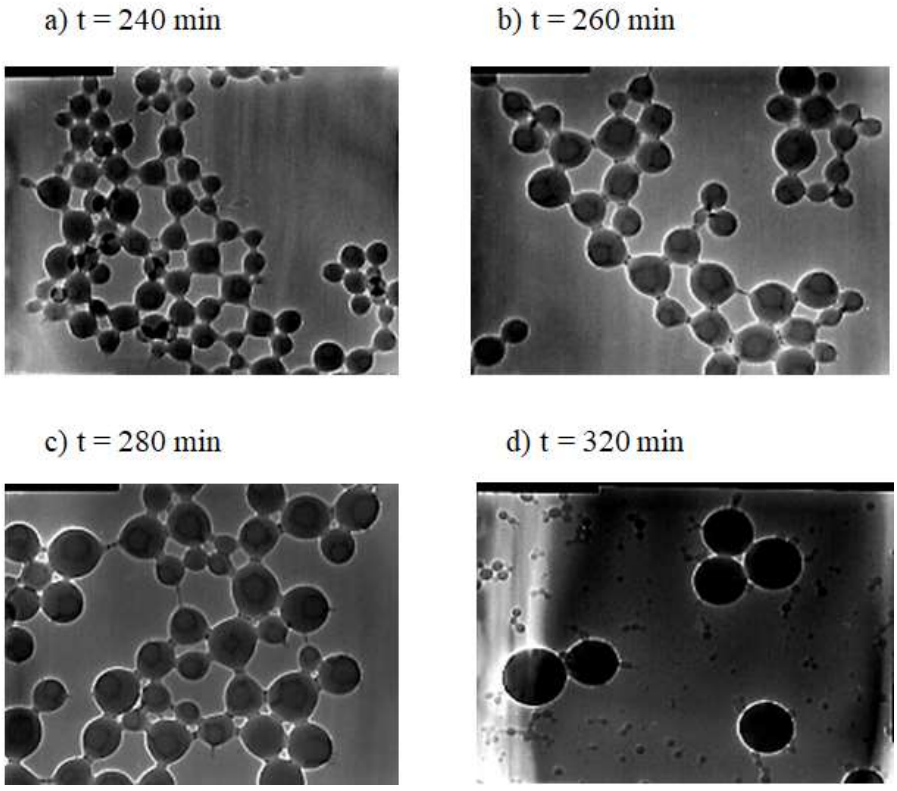

Fig.28.4-7 TEM photographs of latex particles obtained when mean residence time t = 31.1 min. The diameter of the largest particles when t = 320 min is approximately 1 μm.

Fig.28.4-7 clearly indicates the cyclic second stage process of the primary particles growing to the large secondary particles. This implies that a primary grown-up particle become a core of the secondary particle. It can be seen that the relatively small primary particles growing when t = 240 min in the early stage are undergoing the successive growing process due to selective agglomerative precipitation for about 1.5 hr. When t = 320 min, the next stage process starts by the very small primary particles but some of the grown-up secondary largest particles are still left behind in the CSTR reactor.

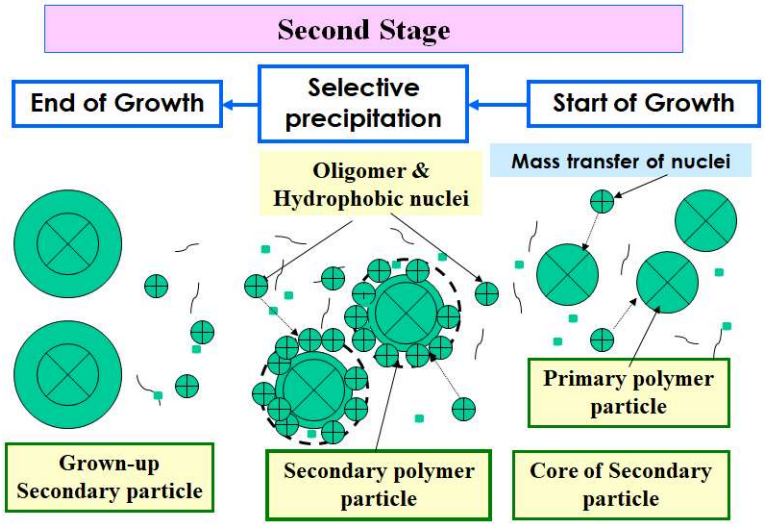

Fig.28.4-8 Second stage of emulsion polymerization controlled by selective agglomerative precipitation

Fig.28.4-8 indicates the second stage process of the growth of the secondary particles due to the selective agglomerative precipitation.

We would like to add a very fair possibilities of periodical or stepwise switching operation for controlling the PSDs of latex particles.[2)]

1. Ohmura, N., Kataoka, K., Watanabe, S., Okubo, M., Controlling Particle Size by Self-Sustained Oscillations in Continuous Emulsion Polymerization of Vinyl Acetate, *Chem. Eng. Sci.,* Vol.53, 2129 (1998)
2. Ohmura, N.,.Kitamoto, K., Yano, T., and Kataoka, K., Novel Operating Method for Controlling Latex Particle Size Distribution in Emulsion Polymerization of Vinyl Acetate, *Ind. Eng. Chem. Research,* Vol.40, 5177-5183 (2001)
3. Kataoka, K., Consideration of Instabilities of Nonlinear Transport and Reaction in the Synthesis of Complex Chemical Process Systems, Plenary Lecture Presentation Record, 2000 Annual Meeting of AIChE, Los Angeles, Nov. 12-17 (2000)

Nomenclature

$C_A,\ C_B$	concentration of reactant A and B, [kmol/m^3]
E	redox potential, [V]
F	feed rate, [kmol/s] or [m^3/s]
f	space velocity, [1/s]
k_1, k_2, k_3	reaction rate constant,
T	temperature, [K]
t	time, [s]
V	reactor volume, [m^3]
$x,\ y$	concentration of intermediate component,
τ	specified time or mean residence time, [s]

Subscripts

A, B	component A, B
ss	stationary state

INDEX

POST FACE

The author has felt very happy to find his way to this place. He has been confining himself to an educational concept as to how to make creative problems rather than how to solve the given problems.

He intends to have given many examples for application of fundamental theories and models to engineering. He hopes that the readers and students will bring themselves to feel like making more challenging problems.

Several special topics given as the starting point for development in PART III will encourage the readers to take further interest for their progressive development.

In particular, in the last half of the text, several miscellaneous topics are dealt to widen the all-round knowledge for chemical engineering for future challenge.

The PART IV gives various complicated topics that the graduates students should have as the fundamental background serviceable for their advanced challenges.

It is hoped that active and practical application of those concepts will be developed in the future for more challenging problems.

KUNIO KATAOKA